

EXAMINATION OF THE HIGH TEMPERATURE EQUILIBRIUM IN THE Ti-Al-Nb  
TERNARY ALLOY SYSTEM

By

ORLANDO RIOS

A DISSERTATION PRESENTED TO THE GRADUATE SCHOOL  
OF THE UNIVERSITY OF FLORIDA IN PARTIAL FULFILLMENT  
OF THE REQUIREMENTS FOR THE DEGREE OF  
DOCTOR OF PHILOSOPHY

UNIVERSITY OF FLORIDA

2009

© 2009 Orlando Rios

To my Mother and Father

## ACKNOWLEDGMENTS

Firstly, I would like to thank Dr. Fereshteh Ebrahimi, who introduced me to this study and provided me the opportunity to work in a great research group. Without this, I would not have an acknowledgment section to write nor would I have such an interesting study to discuss. I admire Dr. Ebrahimi's approach to research and her ability to identify the fundamental questions but what inspires me most is her ability to teach and mentor her students. During my time working on this study, I had the opportunity to teach an undergraduate class in which I learned first-hand how difficult it can be to teach well. I am especially grateful for the hours of discussion we spent together.

I would like to thank my committee members for their support and discussions. Dr. Martin Glicksman's input on many occasions was invaluable. I greatly appreciate the time he spent with me on my research. I would also like to thank Dr. Valentin Craciun, for hours of discussion and support with the development of high temperature X-ray diffraction capabilities for key experiments within this study. I am thankful that Dr. Robert DeHoff taught me many of the fundamentals I will carry with me throughout my professional career. I would also like to thank Dr. William Lear for his participation on my committee and discussion regarding the theory of turbine engines. These discussions were quite helpful on several occasions. I would like to thank Dr. Hans J. Seifert for sharing his expertise in CALPHAD and for use of the facilities at the Technical University of Freiberg.

I am grateful for the continual support and friendship of my current and past research group members Sonalika Goyel, Damian Cupid, Majesh Tanniru, Daniel Tien, Michael S Kesler, Sankara S. V. Tatiparti, Ian Liu and Yanli Wang. It has been a pleasure working in the company of all of them. I would like to thank Sonalika for her collaboration as we both got started on this research as well as the hours of discussion we had throughout. I would especially like to

acknowledge Mike for building and maintaining some of the vital equipment that made my research possible. Damian's constant collaboration was vital over the years as we embarked on this study together. Additionally, I would like to thank Yanli for spending several months providing direct support as I became acquainted with my research. Her guidance was helpful in my quick start in this study. I would also like to acknowledge undergraduate students Daniel Heinz for hours of assistance with developing and conducting HT-XRD measurements and Jonah Klemm-Toole for excellent support with arc-melting and sample preparation.

I would like to thank Dr. Anne Donnelly and SEGEP for their support throughout the entirety of my graduate research. Anne has been a friend and a mentor throughout the years which was important in my professional development and path through graduate school. I know I will miss this group of friends and colleagues.

I would like to thank the MAIC facility for providing a user friendly environment for all my characterization. Without these facilities this research would have been much more difficult. The staff at MAIC has been especially helpful. Dr. Gerald Bourne's guidance during my many hours attempting to prepare difficult TEM samples is most appreciated. Wayne Acree's expertise in EPMA was of prime importance throughout my work and Kerry Siebein's help with STEM was most useful.

I acknowledge the National Science Foundation and the Air Force Office of Scientific Research (NSF/AFOSR) for their interest in and support of this study under grant number DMR-0605702.

I am grateful for all the friends I have met here at the University of Florida. It was really amazing having so many great friends to share time with. I feel especially grateful for Thierry Dubroca's years of friendship throughout my studies in Gainesville. I know we will continue to

be friends for years to come. My friendship to Gary Richards has been most fruitful. I have learned a lot from our many fishing and hunting trips. I would also like to thank Diana Mercado for her friendship through the last years of my studies. Her support in the last few months made a positive impact on this experience.

Last and most importantly I would like to thank my family. Their support made this accomplishment possible. I am glad that distance did not separate us. I am thankful my father spent years teaching me how to understand mechanical problems and my mother for being a role model. I would like to thank Steve for his support and involvement in my life. I especially enjoyed the exciting rides on the experimental aircraft. I am especially grateful to my sisters Jovanna and Jhoslen for being there for me every time I needed them. I am also glad that my grandparents kept close contact throughout these busy years.

## TABLE OF CONTENTS

	<u>page</u>
ACKNOWLEDGMENTS .....	4
LIST OF TABLES .....	10
LIST OF FIGURES .....	11
ABSTRACT.....	18
CHAPTER	
1 INTRODUCTION .....	20
2 BACKGROUND .....	25
2.1 Important Phases in the Ti-Al-Nb Alloy System.....	25
2.2 Liquidus Surfaces .....	27
2.3 Isothermal Sections.....	30
2.4 Invariant Reactions .....	31
2.4.1 Ternary Peritectic .....	32
2.4.2 Ternary Eutectic .....	33
2.5 Interpretation of DTA Data for Ternary Alloys .....	34
2.6 Outstanding Questions.....	37
3 EXPERIMENTAL.....	52
3.1 Alloy Preparation.....	52
3.2 Thermal Analysis.....	52
3.3 Heat Treatments.....	57
3.3.1 Heat Treatment Schedules.....	57
3.3.2 Selection of Isothermal Hold Times.....	58
3.4 Microstructural Analysis .....	60
3.5 High Temperature XRD .....	61
4 $\beta$ -PHASE EXTENSION.....	68
4.1 Introduction.....	68
4.2 Thermal Analysis.....	69
4.2.1 Thermal Analysis of Phase Transformations and Melting.....	70
4.2.2 Stability of Thermal Events.....	71
4.3 Microstructural Evaluations.....	73
4.4 In Situ High Temperature Phase Evaluation .....	74
4.4.1 High Temperature X-Ray Diffraction .....	74
4.4.2 Microstructural Analysis of HT-XRD Samples .....	77
4.5 Summary.....	78

5	TERNARY EUTECTIC REACTION INVOLVING THE L, $\gamma$ , $\sigma$ , $\eta$ PHASES.....	89
5.1	Introduction.....	89
5.2	Thermal Analysis.....	91
5.3	As-Cast Materials .....	92
5.4	Characterization of Heat Treated Alloys .....	95
5.5	Development of the Invariant Reaction.....	98
5.6	Solidification Path in As-Cast Materials .....	100
5.7	Summary.....	102
6	TERNARY PERITECTIC REACTION INVOLVING THE L, $\gamma$ , $\sigma$ , $\beta$ PHASES.....	115
6.1	Introduction.....	115
6.2	The L, $\sigma$ , $\beta$ Bivariant Equilibrium.....	116
6.3	Phase Transformation Path in Alloy A141 .....	119
6.3.1	Phase Reactions in the Interdendritic Region.....	119
6.3.2	Microstructural Evolution of Three-phase Reaction from the Liquid.....	119
6.3.3	Analysis of the Solid State Transformations after Solidification.....	120
6.3.4	TEM Investigation of the L, $\sigma$ , $\beta$ , $\gamma$ Invariant Reaction .....	122
6.3.4	Region 1 Microstructural Evaluations of Phases in Lamellar Structure .....	123
6.3.5	Region 2 Microstructural Evaluations of Phases Formed through the Invariant Reaction.....	124
6.4	Development of the L, $\beta$ , $\gamma$ and $\sigma$ Ternary Peritectic Reaction .....	126
6.5	Summary.....	129
7	HIGH TEMPERATURE EQUILIBRIUM AMONG THE L, $\gamma$ , $\sigma$ , $\beta$ PHASES .....	153
7.1	Introduction.....	153
7.2	Selection of Alloys .....	153
7.3	$\sigma$ + $\gamma$ Equilibrium: Alloys A133, A170, and A171.....	154
7.3.1	Evaluation of A133 Alloy .....	154
7.3.1.1	Thermal analysis .....	154
7.3.1.2	Structural and chemical analyses: as-cast alloys.....	155
7.3.1.3	Structural and chemical analyses: heat-treated alloys at 1510C .....	156
7.3.2	Evaluation of Alloys A170 and A171 .....	156
7.4	$\gamma$ + $\beta$ + $\sigma$ Equilibrium: Alloy 132 .....	157
7.4.1	Thermal Analysis.....	157
7.4.2	Microstructural and Chemical Analyses .....	157
7.5	$\sigma$ + $\beta$ Alloys.....	159
7.5.1	Thermal Analysis.....	159
7.5.2	Microstructural and Chemical Analysis .....	160
7.6	Summary.....	161
8	TRANSFORMATION OF THE $\gamma$ -PHASE UPON QUENCHING .....	177
8.1	Introduction.....	177
8.2	Microstructural Evaluation .....	177

8.3	Compositional Analysis.....	179
8.4	Structural Analysis.....	180
8.5	Discussion.....	182
8.6	Thermal Stability of the Quenched Materials.....	183
8.7	Summary.....	185
9	CONCLUSIONS AND SUGGESTED FUTURE STUDIES .....	194
9.1	Summary and Conclusions .....	194
9.2	Suggested Future Work .....	196
	LIST OF REFERENCES .....	198
	BIOGRAPHICAL SKETCH .....	204

## LIST OF TABLES

<u>Table</u>	<u>page</u>
2-1	Important phases in the Ti-Al-Nb system and their structural data .....25
3-1	Melting temperatures at the respective scan rates of standard materials.....56
5-1	Transformation temperatures of as-cast and thermally cycled materials showing the 1st deviation from the baseline (1st dev), the peak positions (max) and the return to the baseline (return) for the 1st and 2nd peak in the convoluted double peak (DB) as well as the single peak (SP). .....92
5-2	Compositional analysis of the heat-treated bulk materials as well as the composition of the individual phases . .....97
5-3	Calculated wt% of the phases computed from the $\eta/\gamma/\sigma$ tie-triangle, the volume fractions of phases obtained from micrographs, along with the measured wt% of each phase using the vol % of phases. ....98
6-1	Composition of alloys measured by EPMA.....117
6-2	Compositions of interdendritic regions of each experimental alloy.....118
6-3	TEM EDS compositional analysis of each phase in regions 1 and 2.....124
7-1	The bulk composition of the experimental alloys measured by EPMA .....154
7-2	The composition of phases equilibrated at 1510C for each alloy.....157

## LIST OF FIGURES

<u>Figure</u>	<u>page</u>
2-1 A lattice model of the B2 structure based on crystallographic data reported in [18].	38
2-2 A lattice model of a) the $\gamma$ -phase [20] and b) the h-phase [21].	39
2-3 A lattice model of the $\sigma$ -phase based on crystallographic data reported in [22].	40
2-4 A lattice model of the $\eta$ -phase based on crystallographic data reported in [23].	41
2-5 Liquidus projections by a) Perepezko et al (1990). [57] and b) Kattner and Boettinger (1992) [56].	42
2-6 Liquidus projections by a) Zdziobek et al. (1995) [55] and b) Servant and Ansara (1998) [18].	43
2-7 Liquidus projections by a) Leonard et al. (2000) [54] and b) Raghavan (2005) [16].	44
2-8 Isothermal sections at a) 1200C by Hellwig et al. (1998) [25] and b) 1150C by Chen et al. (1996) [47].	45
2-9 Isothermal sections at 1400C by Chen et al. (1996) [47].	46
2-10 Hypothetical ternary peritectic phase diagram taken from Rhines (1956) [67] marked with a theoretical non-equilibrium solidification path.	47
2-11 SEM micrographs showing a reported ternary peritectic reaction in the Ni-Al-Ta alloy system [71].	48
2-12 Hypothetical ternary eutectic phase diagram taken from Rhines (1956) [67] marked with a theoretical non-equilibrium solidification path.	49
2-13 Calculated liquidus projection of the Al-Cu-Fe alloy system showing the solidification path of two alloys through a ternary transition reaction and a ternary eutectic reaction [72].	50
2-14 Calculated DTA response of the solidification of alloy 1 through the liquidus and ternary eutectic reaction [72].	51
2-15 Calculated DTA response of the solidification of alloy 2 through the liquidus, ternary transition reaction and finally through the ternary eutectic reaction [72].	51
3-1 Schematics of a) a DTA comparable to the Setaram used in this study with heat-flow paths [73] and b) the equivalent circuit that models the heat-flow and capacitance through electrical simulations.	63

3-2	Simulation of a DTA modeling the systems response to a high and low conductivity gas. ....	64
3-3	Calibration (Temperature correction) curves using standard high purity reference materials (Ni, Cu and Al).....	64
3-4	DTA curve of alloy A133 at 10K/min. ....	65
3-5	DTA curve of alloy A133 at 10K/min. with isothermal hold at A) 1510C and B) 1600C.....	65
3-6	Ion-generated secondary electron image during the FIB sample preparation showing a) initial area of interest b) deposition of protective Pt layer c) cutting of trenches and d) free standing thin foil.....	66
3-7	Images of a) schematic of HT-XRD stage and sample and b) photograph of the stage after fabrication. ....	67
4-1	Combined liquidus projections of Kattner and Boettinger [56], Servant and Ansara [18] and Leonard et al. [54] which is published in Rios et al. [77] showing the composition of alloy 11. ....	79
4-2	DTA curve of as-cast alloy 11 though the solidus and liquidus at 10K/min. ....	80
4-3	DTA curve of thermally cycled alloy 11 at 10K/min, which is marked with the temperatures at which HT-XRD measurements were taken. ....	80
4-4	DTA curves of solutionized alloy 11 at 10K/min cycled around the a) lower temperature peaks and b) higher temperature peaks.....	81
4-5	Interrupted heating DTA curves of solutionized alloy 11 at 10K/min with isothermal holds within the a) low temperature peaks and b) high temperature peaks. ....	82
4-6	XRD of as-cast alloy 11 which identified the $\beta$ and $\gamma$ phases.....	83
4-7	SEM micrograph of as-cast alloy 11.....	83
4-8	TEM micrographs of as-cast alloy 11 marked with the $\beta$ and $\gamma$ phases.....	84
4-9	a) Transformation path of alloy D2 reported by Hoelzer [19] and b) DTA at 10K/min of alloy D2, which was arc-melted for this study, marked with the temperatures at which XRD measurements were taken. ....	85
4-10	Simulated powder XRD profiles for the $\beta$ , $\gamma$ and $\sigma$ phases marked with the 2 theta range where a minimum number peaks between the three phases were found to overlap.....	86

4-11	HT-XRD measurements of alloy D2 at temperatures 1 and 2 marked on the respective DTA curve in Figure 4-9b. ....	86
4-12	HT-XRD measurements of alloy 11 at a) temperatures within the edge of the two-phase region and b) temperatures 1, 2, 3 and 4 marked on the respective DTA curve in Figure 4-3.....	87
4-13	SEM micrographs of alloy 11 HT-XRD samples that were rapidly cooled from the two-phase $\beta+\gamma$ region at a) low magnification including the samples edge and b) high magnification showing the $\beta$ (bright) and $\gamma$ (dark) phases.....	88
5-1	Calculated liquidus projection marked with the composition of alloys A1 and A2. ....	104
5-2	DTA at 10K/min of alloys A1 and A2 in the a) as-cast condition and b) heating of the thermal cycled materials .....	105
5-3	SEM of as-cast alloy A1 showing a) the overall microstructure b) centered on the primary dendrites c) centered around the lamellar structure and d) high magnification showing three phases in the lamellar structure. The $\eta$ , $\gamma$ and $\sigma$ phases are identified as dark, grey and bright contrasts respectively. ....	106
5-4	TEM of alloy A1 showing a) FIB secondary electron image b) BF image superimposed on FIB image c) BF TEM image of lamellar structure showing the $\sigma$ , $\gamma$ and $\eta$ phases including the respective diffraction patterns for d) $\sigma$ -phase, e) $\gamma$ -phase and f) $\eta$ -phase. ....	107
5-5	A series of TEM micrographs of the $\gamma$ -phase in lamellar structure showing this phase a) adjacent to the $\eta$ -phase in BF b) adjacent to the $\sigma$ -phase in BF c) adjacent to alternating lamella of $\eta$ and $\sigma$ in BF and d) DF of the $\gamma$ -phase in C .....	108
5-6	TEM SAD patterns showing the orientation relationship between the $\eta$ and $\sigma$ phases. .	108
5-7	SEM of as-cast alloy A2 showing a) the overall microstructure b) centered on the coarse primary dendrites c) higher magnification centered around the coarse and fine the primary dendrites d) high magnification showing three phases in the lamellar structure. The $\eta$ , $\gamma$ and $\sigma$ phases are identified as dark, grey and bright contrasts, respectively. ....	109
5-8	XRD of alloy A1 heat-treated subjected to the 1410C heat-treatment that identifies the $\sigma$ , $\eta$ and $\gamma$ phases.....	110
5-9	SEM micrographs of alloys subjected to the 1410C heat-treatment showing a) low magnification of alloy A1 and b) higher magnification next to c) low magnification of alloy A2 and d) higher magnification. The $\eta$ , $\gamma$ and $\sigma$ phases are identified as dark, grey and bright contrasts, respectively.....	111

5-10	SEM micrographs of alloys subjected to the 1510C heat-treatment showing a) low magnification of alloy A1 and b) higher magnification next to c) low magnification of alloy A2 and d) higher magnification. The $\eta$ , $\gamma$ and $\sigma$ phases are identified as dark, grey and bright contrasts, respectively.....	112
5-11	Calculated isothermal sections at a) 1510C and b) 1410C marked with the experimental data obtained from the respective heat-treatments. c) Shows the four phase invariant equilibrium point and participating three phase equilibriums. ....	113
5-12	SEM micrographs of alloy A2 solidified at 10K/min showing A) the overall microstructure and B) high magnification of the primary dendrites and adjacent lamellar structure. The $\eta$ , $\gamma$ and $\sigma$ phases are identified as dark, grey and bright contrasts respectively. ....	114
6-1	Calculated liquidus projection marked with the composition of the experimental alloys. ....	131
6-2	SEM micrograph of as-cast alloy A110 showing revealing a dendritic microstructure in a) low magnification across a grain boundary and b) higher magnification of the dendrites. ....	132
6-3	XRD of a) as-cast alloy A110 from which the $\beta$ -phase was identified and b) of alloy 120 in the as-cast condition and heat-treated at 1550C showing the $\beta$ and $\sigma$ phases with the signatures of the $\beta$ -phase increasing with the heat-treatment. ....	133
6-4	Micrographs of as-cast alloy A120 showing revealing a dendritic microstructure in a) optical at low magnification and SEM showing b) overall dendritic structure, c) centered around interdendritic region and d) higher magnification of the lower z phases within the interdendritic region. ....	134
6-5	DTA of thermally cycled alloy A120 at 10K/min marked with the 1550C heat-treatment temperature. ....	135
6-6	SEM micrographs of as-cast alloy A167 a) revealing a dendritic microstructure and b) and centered around interdendritic region. ....	136
6-7	SEM micrographs of as-cast alloy A141 a) revealing a dendritic microstructure b) centered around interdendritic region c) showing the formation of a coarse phase in the interdendritic region and d) showing three contrast phases with regions 1 and 2 defined.....	137
6-8	XRD of alloy A141 in a) the as-cast condition and b) heat-treated at 1520C. ....	138
6-9	Optical micrographs of alloy A141 which are a) centered around the interdendritic region and b) higher magnification showing the lamellar structure continuing though the coarse phase, this micrograph is also marked with region 1 and 2. ....	139

6-10	DTA of thermally cycled alloy A141 at 10K/min with peaks 1 and 2 marked along with the heat-treatment temperatures (1535C and 1155C). .....	140
6-11	SEM of heat-treated alloy A141 at a) 1535C and b) 1155C which shows the $\sigma$ and $\gamma$ phases which appear bright and dark, respectively.....	141
6-12	SEM micrographs of a) as-cast alloy 141 marked with region 1 and 2. TEM micrographs showing b) a bright field image marked with region 1 and 2 and c) compound TEM micrograph generated by combining 3 adjacent STEM images across regions 1 and 2. ....	142
6-13	TEM SAD zone axis diffraction patterns of alloy A141 for a) $\gamma$ -phase, b) $\sigma$ -phase and c) $\beta$ -phase. ....	143
6-14	TEM micrographs of alloy A141 a) centered on region 1 and b) corresponding dark field image of the $\gamma$ -phase. ....	144
6-15	TEM micrographs of alloy A141 a) centered on region 1 and b) corresponding dark field image of the $\sigma$ -phase and c) higher magnification of the $\sigma$ and $\gamma$ phases and d) corresponding dark field image of the $\sigma$ -phase. ....	145
6-16	STEM micrograph of region 1 showing a) the $\sigma$ and $\gamma$ phases. TEM EDS compositional analysis of b) the $\sigma$ and $\gamma$ phases (blue) in region 1 plotted on a calculated liquidus projection along with the bulk composition of alloy A 141. ....	146
6-17	TEM micrographs of alloy A141 a) centered on region 2 and b) corresponding dark field image of the $\gamma$ -phase. ....	147
6-18	TEM micrographs of alloy A141 a) centered on region 2 and b) corresponding dark field image of the $\sigma$ -phase and c) higher magnification of the $\sigma$ and $\gamma$ phases and d) corresponding dark field image of the $\sigma$ -phase. ....	148
6-19	TEM micrographs of alloy A141 a) centered on region 2 showing the $\sigma$ and $\gamma$ phases and b) corresponding dark field image of the $\beta$ -phase adjacent to the $\sigma$ and $\gamma$ phases....	149
6-20	TEM micrograph of region 2 showing a) the $\gamma$ , $\sigma$ and $\beta$ phases b) corresponding STEM image of the same region and c) TEM EDS compositional analysis of the $\sigma$ , $\gamma$ and $\beta$ phases in region 1 plotted on a calculated liquidus projection. ....	150
6-21	Three-phase tie-triangles that react at the invariant temperature shown slightly above and below the reaction shown for the ternary peritectic and transition reactions along with the respective liquidus projections.....	151
6-22	SEM micrographs of as-cast alloys a) Pg1 b) Pg2 and c) Pg3.....	151
6-23	DTA curves at 10K/min of thermally cycled alloys Pg1, Pg2 and Pg2 marked with peaks a and b as well as solidus peak M in alloys Pg2 and Pg3. ....	152

7-1	DTA of thermally cycled alloy A133 at 10K/min marked with the 1510C heat-treatment temperature. ....	162
7-2	Optical micrographs of as-cast alloy A133 showing a) a dendritic structure and grain boundaries and b) a more uniform structure near the copper chill centered on the grain boundaries within the uniform region.....	163
7-3	SEM micrographs of as-cast alloy A133 showing a) a dendritic structure and b) higher magnification of the dendritic structure while in the micrographs are c) centered around the grain boundary phase and d) higher magnification showing phase that nucleates at the grain boundaries. ....	164
7-4	Optical micrographs and XRD of alloy A133 heat-treated at 1510C showing a) the overall microstructure, b) higher magnification marked with the $\sigma$ and $\gamma$ phases, and c) XRD profile of alloy A133 identifying the $\sigma$ and $\gamma$ phases. ....	165
7-5	a) A bright field TEM micrograph centered on the $\gamma$ -phase in alloy A133 heat-treated at 1510C and b) the corresponding SAD pattern. ....	166
7-6	SEM micrographs of alloys heat-treated at 1510C showing a) the overall microstructure of alloy A170, b) higher magnification of (a) marked with the $\sigma$ and $\gamma$ phases, c) the overall microstructure of alloy A171 and d) higher magnification of (c) marked with the $\sigma$ and $\gamma$ phases. ....	167
7-7	DTA of thermally cycled alloy A132 at 10K/min marked with the 1510C heat-treatment temperature. ....	168
7-8	XRD profile of alloy A132 heat-treated at 1510C identifying the $\sigma$ and $\gamma$ phases. ....	168
7-9	Optical micrograph of alloy A132 heat-treated at 1510C showing the overall microstructure in which the $\gamma$ , $\sigma$ and $\beta$ phases are marked. ....	169
7-10	BF-TEM micrograph of alloy A132 heat-treated and quenched from 1510C showing a) the transformed $\gamma$ -phase and b) TEM EDS compositional analysis of the phases that form upon quenching along with the bulk compositions of the $\beta$ , $\sigma$ and $\gamma$ phases...	170
7-11	DTA at 10K/min of thermally cycled alloy a) A120 b) A134 c) 138 and d) A139. The arrow indicates the 1510C heat-treatment temperature. ....	171
7-12	SEM micrographs of alloy A138 heat-treated at 1510C.....	172
7-13	Alloy A134 heat-treated at 1510C that shows a) optical micrographs of two phases, b) SEM micrograph of overall two phase region, c) higher magnification SEM with $\sigma$ and $\beta$ phases marked, and d) XRD profile identifying the presence of the $\sigma$ and $\gamma$ phases. ....	173

7-14	SEM micrographs of alloys heat-treated at 1510C showing a) the overall microstructure of alloy A120, b) higher magnification of (a) marked with the $\sigma$ and $\gamma$ phases, c) the overall microstructure of alloy A139, and d) higher magnification of (c) marked with the $\sigma$ and $\gamma$ phases.....	174
7-15	SEM micrographs of alloy A163 heat-treated at 1510C showing a) the overall microstructure and b) a higher magnification micrograph marked with the $\sigma$ and $\beta$ phases.....	175
7-16	Calculated isothermal sections at a) 1510C and b) 1410C marked with the experimental data obtained from the respective heat-treatments.....	176
8-1	SEM micrograph of alloy A1 heat-treated at 1510C and quenched marked with the location of the thin foil machined via FIB.....	186
8-2	STEM micrographs of alloy A1 showing a) bright field image marked with the $\sigma$ and prior $\gamma$ -phase, and b) corresponding dark field micrograph, c) higher magnification bright field image with regions 1 and 2 defined, and d) corresponding dark field image.....	187
8-3	TEM micrograph of alloy A1 heat-treated and quenched from 1510C showing a) the transformed $\gamma$ -phase and b) TEM EDS compositional analysis of the phases that form upon quenching along with the 1510C and 1410C tie-triangles.....	188
8-4	SAD patterns of the phases found within the prior $\gamma$ -phase boundary in that a) shows the [110] zone axis of the $\gamma$ -phase and b) shows the [001] zone axis pertaining of the h-phase.....	189
8-5	Lattice models of a) the $\gamma$ -phase and b) the h-phase along with the relative orientation each crystal as measured in heat-treated and quenched alloy A1 which is also marked with coincidence sites in c) the $\gamma$ -phase and d) the h-phase.....	190
8-6	SAD patterns of a) the $\gamma$ and h phases along with b) a two beam condition off the $\gamma$ -phase's zone axis.....	191
8-7	TEM micrographs of the transformed $\gamma$ -phase region in a) and b) which are bright field images of the $\gamma$ and h phases at two different magnifications. c) and d) show dark field images of the $\gamma$ -phase corresponding to (a) and (d), while e) and f) are dark field images of the h-phase corresponding to bright field images in (a) and (b). .....	192
8-8	TEM SAD diffraction patterns with a) $\gamma$ [110] and h[001] zone axes, b) formation of the $\eta$ -phase after high intensity e-beam exposure, and c) complete transformation of the $\gamma$ and h phases to the $\eta$ -phase after further exposure to the high intensity e-beam. ..	193

Abstract of Dissertation Presented to the Graduate School  
of the University of Florida in Partial Fulfillment of the  
Requirements for the Degree of Doctor of Philosophy

EXAMINATION OF THE HIGH TEMPERATURE EQUILIBRIUM IN THE Ti-Al-Nb  
TERNARY ALLOY SYSTEM

By

Orlando Rios

December 2009

Chair: Fereshteh Ebrahimi

Major: Material Science and Engineering

Aeronautical jet engine applications require turbine blade materials that are light weight and exhibit good high-temperature mechanical properties. Single-crystal Ni-based super alloys are the common turbine blade materials used today. There is an interest to increase the strength-to-weight ratio of turbine blade materials in order to improve the performance of the engines. Ti-Al-Nb alloys based on  $\gamma+\sigma$  microstructures are light weight and have shown potential for use in high-temperature turbine engines. Research has shown that through the control of morphology and fraction of the  $\sigma$  and  $\gamma$  phases the mechanical properties of these alloys is improved. The design of alloys and heat-treatments requires an accurate understanding of the high-temperature phase equilibrium between these phases and the  $\beta$ -phase, from which they form. In this study the invariant reactions and high-temperature equilibria were investigated experimentally in the Al-rich corner of the Ti-Al-Nb system. Through a collaborative activity, the phase diagram was optimized using the CALPHAD (Calculation of Phase Diagrams) method, and the results were compared with experimental results.

Equilibrium was examined through evaluation of microstructure, transformation temperatures, composition and structure. The areas that were investigated in this study are the

extension of the  $\beta$ -phase field, the invariant reactions involving the L,  $\gamma$ ,  $\sigma$ ,  $\beta$  and L,  $\eta$ ,  $\sigma$ ,  $\beta$  phases, high-temperature equilibrium among L,  $\gamma$ ,  $\sigma$ ,  $\beta$  phases and the instability of the  $\gamma$ -phase upon quenching.

The results of high temperature X-ray diffraction (HT-XRD) confirmed the expansion of the primary  $\beta$ -phase field upon solidification to higher Al contents. This finding allows the design of Nb-rich alloys with a high concentration of Al for high-temperature applications. The invariant reaction involving the L,  $\gamma$ ,  $\sigma$  and  $\eta$  phases was found to be a ternary eutectic reaction through the evaluation of two alloys which cross through the invariant plane. The L,  $\gamma$ ,  $\sigma$ ,  $\beta$  invariant reaction cascades into the L,  $\gamma$ ,  $\sigma$ ,  $\eta$  eutectic reaction. This somewhat elusive reaction was found to be a ternary peritectic reaction through the evaluation of seven alloys. An isothermal section of the phase diagram at 1510C involving the  $\beta$ ,  $\gamma$ ,  $\sigma$ ,  $\eta$  phases revealed that the  $\gamma$ -phase extends to higher Nb contents than previously reported and retracts by lowering the temperature to 1410C. The  $\gamma$ -phase was found to undergo a spinodal decomposition upon quenching from 1510C.

## CHAPTER 1 INTRODUCTION

The advent of turbine engines revolutionized the aeronautical industry by serving as an efficient power source. Over the years turbine engines have undergone successive iterations of improvement focused around their power-to-weight ratio and efficiency. Among improvements to turbine blade and vane designs, the incorporation of better performing materials has made a significant impact on modern engines. The efficiency of these engines may be improved by increasing the firing temperature, increasing the rotational speed of the turbine as well as decreasing the weight of the engine [1]. This brings forth a unique set of engineering challenges to the material scientist, which is a dynamic area of research for the foreseeable future.

As turbine engines are required at higher operating temperatures and rotational speeds there is a demand for light-weight materials with better creep properties. Ni-based superalloy single crystals alloys are used at present as the blade material in jet engines. In modern superalloys reasonable creep properties have been attained up to 0.85 of their melting point while maintaining mechanical properties at room temperature [2]. However, these alloys have a high density that increases their weight, thus limiting the rotational speed and efficiency of jet engines. Additionally, the engine's maximum operating temperature is limited by the melting point of the blade material. These limitations provide the driving force behind the research and development of new turbine blade materials.

Intermetallics show promise for use as turbine blade materials [3, 4]. This class of materials exhibits good elevated temperature mechanical properties combined with a low density. Several shortcomings have prevented their full implementation into turbine engines. In their current state of development they have decreased room-temperature fracture toughness when compared to conventional blade materials. Intermetallics based on the Ti-Al alloy system

show attractive properties, and have begun to be incorporated into the low-temperature section of modern engines. These alloys are based on a two-phase microstructure consisting of  $\gamma$ -TiAl matrix and  $\alpha_2$ -Ti<sub>3</sub>Al. Although the fracture toughness and room-temperature mechanical properties of  $\gamma$ -TiAl based alloys are acceptable, these alloys have limited service temperatures in comparison to Ni-based superalloys.

Alloys based on the Ti-Al-Nb system were shown to have good properties for high temperature turbine blade applications [5, 6]. The alloying of  $\gamma$ -TiAl with Nb was shown to improve its mechanical properties [7, 8]. Additionally, the low ductility of the  $\gamma$ -phase limits thermomechanical processing, thus  $\beta$ -modified TiAl alloys were shown to improve high-temperature formability resulting from the stabilization of the ductile BCC (body-centered cubic) solid-solution  $\beta$ -phase [9, 10]. However, the  $\beta$ -phase is detrimental to the material's mechanical properties at elevated temperatures by increasing creep rates.

Our research group has demonstrated that high-Nb Ti-Al based alloys that have a  $\gamma+\sigma$  microstructure exhibit improved high-temperature mechanical properties [11], by maintaining a sufficient aluminum content for high-temperature oxidation resistance [12]. The  $\sigma$ -phase is a high temperature brittle intermetallic phase. Prior studies show that optimizing  $\gamma+\sigma$  microstructure and morphology improve in the fracture behavior of Ti-Al-Nb alloys [13-15]. This was accomplished through specialized heat-treatments that disrupted the connectivity of this phase. In order to improve the mechanical properties of  $\gamma+\sigma$  alloys further, precise control of the fraction of the  $\sigma$ -phase is sought after.

The collective focus of this project is to design alloys that have a high-temperature single-phase  $\beta$  region for enhanced thermo-mechanical processing, as well as microstructural control to obtain the desired  $\gamma+\sigma$  microstructure for optimized mechanical properties. The design of such

alloys and their proper heat-treatments require an accurate understanding of the equilibrium phase diagram. Although significant work has been performed on this system, as reviewed in [16], there remains a lack of understanding regarding high-temperature equilibrium, which is essential to the design and development of alloys with optimized microstructures. The majority of the published studies address equilibrium up to 1200C [16]. In this complex alloy system multiple invariant reactions cascade into each other, and there are strongly temperature-dependent solubility limits. Therefore, in order to predict the high-temperature equilibrium better an experimental assessment of the relevant regions was required.

The objective of this study was to measure equilibrium parameters accurately and verify the calculated phase diagrams at high temperatures where sparse data are available. The optimization of the phase diagram was performed in a collaborated effort using the CALPHAD method [17]. CALPHAD, or Calculation of Phase Diagrams, links physical data attained experimentally and/or from first principles calculations with thermodynamic models. The adjustable parameters of these models are optimized based on the available experimental data. Three main types of data were measured in the regions of interest. These data types consist of descriptions of single-phase equilibria and the associated transformation temperatures, multi-phase equilibrium and the invariant reactions involving the liquid phase. The experimental methodology consists of differential thermal analysis (DTA) in conjunction with detailed microstructural analysis of the as-cast as well as heat-treated samples. Heat-treatments were mostly conducted in a specialized furnace with drop quenching capabilities. On select materials where phase transformations could not be suppressed by water quenching, high temperature X-ray diffraction (HT-XRD) was employed to investigate high-temperature equilibrium.

In Chapter 4 the extension of the primary  $\beta$ -phase field is addressed, and it is determined that prior phase diagrams did not accurately predict high-temperature equilibrium in the region of interest. Through the use of thermal analysis and the development of specialized high temperature X-ray diffraction equipment it was determined that the  $L/\beta/\gamma$  bivariant equilibria should be adjusted. The bivariant equilibrium lines are connected to each other at a point on the invariant plane. This led us to address the invariant reactions relevant to the high Al region of the phase diagram, which is of interest for high-temperature alloy design.

The relationship between the  $\gamma+\sigma$  two-phase region and how the  $\gamma+\sigma+\eta$  three-phase region evolves from the liquid phase through its invariant reaction were the motivation behind the study reported in Chapter 5. The invariant reactions dictate the formation of solid-phase equilibrium from the liquid and are represented by the reacting three-phase tie-triangles. The sides of two three-phase tie-triangles ( $\gamma+\sigma+\eta$  and  $\gamma+\sigma+\beta$ ) are connected by the  $\gamma+\sigma$  two-phase region that is of prime interest. The  $\eta$ -phase extends from the Al corner of the ternary system and exists in both the Ti-Al and Nb-Al binaries. The invariant reaction was examined by thermal and microstructural analysis of the as-cast and heat-treated materials.

In Chapter 6 the invariant reaction involving the L,  $\gamma$ ,  $\sigma$ ,  $\beta$  phases, which dictates how the (L,  $\gamma$ ,  $\sigma$ ), (L,  $\sigma$ ,  $\beta$ ) and (L,  $\gamma$ ,  $\beta$ ) bivariant equilibrium lines evolve, and, most importantly, identifies the reaction from which the ( $\beta$ ,  $\gamma$ ,  $\sigma$ ) tie-triangle develops, is discussed. The location of this invariant reaction is key to the development of alloys that solidify as the  $\beta$ -phase and precipitate out the  $\gamma$  and  $\sigma$  at lower temperatures. Essentially this solid-state reaction divides alloys that solidify as primary  $\beta$ ,  $\sigma$  or  $\gamma$  and dictates the initial location of the ( $\beta$ ,  $\gamma$ ,  $\sigma$ ) tie-triangle.

During the examination of the L,  $\gamma$ ,  $\sigma$ ,  $\eta$  invariant reaction a significant retraction of the  $\gamma$ -phase field was observed between the temperatures of 1510C and 1410C. This inspired further investigation of the high-temperature equilibrium among the  $\gamma$ ,  $\sigma$ ,  $\beta$  phases at 1510C. At this temperature the  $\gamma$ -phase was noticed to extend furthest into the Nb corner of the ternary phase diagram. A series of alloys were heat-treated and characterized in order to develop a 1510C isothermal section, which is discussed in Chapter 7. Upon quenching of the  $\gamma$ -phase from 1510C a solid state transformation was observed. This solid state transformation did not occur in samples quenched from 1410C therefore it is associated with the retraction of the  $\gamma$ -phase between the temperatures of 1510C and 1410C. The instability of the  $\gamma$ -phase during quenching was further investigated and discussed in Chapter 8.

CHAPTER 2  
BACKGROUND

**2.1 Important Phases in the Ti-Al-Nb Alloy System**

The goal of this study is to provide an accurate assessment of high-temperature equilibrium in the Ti-Al-Nb alloy system in support of the development of  $\sigma+\gamma$  phase alloys. Several equilibrium and metastable phases with ternary extension within this system are important for the development of such alloys. The important equilibrium phases are the  $\beta$ ,  $\sigma$ ,  $\gamma$  and  $\eta$  phases along with the non-equilibrium O and h phases. A crystal structure summary of these phases are given in Table 2-1. Each phase is also discussed in further detail in this chapter.

Table 2-1 Important phases in the Ti-Al-Nb system and their structural data

Phase	System	Prototype	Space Group	reference
$\beta$	Cubic	W	$Im\bar{3}m$	[18]
O	Orthorhombic	NaHg	Cmcm	[19]
$\gamma$	Tetragonal	AuCu	P4/mmm	[20]
h	Orthorhombic	ZrGa <sub>2</sub>	Cmmm	[21]
$\sigma$	Tetragonal	sCrFe	P4 <sub>2</sub> /mnm	[22]
$\eta$	Tetragonal	Al <sub>3</sub> Ti	I4/mmm	[23]

The  $\beta$ -phase is a BCC phase that extends from across the Ti-Nb binary and Ti side of the Ti-Al binary into the ternary system. This phase has received significant attention within our group and recently in the literature due to its ductile nature. The incorporation of this phase in  $\gamma$ -based Ti-Al-Nb alloys enhances the forgeability of these alloys [9, 10]. Our work seeks to process materials within this phase field and precipitate out the desired microstructure from it. The  $\beta$ -phase undergoes an ordering transformation within the ternary system forming a B2 or CsCl structure that is associated with a decrease in ductility. The B2 structure has been shown to form in the Nb-Al binary within the composition range of 13.5-16.9 Al at% [24] from which it extends into the ternary system [25]. Based on available structural data [23], a lattice model for

this structure is generated and is shown in Figure 2-1 for the binary Ti-Al. The high temperature BCC  $\beta$ -phase undergoes a shear transformation to a metastable orthorhombic phase (O-phase) [19]. This phase is often found within the  $\beta$ -phase in materials that are rapidly cooled into the  $\beta$ -phase phase field [26-38].

The  $\gamma$ -phase has received significant attention since the 1980's due to its good combination of mechanical properties and low density. The majority of the research is based on  $\gamma+\alpha_2$  alloys. The  $\alpha_2$  Ti<sub>3</sub>Al phase is used as a second phases strengthener in this class of alloys. The  $\gamma$ -phase also known as the TiAl phase, has an L1<sub>0</sub> structure. This phase extends from the binary well into the ternary phase diagram. A lattice model of this phase is generated based on the available structural data [39-41] and is shown in Figure 2-2a. The solubility range for off-stoichiometric compositions extends to the Al-rich side of TiAl at high temperatures. A metastable orthorhombic phase (Al<sub>2</sub>Ti) has been shown to form when off-stoichiometric  $\gamma$ -phase is rapidly cooled [21, 42-44]. A lattice model shown in Figure 2-2b is generated here based on structural data available in the literature. The Al<sub>2</sub>Ti structure is a super lattice that forms by the ordering of the Al atoms on the (100) and (002) planes of the TiAl L1<sub>0</sub> structure, thus, its lattice parameter is inherent to that of parent  $\gamma$ -phase.

A double ordering of high Nb-containing  $\gamma$ -phase has been discussed in the literature, although this is still a topic of much debate. Initial investigations showed that this phase is a stable equilibrium phase that exists only in the ternary system, and has a wide range of solubility near the stoichiometric formula Ti<sub>4</sub>Nb<sub>3</sub>Al<sub>9</sub> [45-47]. Independent studies argued that this ternary phase is not an equilibrium phase, and, in fact, does not exist in the ternary phase diagram [48]. A separate series of studies has also confirmed this phase's existence [49, 50]. Currently this area remains under investigation, as it has implications in the phase diagrams at 1200C and below.

The  $\sigma$ -phase is a complex tetragonal structure that contains over 30 atoms in its unit cell. It has been viewed as a topologically closed-packed structure similar to a distorted hexagonal closed-packed lattice [41]. A lattice model of this phase is shown in Figure 2-3 [22, 41, 51]. This phase exists in the Nb-Al binary and extend well into the ternary phase diagram. It forms in the binary system through a peritectic reaction with the  $\beta$ -phase at 1940C [52]. This intermetallic phase is hard and brittle, and therefore it has been generally avoided in Ti-Al alloys. Its high melting point has inspired some interest in incorporating the  $\sigma$ -phase in TiAl as a second phase in order to improve the high temperature mechanical properties. Ti-Al-Nb alloys based on  $\sigma+\gamma$  microstructures have shown promise within our group for high-temperature applications [11, 15]. These microstructures have shown improved creep life over TiAl-based alloys.

The  $\eta$ -phase is a tetragonal phase that exists on the Al-rich sides of the Nb-Al and Al-Ti binaries, and extends into the Al-rich corner of the ternary. This phase is brittle with a low melting point, however, it remains of interest due to its interaction with the L,  $\sigma$  and  $\gamma$  phases though an invariant reaction. A lattice model of the  $\eta$ -phase is shown in Figure 2-4 [23]. The lattice models shown here are used for structure-factor calculations and the subsequent simulation of single crystal and powder diffraction patterns.

## **2.2 Liquidus Surfaces**

The liquidus surfaces and the representative liquidus projections have been successively modified over the years based mostly on fairly limited experimental evaluations of as-cast materials. The melting point and as-cast microstructures were analyzed for clues retained from the liquid/solid interactions [23, 53-55]. These data have been used to optimize several phase diagrams, from which liquidus projections have been reported [18, 56]. A critical reevaluation of the Ti-Al-Nb system was performed in [16], which included a redrawing of the bivariant

equilibrium lines. In this section, the experimental and computational liquidus projections considered in this study are discussed.

Focusing on the development of  $\sigma+\gamma$  alloys, our main interest is among the L,  $\gamma$ ,  $\sigma$  and  $\beta$  phases. These phases are involved in two important interconnected reactions, namely the (L,  $\gamma$ ,  $\sigma$ ,  $\beta$ ) and (L,  $\gamma$ ,  $\sigma$ ,  $\eta$ ) invariant reactions. These invariant reactions define the extent of the adjacent liquidus surfaces and are connected by the bivariant equilibrium lines. The first experimental evaluations of the liquidus projections were reported independently by Kaltenbach et al. [53] and later Perepezko et al. [57]. The as-cast microstructures reported in these examinations of alloys ranging across the ternary system were examined. A liquidus projection was generated based on the analysis of alloys near the invariant reactions. The slope of the liquidus surfaces is determined by thermal analysis, which is shown in Figure 2-5a [57]. It was determined in this study that the two invariant reactions involving the (L,  $\gamma$ ,  $\sigma$ ,  $\eta$ ,  $\beta$ ) phases consist of a transition reaction ( $L+\eta\rightarrow\sigma+\gamma$ ) which cascades into a second transition reaction ( $L+\sigma\rightarrow\beta+\gamma$ ). Based on the work of Kaltenbach et al. [53] and in collaboration with Perepezko along with unpublished work, Kattner and Boettinger made the first published thermodynamic calculation of this system's phase diagram [56]. The liquidus projection from this assessment, shown in Figure 2-5b, disagreed with the transition reaction ( $L+\eta\rightarrow\sigma+\gamma$ ) as well as the second transition reaction. A maxima was calculated in the L,  $\beta$  and  $\gamma$  and L,  $\beta$  and  $\gamma$  bivariant equilibrium lines that resulted in the computation of two adjacent ternary eutectic reactions among the (L,  $\gamma$ ,  $\sigma$ ,  $\beta$ ) and (L,  $\gamma$ ,  $\sigma$ ,  $\eta$ ) phases.

A reinvestigation was performed by Zdziobek et al. [55] that addressed the invariant reaction and bivariant equilibrium based the pyrometric measurements of the melting point of as-cast samples. In this study he used the melting points of a series of alloys to develop the slope of

the liquidus surface, thus attaining possible invariant reaction type and location. Within this study Zdziobek generated the experimental liquidus projection shown in Figure 2-6a [55].

Similar to the work of Perepezko et al. [57] he determined that the liquid undergoes two consecutive transition reactions that are the  $(L+\eta\rightarrow\sigma+\gamma)$  reaction, which cascades into the  $(L+\sigma\rightarrow\beta+\gamma)$  reaction.

Servant and Ansara also published a thermodynamic assessment of the phase diagram in 1998 based on the available literature [18]. A liquidus projection based on their database was calculated, and is shown in Figure 2-6b. Similar to the calculations of Kattner and Boettinger, Servant and Ansara found a maximum in the L,  $\beta$  and  $\gamma$  bivariant equilibrium line, however, this line connects to a different invariant reaction. They calculated that the liquid reacts with the  $\beta$  phase through a transition reaction that forms the  $\sigma+\gamma$  phases. The invariant reaction then connects into a eutectic reaction between the L,  $\gamma$ ,  $\sigma$ ,  $\eta$  phases.

Leonard et al. [54] experimentally reinvestigated the liquidus projection reported by Zdziobek et al. [55]. The two transition reactions were in general agreement, although Leonard's work did not focus on the invariant reactions. Rather his work focused on the two bivariant equilibrium lines (L,  $\beta$ ,  $\sigma$ ), (L,  $\beta$ ,  $\delta$ ) involving the L,  $\beta$ ,  $\sigma$ ,  $\delta$  phases. Leonard examined the as-cast microstructures of several alloys along these bivariant lines. It was determined that both of these bivariant equilibrium lines should be moved closer toward Nb-Al side of the ternary phase diagram as shown in Figure 2-7a [54]. Based on the results in Zdziobek et al. [55] and Leonard et al. [54], Raghavan redrew the liquidus projection to match the binary phase diagrams and included the extension of the  $\beta$ -phase into the prior  $\delta$  and  $\sigma$  primary phase regions [16]. Raghavan's liquidus projection is shown in Figure 2-7b which also agrees with the two transition reactions involving the (L,  $\gamma$ ,  $\sigma$ ,  $\eta$ ,  $\beta$ ) phases.

In summary several discrepancies were found among the two invariant reactions involving the (L,  $\sigma$ ,  $\eta$ ,  $\gamma$ ) and (L,  $\gamma$ ,  $\sigma$ ,  $\eta$ ) phases. The reaction class and composition were found to be inconsistent. With the exception of the study in Perepezko et al. [57], where the L,  $\gamma$ ,  $\sigma$ ,  $\eta$  was studied, the experimental investigations reviewed here did not directly target the invariant reactions. These studies mostly focused on the contours of the liquidus surfaces to determine the possible reaction class and composition. These data were used to optimize the liquidus surfaces and high-temperature equilibrium in the Ti-Al-Nb phase diagram.

### 2.3 Isothermal Sections

There has been significant work on complete isothermal sections at 1200C and below [25, 53, 55, 57]. Independent phase fields and multi-phase stability have also been investigated significantly [10, 58-66]. An isothermal section by Hellwig et al. is shown in Figure 2-8 taken from reference [25]. The majority of the isothermal sections published are in agreement, although there is series of papers on a disputed  $\gamma_1$  single-phase field. Chen et al, has reported an extended solubility range of the  $\gamma_1$  phase, which is shown in Figure 2-8b [47]. The  $\gamma_1$  phase, however, is under current investigation and several comments and replies have been published that disagree whether this is a true equilibrium phase or a metastable phase [46, 47]. In 2005, Chen et al. demonstrated the existence of this phase, although the solubility range and relevance of this phase in the equilibrium phase diagram is still not well established [45].

Limited experimental data have been published in isothermal sections above 1200C. Chen et al. investigated heat-treated alloy in order to determine equilibrium at 1400C [46, 47]. The majority of these alloys existed in the single-phase fields at the equilibrating temperatures. The samples were sealed in quartz tubes during the heat-treatment at 1400C, a temperature at which reactions between the quartz and sample is possible. The author discussed a relatively large

environmentally affected zone that was removed. A series of liquid-phase diffusion couples were investigated in order to determine the multi-phase equilibrium regions. These were combined in order to generate the phase diagram shown in Figure 2-9.

## 2.4 Invariant Reactions

The Ti-Al-Nb ternary alloy system has a complex phase diagram with several interconnected ternary invariant reactions with the liquid phase. These invariant reactions are connected by the bivariant equilibrium lines involving the liquid. The convention set by Rhines is used in this work, which defines valleys formed by adjacent liquidus surfaces as a bivariant equilibria [67]. Recently in the literature the bivariant equilibria are called univariant equilibria, based on the assumption that pressure is fixed. The difference between the terms is, in reality, semantic. In the current study the author will use the term “bivariant equilibria”. The solidification path an alloy takes is dependent on the composition of the alloy relative to the invariant reaction, and on the rate at which the alloy solidifies. Two solidification models are applied in order to link the equilibrium phase diagram with the observed solidification path. The first model is based on direct interpretation of the equilibrium phase diagram. This model best fits infinitely slow cooling rates, where the phases present in the microstructure at any temperature are directly “read off” the equilibrium phase diagram. At non-equilibrium cooling rates, an application of the Gulliver-Scheil solidification model is applied. In this model it is assumed that diffusion rates are infinite in the liquid and non-existent in the solid [68, 69]. Although Scheil was the first to demonstrate the application of his model to linear phase diagrams [69], Gulliver’s derivation preceded [68], therefore the model is called the Gulliver-Scheil model [70]. A modification of the Gulliver-Scheil model allows for some back diffusion in the solid during solidification. This modification best predicts the solidification of as-cast materials, therefore it is also employed here. The equilibrium “lever law” and Gulliver-Scheil

models are the extreme limits, and the addition of “back diffusion” through the solid essentially bridges the gap between these limits.

### 2.4.1 Ternary Peritectic

Ternary peritectics are seldom found in metallic systems. This reaction consists of a liquid and two solid phases reacting isothermally to form a third solid phase. A classic example of a theoretical simple ternary peritectic was conceptualized and reported by Rhines [67]. His phase diagram was based on thermodynamic laws and not on a particular observed system. The ternary phase diagram as he presented it is shown in Figure 2-10.

The two solidification models are applied to a hypothetical alloy within this phase diagram. The equilibrium cooling path of a hypothetical alloy composition is marked directly on Figure 2-10 with a red solid line, whereas the related non-equilibrium cooling path is marked with a blue dotted line. In the case of equilibrium cooling, this alloy would solidify as primary  $L+\beta$  followed by  $L+\beta+\alpha$ . Upon reaching the invariant plane, the liquid phase will react with all of the  $\alpha$ -phase and part of the  $\beta$ -phase to form the  $\gamma$ -phase. In reality, the formation of the  $\gamma$ -phase will obstruct the liquid's ability to react with the  $\beta$  and  $\alpha$  phases “peritectic walling”, thus preventing the peritectic reaction from reaching completion.

Under non-equilibrium cooling following the Gulliver-Scheil model the solidification paths is significantly different. Mainly, this model is based on the fact that one always has local equilibrium at the interface, and any solid that forms does not change in composition. In Figure 2-10 the blue dotted line shows the non-equilibrium cooling path. This alloy will solidify as cored primary  $\beta$ , which remains unchanged throughout the solidification path. Next to solidify are the  $\alpha$  and  $\beta$  phases, which form together while the liquids composition follows the path delineated by the dotted line along the bivariant equilibrium troughs on Figure 2-10. Finally

upon reaching the invariant plane, the  $\alpha$  and  $\beta$  phases cease to form, and the  $\gamma$ -phase forms directly from the liquid. A key difference between this solidification path and the equilibrium path is the fact that the  $\gamma$ -phase forms directly from the liquid without interaction with the prior  $\alpha$  and  $\beta$  phases. Additionally, any solids formed during solidification are predicted to be retained in the microstructure, unchanged in composition, essentially forming a cored structure. In the case where back diffusion has occurred within the solid, it is predicted that the  $\gamma$ -phase grows from the liquid as well as partially consumes the adjacent  $\alpha$  and  $\beta$  phases.

There are limited examples available of ternary peritectic reactions in metallic systems. An example of a high temperature ternary peritectic reaction in the Ni-Al-Ta system was reported by Johnson and Oliver [71]. The solidification path of an alloy within this system was found to occur by the simultaneous growth of two phases, namely the NiAl and NiAlTa phases. The third peritectic phase Ni<sub>2</sub>AlTa forms within the interdendritic region between the coupled growth microstructure of the two primaries. An SEM micrograph taken from [71] is shown in Figure 2-11. This micrograph shows a lamellar structure consisting of the NiAl and NiAlTa microconstituents, with the Ni<sub>2</sub>AlTa phase located in the region adjacent to them.

#### **2.4.2 Ternary Eutectic**

A similar treatment is conducted on a hypothetical ternary eutectic reaction. In this case however an alloy composition that does not cross through the invariant plane is selected. The composition of this alloy on a hypothetical ternary eutectic taken from Rhines [67] is shown in Figure 2-12 and is marked with a solid red line. The first phase to solidify under equilibrium is the  $\beta$ -phase, followed by the  $\beta$  and  $\gamma$  phases growing simultaneously from the liquid. Finally, a  $\beta+\gamma$  microstructure forms, since this alloy never crosses through the invariant plane. Under non-equilibrium cooling, the solidification path is significantly different, as is shown in Figure 2-12.

Again a dotted line represents the compositional path of the liquid phase during non-equilibrium solidification. The Gulliver-Scheil model shows that this alloy will solidify as primary  $\beta$ . In contrast to the equilibrium solidification, the liquid's composition will drift into the bivariant equilibrium with the  $\beta$  and  $\alpha$  phases, where these phases begin to form together. The liquid's composition will fall into the invariant reaction point and, finally, the last remaining liquid will solidify through the eutectic reaction. In this case, although the equilibrium solidification path misses the invariant plane all together, during non-equilibrium cooling the liquid composition passes through the invariant point.

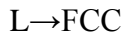
### **2.5 Interpretation of DTA Data for Ternary Alloys**

The analysis of DTA data pertaining to the solidification of ternary alloys is best interpreted with an understanding of the associated bivariant equilibria and invariant reactions. As ternary alloys solidify, the nucleation and growth of phases has an associated heat-evolution. The DTA response is mainly dependent on the heat capacity of the material and the enthalpy of formation of the solid phases. Nucleation events are seen as inflection points and subsequent changes in curvature. Invariant reactions that occur isothermally are seen as peaks, which are smeared across the temperature axis due to transformation kinetics and the instrument's thermal lag. Thermal lag is discussed in Chapter 3. Two examples of a DTA's response to the solidification of ternary alloys are described in a NIST special publication by Boettinger et al [72]. These examples are discussed here and are used in the analysis throughout this work.

These examples are based on the non-equilibrium solidification of two alloys within the Al-Cu-Fe ternary alloy system. A liquidus projection of the composition range pertinent to the solidification of these two alloys is shown in Figure 2-13. The invariant reactions in this region are marked alphabetically (A-E). The invariant reactions that these two alloys cross through

during solidification are a ternary transition reaction marked with a D, which cascades into a ternary eutectic reaction marked with an E. These reactions are connected by the L,  $\alpha$ , FCC bivariant equilibria line.

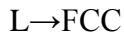
The 1<sup>st</sup> alloy discussed here is marked with a 1 on Figure 2-13. This alloy is predicted to solidify through the following solidification path.



Alloy 1 solidifies with a formation of a primary phase (FCC) followed by the solidification of the primary and the  $\beta$ -phase together. This occurs when the composition of the liquid drifts into the bivariant equilibrium line as shown in Figure 2-13. The liquid composition continually follows the bivariant equilibria line while forming the FCC and  $\beta$  phases together, until it finally reaches the invariant point. At the invariant point, the remaining liquid forms the FCC,  $\beta$  and  $\theta$  phases together through the eutectic reaction.

A DTA curve representative of alloy 1's solidification was simulated in [72] using the thermodynamic parameters (heat capacity and enthalpy data) for this system and reproduced in Figure 2-14. Three inflection points are seen on this curve. The first inflection point corresponds to the liquidus surface, whereas the second point corresponds to the FCC and  $\beta$  phase forming together. Finally, the last inflection point corresponds to the invariant reaction. The invariant reaction in this case is a ternary eutectic reaction. This reaction occurs isothermally, which is represented by a narrow and sharp peak. Due to the thermal lag of the instrument, however, this reaction is spread across a temperature range.

The 2<sup>nd</sup> alloy marked with a 2 solidifies through two invariant reactions. This alloy first crosses through the ternary transition reaction at point D, before finally reaching the eutectic reaction at point E. The solidification path of this alloy is as follows:



This alloy differs in that as it crosses through the transition reaction the growth of the FCC and  $\alpha$  phases ceases and the FCC and  $\beta$  phases begin to form. This occurs when the liquid's composition crosses from the L, FCC,  $\alpha$  bivariate equilibria to the L, FCC,  $\beta$  bivariate equilibria. Similar to alloy 1, the remaining liquid finally crosses through the ternary eutectic reaction.

A DTA curve is simulated by once again using the thermodynamic parameters for this system, and is shown in Figure 2-15. Two main features are of interest in this curve and how it relates to the invariant reactions. The first is the fact that although the transition reaction is an isothermal reaction among four phases, it reveals itself as a subtle change in slope. This is due to the fact that during non-equilibrium cooling the transition reaction manifests itself as a switching between the two primary phases that form together from the liquid. Thus, the DTA only measures a change in slope due to differences in the heat capacity and enthalpy of formation among these phases. Further cooling of this alloy forces the liquid to cross through the ternary eutectic plane, resulting in a sharp peak. In the current study, the DTA data were analyzed using a methodology parallel to the one set forth by Boettinger et al. [72]. Further details of the analysis are discussed in the associated sections where thermal data are presented.

## 2.6 Outstanding Questions

Our work is primarily interested in the stability of the  $\beta$ -phase at high-temperatures and the interrelationship between this phase and the  $\sigma$  and  $\gamma$  phases. Literature review brings forward a number of outstanding questions pertaining to this region in the high temperature equilibrium phase diagram. The literature revealed that the extent of the  $\beta$ -phase was not well known. This was due mostly to the experimental difficulties in the examination of high temperature equilibrium. Secondly, the invariant reactions between the (L,  $\beta$ ,  $\gamma$ ,  $\sigma$ ) and (L,  $\sigma$ ,  $\gamma$ ,  $\eta$ ) are not well understood. These two areas where significant controversies exist are critical in the assessment of the Ti-Al-Nb phase diagram in particular for its application in the development of  $\sigma+\gamma$  alloys.

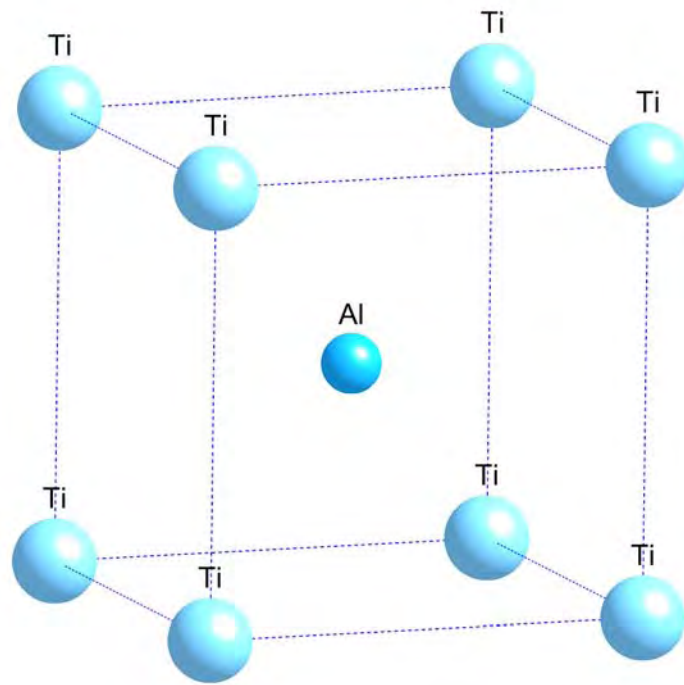


Figure 2-1 A lattice model of the B2 structure based on crystallographic data reported in [18].

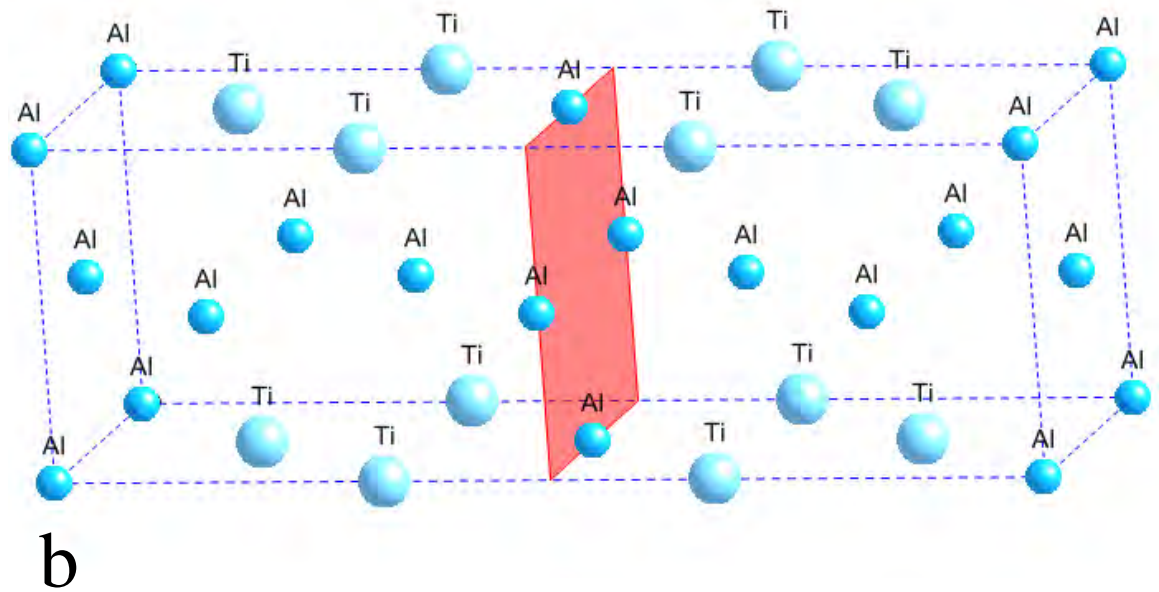
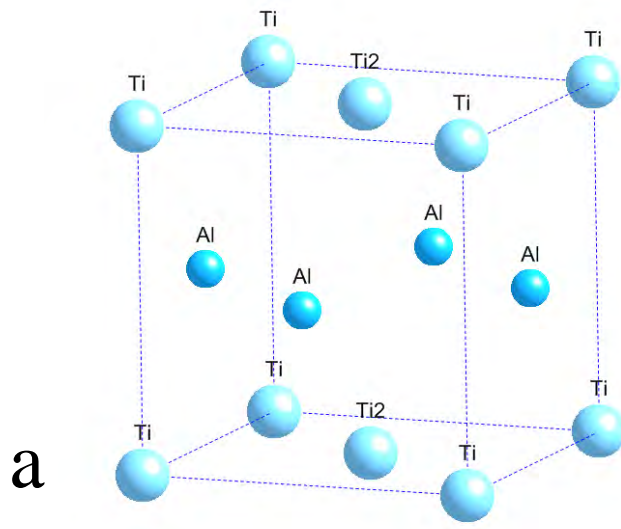


Figure 2-2 A lattice model of a) the  $\gamma$ -phase [20] and b) the h-phase [21].

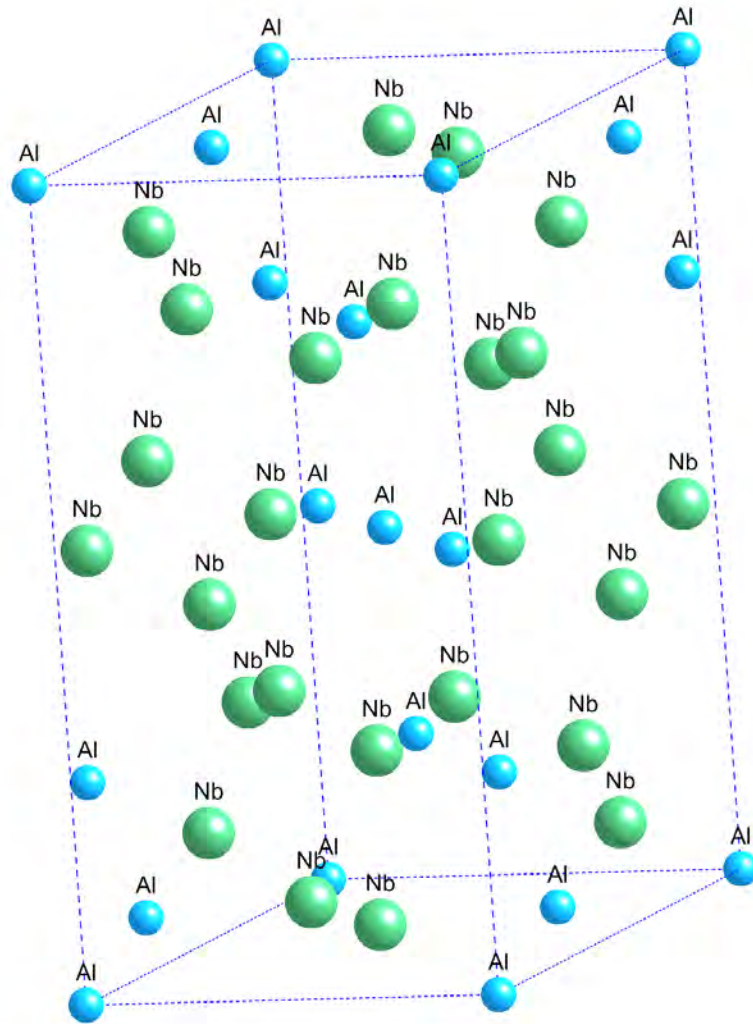


Figure 2-3 A lattice model of the  $\sigma$ -phase based on crystallographic data reported in [22].

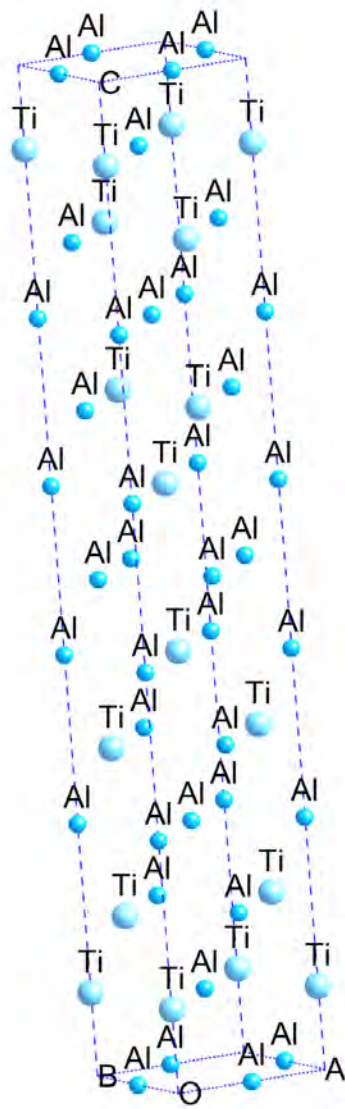


Figure 2-4 A lattice model of the  $\eta$ -phase based on crystallographic data reported in [23].

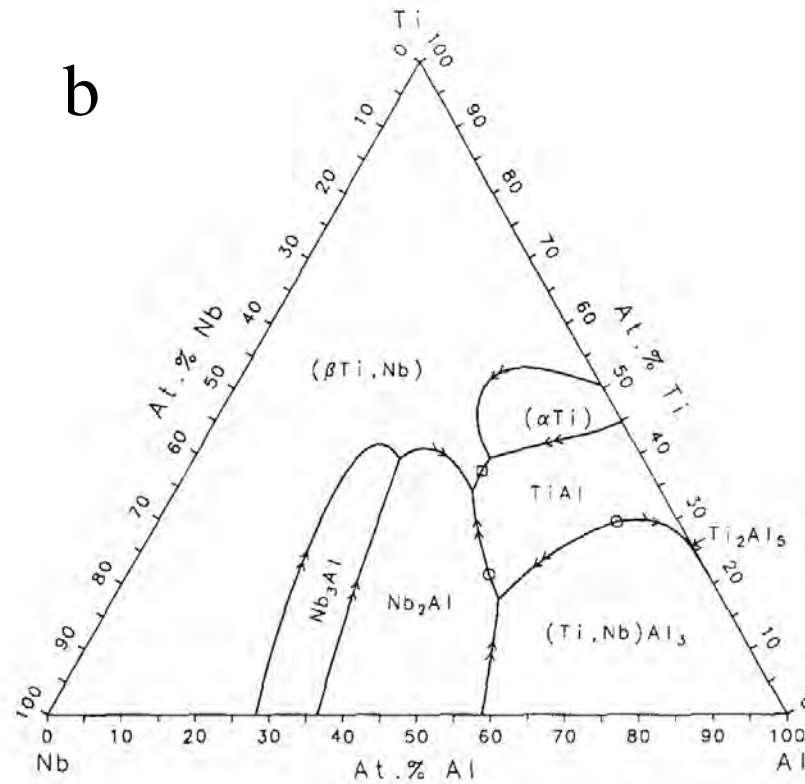
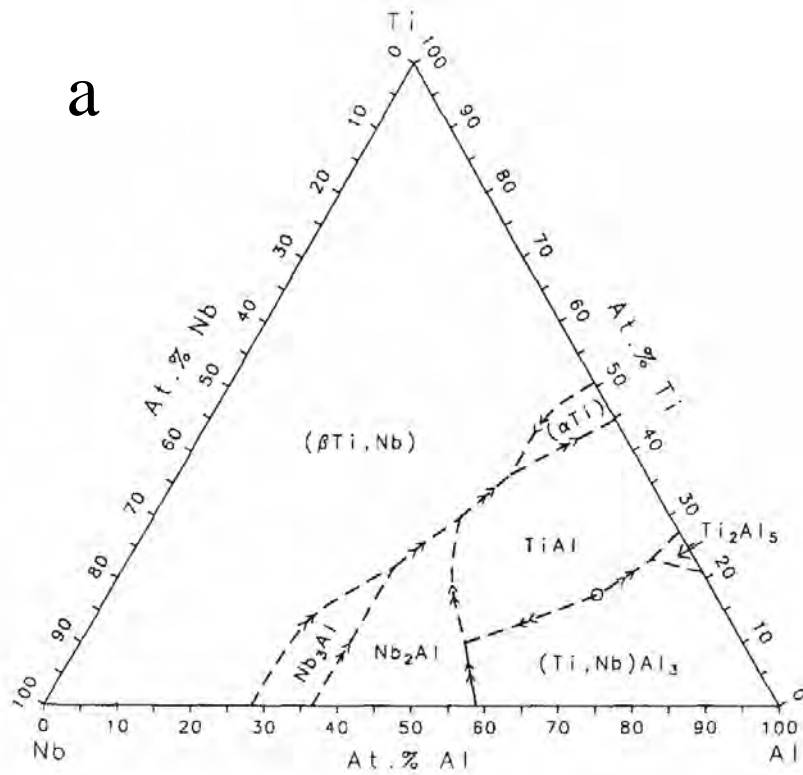


Figure 2-5 Liquidus projections by a) Perepezko et al (1990). [57] and b) Kattner and Boettinger (1992) [56].

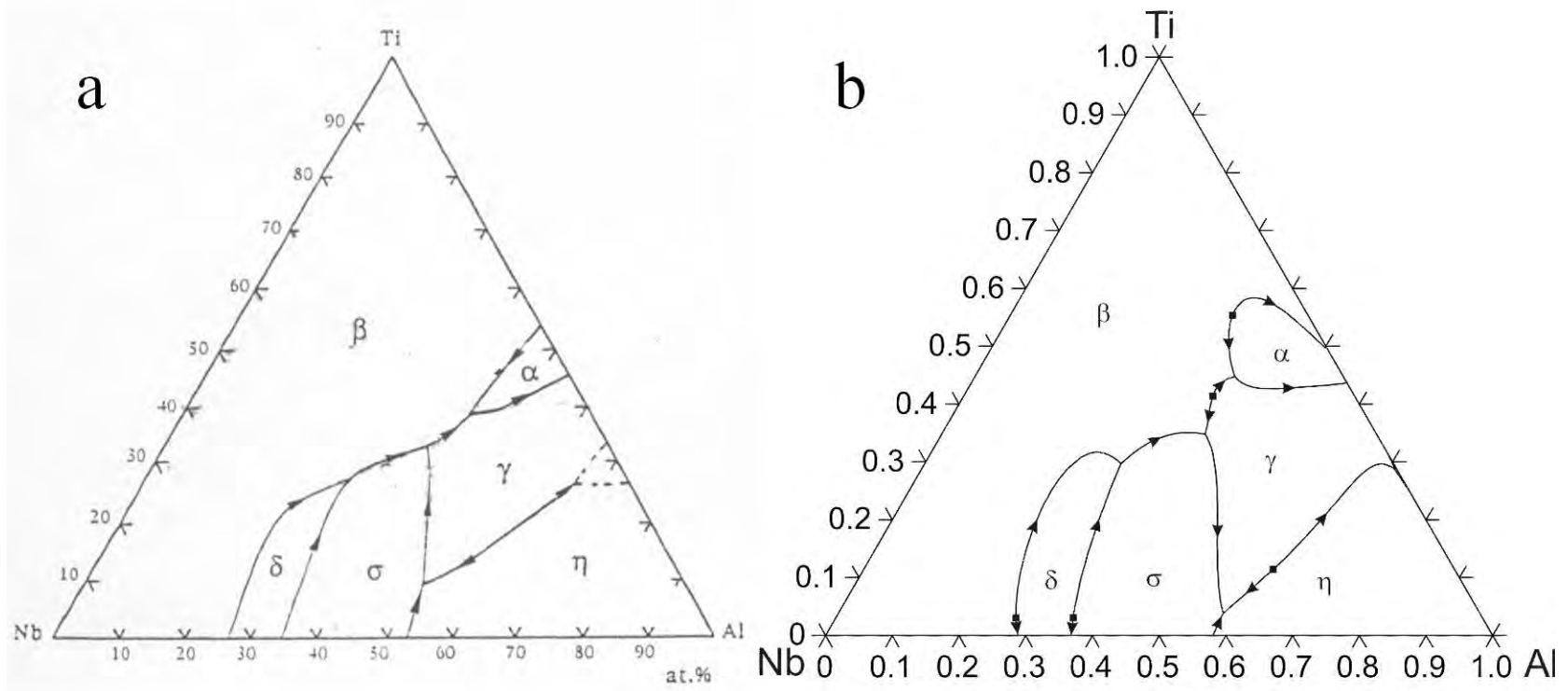


Figure 2-6 Liquidus projections by a) Zdziobek et al. (1995) [55] and b) Servant and Ansara (1998) [18].

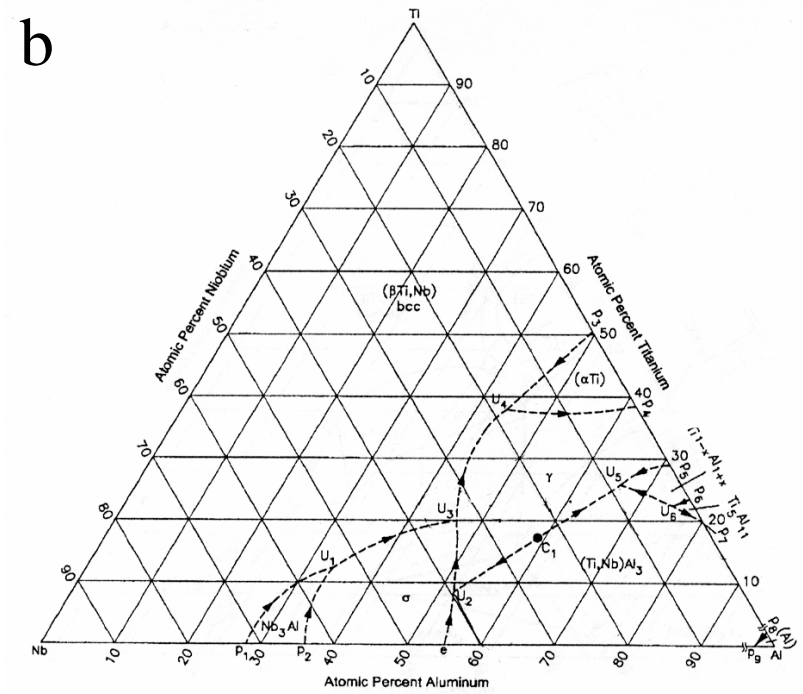
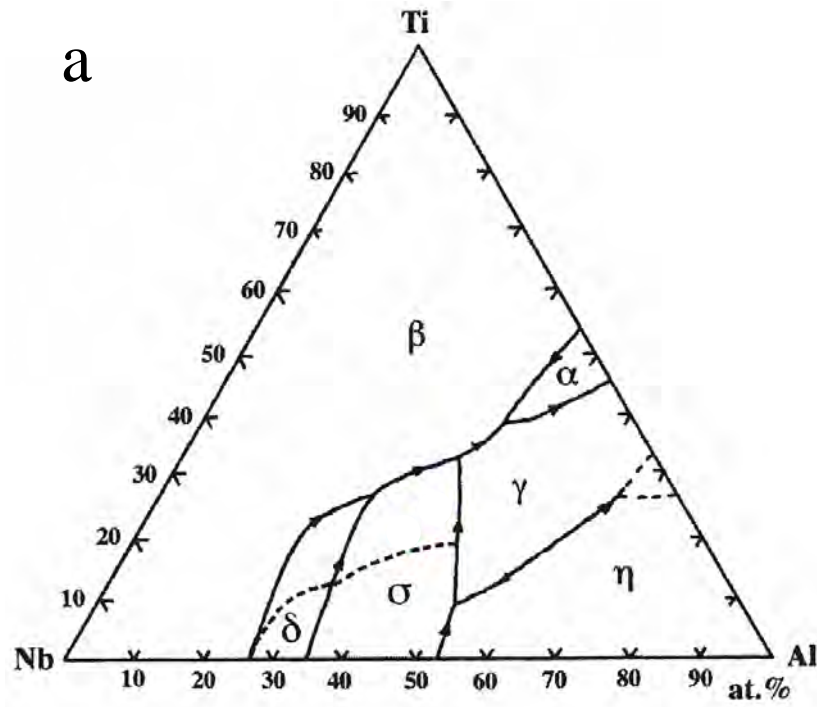


Figure 2-7 Liquidus projections by a) Leonard et al. (2000) [54] and b) Raghavan (2005) [16].

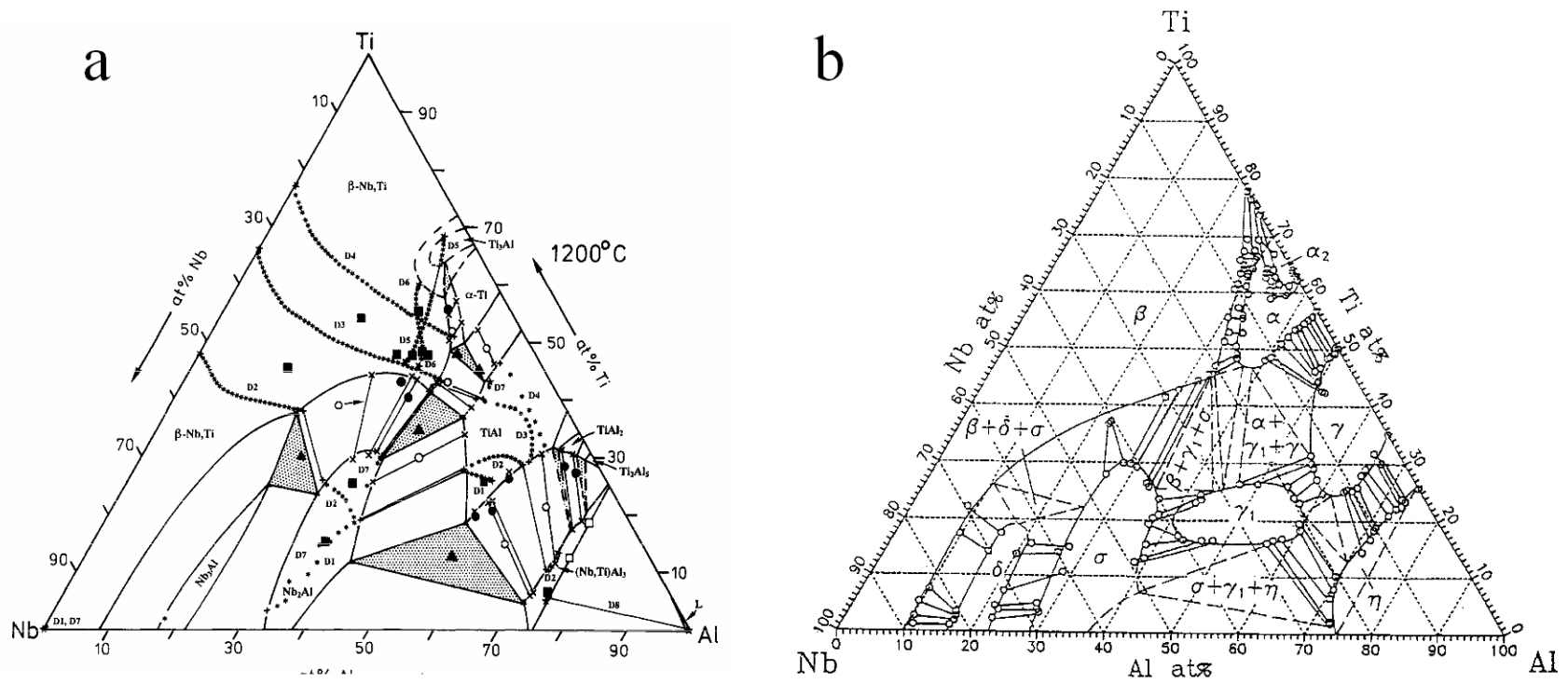


Figure 2-8 Isothermal sections at a) 1200C by Hellwig et al. (1998) [25] and b) 1150C by Chen et al. (1996) [47].

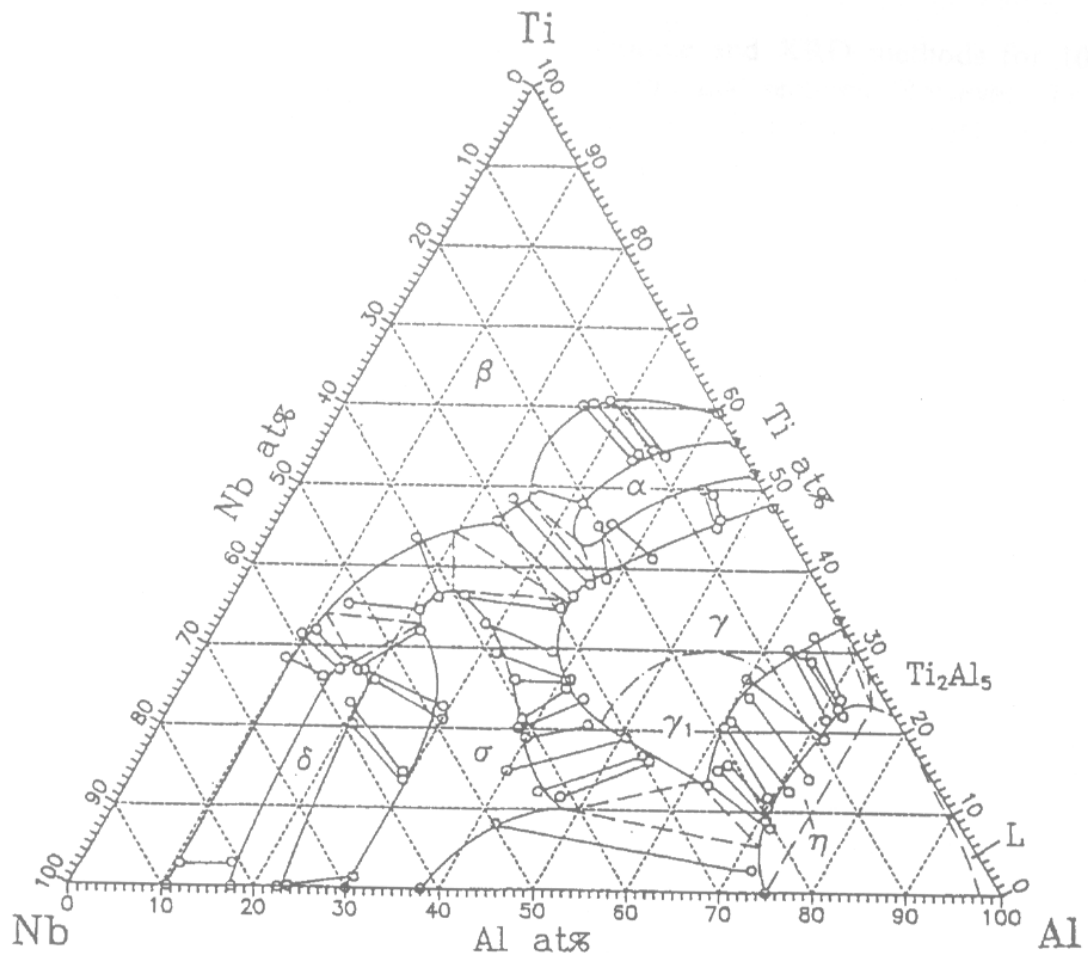


Figure 2-9 Isothermal sections at 1400C by Chen et al. (1996) [47].

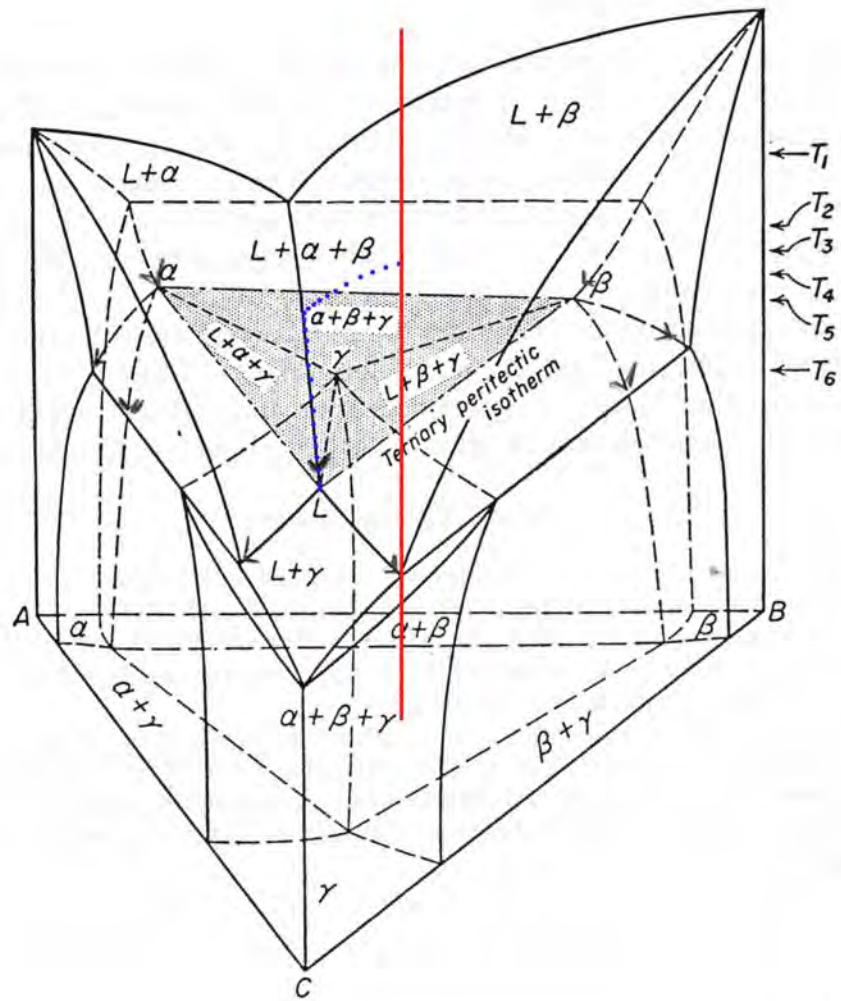


Figure 2-10 Hypothetical ternary peritectic phase diagram taken from Rhines (1956) [67] marked with a theoretical non-equilibrium solidification path.

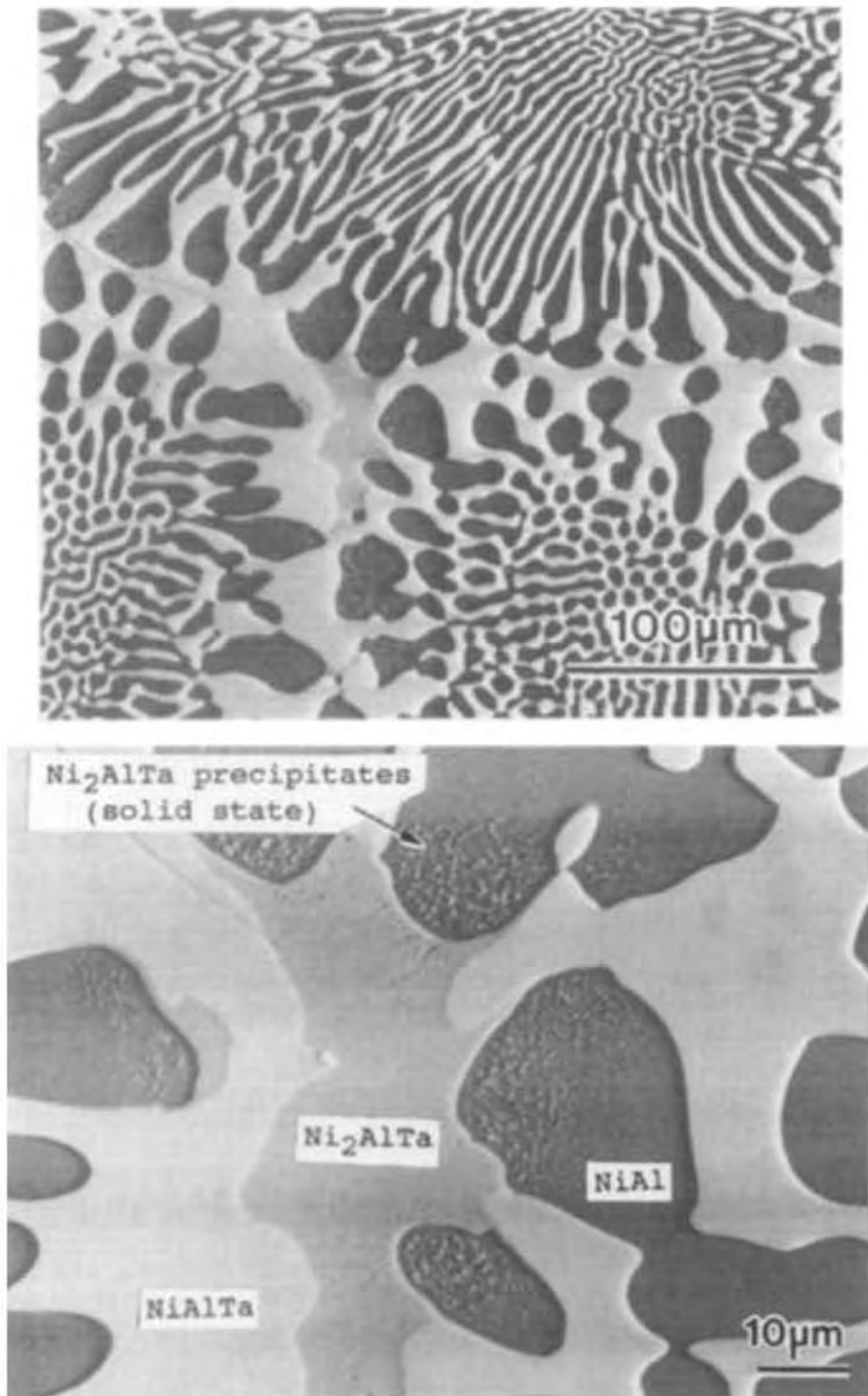


Figure 2-11 SEM micrographs showing a reported ternary peritectic reaction in the Ni-Al-Ta alloy system [71].

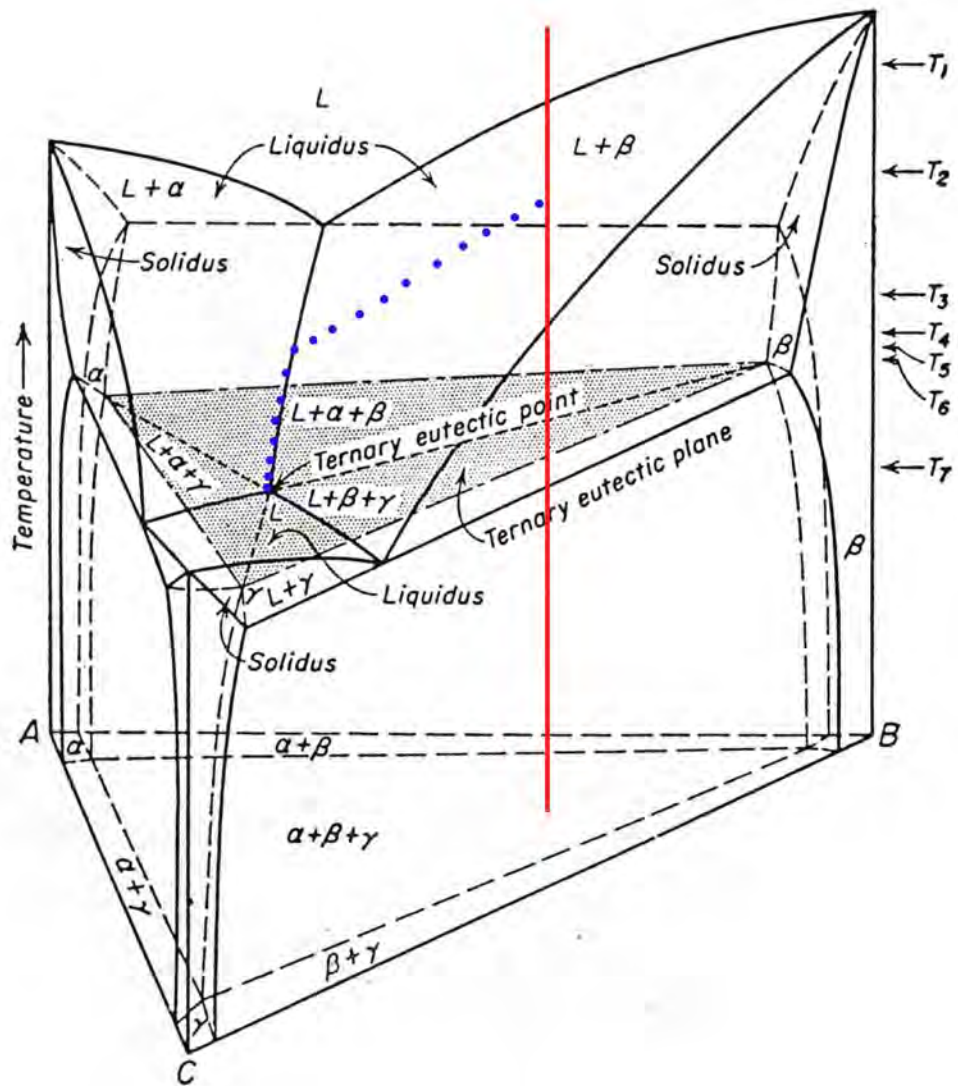


Figure 2-12 Hypothetical ternary eutectic phase diagram taken from Rhines (1956) [67] marked with a theoretical non-equilibrium solidification path.

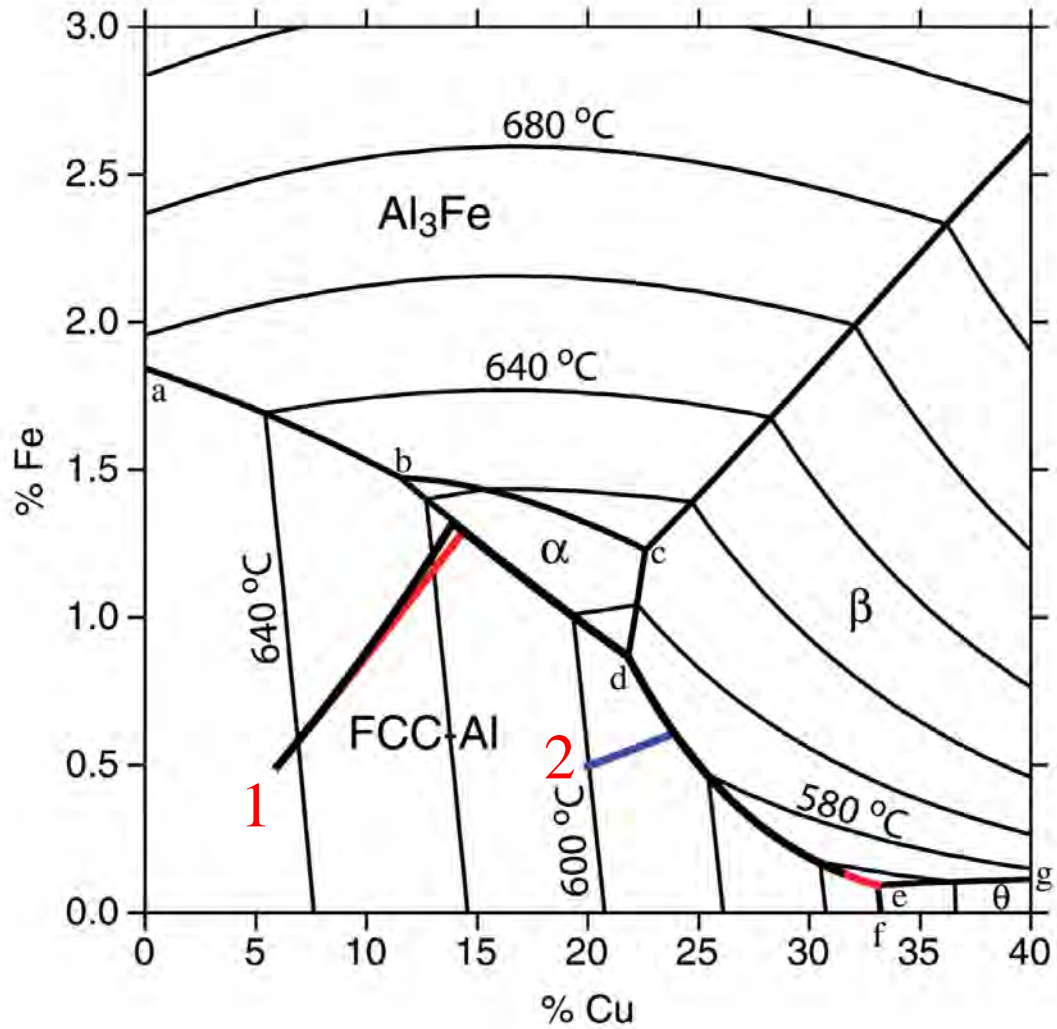


Figure 2-13 Calculated liquidus projection of the Al-Cu-Fe alloy system showing the solidification path of two alloys through a ternary transition reaction and a ternary eutectic reaction [72].

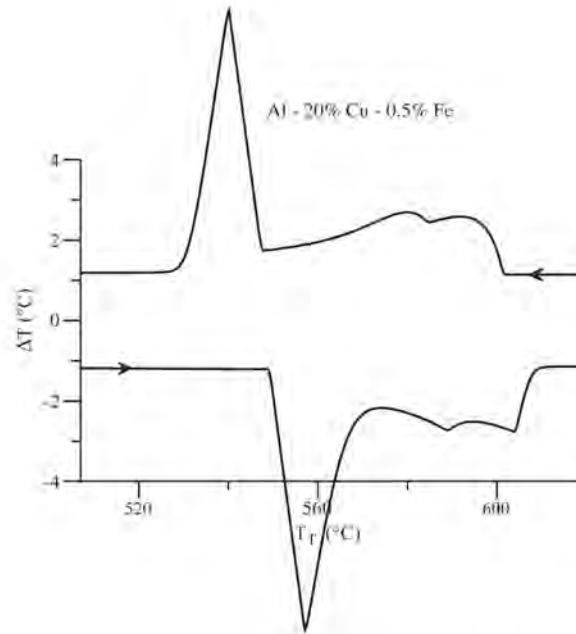


Figure 2-14 Calculated DTA response of the solidification of alloy 1 through the liquidus and ternary eutectic reaction [72].

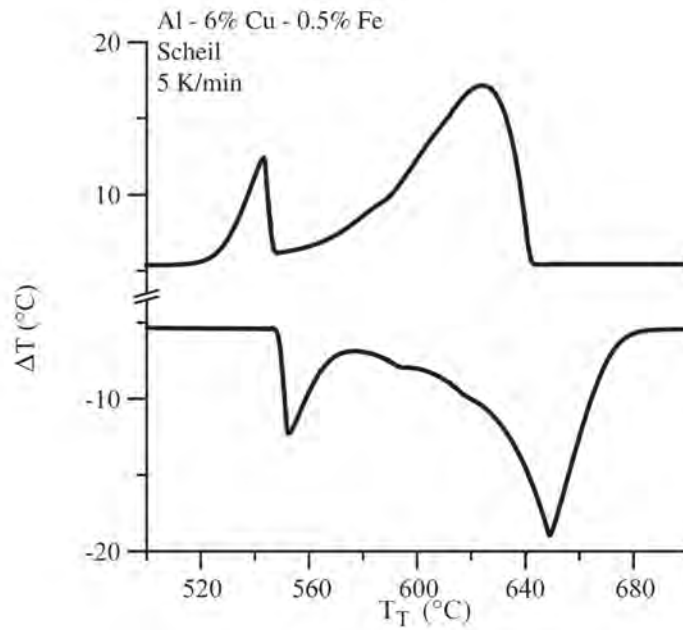


Figure 2-15 Calculated DTA response of the solidification of alloy 2 through the liquidus, ternary transition reaction and finally through the ternary eutectic reaction [72].

## CHAPTER 3 EXPERIMENTAL

### 3.1 Alloy Preparation

All experimental alloys were produced by non-consumable arc melting (tungsten electrode) of high-purity starting components (Ti, Al, Nb) (99.99at% purity) using a water-cooled copper crucible in a gettered ultra high-purity argon atmosphere. The chamber was evacuated and backfilled with argon at least 3 times, upon which the final fill was allowed to continuously exhaust gas through a >1 atm relief valve, thus ensuring a slight positive pressure throughout the duration of the melting procedure. Due to the substantial differences in density and melting points among the starting materials, it was difficult to melt the approximately 5 gram buttons completely in one step. Consequently, the buttons were turned over and remelted 4-6 times in an attempt to insure homogeneity. Prior to each melt, the chamber was gettered by melting approximately 1 gram of Ti. The Ti was inspected for surface oxides after each melt in order to verify that no gross oxidation had occurred.

### 3.2 Thermal Analysis

A Setaram Setsys Evolution 1750 equipped with a DSC 1600 sensor was used for thermal analysis. Solid state transformation temperatures as well as solidus and liquidus temperatures were measured by a DTA technique. Although a DSC style sensor was used, at high temperatures the capabilities of this sensor to measure heat-flow are limited due to heat transfer by radiation to and from the sample. Therefore this sensor was used in “DTA mode”. In a DTA the sample and the reference are placed in a temperature-controlled environment (furnace) surrounded by a gas called the “carrier gas”. The function of this gas is to assist the transfer of heat to and from the sample, and in the present study, provided a shielding atmosphere. As the temperature of the furnace is changed, heat is transferred to and from the sample and reference.

Due to the heat capacity differences and thermal events associated with transformations a temperature difference develops between the sample and the reference. This signal is measured as a function of the sample's temperature.

A schematic taken from Flemings [73], which is representative of the system used here, is shown in Figure 3-1a. Several main heat flow contributions are relevant to this work. In every system the transfer of heat flow into the sample and reference by radiation and the carrier gas are critical. The latter is controlled by the thermal conductivity of the carrier gas. A second major contribution is the heat flow between the sample and reference through the heat flow plate. This is referred to as "cross talk" between the sample and reference.

There are two main considerations in the design and interpretation of DTA experiments. The first is the sensitivity, which is directly proportional to the temperature difference that develops between the sample and reference. The second is the temperature resolution, which is linked to the thermal lag, or time required to transfer heat between the sample and reference. Thermal lag and the sensitivity are mutually exclusive. In the extreme case where there is no thermal lag, the sample and reference would not develop a temperature difference, therefore sensitivity is not possible. Conversely, in the case where the thermal lag is large, heat transfer from the furnace is sluggish and magnifies the temperature difference causing an increase in sensitivity. In the study discussed here, an accurate measurement of the temperatures at which thermal events occur is sought after. Therefore, a compromise in sensitivity is acceptable in order to maximize the temperature resolution of the measurements.

In practice, it is common to model thermal analysis equipment with equivalent electrical circuits for the purpose of making calculations and simulations. In this type of model, temperature is equivalent to voltage and heat flow is equivalent to current. An equivalent circuit

for the system described above was generated using the Pspice software package. A schematic of this system is shown in Figure 3-1b, where the thermal conduction between the gas and sample is modeled by the resistors ( $R_{\text{sample}}$  and  $R_{\text{reference}}$ ). Thermal conduction between the sample and reference is labeled as  $R_{\text{crossTalk}}$ . The heat capacities of the sample and reference are modeled by capacitors  $C_{\text{sample}}$  and  $C_{\text{reference}}$ , whereas the furnace temperature or voltage is supplied by a programmable voltage source. The equivalent temperature of the sample, reference and furnace are measured by marked voltage leads.

Two simulations were run on Pspice in order to investigate the effects of varying the thermal conductivity between the furnace and both the sample and reference. Both of these are controlled by the selection of the carrier gas. Investigations of this effect were accomplished by varying the resistance values related to conduction between the furnace and the sample and reference ( $R_{\text{sample}}$  and  $R_{\text{reference}}$ ) in each simulation by the same amount. For the first simulation, a value of 10K was used for both  $R_{\text{sample}}$  and  $R_{\text{reference}}$  and for the second simulation the value was changed to 1K. The 10K resistance was used to model the low conductivity gas and the 1K to model the high conductivity gas.

The furnace in this simulation was ramped up at a constant rate and the difference between the sample and reference was measured as a function of time. The results of the simulations are shown in Figure 3-2. The red curve represents the furnace temperature, whereas the two dashed curves (grey and blue) represent the temperature difference between the sample and reference for each simulation. The blue curve shows the temperature difference that develops when using a high conductivity carrier gas, and the grey curve represents it for the low-conductivity carrier gas. Comparison of the curves associated with the high-conductivity and low-conductivity gases reveals that a high-conductivity gas results in higher temporal resolution. This is evident from

the fact that the high-conductivity gas develops a greater temperature difference at the beginning of ramping the furnace. For the low-conductivity gas, the temperature difference surpasses the other gas after 23 seconds, demonstrating that the low-conductivity gas yields a higher sensitivity.

He and Ar gases were considered as possible candidates in this study. The thermal conductivities are  $0.1513 \text{ W m}^{-1} \text{ K}^{-1}$  for He, and  $0.01772 \text{ W m}^{-1} \text{ K}^{-1}$  for Ar . There is nearly an order of magnitude difference between them, which will directly affect the temperature difference that develops between the sample and the reference, as well as the thermal lag of the instrument. Based on the objective of maximizing the temperature resolution of the instrument at the expense of some sensitivity, ultra high-purity He gas was selected for all measurements.

High-temperature calibrations (temperature correction) were performed by melting three pure elements at three heating rates. The elements used were high purity Al, Cu and Ni. Standard pure Cu and Ni were purchased from NIST, whereas the pure Al was purchased from Alfa Aesar. The samples were placed in alumina crucibles with alumina caps. The standard materials were each heated at 20 K/min to 50C above the melting temperature and held isothermally for 5 min. The samples were then cooled to 150C below the melting temperature, thus allowing them to solidify against the crucible and ensure a good thermal contact between the standard material and the crucible. The samples were heated at scan rates of 10, 5 and 2 K/min to approximately 50C above the melting temperature. The melting point of each element at each scan rate was determined using the extrapolated onset method [73]. The melting temperatures at each scan rate are listed in Table 3-1, along with the standard melting temperature reported for each element. The melting temperatures as function of the scan rate are plotted in Figure 3-3. These curves were used to calculate the theoretical melting temperature associated with the zero heating rate

by linear regression. These values were used to obtain the adjustable parameters of a temperature correction equation.

Table 3-1 Melting temperatures at the respective scan rates of standard materials.

Standard	Scan rate (K/min)	Melt temp (C)	Theoretical melt temp (C)
Ni	2	1449.69	1455
Ni	5	1449.47	1455
Ni	10	1449.5	1455
Cu	2	1080.04	1084.62
Cu	5	1080.31	1084.62
Cu	10	1080.38	1084.62
Al	2	658.2	660.32
Al	5	658.22	660.32
Al	10	658.32	660.32

The heat flow dynamics of the furnace, crucible and DSC plate are accounted for by a temperature correction equation. This equation is a function of the scan rate and sample temperature. In theory once tuned to the system, this model corrects for thermal lag and errors associated with the thermocouples location relative to the sample. The temperature correction equation is:

$$Dt = b_0 + b_1.T + b_2.V + b_3.V^2$$

Where

T: Sample temperature in °C

V: Scan rate in K.min<sup>-1</sup>

Dt: Temperature correction

bx: Adjustable Parameters

The melting temperatures as a function of the scan rate are used to calculate the adjustable parameters through statistical analysis. Data points for each material consisted of the scan rate, the melting point measured at that scan rate, and the theoretical melting point or melting point at the infinitely slow scan rate. This data matrix is then used to calculate the coefficients of the temperature-correction equation.

### 3.3 Heat Treatments

#### 3.3.1 Heat Treatment Schedules

Heat treatments were conducted in a vertical vacuum tube furnace under a flowing ultra high purity gettered argon atmosphere. Heat-treatment specimens, sectioned from the as-cast material were wrapped with tantalum foil and suspended. The wrapped samples were tied off with a Ta wire, which extended approximately one inch off the sample. This “loose end” was then inserted through a braided zirconia rope. This braided rope was approximately one foot long and extended outside the furnace’s hot zone. The cool end of the rope was attached to a steel wire and suspended from the drop quenching fixture. The water-cooled drop quenching fixture consisted of a rotating rod attached to a hook mechanism upon which the steel wire was attached. Rotation of the rod released the attachment between the steel wire and the fixture’s hook, allowing the entire suspension system to drop to the bottom of the sealed alumina tube. All heat-treatments discussed were terminated by direct immersion water quenching. Water quenching was done by removing the bottom cap and nearly simultaneously dropping the sample into the water bath. The sample temperature was recorded from a B-type thermocouple located inside the alumina tube, situated near the furnace’s hot zone and the sample. After the quenching procedure, the specimen was polished to remove any environmentally affected zones that may have formed as well as yield a smooth surface. The Ta suspension wires and foil were inspected in order to gauge if any gross oxidation had occurred.

The heat-treatments conducted in this study are described by two generic heat-treatment schedules. The first schedule consisted of a 12K/min ramp to the heat-treatment temperature. After the required time at the isothermal hold temperature the sample was drop quenched and the furnace was ramped back down. The second schedule consisted of a 12K/min ramp to the upper isothermal hold temperature. After the isothermal hold the furnace was ramped down to a lower

temperature, where the sample was held for a specific time (double heat treatment). After the second isothermal hold the sample was quenched and the furnace was ramped down. The second heat-treatment schedule or double heat treatment was applied in the investigation of solid-state transformations detected by thermal analysis.

### **3.3.2 Selection of Isothermal Hold Times**

In the study of phase equilibria the selection of holding times is important. During an equilibrating isothermal heat-treatment several events occur. These events consist of the formation of the equilibrium phases, equilibrium compositions and coarsening of the microstructure. Although coarsening does affect the equilibrium compositions through the contributions of surface energy to Gibbs free energy [74], these effects are negligible after coarsening. Ideally, an equilibrating heat-treatment will allow the material sufficient time to allow the equilibrium phases and compositions to develop. Therefore it is critical to determine the time sufficient to reach such a condition.

The hold time selected for equilibrating heat-treatments was 4hrs. This was based on a series of DTA experiments designed to investigate the effect of the hold time. One such experiment based on alloy A133 (Nb42.7 Al42.6 Ti14.7) is described here. The details of this alloy are given in Chapter 7. A DTA curve of alloy A133 cycled through the transformation temperatures is shown in Figure 3-4. The peaks on this DTA curve were identified based on microstructural evaluations described in Chapter 7. Alloy A133 enters the  $\sigma+\gamma$  phase field at 1410C and then crosses into the  $\gamma$ -phase field at 1562C. On this curve one of the heat-treatment temperatures used in this study is marked as  $T_h$ . Based on this DTA a series of tests was designed. The results and analysis of one of these tests is discussed here.

Four separate DTA samples were prepared from the center of the same arc-melted button. Two series of tests were designed in order to investigate the selection of the isothermal hold time. The first series consisted of heating a sample to 1520C and holding it isothermally for 20hr. After a 20hr hold the sample was cooled to 1240C and then thermally cycled between the temperatures of 1240C and 1520C. The second test in this series consisted of subjecting a separate sample to the same thermal path, except the isothermal hold time was reduced to 4hrs. The 20hr isothermal hold time was used as the baseline for comparison to near equilibrium conditions. The DTA curves associated with each test are plotted in Figure 3-5a. The curves associated with the 4hr and 20hr heat-treatments are comparable, indicating that a 4hr heat-treatment at 1520C resulted in an equilibrium microstructure. The logic behind this is that the transformation temperatures are dependent on the phases and compositions which constitute the microstructure. Had the microstructure that developed during the 4hr hold differed significantly in composition and structure from that of the 20hr hold, then the transformation temperatures would also be different. In these results a variation was not seen, therefore 4hrs at 1520C was considered to be equivalent to 20hrs in respect to the assessment of equilibrium.

A second thermal cycle was designed to investigate the 4hr isothermal hold time further. This test however differed from the first in that it targeted the full transformation path by including the transformations above 1520C. This test consisted of heating a DTA sample of the same material to the isothermal hold temperature of 1590C for 20hrs. After the isothermal hold the sample was cycled between the temperatures of 1240C and 1590C. The second sample was subjected to an equivalent cycle, except the isothermal hold was 4hrs instead of 20hrs. A comparison of both DTA cycles is shown in Figure 3-5b. As with the first set of tests the

transformation temperatures did not vary, indicating that 4hrs is a sufficient time to bring the samples near to their chemical equilibrium.

### **3.4 Microstructural Analysis**

As-cast and heat-treated materials were prepared for microstructural evaluations by standard metallographic techniques. The samples were pressed into a thermoset epoxy mold and later polished. Alumina water-based slurries were used for most of the polishing steps except the final step where a silica based slurry was used. The final step minimized contamination of the optical surface with alumina, which could possibly result in errors during chemical analysis. Optical microscopy of etched samples and SEM-BSE on a (JOEL 6400) were employed for microstructural evaluation. EPMA (electron probe microanalysis) using a JOEL Super Probe 733 was employed for compositional measurements of the alloying elements, that constitute the bulk material as well as within each phase.

TEM analysis was performed on select samples in particular regions of interest. Conventional TEM was performed on a JEOL 200CX, whereas STEM and TEM EDS was performed on a JEOL TEM 2010F. High Angle Annular Dark Field imaging (dark field STEM) was employed to facilitate z-contrast based imaging by the acquisition of only the incoherently scattered electrons. These electrons are highly sensitive to atomic mass and mostly insensitive to crystallography.

In most cases conventional TEM sample preparation was not feasible, due to either the need of a site-specific TEM foil, or due to the mechanical integrity of the material itself. The latter is related to the fact that some mechanical integrity was required in order to thin, punch or drill out a thin disk and finally jet polishing. In those cases the samples were prepared by FIB specimen preparation methods using a FEI Strata DB235.

Several major drawbacks were unavoidable when using the FIB. This technique is time consuming, and the amount of electron transparent material attained within each foil is small compared to the more conventional methods. Additionally in micron-scale polycrystalline samples the number of crystallographic orientations available within each foil is limited by the small area. This reduces the number of zone axes that are reachable within the tilting limits of the instrument. Finally there is some beam damage that occurs even with careful sample preparation using this technique.

A series of micrographs outlining the TEM foil preparation technique of a Ti-Al-Nb sample is shown in Figure 3-6. The sample was mounted on an aluminum stub using conductive carbon tape and pumped down in the FIB chamber. The region of interest was located using ion-beam imaging. This imaging method provides sufficient z-contrast to allow for the identification of microstructural regions. Figure 3-6a exhibits the region of interest which in this example consist of the  $\beta$  and  $\gamma$  phases. Two X-shaped marks are cut into the sample to facilitate alignment of the beam and the sample's region of interest. A strip of Pt is deposited directly across the region of interest to protect it from beam damage (Figure 3-6b). Two wedges are then milled on either side of the Pt strip using 5000 pA beam current (Figure 3-6c). The Pt protected area was next thinned with consecutively smaller beam currents up to the final thickness (Figure 3-6d). Care is taken in order to assure that the sample is thinned and scanned with a glancing angle thus minimizing the amount of implanted Ga ions. The 15 $\mu$ m wide sample is then mounted on a carbon coated Cu grid using an ex-situ micromanipulator and is ready for TEM analysis.

### **3.5 High Temperature XRD**

High temperature XRD experiments were performed on a Philips High Temperature XRD. The high temperature XRD heating stage was redesigned in order to increase its temperature

capabilities from 900C to 1600C while under an inert He atmosphere. Analysis of the instruments power capabilities indicated that the primary limitation to its temperature capabilities were attributed to exceeding the current capacity of the power supply. A new heating stage was implemented that has a reduced cross section in the region where the sample is mounted, in contrast to the conventional heating stage that maintains a constant cross-section throughout its length. This reduced area resulted in a local increase in the current density, which yielded a higher temperature underneath the sample.

Several iterations were tested to arrive at an optimal stage design. The final design consisted of 3 components shown in Figure 3-7a. The 2 to 3 mm thick Ta sections were cut and a thin section was prepared by rolling Ta sheet down to a foil. The three sections were then spot welded together. A Ta wire was also spot welded across the two thick Ta sections, bypassing the thin section. The function of this wire is to act as a continuous Ta getter during heating. A 1.2mm thick slice of the as-cast material was lightly spot welded on a tantalum stage. The thermocouple was located directly underneath the thin foil. A photograph of a finished stage with a mounted sample is shown in Figure 3-7b.

The HT-XRD stage and sample were removed after every test. Therefore, it was necessary to align the sample and calibrate the angular relationship between the source, detector and stage. All samples were aligned to a known peak position determined by conventional powder XRD measurements that were taken on a Philips APD 3720. The alignment was performed by making a series of small scans around the known peak. The height of the stage was adjusted in between each scan until the intensity of the peak is maximized. Once the intensity was maximized, a slow scan is conducted over the known peak. The peak position was found, and this angle was set to the known Bragg angle of the correspondent diffracting plane.

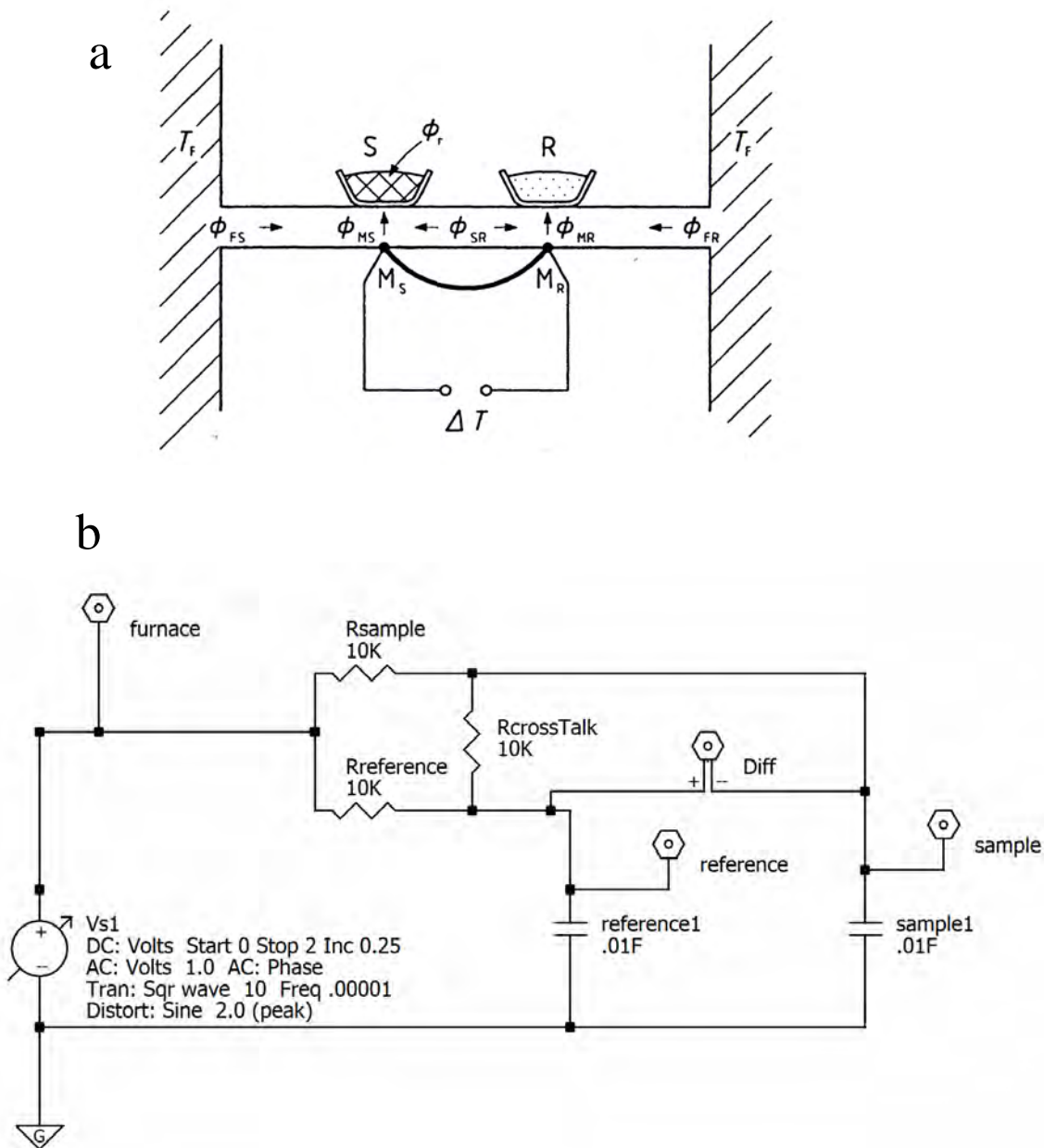


Figure 3-1 Schematics of a) a DTA comparable to the Setaram used in this study with heat-flow paths [73] and b) the equivalent circuit that models the heat-flow and capacitance through electrical simulations.

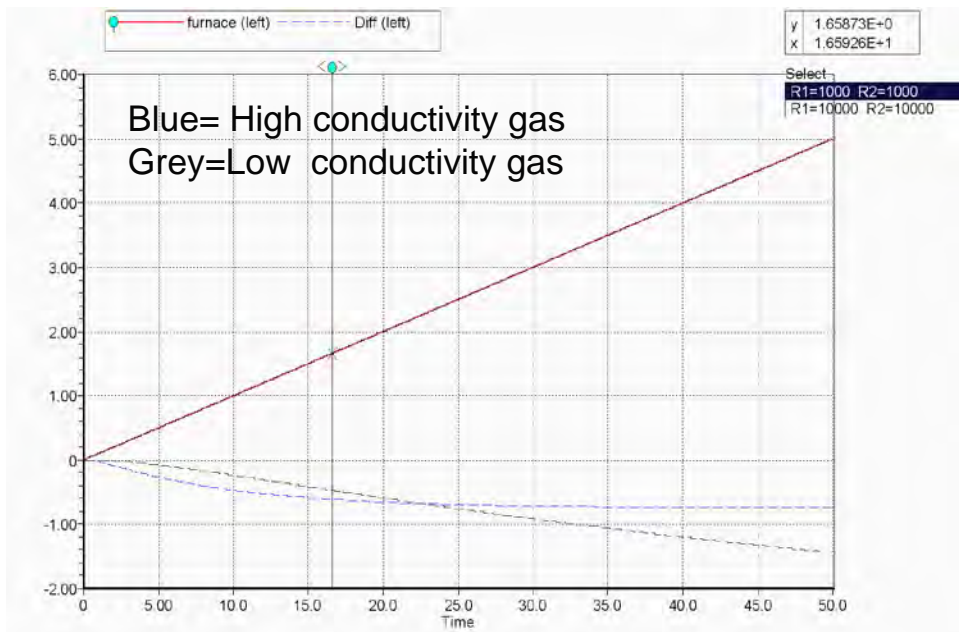


Figure 3-2 Simulation of a DTA modeling the systems response to a high and low conductivity gas.

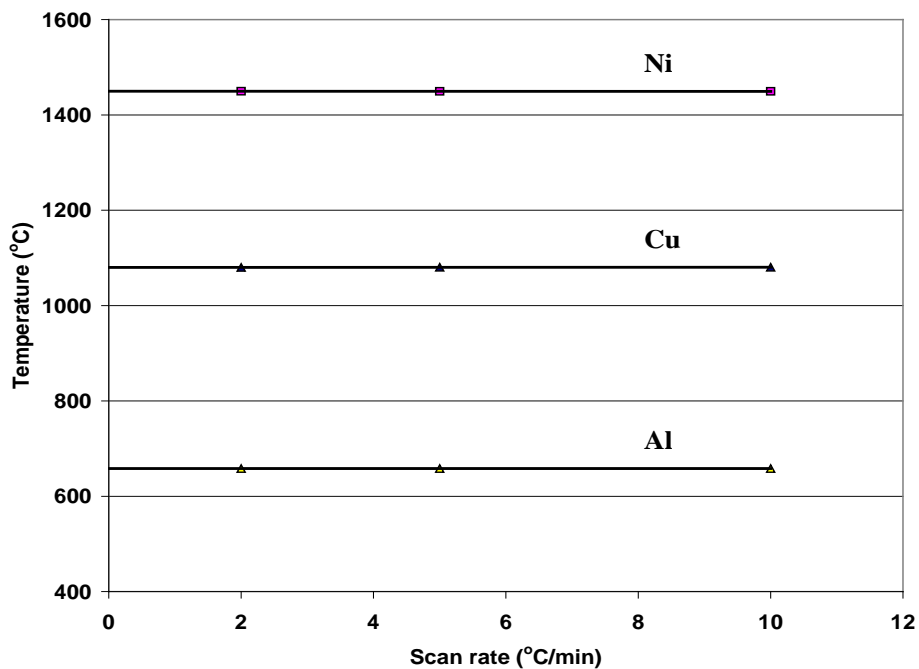


Figure 3-3 Calibration (Temperature correction) curves using standard high purity reference materials (Ni, Cu and Al).

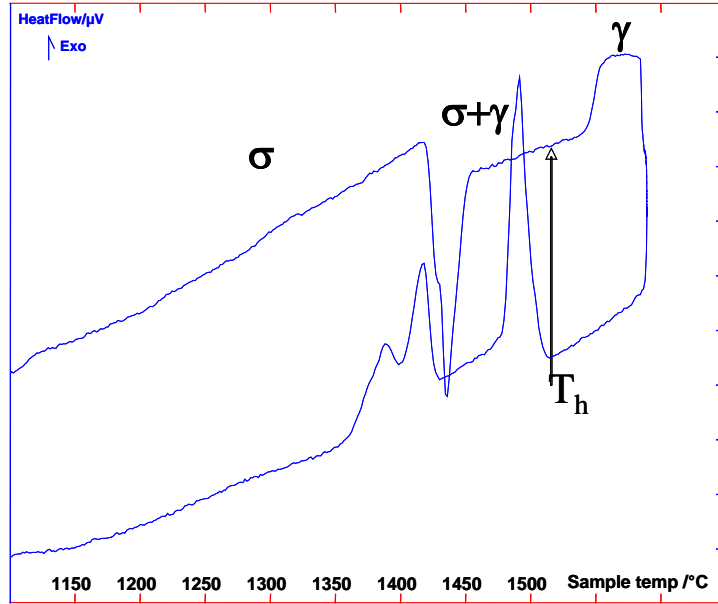


Figure 3-4 DTA curve of alloy A133 at 10K/min.

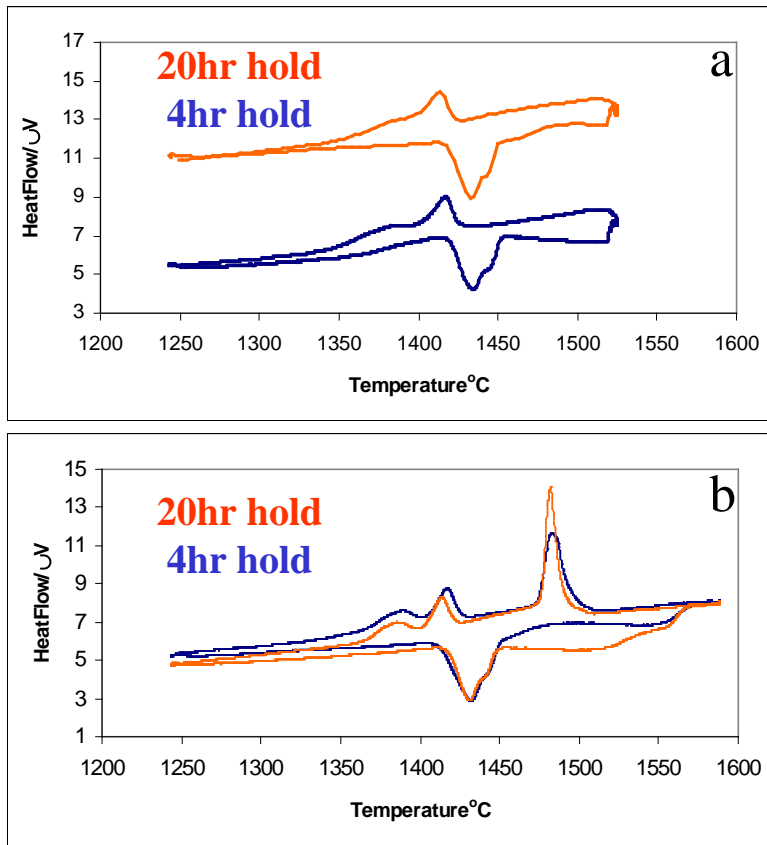


Figure 3-5 DTA curve of alloy A133 at 10K/min. with isothermal hold at A) 1510C and B) 1600C.

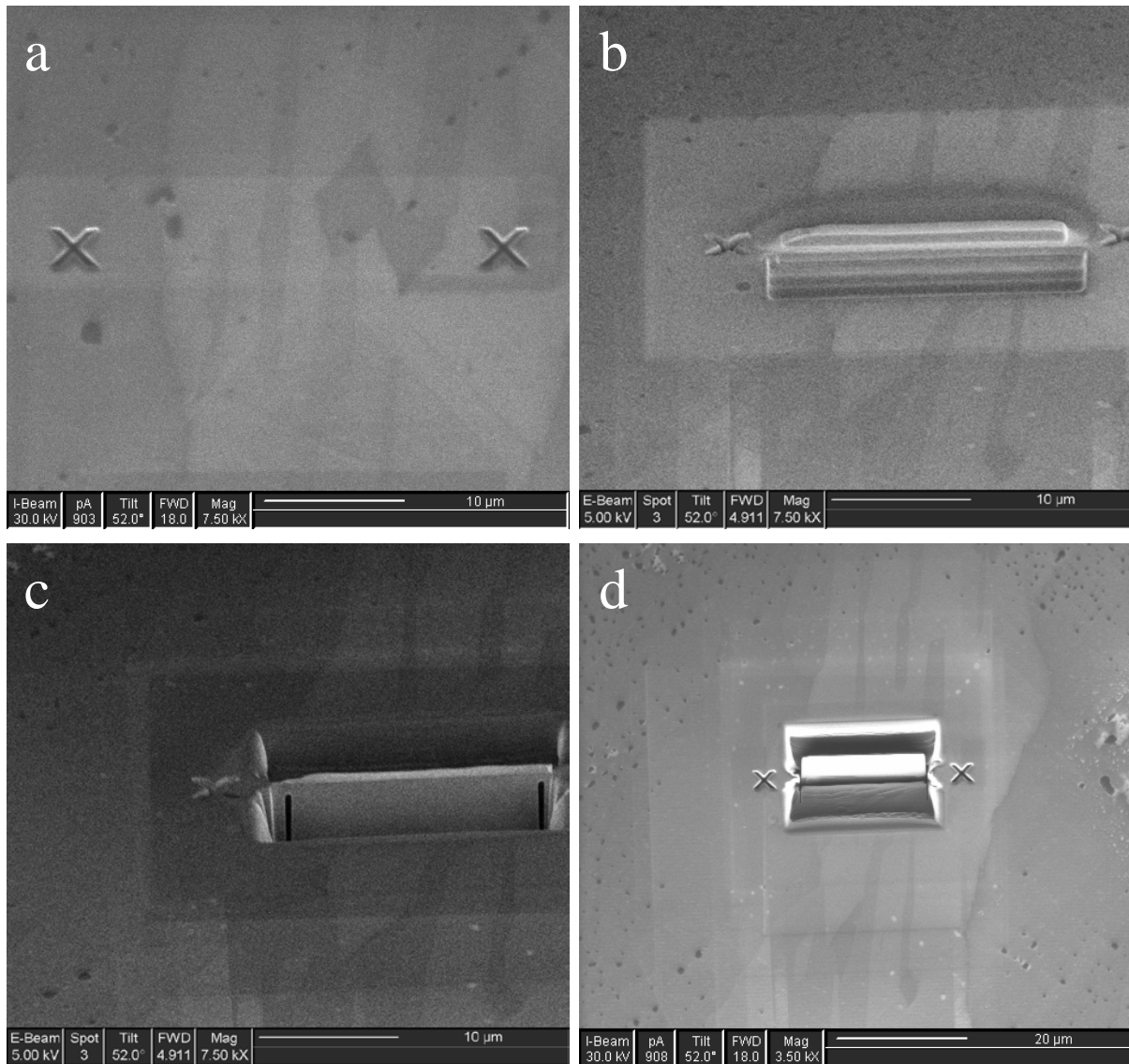


Figure 3-6 Ion-generated secondary electron image during the FIB sample preparation showing a) initial area of interest b) deposition of protective Pt layer c) cutting of trenches and d) free standing thin foil.

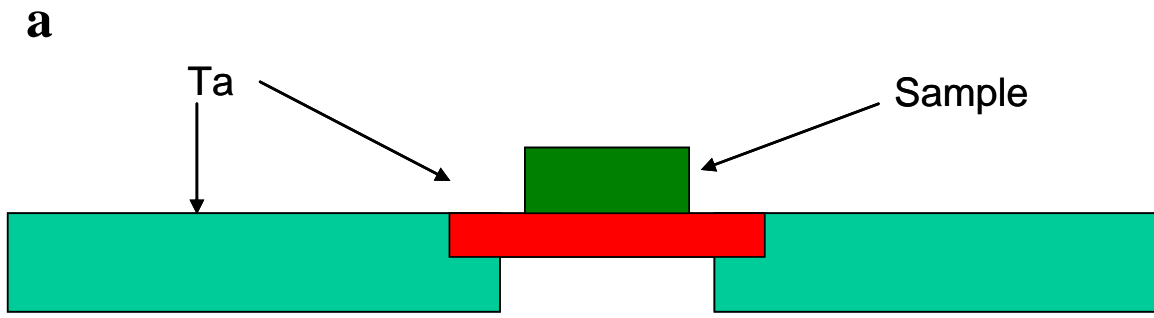


Figure 3-7 Images of a) schematic of HT-XRD stage and sample and b) photograph of the stage after fabrication.

## CHAPTER 4 β-PHASE EXTENSION

### 4.1 Introduction

Much controversy exists regarding the extent of the β-field on the liquidus projection as discussed in Chapter 2. Although this region of the ternary phase diagram is an important compositional area for alloy development, limited experimental data exist to examine the validity of the calculated liquidus surfaces. The current chapter focuses on an accurate understanding of L/β/γ bivariant equilibria in order to develop optimized σ+γ phase microstructures. Past work within our research group demonstrated that high Nb additions to TiAl based alloys brought out a σ+γ microstructure that exhibited improved mechanical properties over γ+α<sub>2</sub> based alloys [11]. The σ-phase, however, is a brittle intermetallic phase that reduces forgeability and fracture toughness. The β-phase, which is stable in these alloys at high temperatures is a ductile BCC phase, therefore there is much interest in its stability. In order to have an accurate understanding of the interrelation between the stability of the β-phase at high temperatures and how the σ and γ phases precipitate from the β-phase as temperature is decreased, the extension of this phase into the ternary phase diagram was examined.

Figure 4-1 shows two superimposed calculated liquidus projections presented in the thermodynamics assessments of Servant and Ansara [18] and Kattner and Boettinger [56]. As far as the extension of the β-field is concerned, these calculations are somewhat similar and in accordance with the experimental work based on the analysis of the as-cast microstructures performed by Zdziobek et al. [55] and Perepezko et al. [57]. Leonard et al. [75] showed experimentally that the β-field should be expanded by pushing the L/β/η and L/β/σ bivariant

equilibrium towards the lower Ti contents also shown in Figure 4-1. These experimental results were analyzed and combined in a phase diagram evaluation conducted by Raghavan [16].

The stability of the  $\beta$ -phase in the current region of interest was first examined by our group on an alloy of composition 33Ti-40Al-27Nb, at% (alloy D2) [19]. A detailed series of heat-treatments combined with microstructural evaluation determined that this alloy solidifies as the  $\beta$ -phase, which precipitates a  $\sigma+\gamma$  phase microstructure at lower temperatures. In order to address the L/ $\beta$ / $\gamma$  bivariant equilibria, the phase stability of an alloy that is in the calculated  $\gamma$ -field was investigated, as marked in Figure 4-1. The composition of the arc-melted alloy 11 (37Ti-44.5Al-18.5Nb, at%) was identified by EPMA of the as-cast materials. Alloy 11's composition was higher in Ti and Al than alloy D2. Based on the existing liquidus projections, alloy 11 composition is predicted to solidify as  $\gamma$ -TiAl by calculations and experiment. Microstructural observations of the as-cast material, however, suggested that the  $\gamma$ -phase forms through a solid-state transformation, therefore the high-temperature stability of this alloy was analyzed for evidence of the  $\beta$ -phase.

## 4.2 Thermal Analysis

The liquidus, solidus and solid-state transformation temperatures were determined by DTA following the recommended practices guidelines [72]. The as-cast material was sectioned and placed in a covered alumina DTA crucible. The initial DTA thermal cycle was performed with a scan rate of 10K/min up to a temperature of 1600C after which the sample was held isothermally for 30 min in order to equilibrate the temperature and finally ramp down at a rate of 10K/min. Cursory microstructural evaluations of the DTA sample revealed complete melting.

#### 4.2.1 Thermal Analysis of Phase Transformations and Melting

The DTA temperature vs. heat-flow curve for both heating and cooling of the as-cast material are shown in Figure 4-2. Two pieces of information were sought after by this test, primarily the solidus temperature and, secondly, solid state phase transformation temperatures. The peak associated with melting was sharp and symmetric suggesting that the alloy melted as a single phase. The solidus temperature was measured to be 1532C, whereas the highest temperature solid-state transformation was complete at 1470C.

A solutionizing temperature of 1500C was selected based on these temperatures and the thermal signatures indicating that the majority of the microstructure consisted of a single solid phase prior to melting. The solutionizing temperature was designed to be below the melting point of the alloy, but above the highest solid-state reaction. This temperature was used to equilibrate the material in the single-phase field, with the goal of erasing the microstructural characteristics inherent from the thermal history of the as-cast material. An isothermal hold time of 30 min was selected for solutionizing.

The DTA curve exhibits two main peaks upon cooling indicating two major solid-state reactions. The heat flow signal returns to the baseline at 1161C, which is below the solid-state transformations, whereas upon heating above the transformation temperature, the baseline is reached at 1482C. Based on these results a thermal cycling profile was designed for A11, which was within the temperature range of 1100C to 1500C, in order to investigate the solid-state transformations. The thermal cycling profile consisted of heating to the solutionizing temperature followed by an isothermal hold, after which thermal cycling between the selected temperature range was performed.

The DTA results of the homogenized structure are presented in Figure 4-3. The initial heating of the as-cast structure resulted in slightly lower transformation temperatures, which can

be attributed to its finer microstructure formed upon arc melting. Two sets of endothermic peaks were observed during heating, a double peak and a shallow peak. The shape of the double peak provided strong evidence of a convolution of two peaks, which exhibited maxima at 1277C and 1322C and a first deviation from the baseline at 1239C that returns to the baseline at 1356C. The shallow peak begins near the end of the double peak, which exhibits maxima at 1463C before returning to the baseline at 1479C.

#### **4.2.2 Stability of Thermal Events**

Calculated phase equilibria predicted that there should only be one phase undergoing dissolution upon heating, namely, the  $\sigma$ -phase dissolving from a  $\sigma+\gamma$  microstructure. Yet, thermal analysis revealed a relatively complex set of peaks. This brought into question the validity of the DTA peaks shown in Figure 4-3. In particular, the accuracy of these DTA peaks at representing equilibrium phase transformations was not clear. To investigate this further, two series of test were designed: the first series targeted the cyclic stability of the thermal results, whereas the second series inspected the temporal stability of the transformation peaks.

A series of tests were devised to target each set of peaks considering the two main events that could affect the cyclic stability of the phase transformations. The first phenomenon that could influence the cyclic stability of the thermal events arises from the high vapor pressure of aluminum at elevated temperatures. If the sample is exposed to high temperatures for too long, it is possible that the alloy will drift towards a leaner aluminum composition, thus changing the transformation temperatures. Secondly, in a material that is thermally cycled, the forward and reverse phase transformations result in a transient microstructural evolution with variations in morphology and scale between cycles. This transient microstructure may persist for several thermal cycles until a reversible condition is reached [72]. The transformation temperatures and

the peak shape are, in turn, directly linked to the microstructural evolution. Either event obscures the measurement of equilibrium, therefore the cyclic stability is examined.

The cyclic stability of the phase transformations was examined by thermally cycling the DTA in a temperature range encompassing the lower temperature double peak, and a second range centered around the higher temperature shallow peak, both of which are shown in Figure 4-4 and Figure 4-5, respectively. The first three cycles at a constant scan rate of 10K/min are plotted continuously on the same graph. Only minor changes were observed around the double peak between the first and second cycle, whereas significant changes did not occur between the second and third cycle. In contrast, the higher temperature shallow peak revealed no changes between any of the cycles. This result provided evidence that firstly the samples composition was relatively stable, and, secondly, after the solutionizing step the microstructure that evolves from cycling above and below the peaks is reversible on subsequent cycles.

The temporal stability of the thermal events was also examined by a test termed the interrupted heating cyclic thermal analysis. This test was designed to evaluate if the solid-state transformation temperatures and peak widths are being affected by transformation kinetics. Essentially the interrupted heating thermal cycle consists of segmenting the heating leg of the ramp with isothermal holds at various temperatures around and/or within the peak. In the event that the scan rate exceeds the transformation kinetics, an isothermal hold at or around the peak will supply the additional time required for the phases to reach a minimum free energy state. A fraction or all of the thermal events would have occurred during the isothermal hold. Thus, upon the continuation of heating the measured peak position and shape is different from the uninterrupted cycle. The comparison between cycles with and without an interrupted heating allows for the characterization of the effects of kinetics on the analysis of transformations

occurring at equilibrium. Both the double peak and the shallow peak are examined by this method.

The DTA curves for the interrupted heating of the double peak and shallow peak are shown in Figure 4-5a and b respectively. Four 30-min isothermal holds at various temperatures within the double peak, and six holds within the shallow peak upon heating, are selected. These isothermal holds appear in Figure 4-5 as a sharp endothermic drop due to the abrupt break in the heating segment and associated heat-flow reduction into the sample.

After the hold, and upon the continuation of heating at the prescribed scan rate, the heat flow curve may either immediately return to the baseline or continue the peak, as if the isothermal hold had no significant effect. In the case that the curve returns to the baseline it may be assessed that the isothermal hold was actually outside the equilibrium transformation temperatures, and the peak which exists at this temperature during the conventional scan was only evident due to sluggish kinetics or too high of a scan rate. In alloy 11, the interrupted heating of both peaks resulted in the curve continuing on, thus validating the start and finish temperatures as true near-equilibrium transformation temperatures. In addition, the scan rate of 10K/min was considered to be acceptable in these materials. The transformation temperatures were subsequently used as a guide to design heat treatments and high temperature XRD experiments in alloy 11.

### **4.3 Microstructural Evaluations**

XRD results revealed that the as-cast alloy consisted of mostly the  $\gamma$ -phase with some  $\beta$ -phase (Figure 4-6). The as-cast microstructure shown in Figure 4-7 suggests that the major phase had formed by a solid-state phase transformation as evident in the acicular morphology. The SEM micrograph revealed that at least two different composition phases existed in the as-cast

microstructure. This observation implies that a single-phase existed at high temperatures, which transformed to form a multi-phase structure through a solid-state reaction.

Bright field TEM micrographs are shown in Figure 4-8. The low magnification TEM (Figure 4-8a) exhibits a morphology which confirms nucleation and growth of a phase through solid-state transformation. The aspect ratio suggests that particular growth directions into the parent phase are preferred. At higher magnifications (Figure 4-8b) the  $\gamma$ -phase (which appears bright) grows into the  $\beta$ -phase (which appears dark) forming micron-scale Widmanstätten-like morphology. The retained  $\beta$ -phase is located in between the  $\gamma$ -phase laths. A third submicron scale precipitate was found to form within the  $\gamma$ -phase. This phenomenon is an important area of interest that currently is being analyzed in detail by the group member, Sonalika Goyel.

#### **4.4 In Situ High Temperature Phase Evaluation**

##### **4.4.1 High Temperature X-Ray Diffraction**

The microstructural evidence suggesting the  $\gamma$ -phase formed through a solid-state transformation motivated the development of specialized equipment for a high temperature X-ray diffraction study. Thermal analysis revealed that temperature capabilities approaching 1550C were required in order to investigate the highest temperature solid-state reactions. Alloy D2 in contrast to alloy 11 retained the  $\beta$ -phase to room temperature when subjected to fast cooling rates. Prior work established the phase transformation path of alloy D2 with a series of heat-treatments combined with microstructural evaluation of quenched samples. The transformation path of this alloy established in [19] is outlined in Figure 4-9a. Alloy D2 was selected to develop instrumentation capabilities for high-temperature structural measurements. A sample with alloy D2's composition was arc-melted and thermally cycled in the DTA (Figure 4-9b). The transformation temperatures were determined to be consistent with those reported in [19]. With

the prior knowledge of this alloy's phase transformation path, high-temperature XRD measurements were performed in order to take an in-situ structural measurement of the high-temperature  $\beta$ -phase.

Simulated XRD patterns were generated from available structural data for the sigma ( $\sigma$ ) [22, 41, 51], gamma ( $\gamma$ ) [39-41], beta ( $\beta$ ) [39] and orthorhombic (O) phases [19] and compared to the room temperature XRD patterns. The O-phase forms via a martensitic transformation from the  $\beta$ -phase only upon quenching [19]. In order to investigate the identity of the high temperature phase and confirm the formation of the  $\gamma$ -phase upon cooling, HT-XRD was conducted for this alloy using a custom Ta heating stage. The details of the design and alignment of this stage were discussed in Chapter 3. The sample was aligned to the Bragg's angle of the  $\gamma$ -(202), based on the room temperature XRD profile of the as-cast material. The simulated patterns for the  $\beta$ ,  $\sigma$  and  $\gamma$  phases revealed distinct non-overlapping diffraction peaks in the two-theta range of 50 to 80 degrees, as shown in Figure 4-10. Although this range does not include the maximum intensity peaks, all high-temperature scans were performed over this range in order to provide a clear distinction between the  $\beta$ ,  $\sigma$  and  $\gamma$ -phases. A minor amount of diffraction from the Ta-(200) stage was recorded in some of the HT-XRD scans.

Alloy D2 was heated to approximately 1500C in the HT-XRD. This temperature is marked with a 1 on the DTA curve shown in Figure 4-9b. At this temperature the  $\beta$ -phase should be stable according to the DTA curve and Figure 4-9a. After a 30min isothermal hold in the HT-XRD, a 15min scan, shown in Figure 4-11, was performed over the two-theta range of 50 to 80 degrees, revealing the presence of the  $\beta$ -phase in the microstructure. The temperature was then lowered to 1100C in the HT-XRD (marked with a 2 in Figure 4-9b). After a 30min isothermal hold a second 15min scan was performed. As established in [19] the  $\sigma$ + $\gamma$  phases were identified

and all diffraction peaks associated with the  $\beta$ -phase were not detected (Figure 4-11). This result established the ability of the HT-XRD at taking in-situ structural measurements at elevated temperatures near 1500C as well as confirmed that the  $\beta$ -phase extends past alloy D2's composition at high temperatures.

In order to investigate if the  $\beta$ -phase field also extends over alloy 11, and if this alloy is near the bivariant equilibria, a sample was heated to near the edge of the highest temperature peak, as indicated by pointer 1 in Figure 4-3, and held isothermally for 15min. The 15min scan at this temperature, as shown in Figure 4-12a scan 1a, reveals a strong signal from the  $\beta$ -phase with diminished intensity of the  $\gamma$ -peaks in comparison to the as-cast structure (Figure 4-6). Immediately upon the completion of the first scan, a second 15 min scan shown in Figure 4-12a 1b (also in Figure 4-12b curve 1) was run, which exhibits further intensifying of the  $\beta$ -phase's (200) peak. This finding confirms that indeed the  $\beta$ -phase, in contrast to the computed liquidus projections, is the primary phase that solidifies in this alloy. It should be noted, although the  $\beta$ -(211) peak is the prominent peak in the standard powder XRD pattern, texturing combined with a relatively large grain size resulted in a higher relative intensity from the  $\beta$ -(200) than from the  $\beta$ -(211) in the microstructure studied.

The temperature was lowered after the second scan at marker 1 below the second solid-state transformation temperature range, as indicated by pointer 2 also in Figure 4-2. After a 30min isothermal hold, the XRD profile shown in Figure 4-12b revealed that the  $\beta$ -phase was completely eliminated at this temperature, while the  $\sigma$ -phase appeared and the  $\gamma$ -phase signals became stronger. This result shows that  $\sigma+\gamma$  phases are stable at this temperature, consistent with the calculated and experimental phase diagrams [25, 57].

Next, the temperature was raised into the range encompassed by the lowest temperature peak, which is marked by pointer 3 in Figure 4-2. Following a 30 min isothermal hold the HT-XRD scan (Figure 4-12b curve 3) revealed the re-appearance of the  $\beta$ -phase as indicated by the  $\beta$ -(211) peak and the dissolution of some of the  $\sigma$ -phase. A strong  $\beta$ -(211) signal shows upon reheating, instead of the  $\beta$ -(200) peak, due to a change in the microstructure. Now the  $\beta$ -phase forms from a  $\sigma+\gamma$  microstructure that provides many nucleation sites. These results show that three phases exist within this temperature range. Finally, the temperature was raised into the highest temperature region, as indicated by pointer 4 in Figure 4-3, and again held isothermally for 30 min. This scan exhibited increased intensity from the  $\beta$ -(211) peak and the disappearance of the  $\sigma$ -phase signature peaks, as shown in Figure 4-12b curve 4. This finding confirms heat-treatment results, suggesting the presence of  $\gamma+\beta$  phases in this temperature range.

#### **4.4.2 Microstructural Analysis of HT-XRD Samples**

The microstructures of a rapidly cooled HT-XRD samples were analyzed. Rapid cooling was accomplished by abruptly stopping the power to the resistive heating strip, which resulted in the sample cooling to below 500C with 5 seconds. A sample was cooled from the two-phase  $\beta+\gamma$  region in between temperatures 1 and 2 marked on Figure 4-3. SEM analysis of the high temperature XRD sample in cross section (Figure 4-13a) revealed a minimal environmentally-affected zone, verifying the efficiency of the in-chamber Ta oxygen getter at maintaining low oxygen partial pressures. The micrograph shown in Figure 4-13b revealed a two-phase microstructure, comparable to the as-cast material but on a much coarser scale. Prior analysis of the HT-XRD profile identified these as the  $\beta$  and  $\gamma$  phases. The microstructure shown in Figure 4-13b revealed the formation of coarse  $\gamma$ -phase that grows with crystallographic preference. The retained  $\beta$ -phase is situated in the regions between the  $\gamma$ -phase.

## 4.5 Summary

The results of this study indicate that the existing assessed phase diagrams for the Ti-Al-Nb system underestimate the extension of the  $\beta$ -phase on the liquidus projection and, consequently, do not accurately predict the solidification and phase transformation paths of  $\sigma+\gamma$  alloys situated in the central region of the phase diagram. One reason for such discrepancy is that the limited experimental evaluations reported have been based on the analysis of as-cast microstructures. We have demonstrated that the dominant presence of the  $\gamma$ -phase at room temperature in the microstructure is from the transformation of the  $\beta$ -phase to the  $\gamma$ -phase, which can not be avoided even with the fast cooling rates attained during arc-melting.

These findings suggest that in alloys for which the  $\beta$ -phase transforms to the  $\gamma$ -phase upon cooling, the fast kinetics of this transformation obscures the determination of high temperature phase equilibrium. This effect also becomes quite important in the microstructural evaluations of alloys that include the  $\beta$  and  $\gamma$  phases at high temperature. Additionally, we have provided evidences for the extension of the  $\beta$ -phase field to higher Al contents. The high-temperature phase stability investigation presented here has recently aided in the optimization of the Ti-Al-Nb system [76] and has been published in [77]. The existence of a high-temperature single-phase  $\beta$ -field will also assist in the improvement of thermo-mechanical capabilities of these alloys.

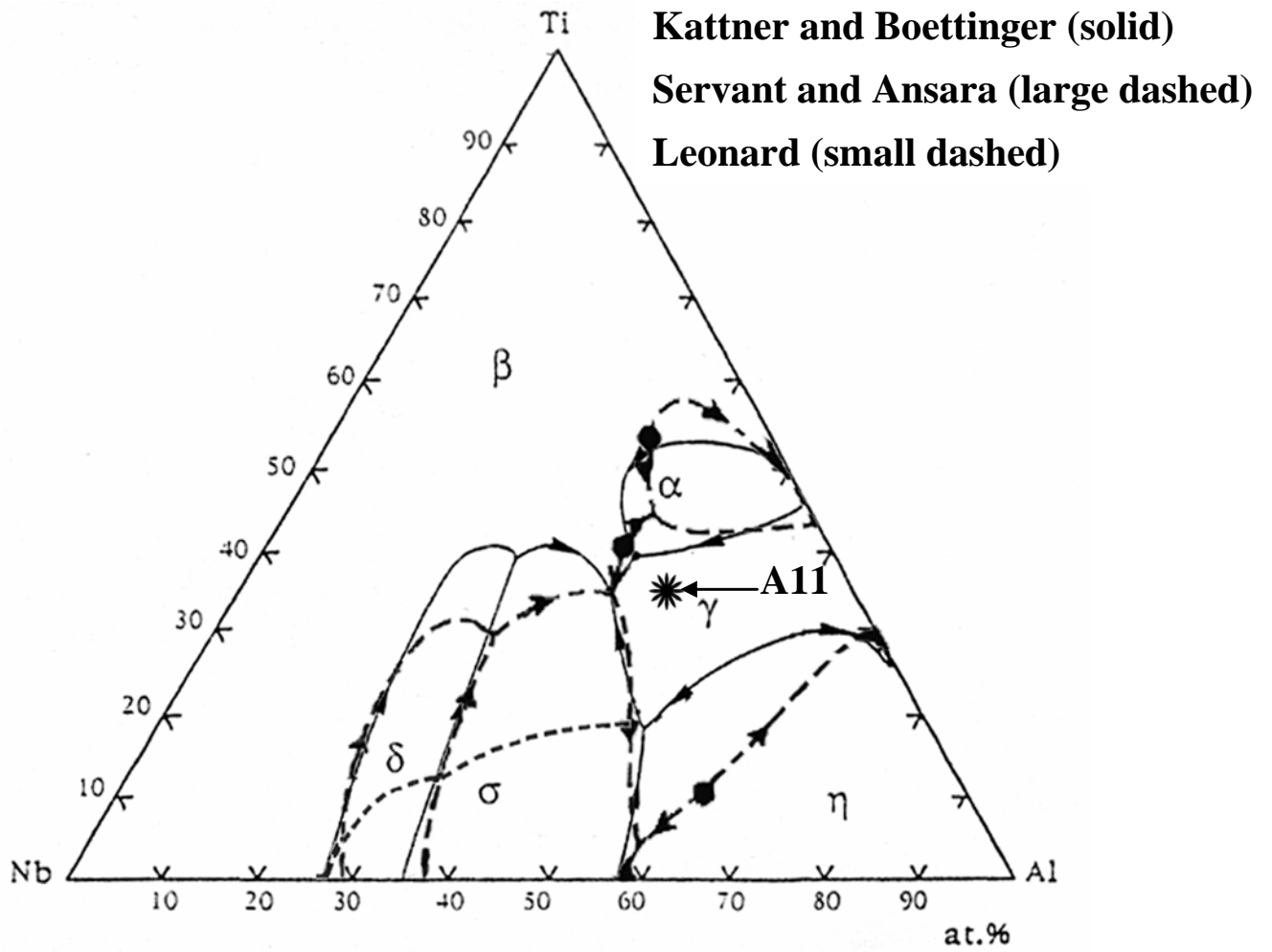


Figure 4-1 Combined liquidus projections of Kattner and Boettinger [56], Servant and Ansara [18] and Leonard et al. [54] which is published in Rios et al. [77] showing the composition of alloy 11.

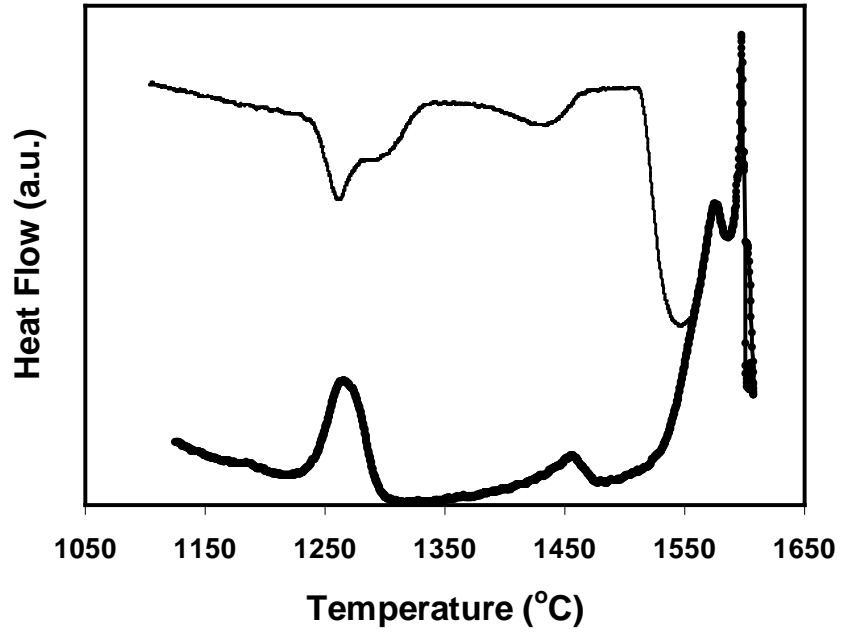


Figure 4-2 DTA curve of as-cast alloy 11 though the solidus and liquidus at 10K/min.

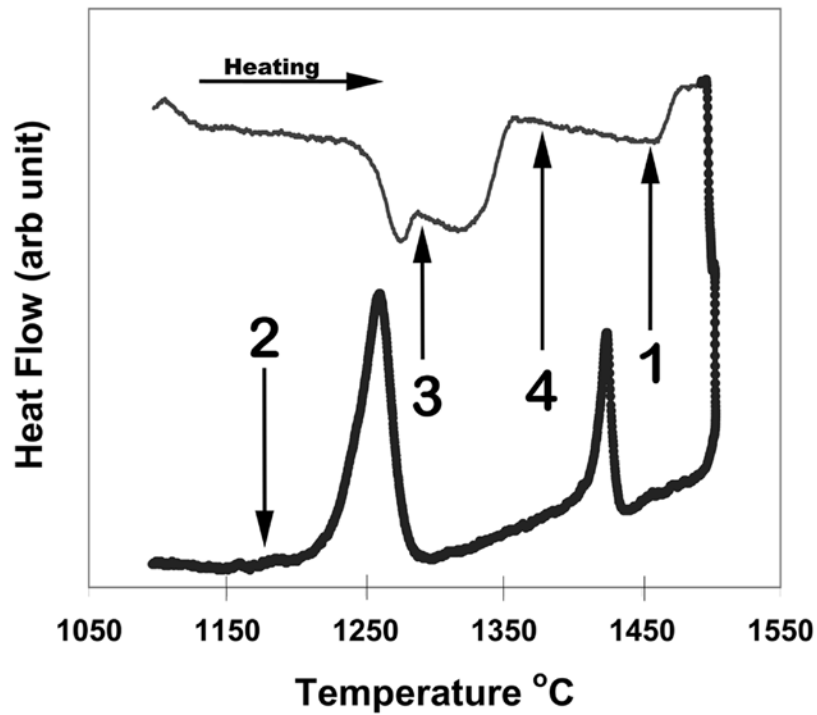


Figure 4-3 DTA curve of thermally cycled alloy 11 at 10K/min, which is marked with the temperatures at which HT-XRD measurements were taken.

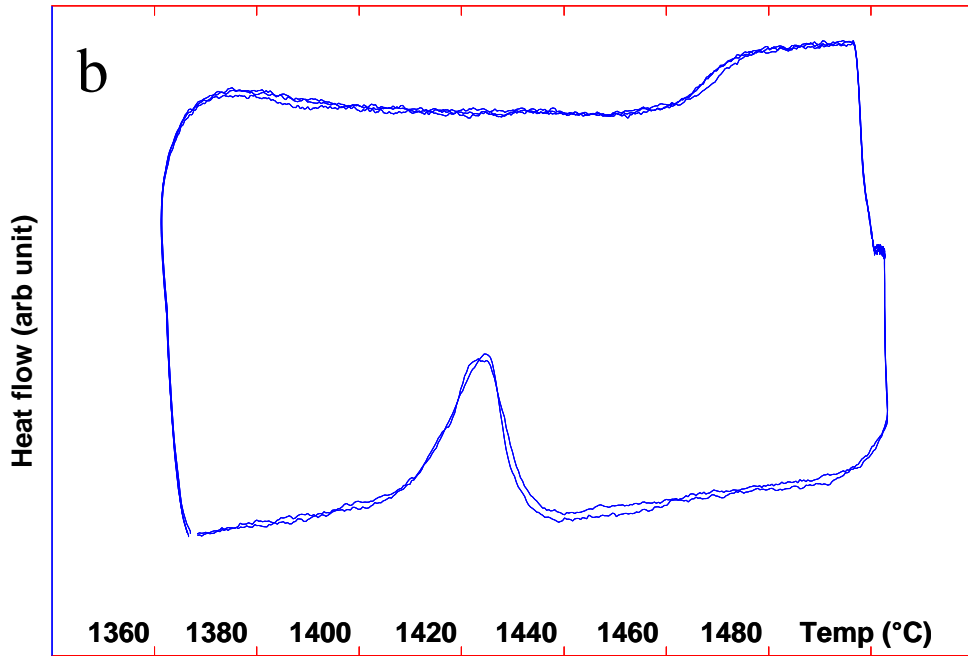
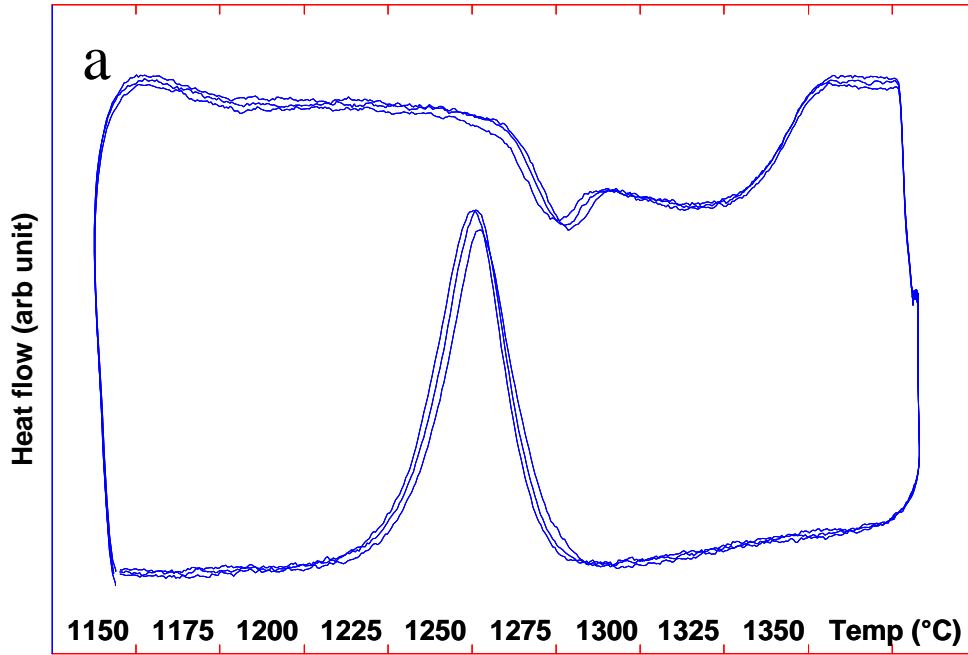


Figure 4-4 DTA curves of solutionized alloy 11 at 10K/min cycled around the a) lower temperature peaks and b) higher temperature peaks.

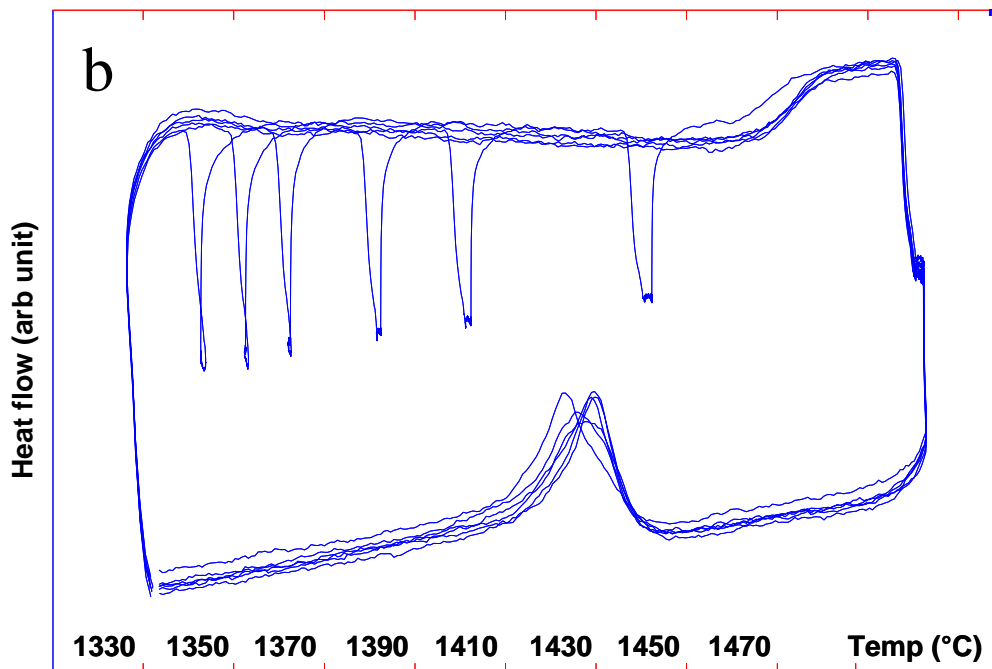
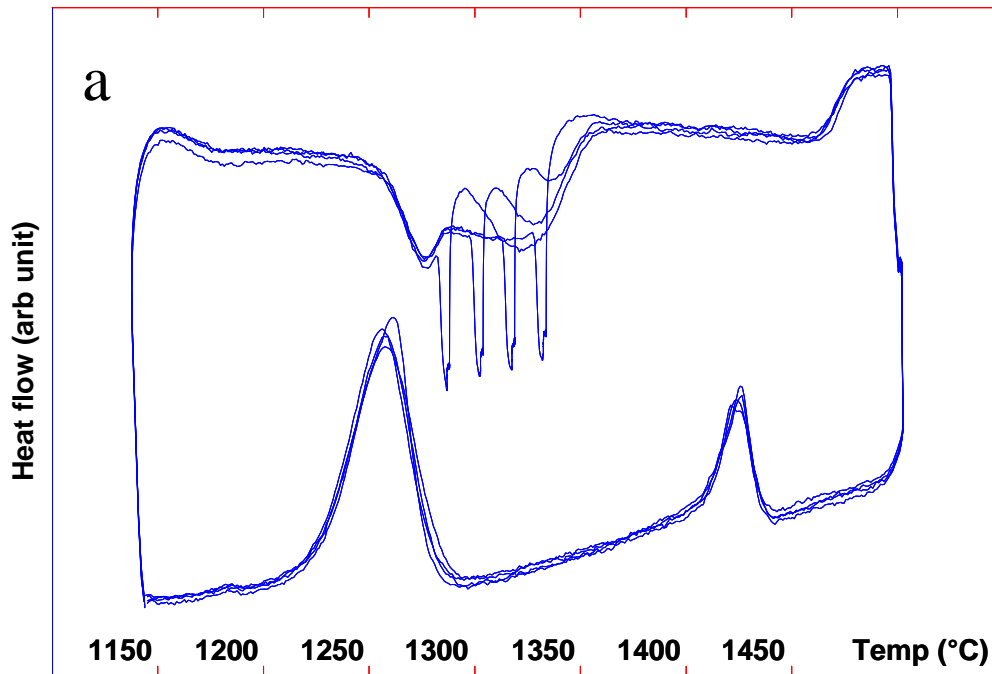


Figure 4-5 Interrupted heating DTA curves of solutionized alloy 11 at 10K/min with isothermal holds within the a) low temperature peaks and b) high temperature peaks.

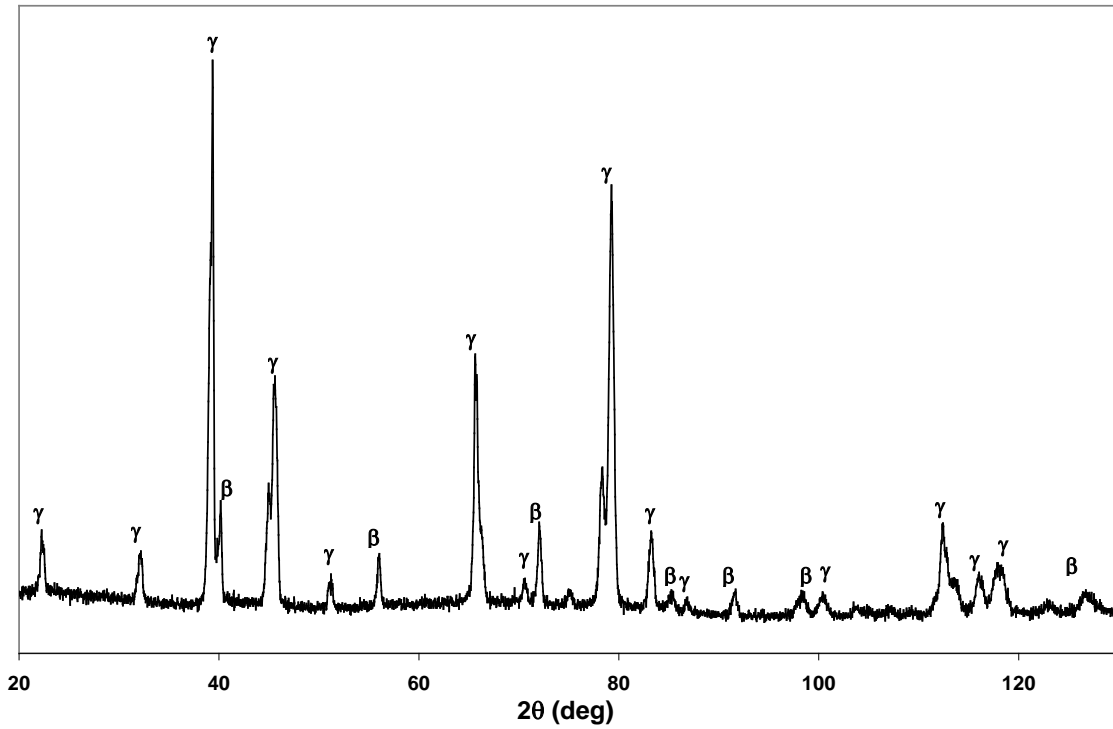


Figure 4-6 XRD of as-cast alloy 11 which identified the  $\beta$  and  $\gamma$  phases.

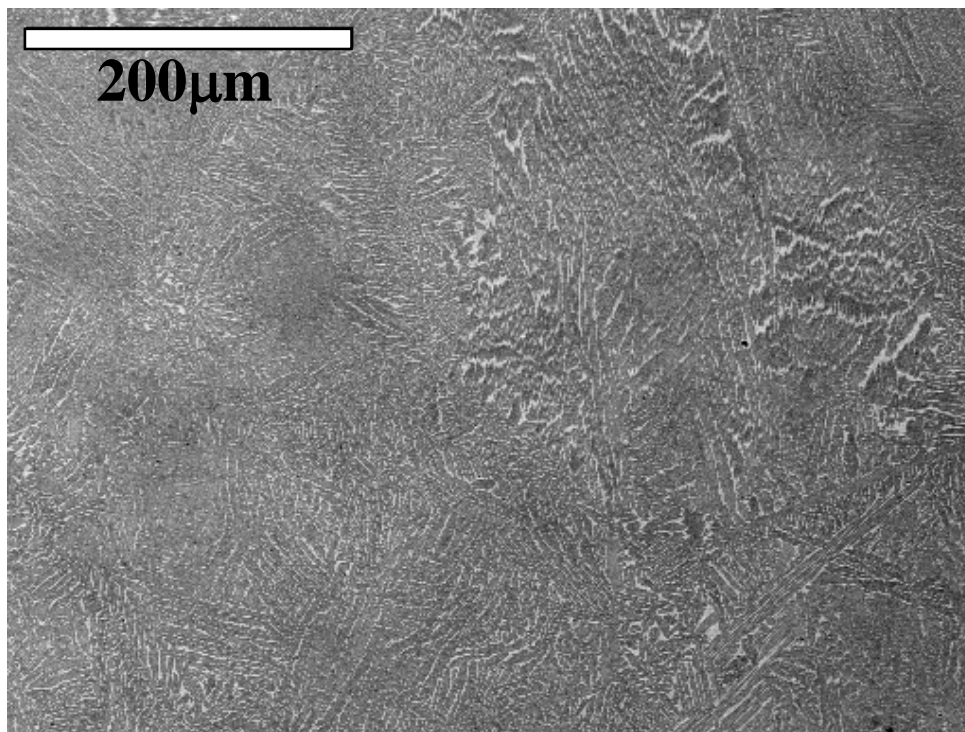


Figure 4-7 SEM micrograph of as-cast alloy 11.

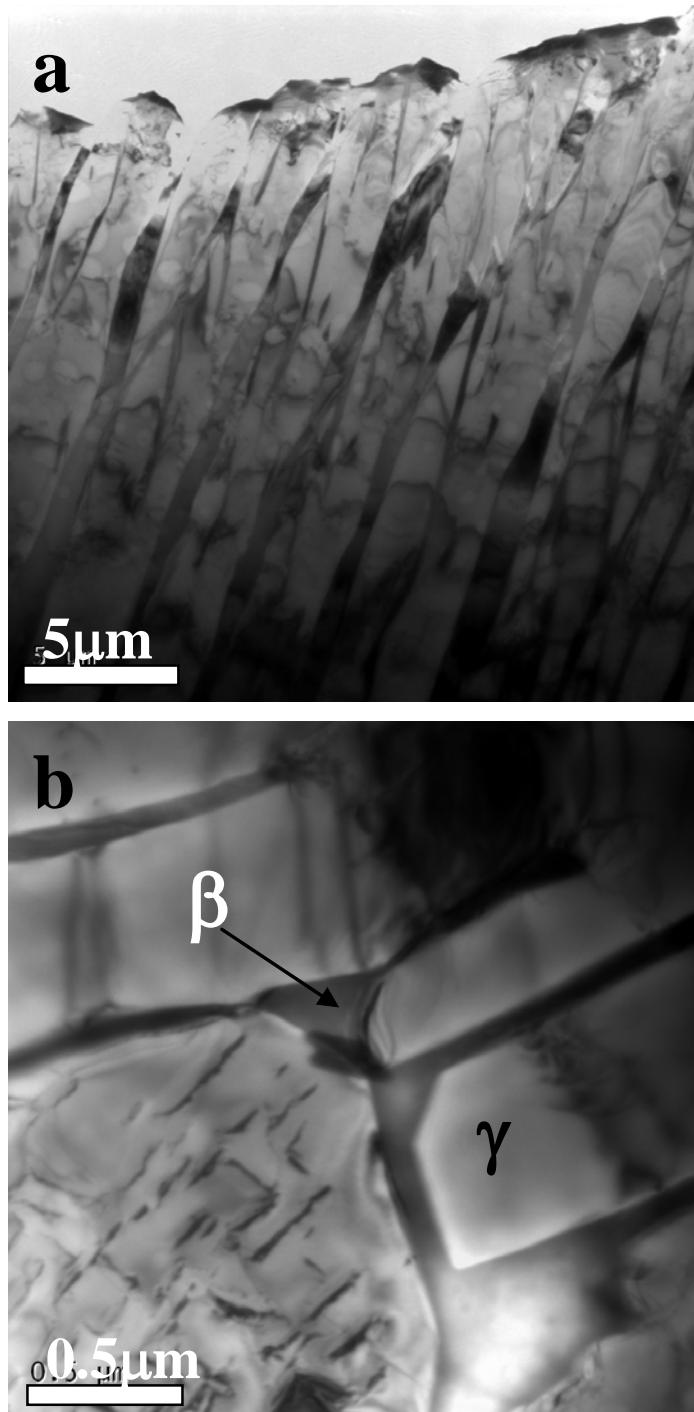


Figure 4-8 TEM micrographs of as-cast alloy 11 marked with the  $\beta$  and  $\gamma$  phases.

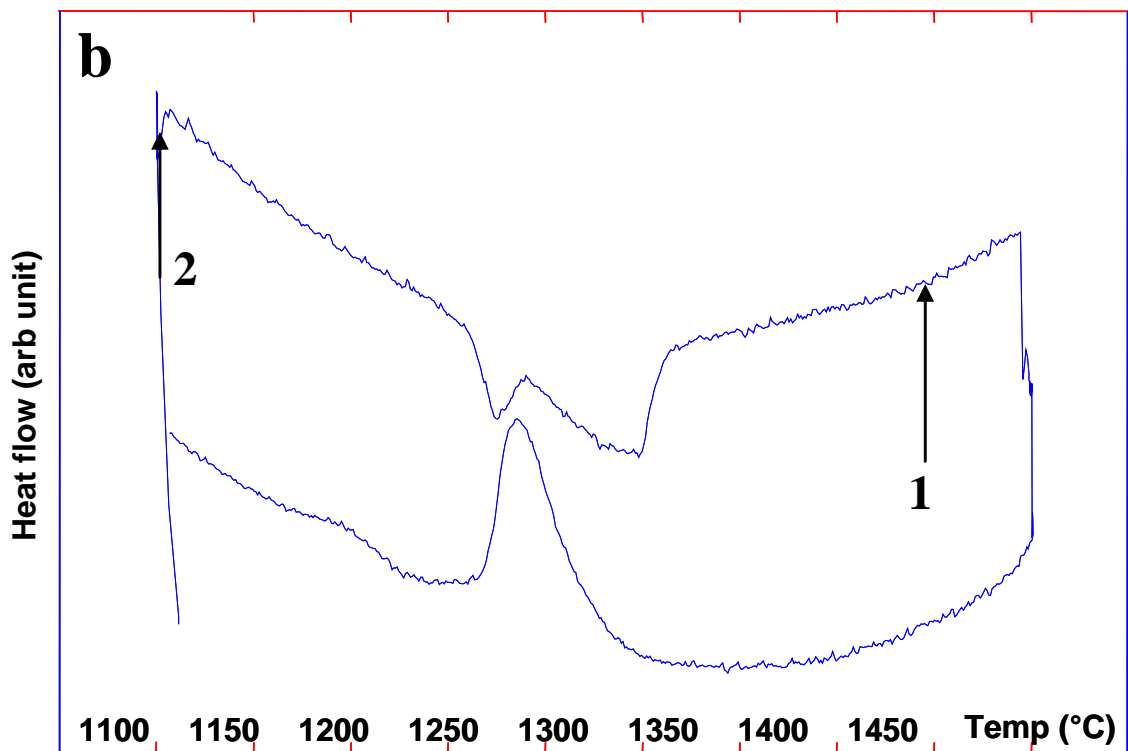
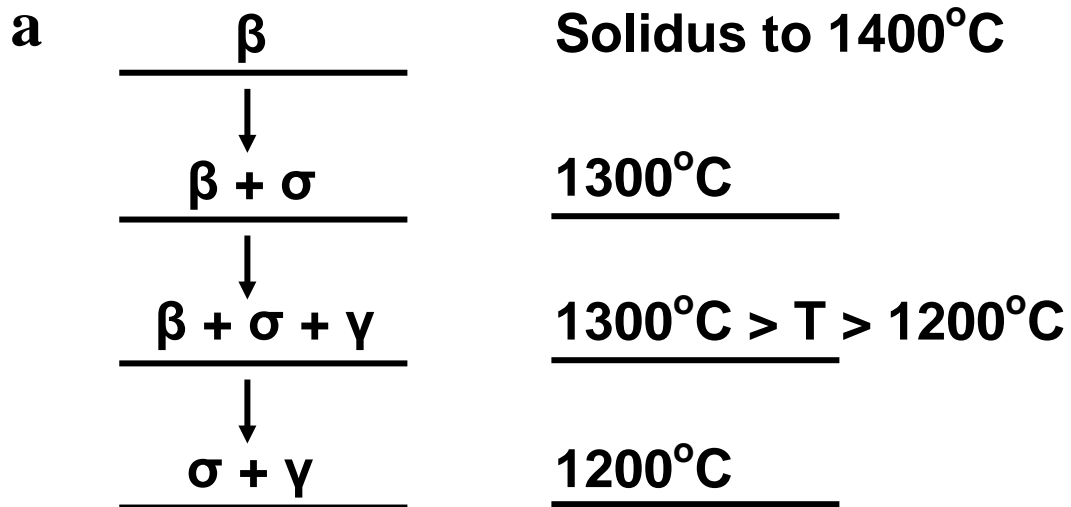


Figure 4-9 a) Transformation path of alloy D2 reported by Hoelzer [19] and b) DTA at 10K/min of alloy D2, which was arc-melted for this study, marked with the temperatures at which XRD measurements were taken.

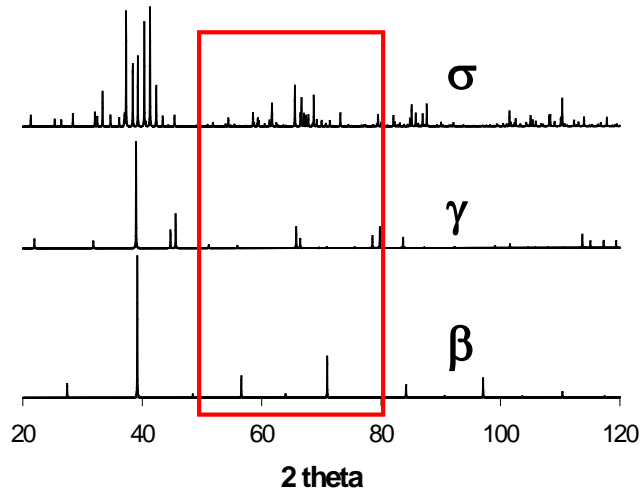


Figure 4-10 Simulated powder XRD profiles for the  $\beta$ ,  $\gamma$  and  $\sigma$  phases marked with the 2 theta range where a minimum number peaks between the three phases were found to overlap.

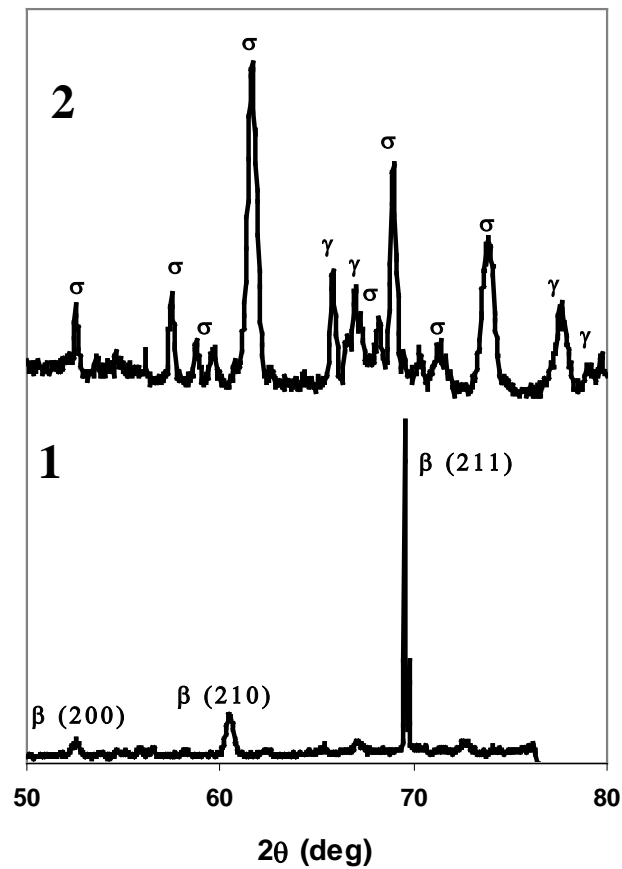


Figure 4-11 HT-XRD measurements of alloy D2 at temperatures 1 and 2 marked on the respective DTA curve in Figure 4-9b.

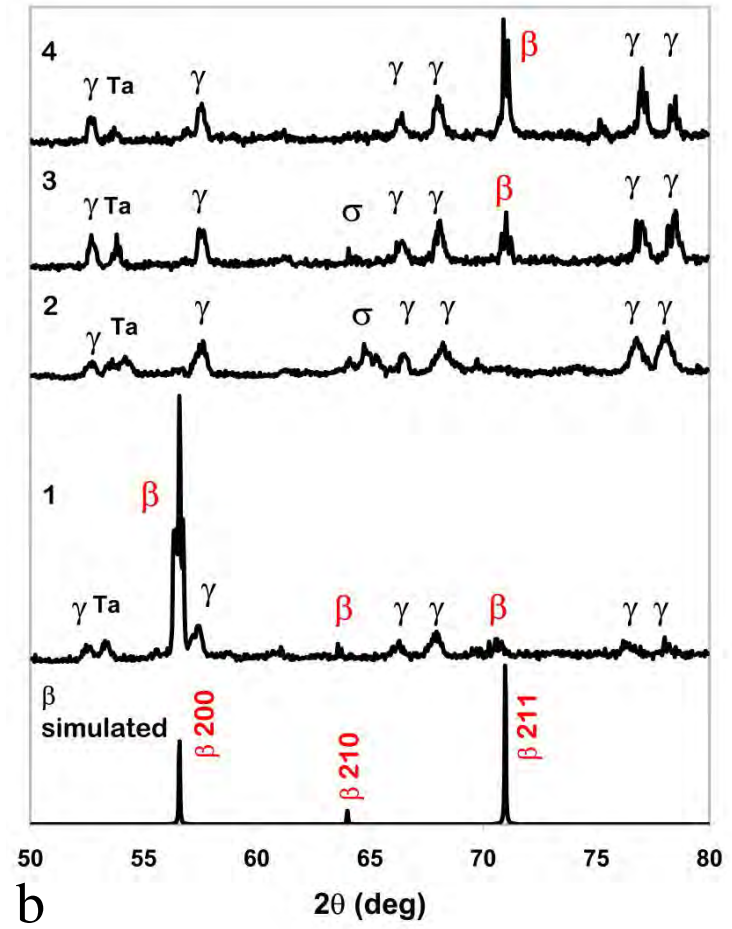
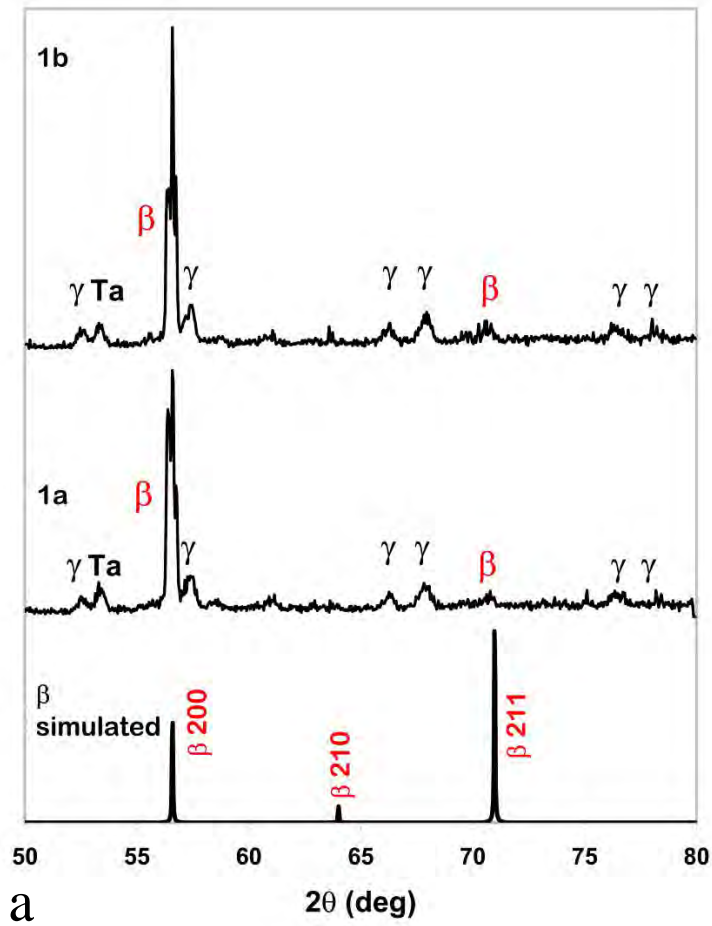


Figure 4-12 HT-XRD measurements of alloy 11 at a) temperatures within the edge of the two-phase region and b) temperatures 1, 2, 3 and 4 marked on the respective DTA curve in Figure 4-3.

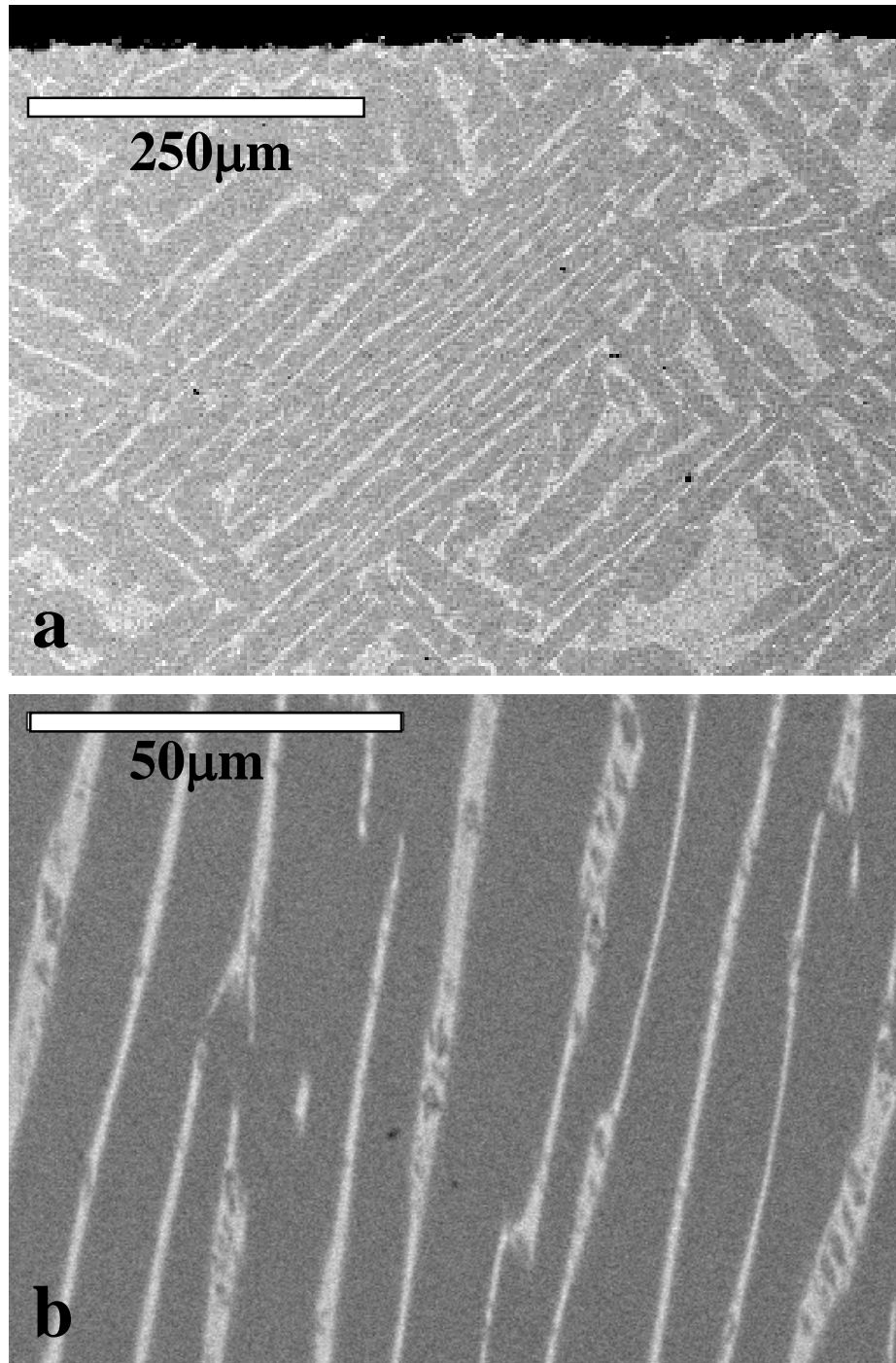


Figure 4-13 SEM micrographs of alloy 11 HT-XRD samples that were rapidly cooled from the two-phase  $\beta+\gamma$  region at a) low magnification including the samples edge and b) high magnification showing the  $\beta$  (bright) and  $\gamma$  (dark) phases.

CHAPTER 5  
TERNARY EUTECTIC REACTION INVOLVING THE L,  $\gamma$ ,  $\sigma$ ,  $\eta$  PHASES

**5.1 Introduction**

In Chapter 4 it was experimentally demonstrated that the  $\beta$ -phase field should be expanded by pushing the L/ $\beta$ / $\gamma$  bivariant equilibria towards the lower Ti contents [77]. Several discrepancies exist in the Ti-Al-Nb phase diagram at temperatures above 1200°C, where there is a lack of experimental data. There are four ternary invariants involving liquid in this system, which cascade into each other. Regarding the invariant reaction involving L, $\sigma$ , $\gamma$ , and  $\eta$  phases, prior computational studies have predicted a class 1 [56] eutectic reaction or a class 2 transition reaction [16], whereas experimental work has supported a class 2 reaction [57]. Recently, at different levels of the optimizations of this system we have arrived at both the class 2 and class 1 reactions [78].

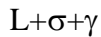
Alloys based on  $\gamma$ + $\sigma$  microstructures show a relatively high creep resistance at elevated temperatures [11]. Our research group therefore has interests in understanding the high temperature phase equilibria in the high-Al corner of the Ti-Al-Nb phase diagram, with specific interest in the evolution of the  $\beta$ ,  $\gamma$  and  $\sigma$  phases from the liquid phase. The  $\gamma$ + $\sigma$  two-phase region connects the sides of two three-phase tie-triangles ( $\sigma$ + $\gamma$ + $\eta$  and  $\sigma$ + $\gamma$ + $\beta$ ). This highlights a need to evaluate how the  $\sigma$ + $\gamma$ + $\eta$  three-phase region evolves from the liquid phase through its invariant reaction.

An important reaction-class (class 1 or 2) dependent difference, results in liquidus projection and related high-temperature equilibrium. Mainly if L/ $\sigma$ / $\gamma$ / $\eta$  exist as a class 2 (transition) reaction then it cascades into the L/ $\beta$ / $\gamma$ / $\sigma$  invariant reaction, whereas if the reaction is a class 1 (ternary eutectic) reaction, the L/ $\sigma$ / $\gamma$  bivariant equilibria must connect into this reaction.

Either reaction implicates fundamental differences in the path that the L/ $\sigma$ / $\gamma$  tie-triangle takes through temperature-composition space.

The class 1 or ternary eutectic reaction has 3 participating three-phase equilibria (L+ $\sigma$ + $\eta$ , L+ $\gamma$ + $\eta$ , L+ $\gamma$ + $\sigma$ ), which all react to form a single  $\sigma$ + $\gamma$ + $\eta$  equilibrium. The class 2 reaction differs in that 2 three-phase equilibria (L+ $\sigma$ + $\eta$ , L+ $\gamma$ + $\eta$ ) react to form the L+ $\gamma$ + $\sigma$  and  $\gamma$ + $\eta$ + $\sigma$  tie-triangles. In order to investigate the nature of this ternary invariant reaction, two alloys were designed, based on prior experimental work and calculations. The bulk alloy compositions of 7Ti-57Al-36Nb at% and 8.5Ti-51.5Al-40Nb at%. are shown on our calculated liquidus projection shown in Figure 5-1. In order to shed light on the class of this invariant reaction, specific heat treatments were designed and the reaction path was investigated through microstructural, thermal and compositional evaluations. The details of the multi-phase equilibria participating in each reaction are summarized below.

The class 1 reaction was defined in this system via the following reaction schemes:



At the class 1 invariant point,



The class 2 reaction was defined in this system via the following reaction schemes:



At the class 2 invariant point,



## 5.2 Thermal Analysis

The liquidus, solidus and solid-state transformation temperatures were determined using DTA. The DTA results for the as-cast alloy samples are given in Figure 5-2a. Care was taken in preparing the as-cast DTA samples such that the mass and geometry of samples were similar, thus allowing for the comparison of peak heights as well as peak positions. The samples were heated at 10K/min to 1600C, held for 5 min to stabilize the temperature followed by a 10K/min ramp down to 1000C. Based on this DTA result a temperature cycling range of 1400C to 1580C was selected for detailed thermal analysis (Figure 5-2b). Several cycles resulted in reproducible results indicating that the transformations were stable and the alloy composition is not exhibiting any major changes.

Table 5-1 presents the transformation temperatures for as-cast and cycled alloys. The initial heating of the as-cast structure resulted in slightly lower transformation temperatures, which can be attributed to its finer microstructure formed upon arc melting. The first and second cycles, after melting and upon cooling exhibited similar transformation temperatures upon heating. Two sets of endothermic peaks were observed during heating of both alloys – a double peak and a sharp peak.

The first set of peaks, i.e. the double peak, was similar in shape for both alloys although the onset temperature differed by 5K. The shape of these peaks provided strong evidence of a convolution of two peaks which showed maxima at 1475C and 1495C for alloy A1 and 1471C and 1486C for alloy A2. Both alloys exhibited a single sharp peak with exactly the same first deviation temperature (Table 5-1).

Within the temperature window between the end of the double peak and the beginning of the sharp peak (1510C to 1535C for alloy A1, and 1499C to 1534C for alloy A2) there is a flat range. The flat range, where the curve is parallel to the base-line, indicated no detectable heat

absorption other than that due to the materials heat capacity. This region is important because it indicates that major phase transformations were not occurring within this temperature range.

Thus it is targeted for subsequent equilibrating heat-treatments.

Table 5-1 Transformation temperatures of as-cast and thermally cycled materials showing the 1st deviation from the baseline (1st dev), the peak positions (max) and the return to the baseline (return) for the 1st and 2nd peak in the convoluted double peak (DB) as well as the single peak (SP).

	DB 1 <sup>st</sup> dev (C)	DB 1 <sup>st</sup> max (C)	DB 2 <sup>nd</sup> max (C)	DB return (C)	SP 1 <sup>st</sup> dev (C)	SP return (C)
A1 as-cast	1454	1461	1484	1503	1528	1563
A2 as-cast	1456	1465	1477	1492	1525	1583
A1 cycled	1467	1475	1495	1514	1534	1571
A2 cycled	1463	1471	1486	1499	1535	1591

### 5.3 As-Cast Materials

Figure 5-3 is a series of SEM micrographs of the as-cast alloy A1. This alloy contained a dendritic primary phase, which appeared dark (Figure 5-3a and b), whereas the remaining microstructure seemed to have a lamellar structure consisting of three distinct composition phases (Figure 5-3c and d)

In order to investigate further the phases present in the lamellar structure a FIB TEM sample was prepared and analyzed. FIB sectioning was performed such that the thin foil was close to being perpendicular to the observed lamellar structure. An ion-beam generated secondary electron image of the specific sectioning site and the foil are shown in Figure 5-4a and b. From this figure it is possible to see the general orientation between the foil normal and the lamellar structure.

Figure 5-4c shows a typical bright field image of the three-phase microstructure. The analysis of the diffraction patterns identified the three phases as  $\sigma$ -Nb<sub>2</sub>Al,  $\gamma$ -TiAl and  $\eta$ -Al<sub>3</sub>Ti. The corresponding selected area diffraction patterns (SAD) with [100] <sub>$\sigma$</sub> , [101] <sub>$\gamma$</sub> , and [010] <sub>$\eta$</sub>  zone

axes are shown in Figure 5-4 (d, e, f), respectively. The morphology of the three phases confirmed that they formed through a coupled growth mechanism.

The  $\gamma$ -phase was found in the smallest phase fractions and always at the interface between the  $\sigma$  and  $\eta$  phase lamella. Examples of this are shown in bright-field images (Figure 5-5a, b and c) and a dark-field image of this corresponding to c in Figure 5-5d. The  $\sigma$  and  $\eta$  phases are also marked in these images. The  $\gamma$ -phase's morphology was indicative of its formation simultaneously with the lamellar structure, however, its location and phase fraction suggested that it underwent a solid-state transformation during cooling. A clear example of this is evident in Figure 5-5a that shows the  $\gamma$ -phase was located with two different interfaces ( $\sigma/\gamma$  and  $\sigma/\eta$ ). The  $\sigma/\gamma$  interface marked on this figure shows regions in which the concavity is into the  $\gamma$ -phase. Several instances of this were found in this alloy.

Each SAD pattern was recorded at the same camera length from equal magnification images, thus eliminating the need for rotation correction. Only a minor amount of tilting (less than 0.5degree) was required to bring the beam to the true zone axis of each phase. Comparing the acquired diffraction patterns revealed a crystallographic relationship between the ( $\sigma$ ,  $\gamma$  and  $\eta$ ) phases. Figure 5-6 shows an SAD diffraction pattern in which the  $\eta$  and  $\gamma$  phases are selected. In this pattern  $\eta$ -phase is on a true zone axis, and  $\sigma$ -phase is slightly off the zone axis, demonstrating the crystallographic relationship between the phases. The beam directions  $\sigma[100]$ ,  $\gamma[101]$  and  $\eta[010]$  are nearly parallel (Figure 5-4). The  $\sigma[011]$  direction revealed in the  $\sigma[100]$  zone axis is parallel to the  $\gamma[11-1]$  direction in gamma's  $[101]$  zone axis. Similarly the  $\gamma[101]$  direction is parallel to the  $\eta[010]$  direction evident in their respective zone axis. These results are summarized in equations 5.6 and 5.7.

$$[100]\sigma//[101]\gamma \text{ beam direction, } [011]\sigma//[11-1]\gamma \text{ direction} \quad (5.6)$$

$$[101]\gamma//[010]\eta \text{ beam direction, } [020]\gamma//[004]\eta \text{ direction} \quad (5.7)$$

In order to establish a correlation between the observed z-contrast and the phases identified by TEM similar magnification images are compared. An ion-beam stimulated secondary electron image was collected near the end of FIB sectioning (Figure 5-4A). The electron signal was collected with a biased secondary electron detector. The intensity of emitted ion beam excited secondary electrons is inversely proportional to effective atomic mass number of the material. This is essentially an atomic mass sensitive contrast mechanism. Superimposed on the ion beam image is a low magnification BF TEM of the same finished FIB sample used for phase identification and analysis (Figure 5-4b). A comparison of the phases identified in the thin foil with the phase contrasts observed in SEM allowed establishing the relationship between them. For example in Figure 5-3b, the dark, grey and bright contrasts are identified as  $\eta$ ,  $\gamma$  and  $\sigma$  phases, respectively.

Alloy A1 showed a small fraction (5 vol%) of primary  $\eta$ -phase (Figure 5-3a and b). The dendritic morphology of this phase confirms that this phase is the first phase to nucleate and grow from the liquid. The lamellar structure (Figure 5-3b), which consists of  $\sigma$ ,  $\gamma$  and  $\eta$  phases, then formed through a cooperative growth from the remaining liquid. The  $\eta$ -phase located in the primaries was found with three distinct morphologies marked numerically on Figure 5-3. The 1<sup>st</sup> morphology and scale are indicative of coarse single-phase dendrites that formed directly from the liquid during cooling. In the 2<sup>nd</sup> morphology of this phase was in the center of most lamellar colonies with highly anisotropic growth directions. The 3<sup>rd</sup> instance of this phase was as a constituent of the lamellar structure. The comparison of these three suggested that the 1<sup>st</sup> morphology precipitates first from the liquid, yielding nucleation sites for the lamellar structure.

The 2<sup>nd</sup> morphology nucleates at higher undercooling, providing constant nucleation sites for the lamellar structure. The bulk composition of the lamellar structure was measured at 37.3Nb, 56.0Al, 6.8Ti at%.

The microstructure of the as-cast A2 alloy is given in Figure 5-7. A significant amount (33 vol%) of alloy A2's microstructure consisted of primary  $\gamma$  dendrites, which appears grey in Figure 5-7 a, b and c. In this alloy higher magnification revealed that in addition to the lamellar structure, the  $\eta$ -phase appears in between the dendrites as well as inside the lamellar structure.

#### **5.4 Characterization of Heat Treated Alloys**

Heat-treatment experiments were designed in order to develop multi-phase equilibria, based on the DTA results shown in Figure 5-2 a and b. Examination of the DTA samples revealed that both alloys had fully melted by the end of the second peak. This presented a predicament in the design of targeted heat-treatments, due to experimental limitations in the vertical tube furnace. In this instrument the sample suspension system described in Chapter 3 is such that the melting of a suspended sample puts the alumina tube and internal thermocouple at risk. Therefore in preparation for heat-treatment experiments it was of high importance to know exactly which peak is linked to melting.

In order to determine whether both peaks are attributed to the enthalpy of melting, or if only the higher temperature sharp peak is linked to melting, a sample was heated in the DTA to 1510C, which is within the flat region of the DTA curve. After a 2 hour isothermal hold the DTA was ramped down to room temperature. Cursory surface evaluations revealed that this sample had not exhibited any signs of bulk melting. Microstructural evaluations confirmed that at 1510C both alloys are solid, thus the double peak is attributed to solid-state transformations.

Two heat-treatment temperatures were selected based on the DTA results shown in Figure 5-2a and b, and the cursory microstructural evaluations of the DTA samples. Each heat-treatment was designed to equilibrate the phases stable in the flat regions. The 1510C heat-treatment is within the region between the double-peaks and the sharp peak, whereas the 1410C heat-treatment is below the double-peaks. One set of samples was heated to 1510C and held isothermally for 4hrs, and the schedule was terminated by drop quenching into a water bath. The second heat-treatment schedule consisted of isothermal hold at 1510C for 1hr, and then the furnace was ramped down at 10K/min to 1410C. After 3 hrs of isothermal hold the samples were also drop quenched. The second heat-treatment consisted of two steps in order to insure the starting microstructure is comparable to that of the 1510C heat-treatment.

Similar to the as-cast structure, three phases ( $\sigma$ ,  $\gamma$  and  $\eta$ ), were identified by XRD (Figure 5-8). The SEM micrographs of alloys A1 and A2 heat-treated at 1410C are shown in Figure 5-9 (a, b) and (c, d), respectively. A comparison of micrographs shown in Figure 5-3 and Figure 5-9 demonstrated that the microstructures were coarsened and equilibrated upon heat treatment. Several EPMA line scans were performed across these phases in both samples. The values of the constant composition section of the EPMA line scan were averaged in order to determine the composition of each phase. The results of compositional analysis of each phase along with the bulk compositions are given in Table 5-2, which demonstrates how Ti, Al and Nb are distributed at the 1510C heat treatment temperature.

Alloys A1 and A2 subjected to the 1510C heat-treatment schedule were examined by SEM, and typical micrographs are shown in Figure 5-10 (a, b) and (c, d), respectively. As in the 1410C heat-treatment, three phases are present, though high magnification of the  $\gamma$ -phase region indicated that a solid-state transformation took place upon quenching. TEM analysis suggested a

spinodal decomposition of the  $\gamma$ -phase upon quenching. The details of this analysis are discussed in Chapter 8. It was possible to analyze the composition and fraction of this phase even though a structural change took place at a lower temperature as the thermal energy was insufficient to allow long-range diffusion to occur. Using the procedure outlined for the 1410C heat-treated samples, the bulk composition and the composition of each phase were measured (Table 5-2).

Table 5-2 Compositional analysis of the heat-treated bulk materials as well as the composition of the individual phases .

Alloy-HT	Bulk Comp. at%			$\sigma$ Comp. at%			$\eta$ Comp. at%			$\gamma$ Comp. at%		
	Al	Ti	Nb	Al	Ti	Nb	Al	Ti	Nb	Al	Ti	Nb
A1-1410°C	57.2	7.1	35.7	42.6	9.5	47.9	69.9	4.5	25.6	54.3	11.5	34.1
A2-1410°C	51.4	8.8	39.8	41.7	9.1	49.2	69.7	3.7	26.6	54.6	12.1	33.3
A1-1510°C	57.4	6.7	35.9	42.2	7.5	50.3	69.9	3.2	26.9	47.8	12.2	40
A2-1510°C	51.3	8.4	40.3	42.3	7.4	50.3	70.0	3.0	27.0	47.3	11.3	41.4

The compositions of the phases ( $\sigma$ ,  $\gamma$  and  $\eta$ ) equilibrated at 1510C (Table 5-2), which is approximately 25K below the melting peak (1535C), as well as at 1410C, which is below the solid-state transformation that occurs between 1510C and 1410C, were plotted on the optimized phase diagrams (Figure 5-11) [76]. These phases form a ternary tie-triangle that represents the ternary equilibrium between these phases. The bulk composition along with the average compositions at the corners of the tie-triangle were used to calculate the theoretical weight percent (wt%) of each phase. The volume fractions of phases were measured from the SEM micrographs in Figure 5-9 and Figure 5-10. The crystal structures and lattice parameters of each phase ( $\sigma$ ) [22, 41, 51], ( $\gamma$ ) [40, 41, 48] and ( $\eta$ ) [23] were combined with the measured compositions to estimate the density and, subsequently, calculate the weight percent (wt%) of each phase from its volume percent (vol%) shown in Table 5-3

Comparison of the calculated wt% (via compositional analysis) and the measured wt% (via microstructural analysis) shown in Table 5-3 are generally in good agreement. The  $\sigma+\gamma+\eta$  tie-triangle that forms from the invariant reaction exists over a relatively tight composition range (Figure 5-11). Therefore, a small change (e.g., 2%) in the bulk composition or the composition of any of the phases may result in up to a 10 wt% difference in the calculated weight fraction. As a result, the differences observed between the measured and the calculated values were considered to be acceptable. These results indicate that sufficient time was allowed for the samples to reach the equilibrium weight fraction after heat treatments at 1410C and 1510C.

Table 5-3 Calculated wt% of the phases computed from the  $\eta/\gamma/\sigma$  tie-triangle, the volume fractions of phases obtained from micrographs, along with the measured wt% of each phase using the vol % of phases.

Alloy-HT	Calculated wt%			Measured Vol%			Measured wt%		
	$\sigma$	$\eta$	$\gamma$	$\sigma$	$\eta$	$\gamma$	$\sigma$	$\eta$	$\gamma$
A1-1410°C	49.0	42.1	8.9	40.4	44.7	14.9	39.4	51.0	9.6
A2-1410°C	59.3	17.6	23.1	45.9	20.5	33.6	49.7	26.4	23.9
A1-1510°C	26.9	43.1	30	18.7	39.5	41.8	18.8	49.8	31.4
A2-1510°C	42.3	19.3	38.4	33.6	17.5	48.9	37.1	23.7	39.2

### 5.5 Development of the Invariant Reaction

The DTA results shown in Figure 5-2 combined with the microstructural observations of samples heat treated at 1510C revealed that the double peak is associated with a solid-state transformation, whereas the sharp peak is linked to melting. Knowing that the sharp peak is only attributed to melting, two main features of this peak are of interest. Firstly, the peak onset temperature is almost equal and at approximately 1535C for both alloys. This is consistent with alloys crossing through an invariant plane during solidification and/or melting. Secondly, the height of the peak for alloy A1 is significantly larger than that of A2 alloy. This observation correlates with the amount (vol %) of the lamellar structure in these alloys (Figure 5-3 and

Figure 5-7). Alloy A1 contained only 5 vol% primary phase with 95% lamellar structure, whereas the fraction of the primary phase in alloy A2 was roughly 7 times greater. Furthermore, the symmetry and sharpness of this peak after thermal cycling are indicative of a eutectic reaction (Figure 5-2b) [72]. The melting of the primary phases can be distinguished as a shallow peak upon heating (Figure 5-2a). However, upon cooling, owing to the extensive undercooling needed for the nucleation of the primary phases, the exothermic solidification peaks for the primary phases overlap the invariant solidification peaks.

Compositional analysis further points to the nature of the invariant reaction. The tie-triangle presented in Figure 5-7a helps in identifying the class of the invariant reaction from which it forms. In a class 1 reaction, the composition of the invariant point lies within the three-phase equilibrium that forms through the eutectic reaction. On the other hand, in any class 2 reaction the invariant point lies on the edge of the two three-phase equilibria and forms through a transition reaction. The overall composition of the lamellar microstructure that forms from the invariant reaction (7.3Nb, 56.0Al, 6.8Ti at%) lies well within this tie-triangle, hence indicating a class 1 or ternary eutectic reaction [67].

The solid-state transformation that takes place between 1510C and 1410C is identified to be a compositional movement of the  $\sigma$ - $\gamma$ - $\eta$  tie-triangle with changing temperature (compare Figure 5-11 a and b). As apparent from the movement of the tie-triangle and the results shown in Table 5-2, the most significant change is in the  $\gamma$ -phase that loses solubility for Nb. The Nb is replaced with Al, whereas the Ti remains almost unchanged. This is a general trend in the phase diagram where the Nb solubility in the  $\gamma$ -TiAl decreases with reducing temperature. It is also interesting to note that the  $\gamma$ -phase contains approximately 12 at% Ti. The rapid change in the

equilibrium concentration of the Nb content upon cooling is believed to be responsible for the instability of the  $\gamma$ -phase upon water quenching directly from 1510C.

### 5.6 Solidification Path in As-Cast Materials

Using the invariant composition and the associated three-phase equilibrium compositions at 1510C, a tie-triangle at 1535°C was developed as shown in Figure 5-11c. The positions of the alloys are also shown on this invariant plane. The information presented in Figure 5-3 suggests that alloy A1 solidifies with primary  $\eta$ -phase followed by a minor amount of the primary  $\gamma$  until the liquidus crosses through the eutectic invariant plane. The A1 alloy is compositionally located near the measured invariant point (Figure 5-11c), thus the majority of the microstructure should be composed of the eutectic structure. Consistently, microstructural evaluations (Figure 5-3) revealed the presence of small volume fraction of the eta phase with a dendritic morphology. Occasionally  $\gamma$ -phase was found adjacent to the primary  $\eta$ , but it was difficult to distinguish it from the  $\gamma$ -phase that formed upon the eutectic reaction. Upon crossing through the invariant plane, the  $\sigma$ ,  $\gamma$  and  $\eta$  phases form isothermally, developing a lamellar structure. The equilibrium fraction of the  $\gamma$ -phase decreased with temperature as the  $\gamma$  corner of the ( $\sigma$ ,  $\gamma$  and  $\eta$ ) tie-triangle moves to lower Nb contents. Since the amount of the primary  $\gamma$ -phase is quite small in this alloy, the volume fraction of this phase closely represents the  $\gamma$  constituent present in the fine lamellar microstructure observed in the as-cast microstructure. As shown in Table 5-3, the amount of the  $\gamma$ -phase reduced sharply from 41.8% to 14.9% upon reducing the temperature from 1510°C to 1410°C. Microstructural evidence of this was also observed in TEM which is shown in Figure 5-5

Close evaluation of the phase diagrams shown in Figure 5-11 revealed that the alloy A2 solidifies through the following equilibrium transformation path:  $L+\sigma$ ;  $L+\sigma+\gamma$ ;  $L+\sigma+\gamma+\eta$ ;

$\sigma+\gamma+\eta$ . The interpretation of the as-cast microstructure of the A2 alloy is somewhat less direct. Phase fraction calculations using the compositions measured in the tie-triangle at 1510C (Figure 5-11c) reveal that approximately 40 wt% of the primary dendrites should be the  $\sigma$ -phase while the remaining 60 wt% of the primaries should be the  $\gamma$ -phase, yet microstructural analysis revealed  $\gamma$ -phase as the primary dendrites (Figure 5-7). This finding suggests that the interfaces that form upon nucleation of the  $\sigma$ -phase are high in energy, thus nucleation requires a substantial driving force. Additionally, the DTA results revealed that for alloy A2 the liquidus surface and the invariant plane are only separated by about 50K, which is a small temperature window for the primary  $\sigma$ -phase to form. Therefore, during solidification of this alloy there is a driving force for primary  $\sigma$ -phase to form but its nucleation is difficult. Thus, the  $\gamma$ -phase, which is the second primary phase to evolve from the liquid, nucleates as the main primary dendrite in this alloy.

Furthermore, primary  $\eta$ -phase was found in the interdendritic regions (Figure 5-7). The composition of the dendritic primary  $\gamma$ -phase was measured to be 42.9Nb, 45.3Al, 11.8Ti at%. This phase has significantly less aluminum content than the alloy composition, hence aluminum is rejected into the interdendritic regions shifting the entrapped liquid's composition such that the primary  $\eta$ -phase can form.

A slow solidification experiment was performed in an attempt to solidify alloy A2 close to its equilibrium solidifications path. As previously discussed it was not possible to melt an alloy in our vertical tube furnace without substantial modifications. Therefore the slow solidification experiments were conducted in the DTA. A sample of this alloy A2 was heated in the DTA to 1600C, which is above the liquidus temperature, and solidified at a rate of 10K/min. Upon reaching the temperature of 1510C the sample was rapidly cooled at 80K/min in order to

preserve the characteristics of the slow solidified sample as best as possible. The cooling rate was set based on the DTA's capabilities and a 20% safety factor from the maximum rate of 99K/min.

The microstructure of slowly cooled A2 is shown in Figure 5-12, in which the  $\gamma$ -phase formed as the main primary with adjacently forming  $\sigma$ -phase as a second primary phase. The  $\eta$ -phase was found to form within the primary  $\gamma$ -phase. This revealed that the  $\sigma$ -phase has difficulties nucleating even at slow solidification rates. A coupled growth microstructure consisting of the  $\sigma$ ,  $\gamma$  and  $\eta$  phases was again found throughout the sample filling in the regions between the primaries.

Addressing the as-cast microstructure of alloy A2 alone one could arrive at the conclusion that this sample solidified through a transition reaction. However, thermal and compositional evidence prove this is not the case. The fact that the  $\gamma$  and  $\eta$  phases seem to make up the primary phases could in the lack of further examination be explained through the solidification path of the  $L+\eta \rightarrow \sigma+\gamma$  invariant reaction. Assuming that this was the actual invariant reaction, and that alloy A2 crosses through the  $L+\gamma+\eta$  tie-triangle during solidification, primaries containing the  $\sigma$  and  $\eta$  phases should be found. Upon crossing through the invariant plane the remaining liquid should form the  $\sigma+\gamma+\eta$  phases isothermally. This reaction is found to be a ternary eutectic in light of the significant compositional and thermal evidence developed here, and the observed as-cast microstructure directly results from the failure of the  $\sigma$ -phase to nucleate from the liquid.

## 5.7 Summary

The invariant reactions among L,  $\gamma$ ,  $\sigma$  and  $\eta$  phases in the Ti-Al-Nb system were investigated using compositional, microstructural and thermal analyses. This reaction was defined by detailed examination of two alloys with nominal compositions of 7Ti 57Al 36Nb and

8.5Ti 51.5Al 40Nb (at%). Compositional analysis of the equilibria comprising the invariant reaction showed that the invariant point lies within the three-phase tie-triangle, thus clearly pointing to a class 1 ternary eutectic reaction. Microstructural evaluation demonstrated that after the primary phases nucleated and grew, a lamellar structure consisting of three phases ( $\gamma$ ,  $\sigma$  and  $\eta$ ) developed from the liquid, which provides morphological evidence of a eutectic reaction. Analysis of the as-cast and slow-solidified microstructures highlighted the failure of the  $\sigma$ -phase to nucleate as a primary phase. DTA revealed that the alloys melted through a single endothermic event typical of a ternary eutectic reaction. The composition of the eutectic was found to be at 37.3Nb, 56.0Al, 6.8Ti all in at% and the invariant temperature was recorded at 1532C.

The solid-state reaction peaks below the melting peak of 1532C were found to be associated with compositional and volume fraction changes in the  $\sigma$ ,  $\gamma$  and  $\eta$  phases as evidenced by microstructural analysis. The  $\gamma$ -phase was shown to lose its solubility for Nb rapidly as temperature was decreased from 1510C to 1410C. This substantial composition shift to higher Al contents resulted in the decomposition of the  $\gamma$ -phase into a nano-scale microstructure upon water quenching.

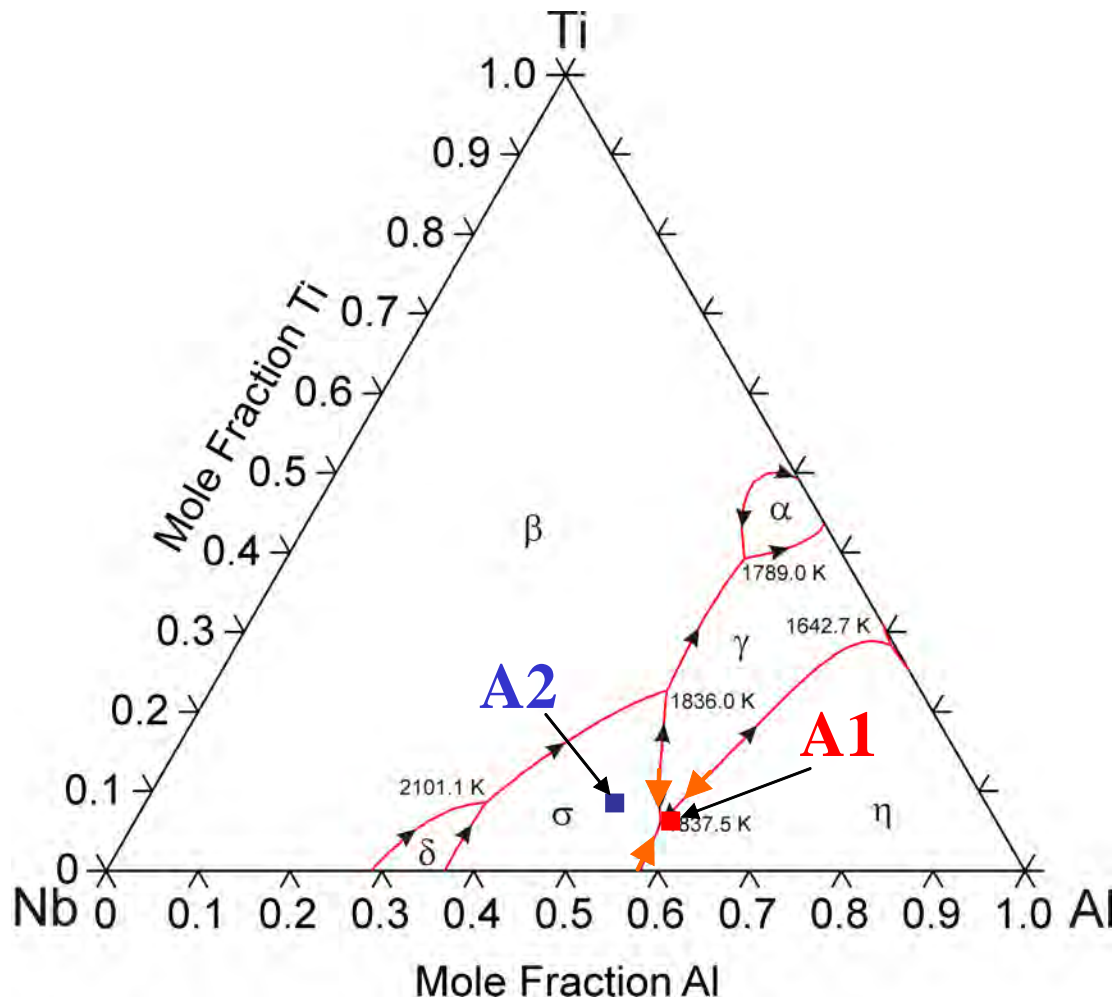


Figure 5-1 Calculated liquidus projection marked with the composition of alloys A1 and A2.

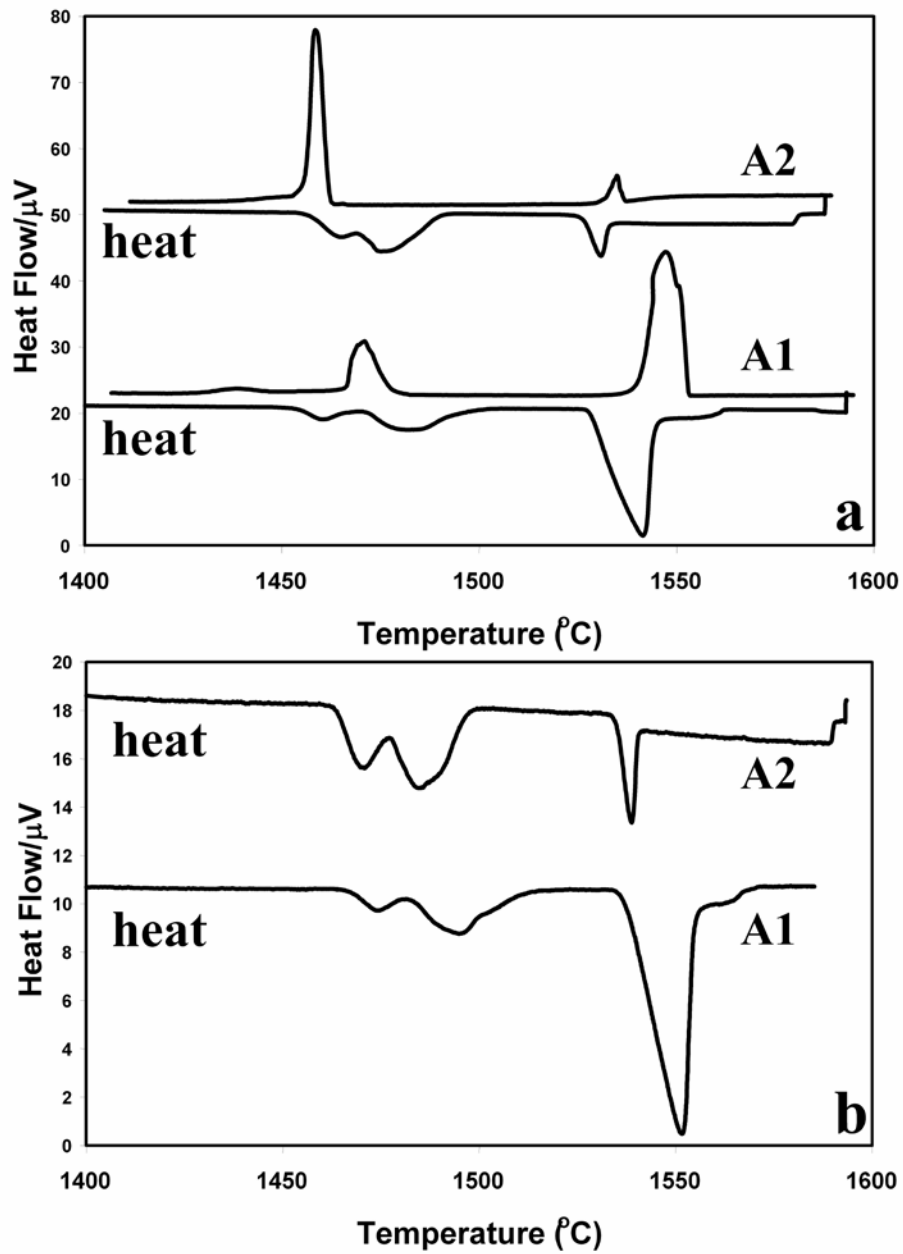


Figure 5-2 DTA at 10K/min of alloys A1 and A2 in the a) as-cast condition and b) heating of the thermal cycled materials

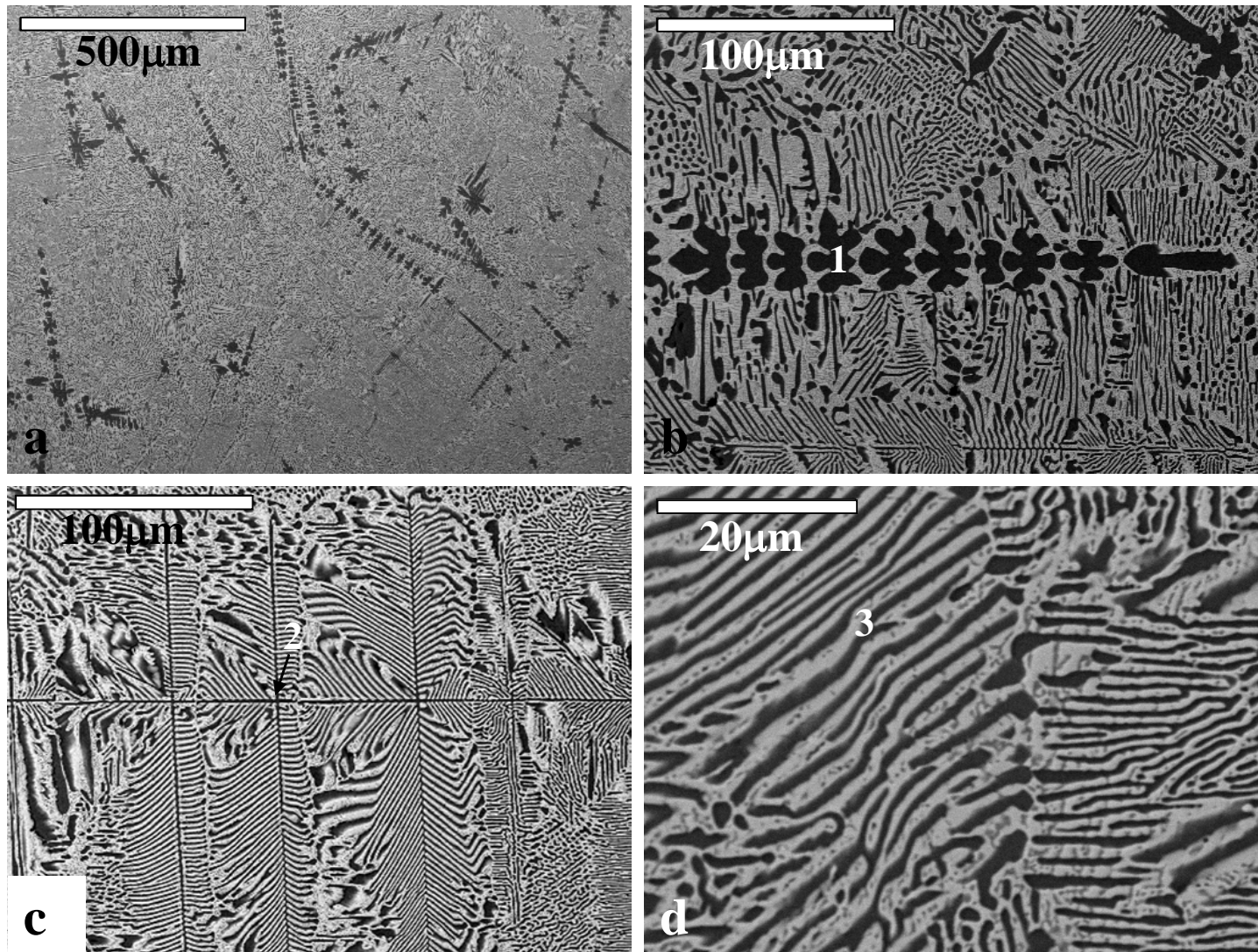


Figure 5-3 SEM of as-cast alloy A1 showing a) the overall microstructure b) centered on the primary dendrites c) centered around the lamellar structure and d) high magnification showing three phases in the lamellar structure. The  $\eta$ ,  $\gamma$  and  $\sigma$  phases are identified as dark, grey and bright contrasts respectively.

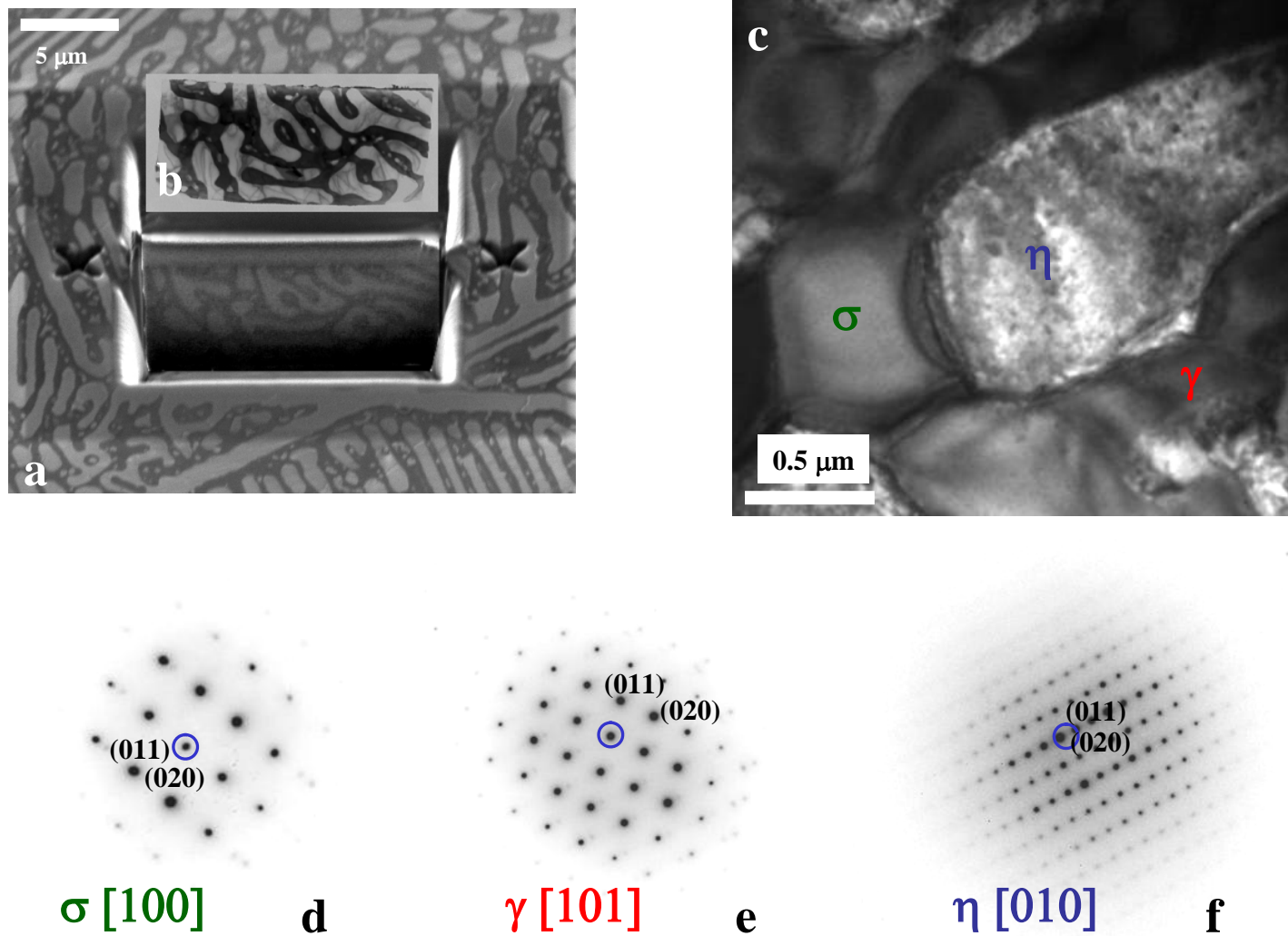


Figure 5-4 TEM of alloy A1 showing a) FIB secondary electron image b) BF image superimposed on FIB image c) BF TEM image of lamellar structure showing the  $\sigma$ ,  $\gamma$  and  $\eta$  phases including the respective diffraction patterns for d)  $\sigma$ -phase, e)  $\gamma$ -phase and f)  $\eta$ -phase.

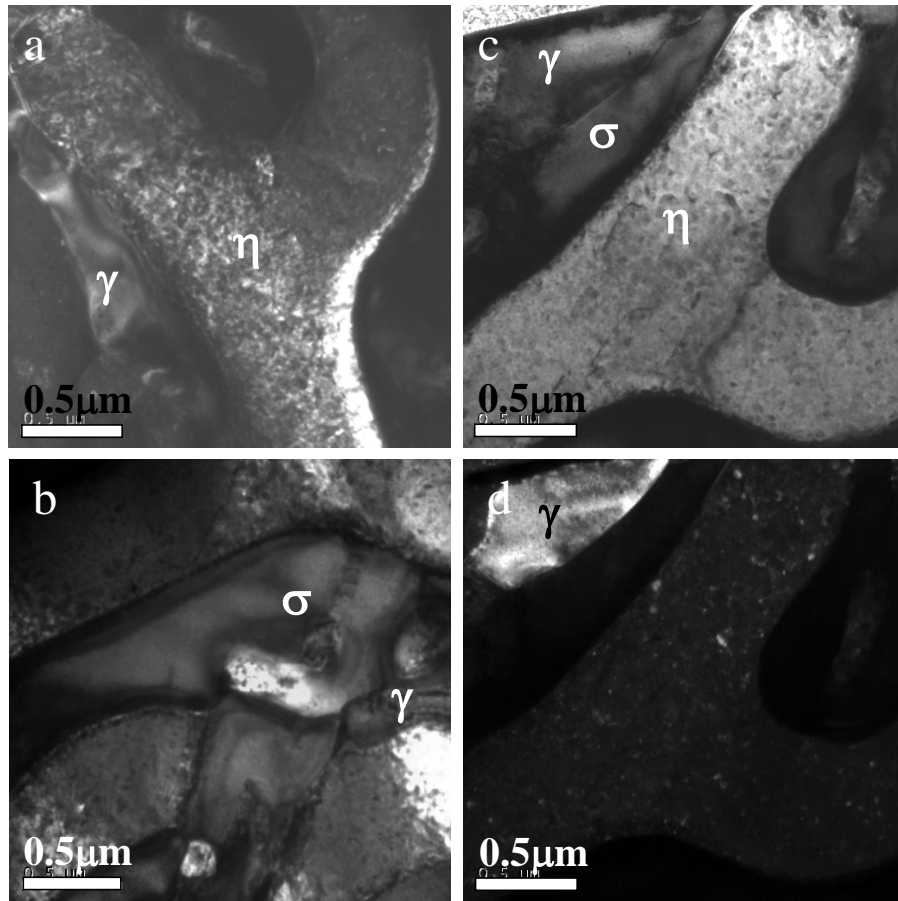


Figure 5-5 A series of TEM micrographs of the  $\gamma$ -phase in lamellar structure showing this phase a) adjacent to the  $\eta$ -phase in BF b) adjacent to the  $\sigma$ -phase in BF c) adjacent to alternating lamella of  $\eta$  and  $\sigma$  in BF and d) DF of the  $\gamma$ -phase in C

$\eta$  [010]       $\sigma$  [100]

Figure 5-6 TEM SAD patterns showing the orientation relationship between the  $\eta$  and  $\sigma$  phases.

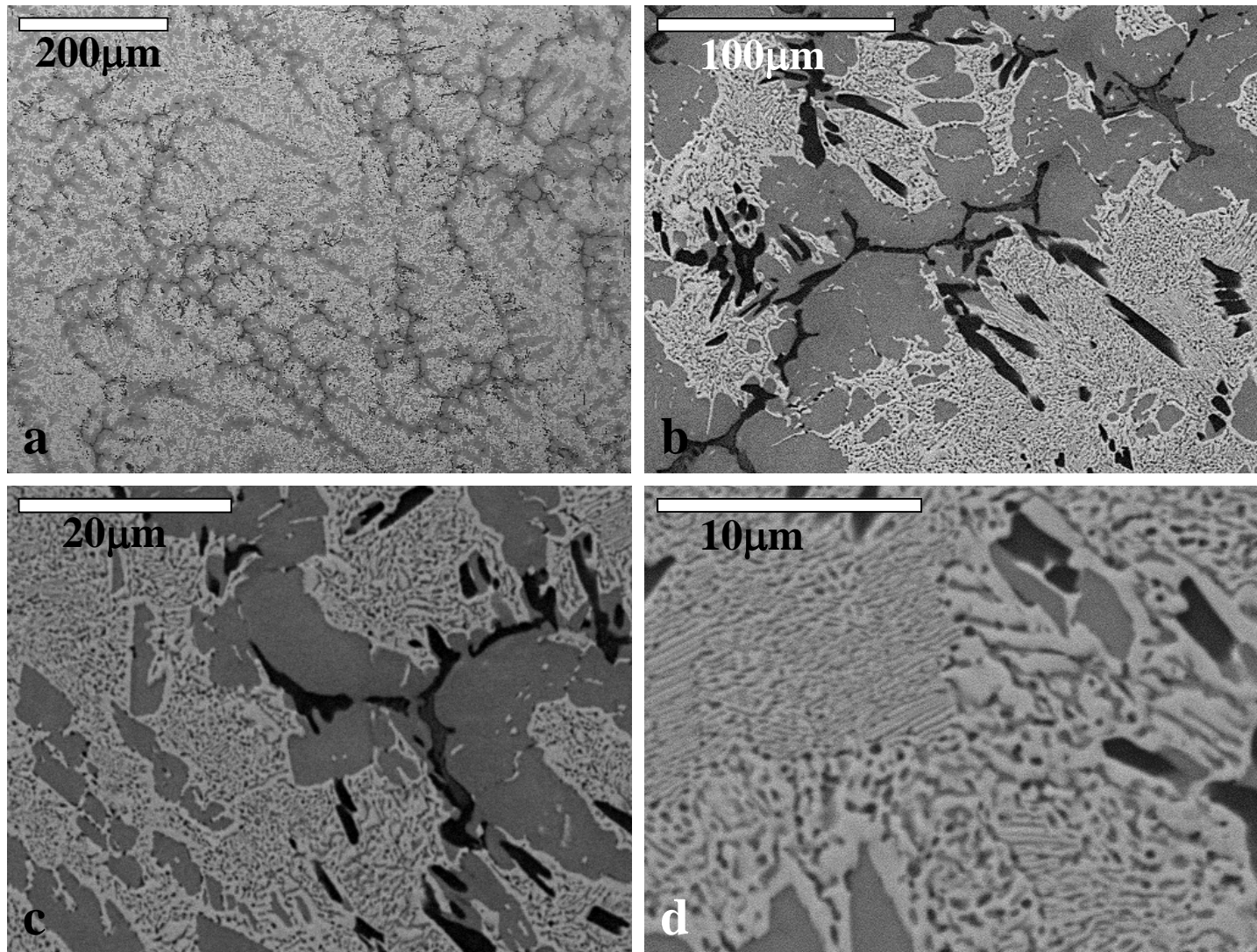


Figure 5-7 SEM of as-cast alloy A2 showing a) the overall microstructure b) centered on the coarse primary dendrites c) higher magnification centered around the coarse and fine the primary dendrites d) high magnification showing three phases in the lamellar structure. The  $\eta$ ,  $\gamma$  and  $\sigma$  phases are identified as dark, grey and bright contrasts, respectively.

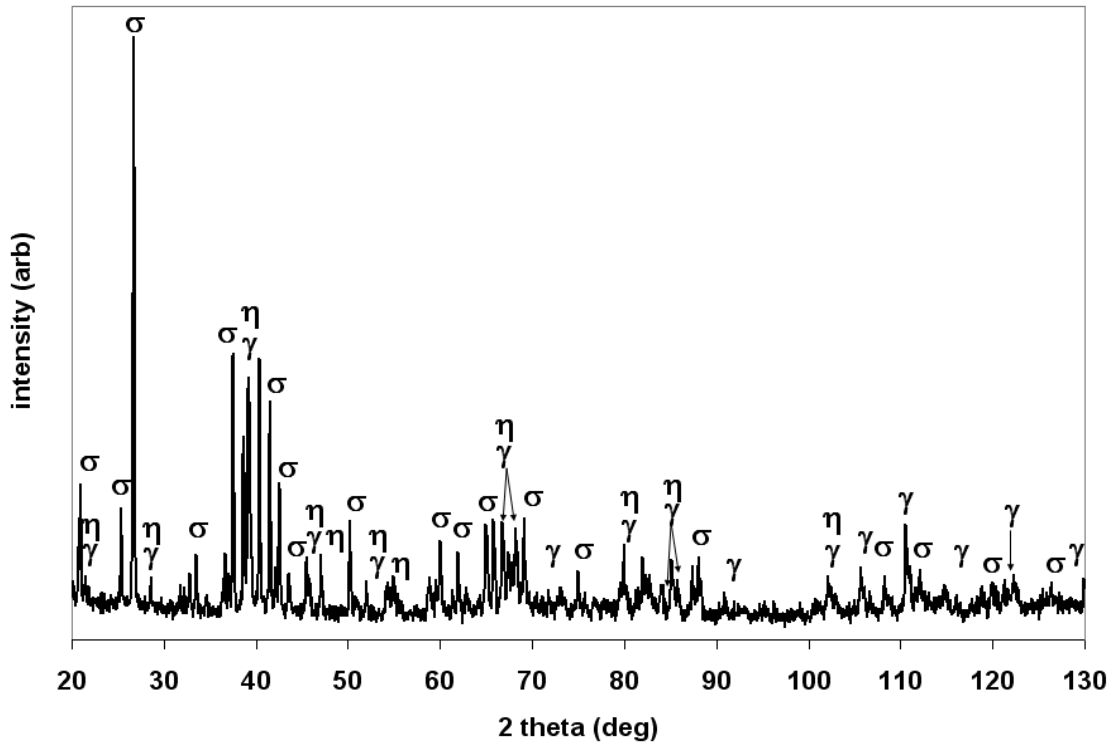


Figure 5-8 XRD of alloy A1 heat-treated subjected to the 1410C heat-treatment that identifies the  $\sigma$ ,  $\eta$  and  $\gamma$  phases.

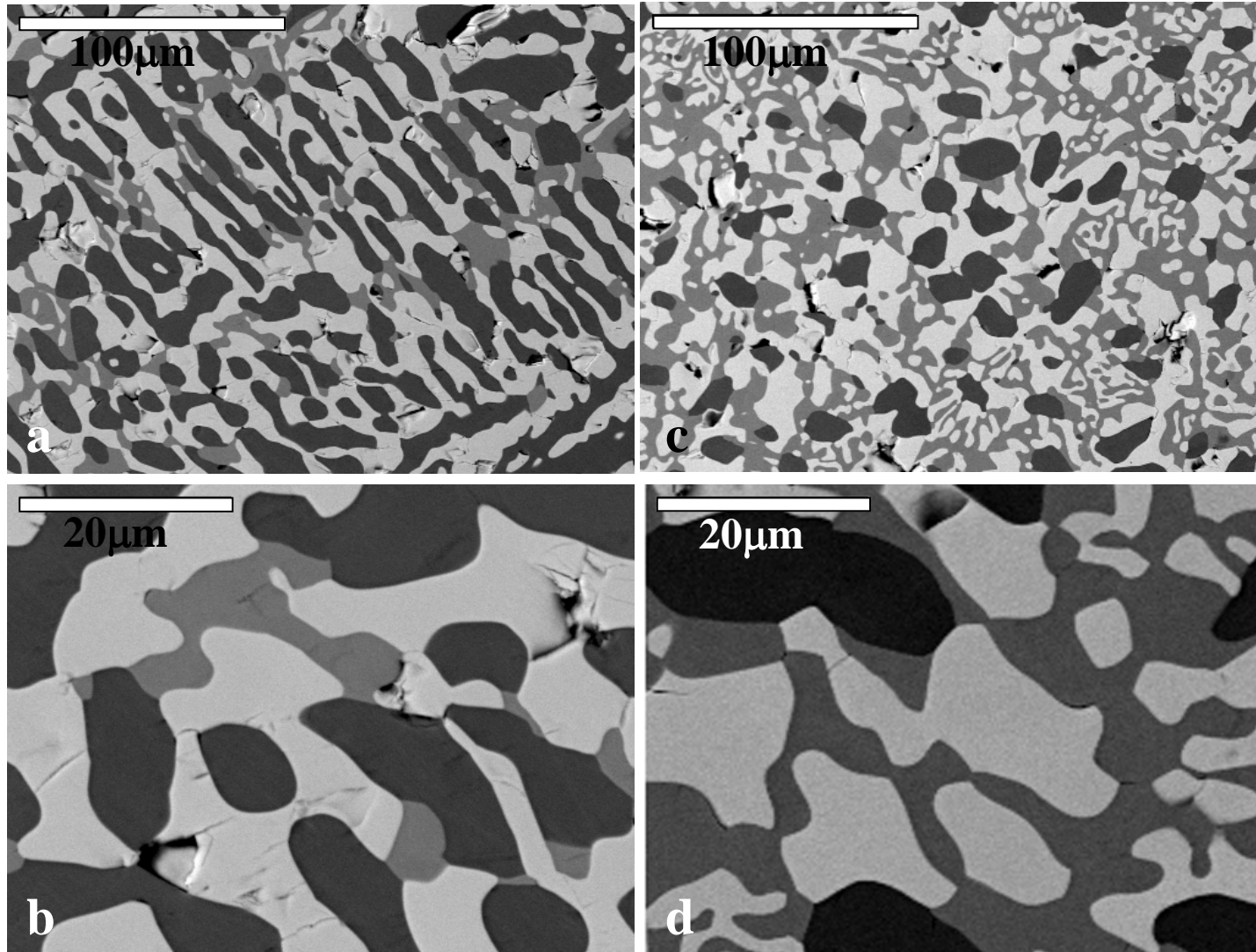


Figure 5-9 SEM micrographs of alloys subjected to the 1410C heat-treatment showing a) low magnification of alloy A1 and b) higher magnification next to c) low magnification of alloy A2 and d) higher magnification. The  $\eta$ ,  $\gamma$  and  $\sigma$  phases are identified as dark, grey and bright contrasts, respectively.

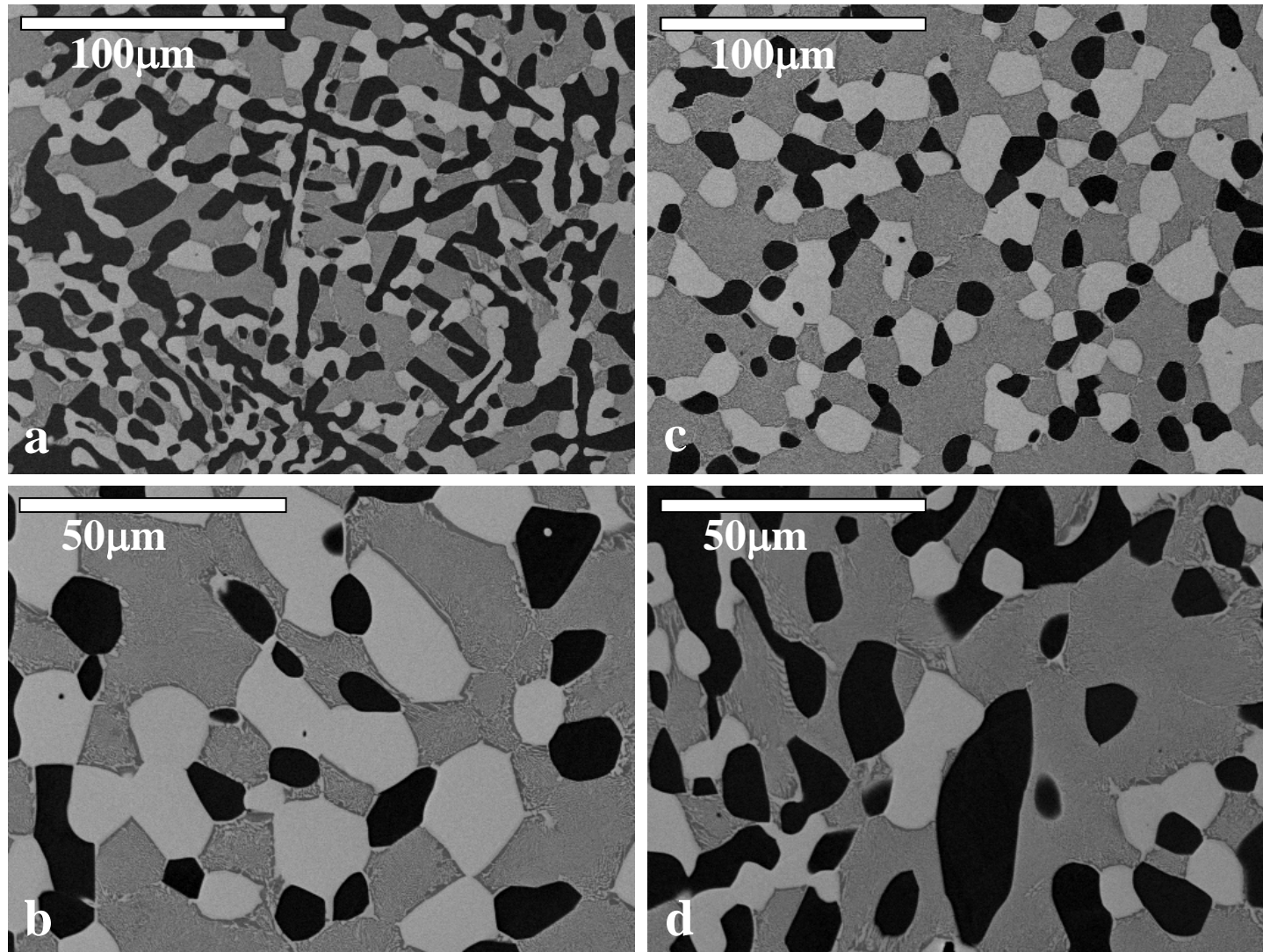


Figure 5-10 SEM micrographs of alloys subjected to the 1510C heat-treatment showing a) low magnification of alloy A1 and b) higher magnification next to c) low magnification of alloy A2 and d) higher magnification. The  $\eta$ ,  $\gamma$  and  $\sigma$  phases are identified as dark, grey and bright contrasts, respectively.

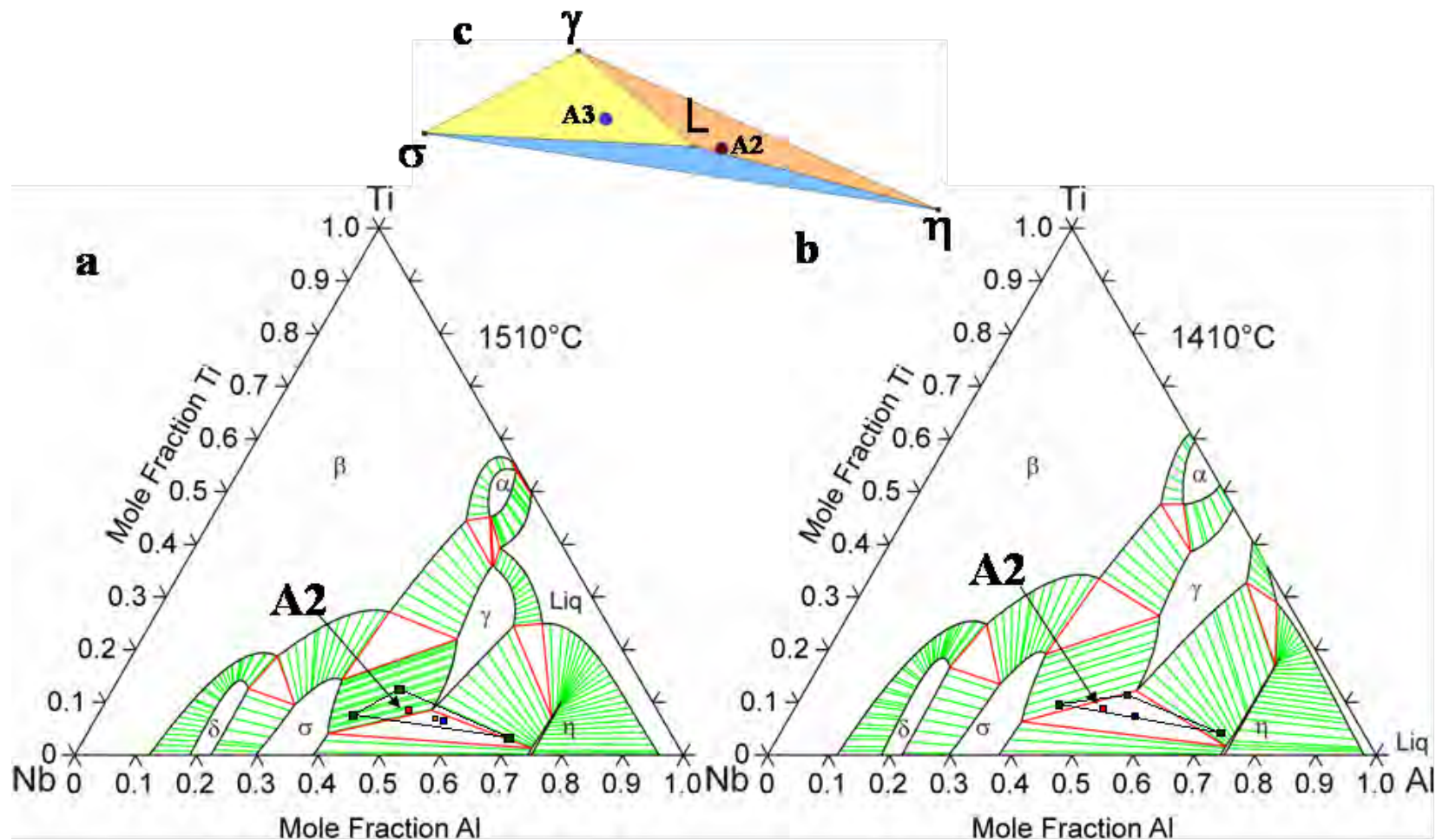


Figure 5-11 Calculated isothermal sections at a) 1510C and b) 1410C marked with the experimental data obtained from the respective heat-treatments. c) Shows the four phase invariant equilibrium point and participating three phase equilibriums.

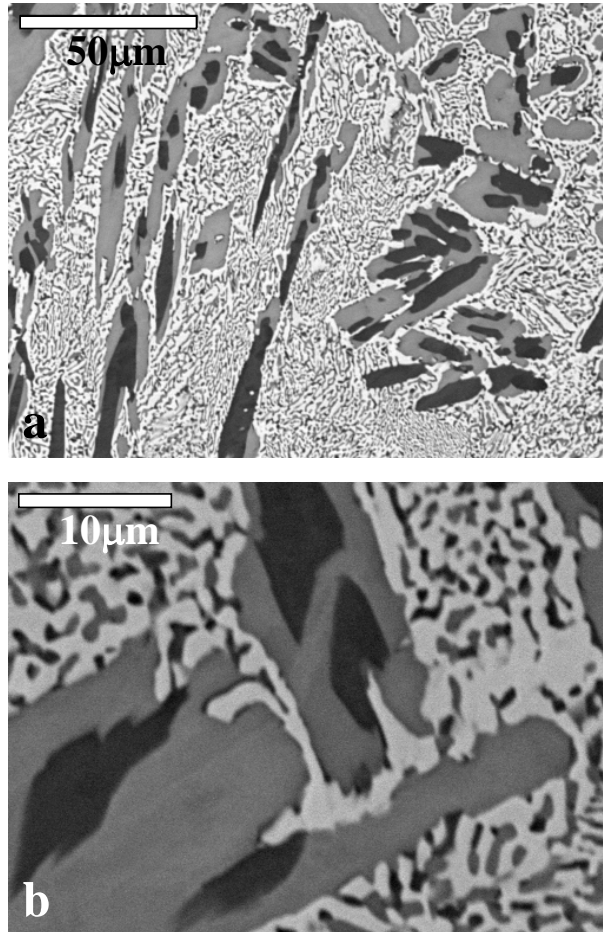


Figure 5-12 SEM micrographs of alloy A2 solidified at 10K/min showing A) the overall microstructure and B) high magnification of the primary dendrites and adjacent lamellar structure. The  $\eta$ ,  $\gamma$  and  $\sigma$  phases are identified as dark, grey and bright contrasts respectively.

CHAPTER 6  
TERNARY PERITECTIC REACTION INVOLVING THE L,  $\gamma$ ,  $\sigma$ ,  $\beta$  PHASES

**6.1 Introduction**

L,  $\gamma$ ,  $\sigma$ ,  $\beta$  invariant reaction is important in the development of  $\sigma+\gamma$  alloys as it connects the (L,  $\gamma$ ,  $\sigma$ ), (L,  $\sigma$ ,  $\beta$ ) and (L,  $\gamma$ ,  $\beta$ ) bivariant equilibrium lines that are shown on the calculated liquidus projection (Figure 6-1) [79]. The details of the composition and reaction class were not known yet they are key for the optimization of the Ti-Al-Nb phase diagram and the development of high-temperature thermomechanical processing schemes. Sparse experimental data have been reported in the literature therefore alloys and heat treatments were designed to investigate the nature of the L,  $\gamma$ ,  $\sigma$ ,  $\beta$  invariant reaction.

Several controversies exist in the Ti-Al-Nb phase diagram at temperatures above 1200°C, where there is a lack of experimental data. There are four ternary invariant reactions involving liquid phase in this system, which cascade into each other. Regarding the invariant reaction involving L,  $\sigma$ ,  $\gamma$ , and  $\beta$  phases, prior computational studies have predicted a class 1 eutectic reaction [56] and a class 2 transition reaction ( $L+\beta\rightarrow\sigma+\gamma$ ) in [18], whereas experimental work has all supported a class 2 reaction transition reaction ( $L+\sigma\rightarrow\beta+\gamma$ ) [16, 54, 55, 57]. Recently, at different levels of the optimizations we have considered both a class 2 transition reaction based on the reported experimental observations and a class 3 ternary peritectic reaction [78].

Available experimental studies and calculated phase diagrams provided some guidance to the development of initial alloys. These combined with the current work on the  $\beta$ -phase extension and the investigation of the L,  $\gamma$ ,  $\sigma$ ,  $\eta$  invariant reaction made it possible to narrow down a compositional window for the probable location of the L,  $\gamma$ ,  $\sigma$ ,  $\beta$  invariant reaction. The compositions of the experimental set of alloys used in the development of the L,  $\gamma$ ,  $\sigma$ ,  $\beta$  invariant

reaction are listed in Table 6-1 and marked on the optimized phase diagram (Figure 6-1). These alloys were cast sequentially and the interdendritic regions were searched for clues leading to the location of this reaction. This methodology was based on the fact that the interdendritic regions always follow the contours of the liquidus surface downward. Essentially, alloys which cross through the liquidus surface at temperatures above the invariant reaction temperature will develop interdendritic regions with compositions closer to the invariant plane than the bulk alloy composition. Conversely, alloys which cross the liquidus surface at temperatures below the invariant temperature will have interdendritic regions compositionally located away from the invariant plane. The analysis of non-equilibrium solidification paths is based on the work of Gulliver-Scheil [68, 69] and its application to complex ternary phase diagrams by Rhines [67] is discussed in Chapter 2. The overall compositions of each interdendritic region are listed in Table 6-2.

## **6.2 The L, $\sigma$ , $\beta$ Bivariant Equilibrium**

Alloys A110 and A120 were cast in order to analyze the L,  $\sigma$ ,  $\beta$  bivariant equilibrium. These alloys were predicted to each lie on one of the sides of the bivariant equilibrium. If this prediction was in fact correct, analysis and comparison of compositional segregation which develops during solidification could provide useful information on the L,  $\sigma$ ,  $\beta$  bivariant equilibrium. Alloy A110 solidified to form a highly segregated dendritic microstructure with large grains of over 0.5mm indicating a single phase existed at high temperature (Figure 6-2). XRD analysis identified the  $\beta$ -phase which was preserved from high temperature in the as-cast material (Figure 6-3a). No other phases were detected by XRD indicating that, if present, their phase fraction was below the instrument's detection limit with the chosen scan time. The z-contrast which develops is therefore due to the compositional segregation within the  $\beta$ -phase

itself. Compositional analysis of the interdendritic region, which is listed in Table 6-2, revealed that near alloy A110 the  $\beta$ -phase liquidus surface slopes down in temperature away from the Ti corner of the ternary. This indicated that the L,  $\sigma$ ,  $\beta$  bivariant equilibrium was compositionally located below the alloy A110 shown in the Figure 6-1.

Table 6-1 Composition of alloys measured by EPMA

Alloy #	Nb at%	Al at%	Ti at%
A110	34	31.9	34.1
A120	41.8	36.8	21.4
A167	38.6	37.6	23.8
A141	33.2	41.1	25.7
PG1	27.1	45	27.9
PG2	24.1	46.7	29.2
PG3	19.8	47.1	33.1

Alloy A120 also formed a dendritic microstructure during solidification. The primary dendrite core and secondary dendrite arms are shown in the optical micrograph presented in Figure 6-4a. Close observation of the interdendritic regions exposed that a second phase nucleated and grew from the last remaining liquid, forming a fine-scale microstructure. The fact that a second phase formed directly from the last remaining liquid, which was entrapped in the interdendritic region, suggested that alloy A120's bulk composition lies near a bivariant equilibria with the liquid phase.

Powder XRD of the as-cast material revealed that the structure consisted of mostly the  $\sigma$ -phase with some intensity from the  $\beta$ -phase (Figure 6-3b). Since alloy A120 was determined to exist near the bivariant equilibria, DTA analysis was performed in order to identify the temperature regions of multi-phase and single-phase stability. As shown in Figure 6-5 the DTA curve revealed a wide peak that indicated that a temperature region of multi-phase stability extended from 1325C to 1552C. A heat-treatment was conducted at 1550C, which is near the end of the multi-phase stability window. The heat-treatment was terminated by drop quenching into

water after 2hrs. XRD structural analysis of a powdered sample is shown in Figure 6-3b revealed that the fraction of the  $\beta$ -phase in the microstructure increased. The evidence that alloy A120 contains a second phase in the interdendritic regions combined with the fact that both the  $\sigma$  and  $\beta$  phases exist at high temperature suggested that this alloy existed near the L,  $\sigma$ ,  $\beta$  bivariant equilibria.

Table 6-2 Compositions of interdendritic regions of each experimental alloy.

Alloy #	Nb at%	Al at%	Ti at%
A110	34.7	35.4	29.9
A120	39.5	36.4	24.1
A167	35.7	40.6	23.7
A141	31.5	44.2	24.3

The interdendritic regions of the as-cast microstructure were further analyzed by SEM-BSE shown in Figure 6-4. There was a clear distinction between the primary dendrites and the secondary nucleation that took place in the interdendritic regions. The overall composition of the interdendritic region was measured by EPMA and listed in Table 6-2. Compositional analysis revealed that the liquidus surface near alloy A120 exhibited a downward slope in temperature toward lower Nb contents. An alloy with approximately the composition of alloy A120's interdendritic region was targeted, namely A167.

Alloy A167 was arc melted and its as-cast microstructure was evaluated through SEM-BSE shown in Figure 6-6. The alloy's bulk composition along with the composition of the interdendritic region are listed in Table 6-1 and Table 6-2, respectively. Again a second phase was found in the interdendritic regions in a greater volume fraction than that of alloy A120. The morphology suggested that this phase formed adjacent to the primary phase. Alloy A167 was determined to be near the L,  $\sigma$ ,  $\beta$  bivariant equilibria based on its second phase nucleation and the composition of the interdendritic regions. Using the interdendritic region as an indicator to

the “flow lines” in the liquidus projection alloy A141 was cast, which is compositionally near alloy A167’s interdendritic region.

### **6.3 Phase Transformation Path in Alloy A141**

#### **6.3.1 Phase Reactions in the Interdendritic Region**

The as-cast structure of alloy A141 was of particular interest as it provided evidence of three phases reacting with the liquid phase, an indication that its interdendritic region composition had drifted into an invariant plane during non-equilibrium solidification. SEM of this alloy’s as-cast microstructure is shown in Figure 6-7. Figure 6-7a and b, which are low magnification micrographs, elucidate a fine structure of two different z-contrast phases in the primary dendrites and a large volume fraction of a third contrast phase in the interdendritic regions. Higher magnification in Figure 6-7 c and d revealed at least 3 contrast phases, which seemed to form directly from the last remaining liquid trapped in the interdendritic regions. XRD structural analysis of the as-cast material revealed three structurally distinct phases, namely the  $\gamma$ ,  $\sigma$  and  $\beta$  phases (Figure 6-8). The O-phase, which is a metastable phase, which forms via a shear transformation occurring in the  $\beta$ -phase upon quenching, was also identified [19]. The evidence showing three structurally and compositionally distinct phases formed directly from the liquid motivated further investigations of A141’s interdendritic regions for evidence of the invariant reactions class and composition.

#### **6.3.2 Microstructural Evolution of Three-phase Reaction from the Liquid**

The evolution of this microstructure became of key interest in the development of the invariant reaction. Two phases provided morphological evidence that their formation was coupled. This region is marked as region 1 in Figure 6-7. A second region marked as region 2 showed a coarse phase surrounded by second composition phase that seemed to grow from the

liquid adjacent to region 1. Regions 1 and 2 are marked in subsequent micrographs throughout this chapter and referenced to throughout the discussion. The microstructure of the as-cast material was analyzed in order to determine the solidification sequence of region 1 and region 2 using optical microscopy shown in Figure 6-9a and b.

**Phase evolution in as-cast materials:** Regions 1 and 2 are also marked on this micrograph. The lamellar morphology of region 1 strongly suggested that it formed through a reaction with the liquid. It may be implied that if region 2 cut through region 1 then region 2 formed via a reaction of the lamellar like structure and the liquid. Examining the optical micrographs shown in Figure 6-9a and b provided several instances of region 2 cutting through region 1 as evident by the continuation of the lamella through the coarser phase. Two examples of this are marked on Figure 6-9b with lines highlighting several laths. This event was found throughout the interdendritic regions examined.

Knowing that region 1 consisted of two phases that formed via a coupled growth mechanism, and the fact that the third phase forms via a reaction of these phases with the liquid, it became evident that this alloy crosses through the invariant plane of either a transition or ternary peritectic reaction. Both the transition reaction and ternary peritectic reactions may produce two primary phases that form together from the liquid followed by a third phase that forms upon crossing through the invariant plane.

### **6.3.3 Analysis of the Solid State Transformations after Solidification**

In this alloy system solid-state transformations during cooling to room temperature often obscure the interpretation of microstructures. To be able to analyze confidently the reactions with the liquid phase occurring within the interdendritic region the solid-state transformations were characterized. Alloy A141's DTA curve for the thermally cycled material between 1150C and

1600C is shown in Figure 6-10. The DTA sample's microstructure was evaluated and showed no evidence of melting therefore the peaks are associated with a solid-state transformation.

Three endothermic peaks were measured upon heating, consisting of a sharp peak and two convoluted wide peaks marked 1 and 2 in Figure 6-10. The sharp peak has an onset temperature of 1299C that ends at 1366C at the beginning of the 1<sup>st</sup> wide peak. This peak persisted up to 1431C where the onset of the last wide peak was located. The signal returned to the baseline at 1528C. Knowing that these peaks were associated with solid-state transformations, heat-treatment temperatures of 1535C and 1155C were selected which are above and below the solid-state transformation, respectively. By addressing the two microstructures it was possible to identify the solid-state transformations.

The microstructure that resulted from the 1535C heat-treatment, shown in Figure 6-11a revealed that the alloy had gone into the edge of a two-phase region at high temperature as indicated by a mostly single-phase microstructure. Evidence of a solid-state transformation was evident upon quenching due to the fine structure microstructure throughout. Just as in the as-cast material, XRD structural analysis shown in Figure 6-8 identified the  $\sigma$ ,  $\gamma$ ,  $\beta$  and O phases, yet the peaks associated with the  $\beta$  and O-phase were significantly greater indicating that the  $\beta$ -phase is the highest temperature phase. The quenched material was then sealed in a quartz tube and heat-treated at 1150C for 8hrs. A coarser  $\sigma$ + $\gamma$  two-phase microstructure evolved after this heat treatment as shown in Figure 6-11b. This set of experiments indicated that the solid-state transformation associated with the DTA peaks result from the  $\beta$ -phase transforming to the  $\sigma$  and  $\gamma$  phases. It is therefore important to note that upon cooling, the  $\beta$ -phase has a significant driving force to transform any traces of this phase that are in the microstructure retained from high

temperature. The driving force for this phase transformation is important in the analysis of as-cast alloy A141.

#### **6.3.4 TEM Investigation of the L, $\sigma$ , $\beta$ , $\gamma$ Invariant Reaction**

The microstructure shown in Figure 6-12a was determined to evolve by the formation of two phases forming through a coupled growth mechanism from the liquid with a third phase finally forming. This led to the notion that the interdendritic region of alloy A141 crossed through the invariant plane of either a transition reaction or a ternary peritectic reaction. Bulk structural evaluations (powder XRD) revealed the presence of the  $\sigma$ ,  $\gamma$  and  $\beta$  phases. With this knowledge it was important to identify the phases and their location in the microstructure in order to classify which reaction is taking place. To address this conventional TEM and STEM were performed.

Compositional analysis also became important in the understanding the location of this reaction. TEM observation revealed that the fine-scale morphology of these phases is such that interaction volume in EPMA is often greater than the depth of the phases in the interdendritic region. As a result TEM EDS was employed in order to identify accurately the composition of the phases partaking in this microstructure. This compositional analysis is used to develop a tie-triangle representative of the high temperature equilibrium.

A site specific TEM foil of the interdendritic region was prepared by FIB from the as-cast material shown in Figure 6-12a. A low-magnification bright-field image and a low-magnification composite bright field STEM image are shown in Figure 6-12b and c respectively. Two main regions are distinguishable in these images, marked as regions 1 and 2 on the micrographs. Following the same convention established in the previous section, we found that region 1 corresponds to the fine-scale two-phase region whereas region 2 corresponds to the region

including the third coarser phase. Figure 6-12b and c exposed the high aspect ratio of the coarse third phase. This is an important feature in TEM analysis as the long side of this phase may be normal or parallel to the foil thickness. In Figure 6-12b the coarse phase marked with a 2 is parallel to the foil normal whereas in Figure 6-12c it is perpendicular to the foil normal.

The  $\sigma$  and  $\gamma$  phases were identified throughout the microstructure while the  $\beta$ -phase was found to be retained in locations adjacent to the coarse phase, which was identified as the  $\gamma$ -phase. Diffraction patterns for the  $\gamma$ [100],  $\sigma$ [001] and  $\beta$ [125] zone axes are shown in Figure 6-13a, b and c, respectively. The bright and dark field images shown throughout this section are all taken from transmitted and diffracted beams in a two-beam condition slightly off the zone axes. Each micrograph is presented with a bright field and corresponding dark field image. STEM images were taken with the transmitted beam.

#### **6.3.4 Region 1 Microstructural Evaluations of Phases in Lamellar Structure**

The  $\gamma$ -phase was identified in the fine two-phase microstructure as demonstrated in Figure 6-14. Dark-field imaging in Figure 6-14a and b showed high intensity from the  $\gamma$ -phase, elucidating the location of this microconstituent. The average cross-section had a diameter of slightly over  $0.5\mu\text{m}$  which is a comparable scale to the lamellar spacing of the L,  $\gamma$ ,  $\sigma$ ,  $\eta$  eutectic discussed in Chapter 5. The morphology between the  $\gamma$ -phase and adjacent phase did show evidence of cooperative growth with another phase although a true lamellar structure was not evident.

In region 1 the  $\gamma$ -phase was always found to be surrounded by a second phase that was identified as the  $\sigma$ -phase. Bright-field images and the corresponding dark field images of the  $\sigma$ -phase are shown in Figure 6-15. It was not possible to make all of the  $\sigma$ -phase in the micrographs “light up” with a single two beam condition, therefore several adjustments were

made for crystallographic variations between them. In doing so it was possible to phase identify most of the microstructure in Figure 6-15. In Figure 6-15a and b there are clear examples of how the  $\sigma$  and  $\gamma$  phases are in direct contact throughout this region of the microstructure.

A STEM bright field image of region 1 is shown in Figure 6-16a. The  $\sigma$  and  $\gamma$  phases are both marked on this micrograph. The compositions of the  $\sigma$  and  $\gamma$  phases were measured by TEM EDS, which are listed in Table 6-3. These are also plotted on Figure 6-16b, which includes a liquidus projection calculated from the optimized phase diagram [79]. These compositions approximately represent the composition of the  $\sigma$  and  $\gamma$  phases forming from the liquid prior to crossing the invariant plane.

Table 6-3 TEM EDS compositional analysis of each phase in regions 1 and 2.

	Nb at%	Al at%	Ti at%
$\gamma$ Region 1	27.4	48.8	23.8
$\sigma$ Region 1	37.8	41.6	20.7
$\gamma$ Region 2	27.4	47.9	24.7
$\sigma$ Region 2	36	43.1	20.8
$\beta$ Region 2	29.2	45.7	25.1

### 6.3.5 Region 2 Microstructural Evaluations of Phases Formed through the Invariant Reaction

The  $\gamma$ ,  $\sigma$  and  $\beta$  phases were identified in the region 2, where the third coarser phase formed adjacent to the fine  $\sigma+\gamma$  phase microstructure. The coarse phase was identified as the  $\gamma$ -phase as evident in the bright and dark field images shown in Figure 6-17. The long side of this phase is parallel to the foil normal in this micrograph. The smooth continuous interface curvature and general morphology indicated that at least some portions of this phase were in direct contact with the liquid during solidification. This evidence reveals the formation of the coarse  $\gamma$ -phase from liquid.

The  $\sigma$ -phase was found adjacent to the  $\gamma$ -phase as marked in Figure 6-18. The dark-field images in Figure 6-18c and d provided significant intensity from the  $\sigma$ -phase. The interface suggests that the  $\gamma$ -phase grows partially into the  $\sigma$ -phase, consuming it. In all cases  $\sigma$ -phase surrounds the  $\gamma$ -phase, indicating that there is a diffusional reaction between the phases.

A small amount of retained  $\beta$  was identified as shown in Figure 6-19. In this figure the  $\gamma$  and  $\sigma$  phases are marked, and the location of the  $\beta$ -phase is revealed in the dark field image in Figure 6-19b. Dark-field imaging revealed that this phase was only retained near the  $\sigma/\gamma$  interfaces. Further analysis exposed that this phase contained many dislocations that is consistent with a disordered BCC phase retained in a high-temperature microstructure down to room temperature.

Compositional analysis was performed on the  $\sigma$ ,  $\gamma$  and  $\beta$  phases retained from high temperature in region 2. A conventional bright field TEM image along with a STEM image of approximately same location are both shown in Figure 6-20a and b. Each phase is marked on the micrographs. The approximate locations used for TEM EDS measurement are marked on these micrographs. The  $\gamma$  and  $\sigma$  phases were relatively coarse compared to the minor amount of retained  $\beta$ -phase that was located near the  $\gamma/\sigma$  interface.

The compositions of the  $\beta$ ,  $\gamma$  and  $\sigma$  phases were used to develop a ternary tie-triangle representative of high-temperature equilibrium near the invariant reaction temperature and composition. The compositions that define this tie-triangle are listed in Table 6-3 and are also plotted on our calculated liquidus projection (Figure 6-20). The  $\beta$  and  $\gamma$  phases have a fairly close composition relative to the  $\sigma$ -phase, which is compositionally located further away. The fact that the  $\beta$  and  $\gamma$  corners of the tie-triangle are close, and both are further from the  $\sigma$ -phase, is consistent with the general trend seen in calculations using a recently published phase diagram

database [80] as well as the  $\beta$ ,  $\gamma$  and  $\sigma$  tie-triangle we measured at 1510C discussed in Chapter 7. At 1510C the  $\beta$  and  $\gamma$  phases were also only separated by a few at% Nb, Al and Ti.

#### **6.4 Development of the L, $\beta$ , $\gamma$ and $\sigma$ Ternary Peritectic Reaction**

In the microstructure there was evidence of the coupled growth of the  $\sigma$  and  $\gamma$  phases followed by what the microstructural evolution suggested to be a peritectic-like formation of the  $\gamma$ -phase. This evidence was found in the heart of the interdendritic region where support in favor of a reaction between the L,  $\sigma$ ,  $\gamma$  and  $\beta$  phases was found. The fact that the  $\gamma$ -phase is forming from the last liquid though this invariant reaction defines this phase as a principal invariant reaction product. This means the  $\gamma$ -phase is forming from a reaction between the L,  $\sigma$  and  $\beta$  phases.

The microstructural evidence suggesting that the coarse  $\gamma$ -phase formed through a reaction between the coupled growth microstructure and the liquid phase, signaled that the  $\gamma$ -phase should not be present in the primary regions. The  $\beta$ -phase was not found in the coupled growth microstructure, however, this does not preclude its existence as a primary microconstituent at high temperature. The development of the  $\beta$ -phase extension discussed in Chapter 4 revealed that this phase readily transforms to the  $\gamma$ -phase even under severe cooling rates. Therefore, in the interdendritic regions of this as-cast microstructure it is likely that most of the high-temperature  $\beta$ -phase transformed to the  $\gamma$ -phase under the less severe cooling rates.

The evolution of the interdendritic region was, therefore, determined to be the  $\sigma+\beta$  phases forming through a coupled growth mechanism, followed by the formation of the  $\gamma$ -phase via a reaction between the  $\sigma+\beta$  phases and L phase. Two possible invariant reactions could cause the evolution of such a microstructure, namely, a transition reaction and a ternary peritectic that are both shown graphically in Figure 6-21. The transition reaction, at the invariant point consists of

the L+ $\beta$  phases reacting to form the  $\sigma$ + $\gamma$  phases. The ternary peritectic reaction on the other hand consists of the L+ $\beta$ + $\sigma$  phases reacting to form peritectic  $\gamma$ -phase.

In the event of a transition reaction there are two three-phase regions, namely the L+ $\beta$ + $\sigma$  and L+ $\gamma$ + $\sigma$  tie-triangles, reacting to yield the L+ $\beta$ + $\gamma$  and  $\beta$ + $\gamma$ + $\sigma$  tie-triangles. These triangles are shown schematically in Figure 6-21. This reaction may yield the observed microstructure if the alloy is compositionally located within the L+ $\beta$ + $\sigma$  tie-triangle above the transition reaction invariant plane and within the  $\beta$ + $\sigma$ + $\gamma$  tie-triangle below the reaction plane. An alloy with such a composition is marked on Figure 6-21. Above the invariant plane the microstructure will evolve by the coupled growth of the  $\beta$ + $\sigma$  phases directly from the liquid. Upon crossing through and under the invariant plane the alloy composition now within the  $\beta$ + $\sigma$ + $\gamma$  tie-triangle with result in the formation of the  $\gamma$ -phase via a reaction with the liquid and  $\beta$ + $\sigma$  phases.

Similarly, if a ternary reaction of the L,  $\sigma$  and  $\beta$  phases form peritectic  $\gamma$ -phase an identical two region microstructure is possible. An alloy that is compositionally located within the L,  $\sigma$  and  $\beta$  tie-triangle above the invariant plane and within the tie-triangle below the invariant plane is shown in Figure 6-21. In this alloy, similar to the transition reaction, a coupled growth microstructure consisting of  $\sigma$  and  $\beta$  phase microconstituent forms from the liquid as the alloy crosses through the L,  $\sigma$  and  $\beta$  tie-triangle. Upon cooling through the invariant plane the liquid phase reacts with a fraction the  $\sigma$  and  $\beta$  phases to form the  $\gamma$ -phase through a peritectic reaction.

#### Thermal Development of the L, $\gamma$ , $\sigma$ , $\beta$ invariant reaction

The microstructural evolution of the as-cast and fast solidified alloy A141 provided evidence of the formation of  $\gamma$ -phase via a reaction between the L,  $\sigma$  and  $\beta$  phases. This information alone however was not sufficient to distinguish between a transition and ternary

peritectic reaction involving these phases. Examination of the bivariant equilibrium involving the liquid phase that feeds into and runs out of the invariant plane revealed a key difference in the contours of the liquidus surfaces.

The lines of intersection between the liquidus surfaces are delineated by the path of the bivariant equilibrium lines through temperature composition space. At the invariant reaction temperature all three bivariant equilibrium meet and react. The three pertinent lines representing the  $(L, \sigma, \gamma)$ ,  $(L, \beta, \gamma)$  and  $(L, \beta, \sigma)$  bivariant equilibrium are expanded and shown in Figure 6-21 for both the transition and ternary peritectic reactions. A principal difference between the paths of the  $(L, \beta, \gamma)$  bivariant equilibria through temperature composition space evident in these projections. In the case of the transition reaction the  $(L, \beta, \gamma)$  bivariant equilibria feeds into the invariant reaction, hence the liquidus temperatures decrease toward the invariant point. In contrast the ternary peritectic reaction case the liquidus temperatures decrease away from the invariant point. This key difference in the thermal behavior between reactions was exploited to provide an experimental distinction between the two types.

**Thermal analysis of liquidus surface contours:** Alloys Pg1, 2 and 3 were designed in order to examine the slope of the liquidus surface. The compositions measured by EPMA are listed in Table 6-1 and plotted on Figure 6-1. The invariant reaction is known to be near alloy A141 and the three-phase equilibrium measured within its interdendritic region. Alloys Pg1, 2 and 3 are successively located further from the location of the invariant reaction along the  $(L, \beta, \gamma)$  bivariant equilibria as can be seen in Figure 6-1. The as-cast SEM micrographs of alloys Pg1, 2 and 3 are shown in Figure 6-22 a, b and c, respectively. These micrographs revealed a two-phase solidification that is consistent with each alloy crossing through the liquidus surface

near the bivariant equilibria. Each of these alloys was thermally cycled in the DTA and the subsequent curves were investigated for signs of melting.

The DTA curves for each alloy are shown on the same graph in Figure 6-23. The solid-state transformations are similar in all three curves. Upon heating alloy Pg1, the first peak related to a solid-state transformation has an onset temperature of 1288C whereas the second solid-state transformation peak started at 1507C. Microstructural evaluations revealed this alloy did not exhibit any signs of melting. Similarly, the heating of alloy Pg2 revealed two peaks related to solid-state transformations that begin at 1274C and 1456C respectively, which are slightly lower than the temperatures measured in alloy Pg1. Alloy Pg 2 however commenced melting at 1544C indicating that the liquidus surface had decreased. Finally alloy Pg3 which is furthest away from the invariant reaction had solid-state transformations at 1270C and 1437C and entered the liquid phase stability range at 1519C and fully melted at 1577C.

Comparison of the DTA curves revealed that liquidus surface was not reached by alloys near the invariant reaction, yet alloy Pg3 furthest away fully melted. This provides clear evidence that the (L,  $\beta$ ,  $\gamma$ ) bivariant equilibria decreases in temperature away from the invariant reaction thus proving the reaction is a ternary peritectic reaction. As a result the interdendritic region of alloys with compositions near the (L,  $\beta$ ,  $\sigma$ ) bivariant equilibria will fall towards the invariant reaction during none equilibrium solidification. Alloys near the (L,  $\beta$ ,  $\gamma$ ) or (L,  $\sigma$ ,  $\gamma$ ) bivariant equilibrium conversely will drift away from the invariant reaction.

## 6.5 Summary

Microstructural analysis revealed the formation of the  $\gamma$ -phase though either a ternary peritectic or transition reaction. The thermodynamic behavior of alloys near the (L,  $\beta$ ,  $\gamma$ ) bivariant equilibria line confirmed the peritectic formation of the  $\gamma$ -phase. In the case that  $\gamma$ -

phase is forming though a peritectic reaction between the L,  $\beta$  and  $\sigma$  phases there should be evidence of coupled growth of the  $\beta$  and  $\sigma$  phases followed by the peritectic formation of the  $\gamma$  in the interdendritic region.

The microstructure of alloy A141 shows that the  $\gamma$ -phase in the interdendritic is surrounded by  $\sigma$  and a small amount of retained  $\beta$ . Two phases namely the  $\gamma$  and  $\sigma$  phases which formed though a cooperative growth process are adjacent to this region. Although the  $\gamma$  phase is not an expected microconstituent, our work on the  $\beta$ -phase extension discussed in Chapter 4 and published in [77] demonstrated that the  $\beta$ -phase readily transforms to the  $\gamma$ -phase upon quenching. From the interdendritic regions it was possible to measure approximately the composition of the  $\beta$  and  $\sigma$  phases in equilibrium just above the invariant plane as well as the resulting ( $\beta$ ,  $\sigma$ ,  $\gamma$ ) tie-triangle from the ternary peritectic reaction. The composition of the peritectic phase ( $\gamma$ -phase) in a ternary peritectic reaction is a close approximation of the invariant point. It was not possible to reach the invariant temperature with the available DTA therefore the invariant temperature is above 1600C.

A110 ■ PG30  
PG20 ▲  
PG10 ▲  
A167 ■ A141  
A120 ■

Figure 6-1 Calculated liquidus projection marked with the composition of the experimental alloys.



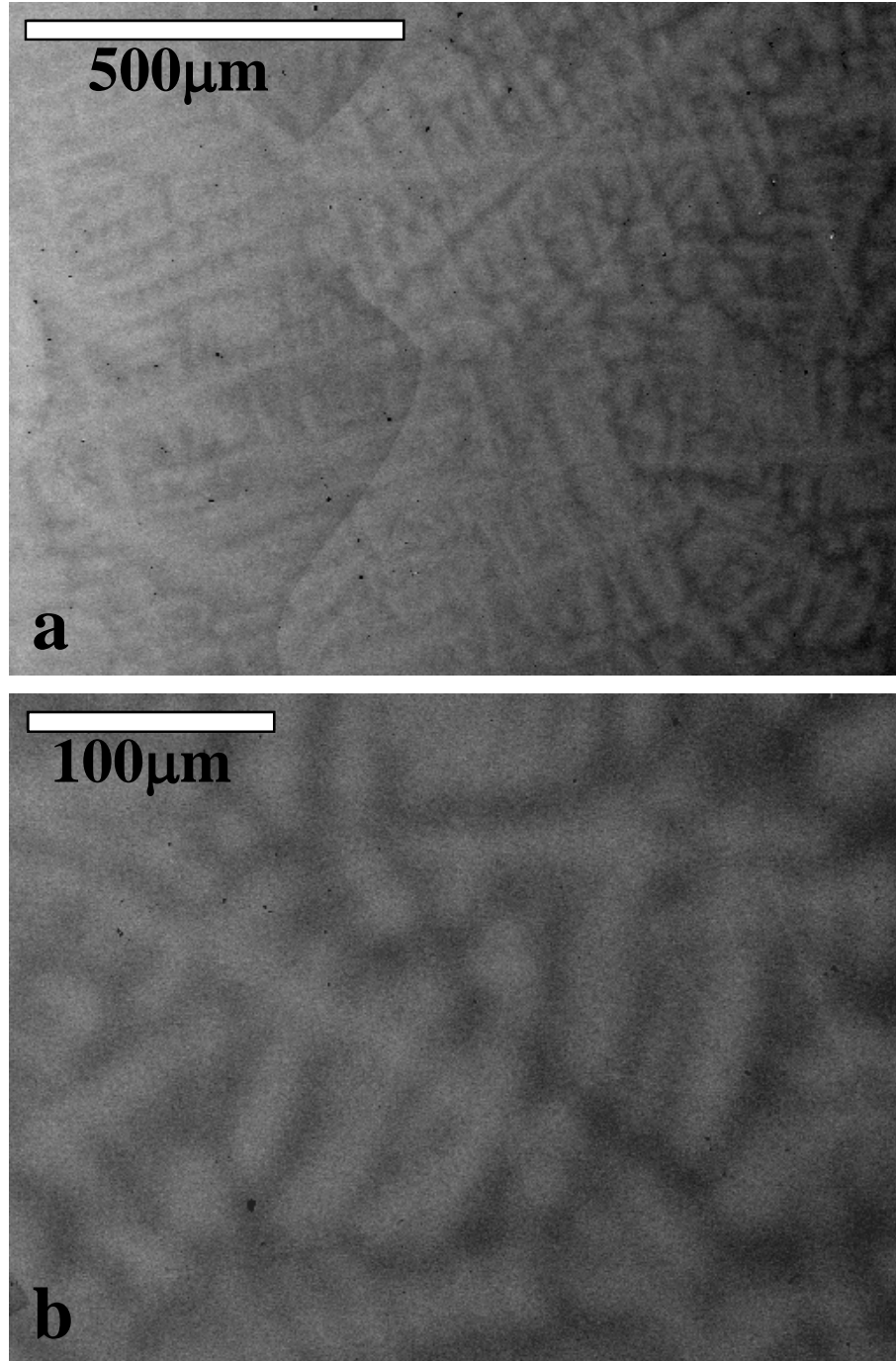


Figure 6-2 SEM micrograph of as-cast alloy A110 showing revealing a dendritic microstructure in a) low magnification across a grain boundary and b) higher magnification of the dendrites.

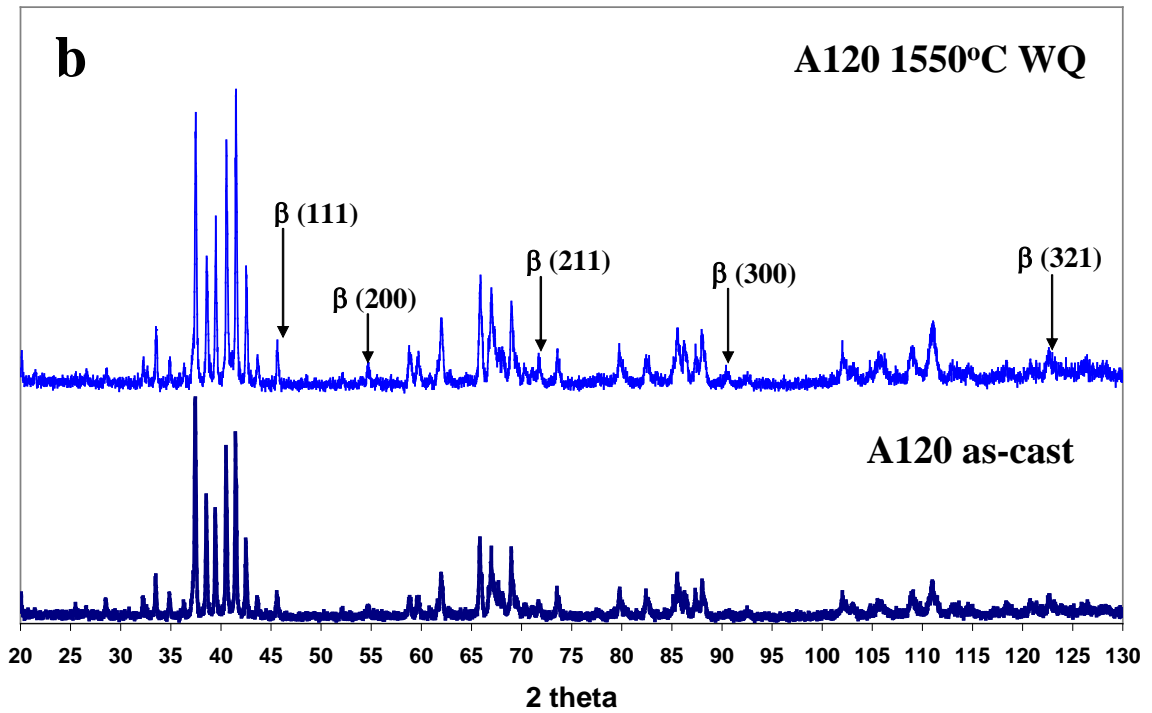
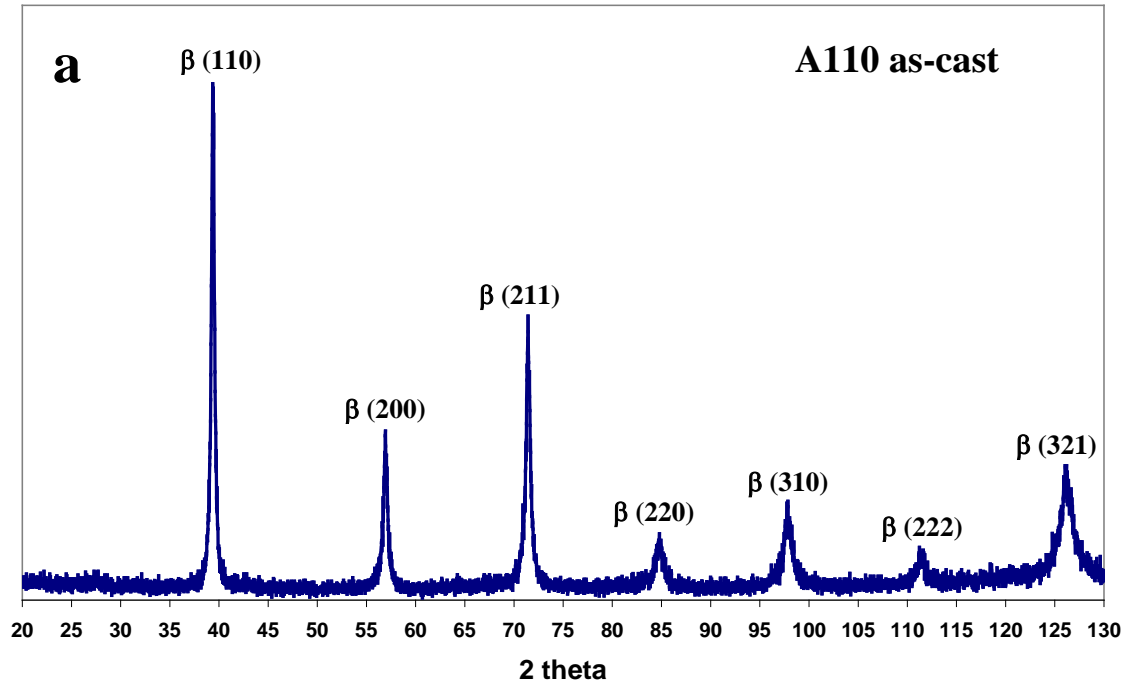


Figure 6-3 XRD of a) as-cast alloy A110 from which the  $\beta$ -phase was identified and b) of alloy 120 in the as-cast condition and heat-treated at 1550C showing the  $\beta$  and  $\sigma$  phases with the signatures of the  $\beta$ -phase increasing with the heat-treatment.

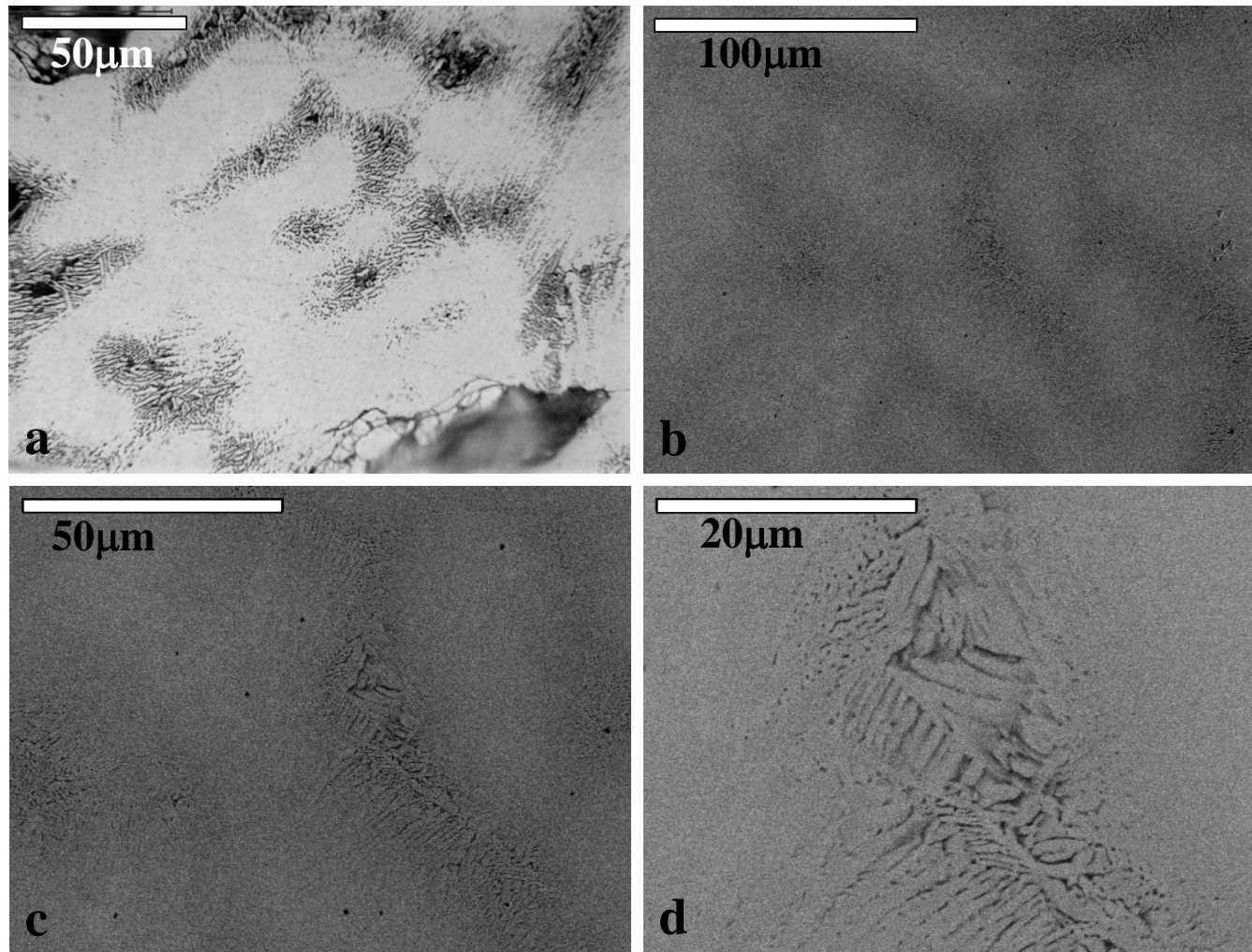


Figure 6-4 Micrographs of as-cast alloy A120 showing revealing a dendritic microstructure in a) optical at low magnification and SEM showing b) overall dendritic structure, c) centered around interdendritic region and d) higher magnification of the lower z phases within the interdendritic region.

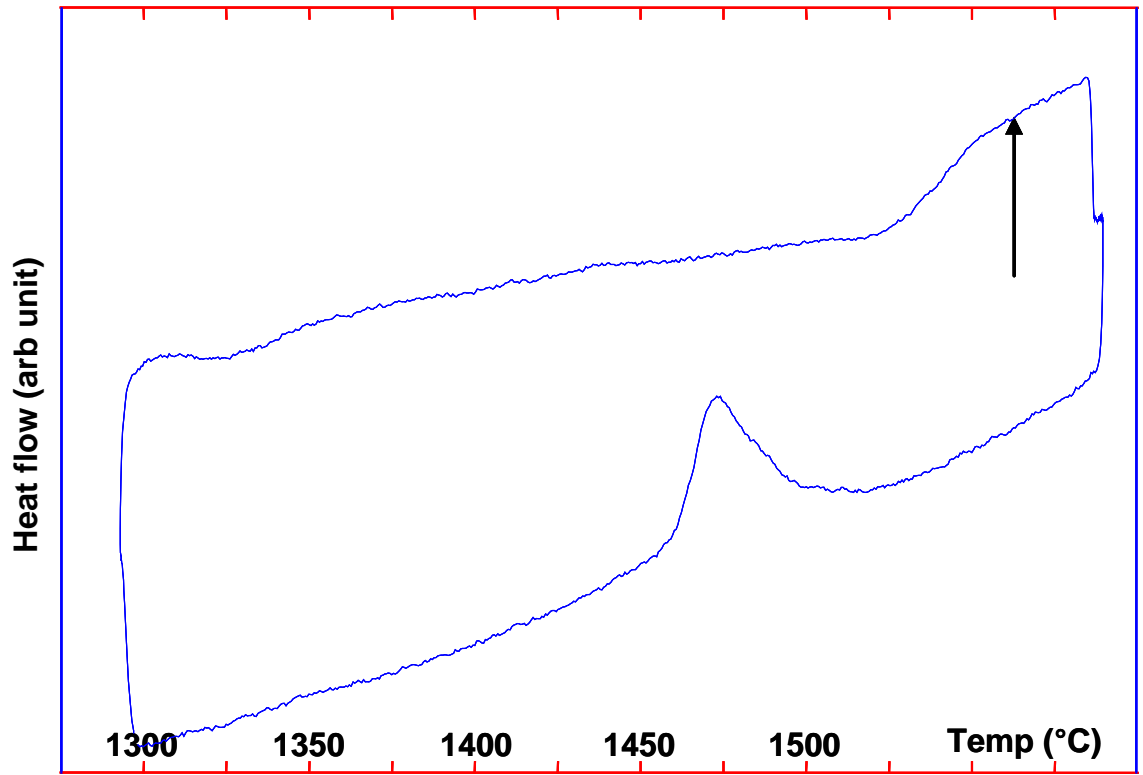


Figure 6-5 DTA of thermally cycled alloy A120 at 10K/min marked with the 1550C heat-treatment temperature.

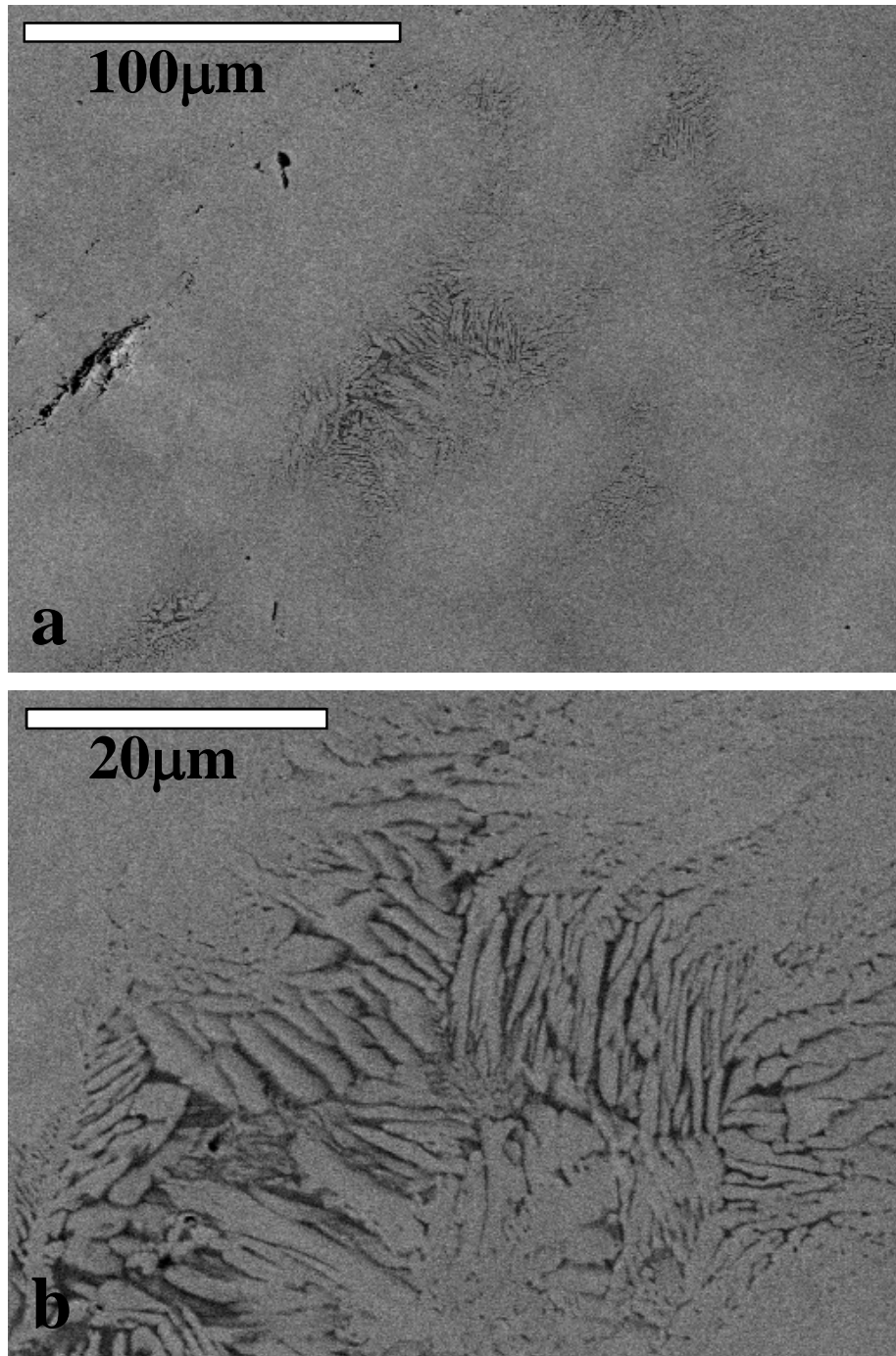


Figure 6-6 SEM micrographs of as-cast alloy A167 a) revealing a dendritic microstructure and b) and centered around interdendritic region.

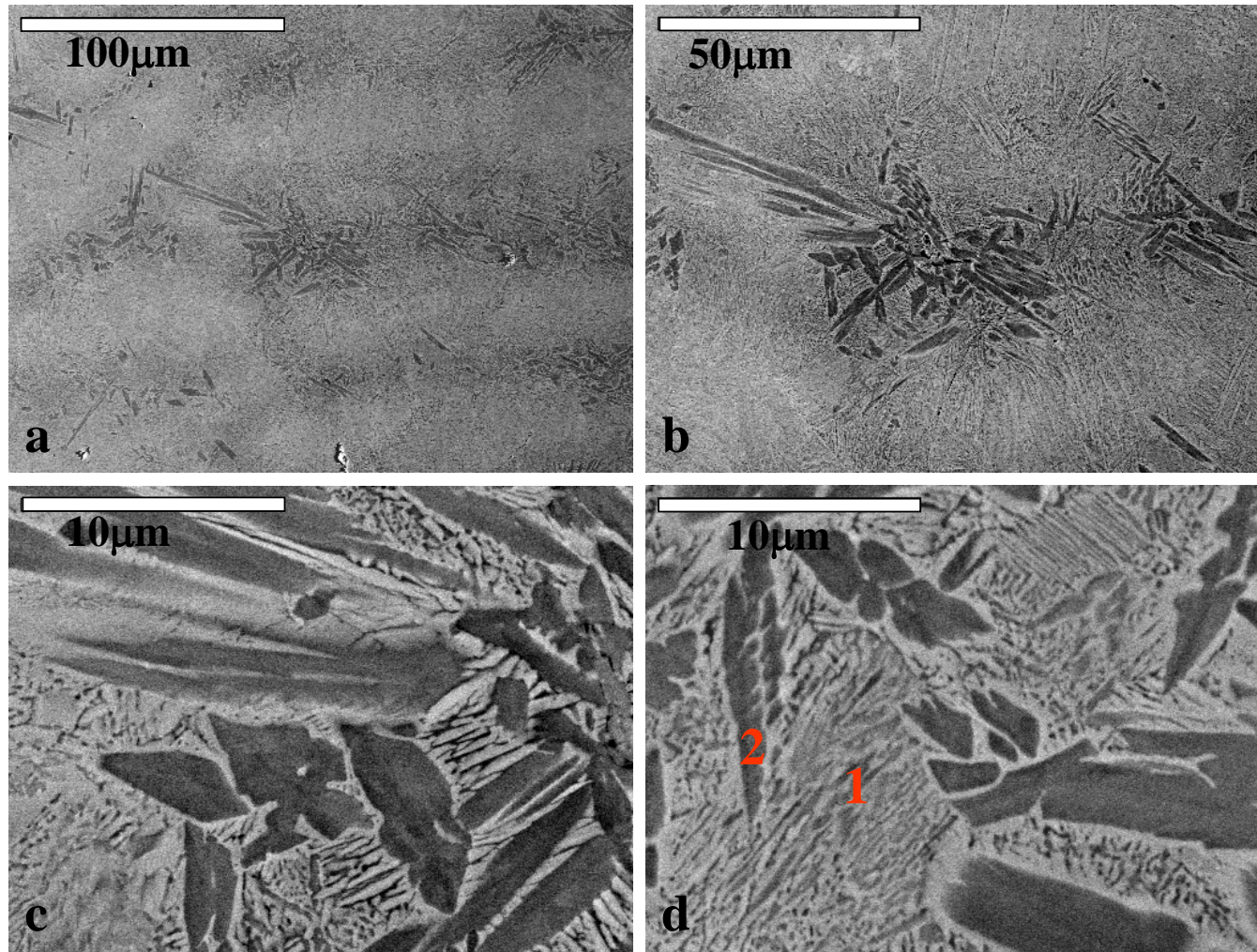


Figure 6-7 SEM micrographs of as-cast alloy A141 a) revealing a dendritic microstructure b) centered around interdendritic region c) showing the formation of a coarse phase in the interdendritic region and d) showing three contrast phases with regions 1 and 2 defined.

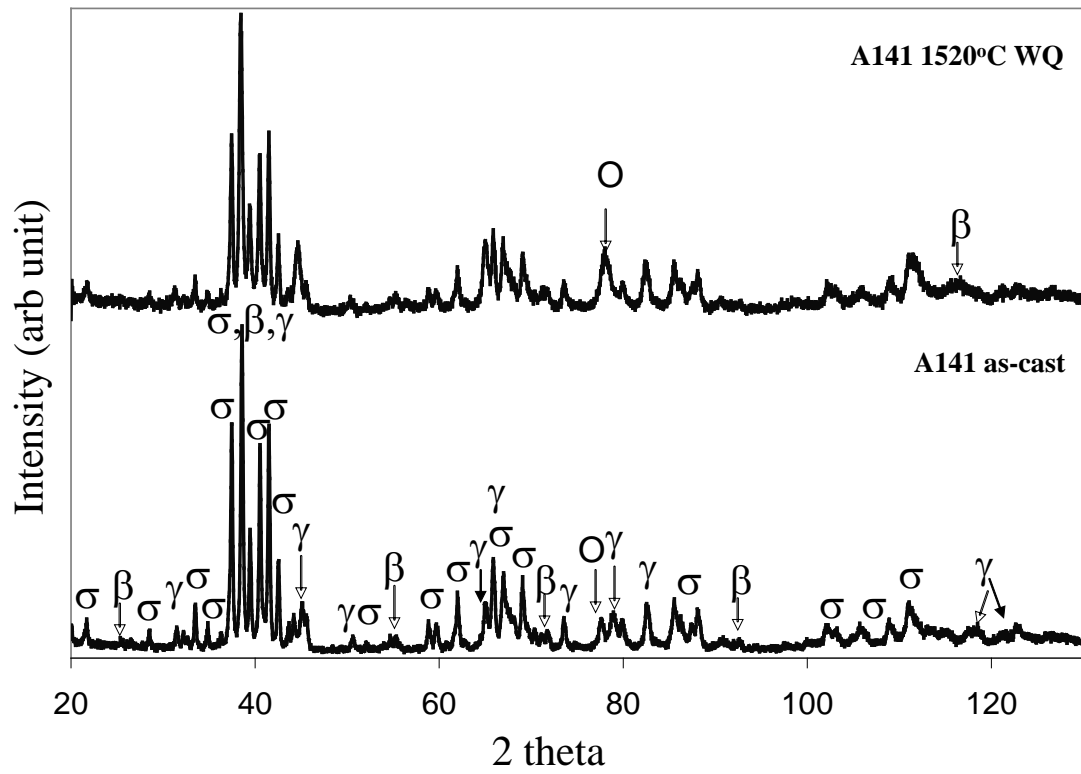


Figure 6-8 XRD of alloy A141 in a) the as-cast condition and b) heat-treated at 1520C.

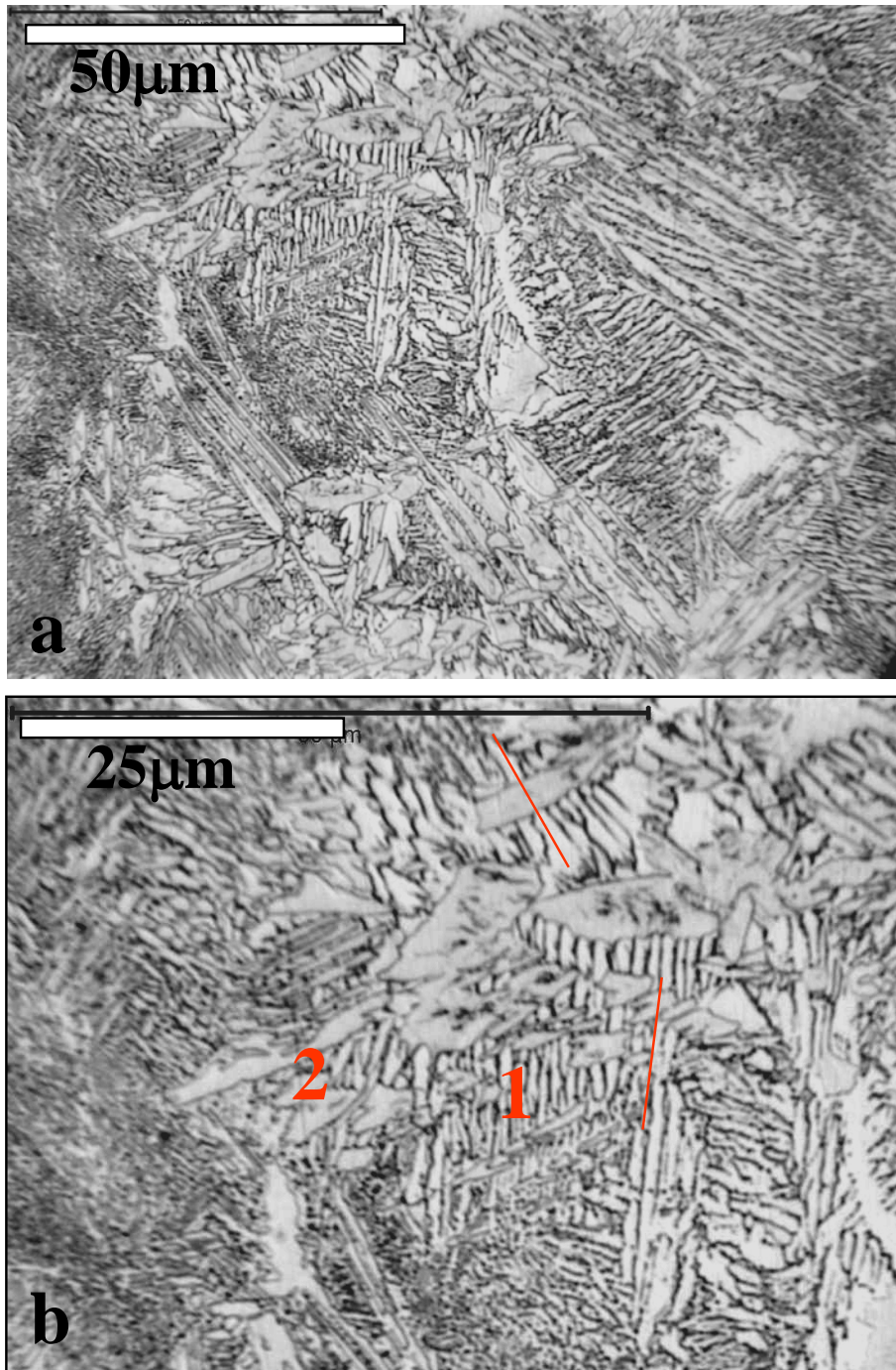


Figure 6-9 Optical micrographs of alloy A141 which are a) centered around the interdendritic region and b) higher magnification showing the lamellar structure continuing through the coarse phase, this micrograph is also marked with region 1 and 2.

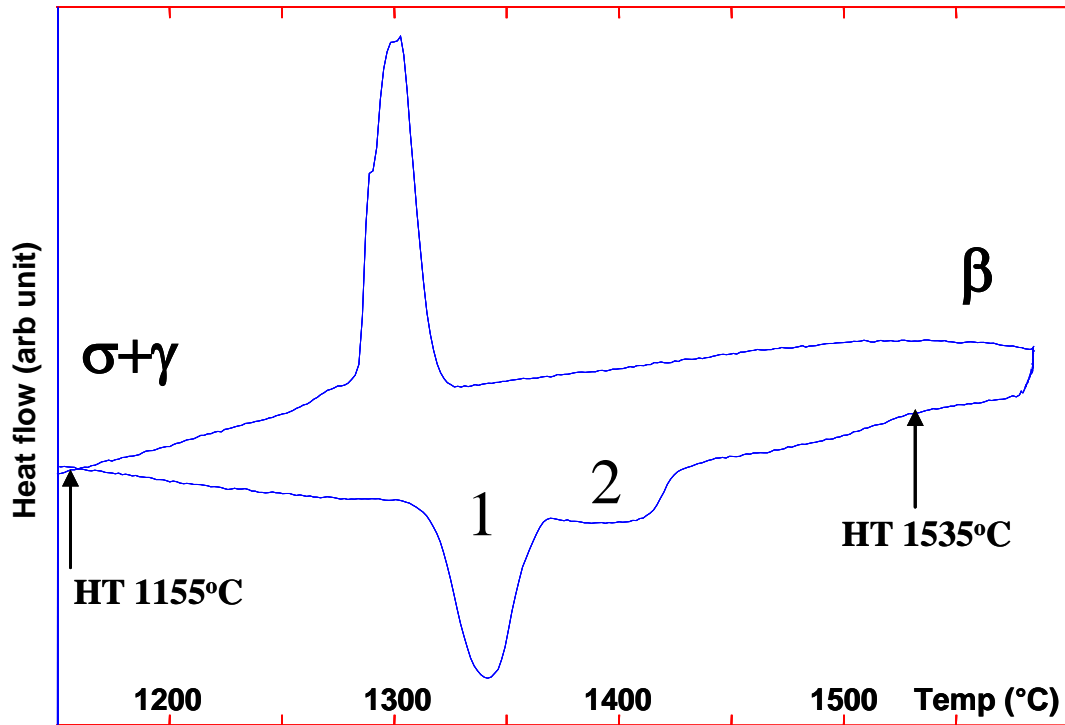


Figure 6-10 DTA of thermally cycled alloy A141 at 10K/min with peaks 1 and 2 marked along with the heat-treatment temperatures (1535C and 1155C).

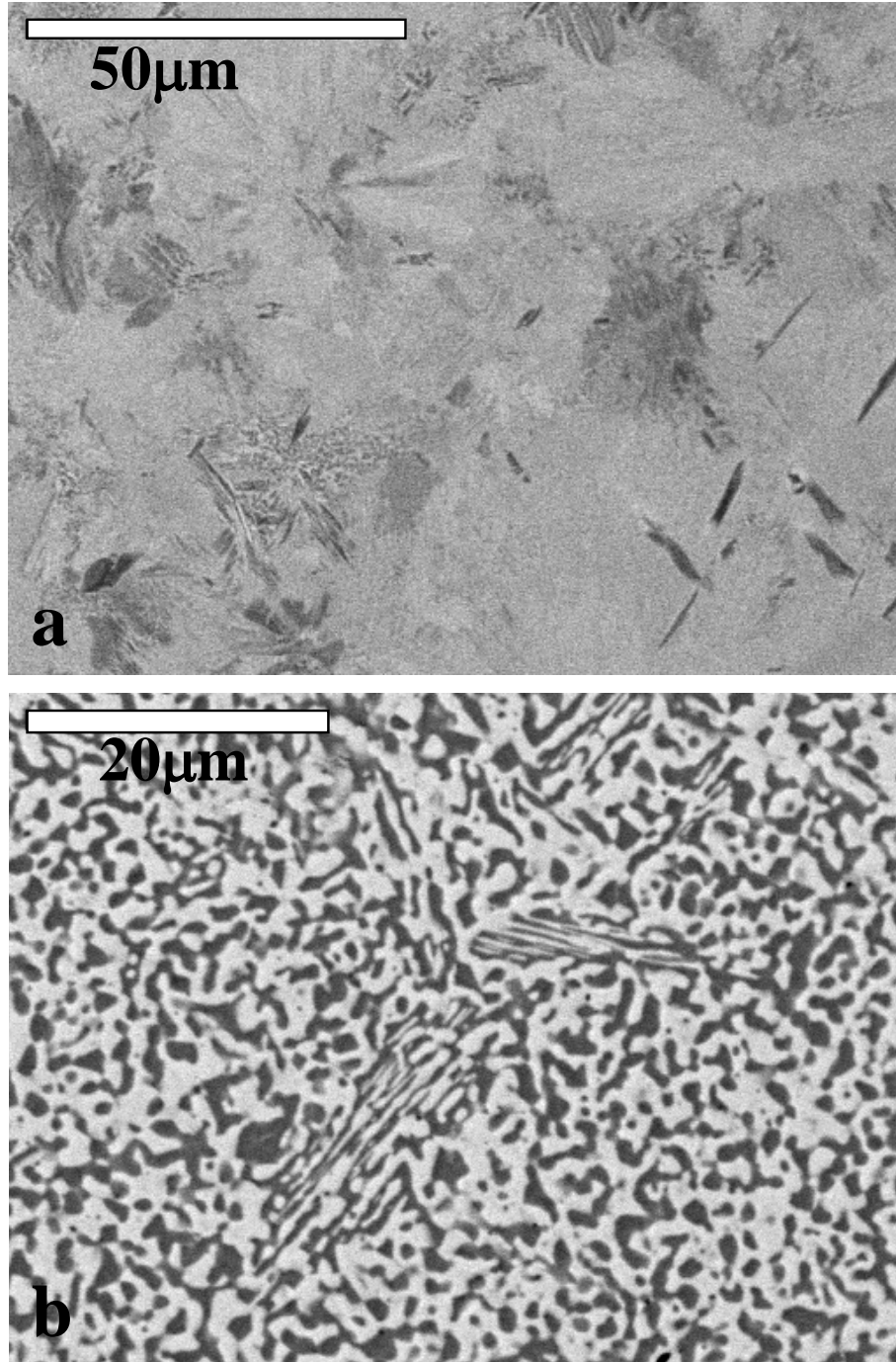


Figure 6-11 SEM of heat-treated alloy A141 at a) 1535C and b) 1155C which shows the  $\sigma$  and  $\gamma$  phases which appear bright and dark, respectively.

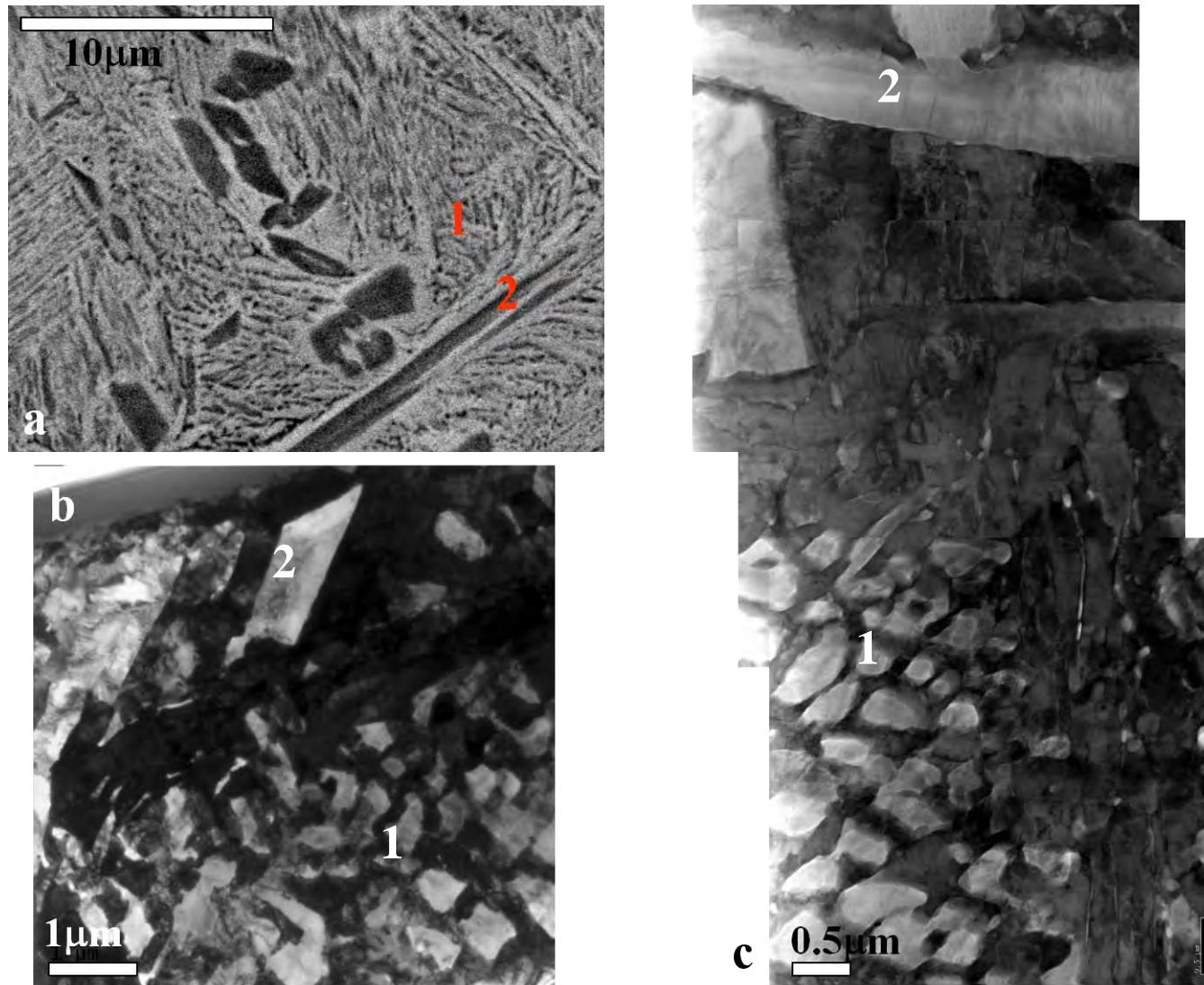


Figure 6-12 SEM micrographs of a) as-cast alloy 141 marked with region 1 and 2. TEM micrographs showing b) a bright field image marked with region 1 and 2 and c) compound TEM micrograph generated by combining 3 adjacent STEM images across regions 1 and 2.

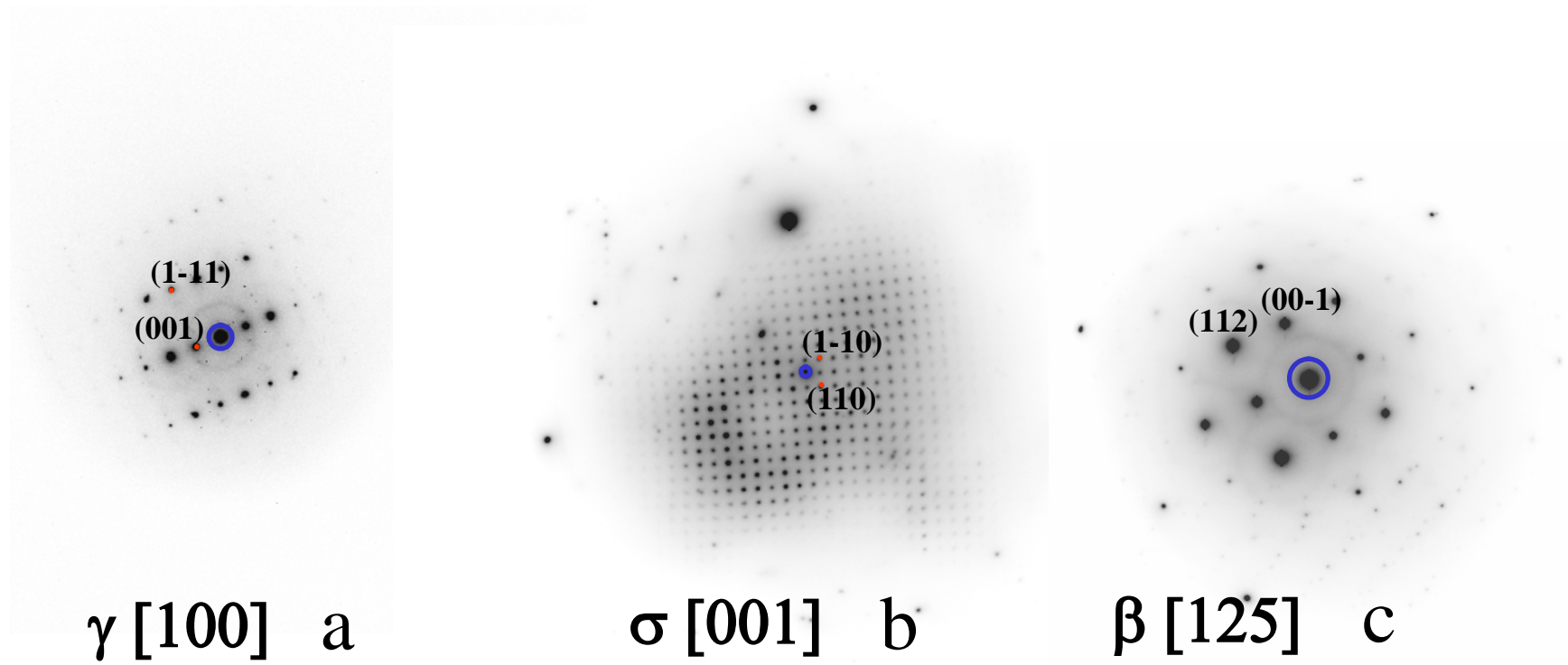


Figure 6-13 TEM SAD zone axis diffraction patterns of alloy A141 for a)  $\gamma$ -phase, b)  $\sigma$ -phase and c)  $\beta$ -phase.

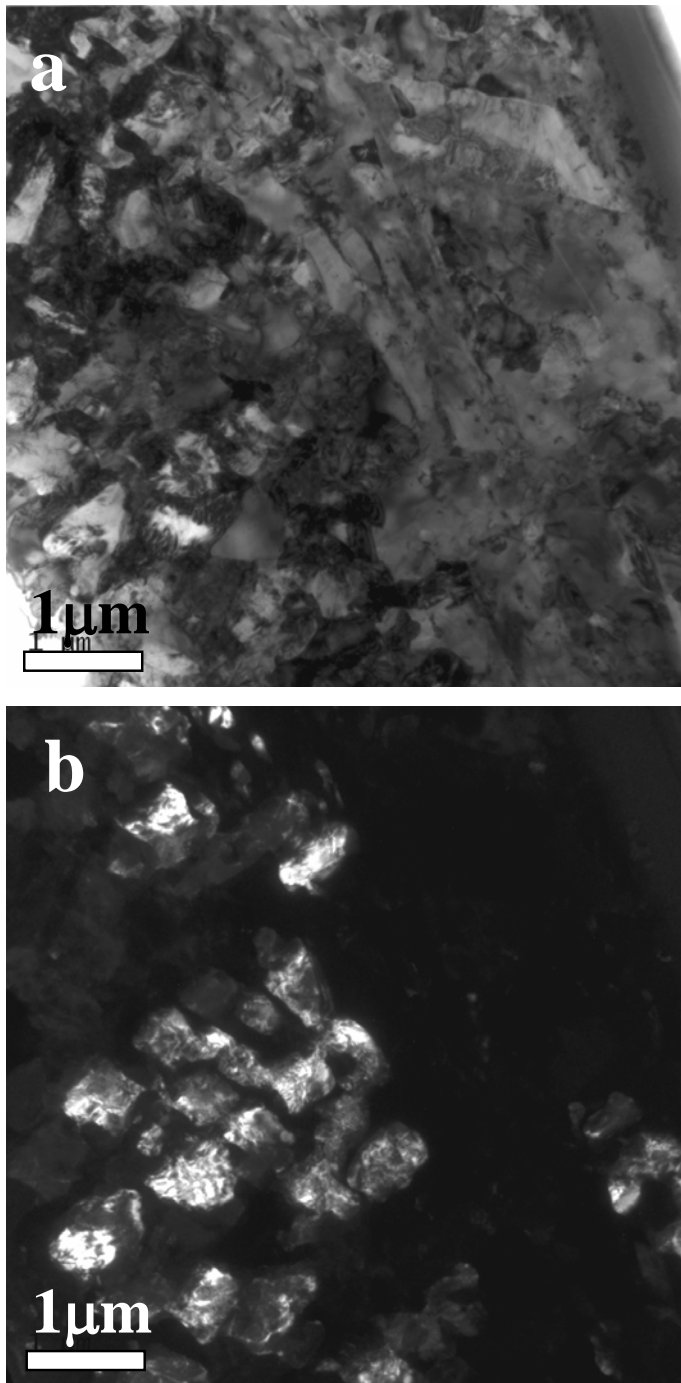


Figure 6-14 TEM micrographs of alloy A141 a) centered on region 1 and b) corresponding dark field image of the  $\gamma$ -phase.

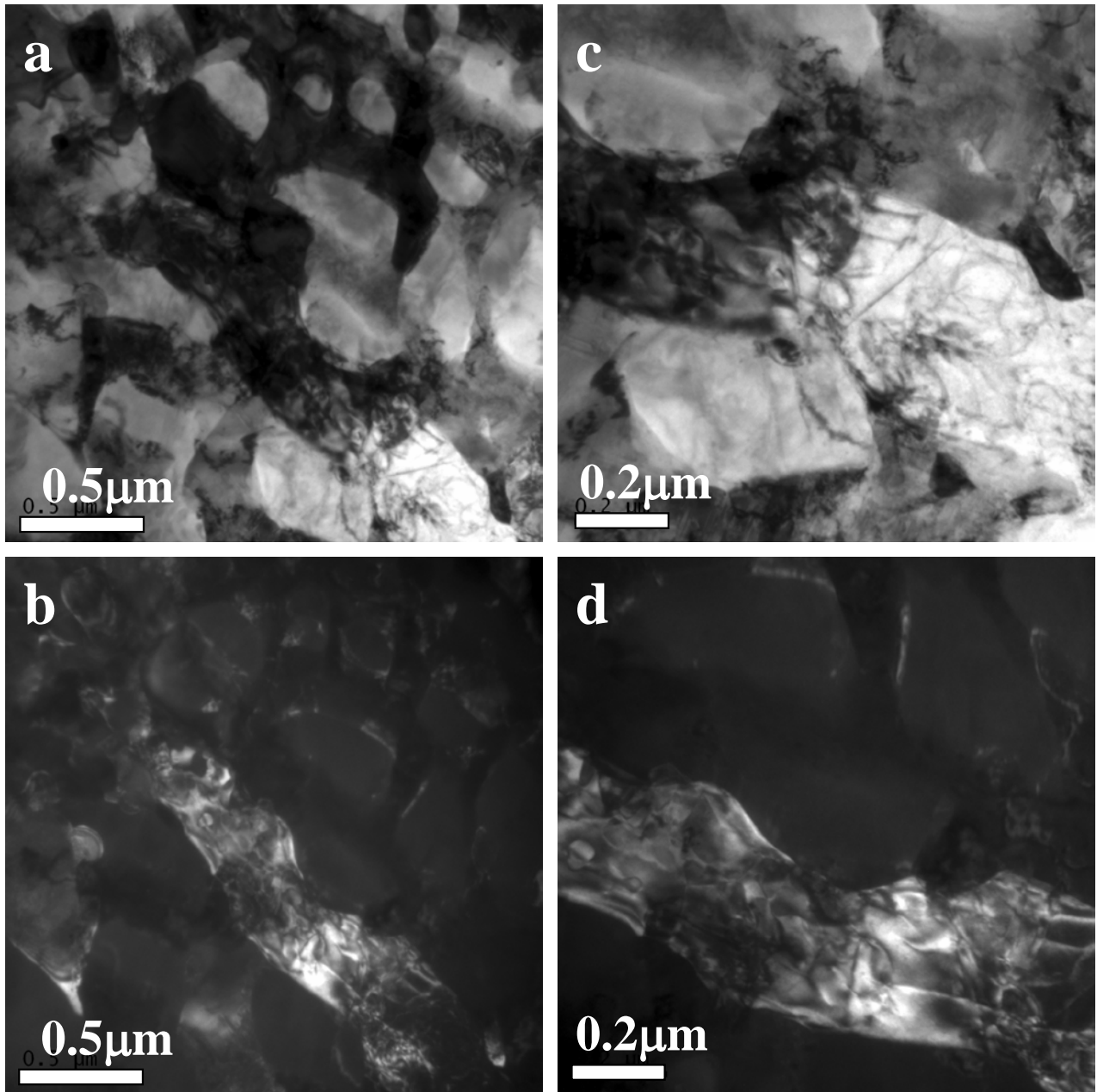


Figure 6-15 TEM micrographs of alloy A141 a) centered on region 1 and b) corresponding dark field image of the  $\sigma$ -phase and c) higher magnification of the  $\sigma$  and  $\gamma$  phases and d) corresponding dark field image of the  $\sigma$ -phase.

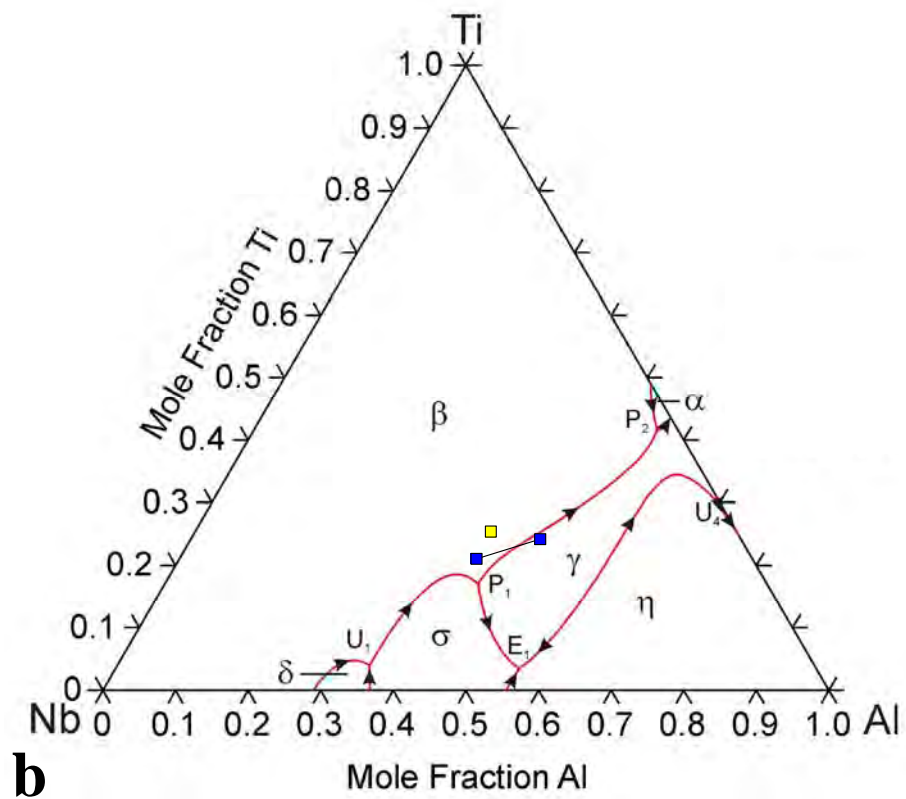
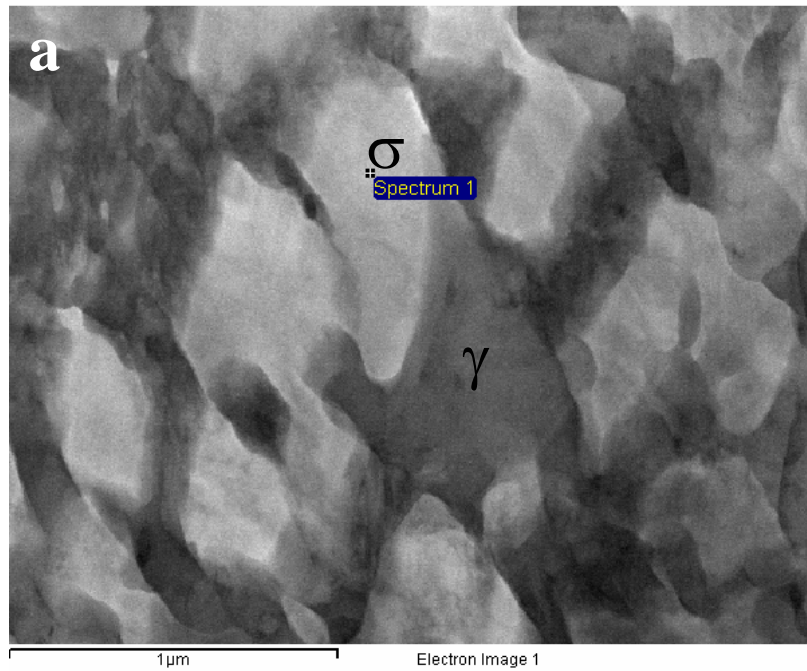


Figure 6-16 STEM micrograph of region 1 showing a) the  $\sigma$  and  $\gamma$  phases. TEM EDS compositional analysis of b) the  $\sigma$  and  $\gamma$  phases (blue) in region 1 plotted on a calculated liquidus projection along with the bulk composition of alloy A 141.

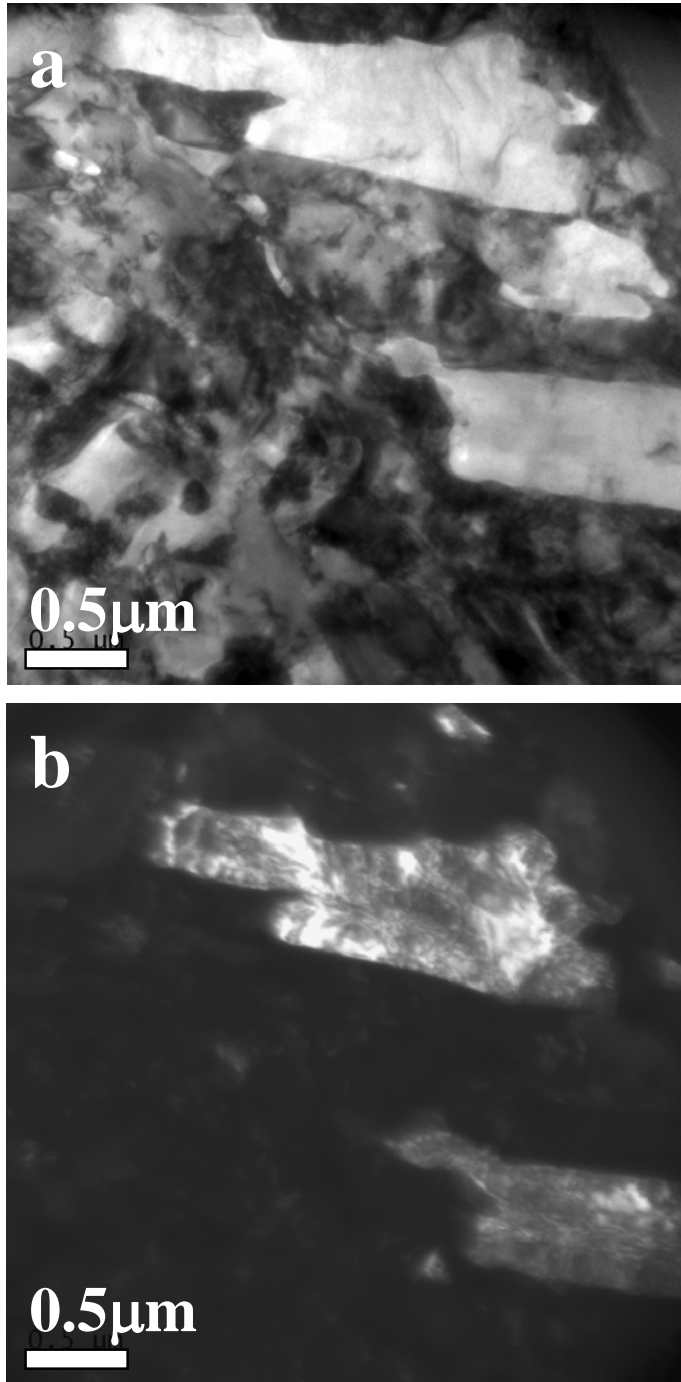


Figure 6-17 TEM micrographs of alloy A141 a) centered on region 2 and b) corresponding dark field image of the  $\gamma$ -phase.

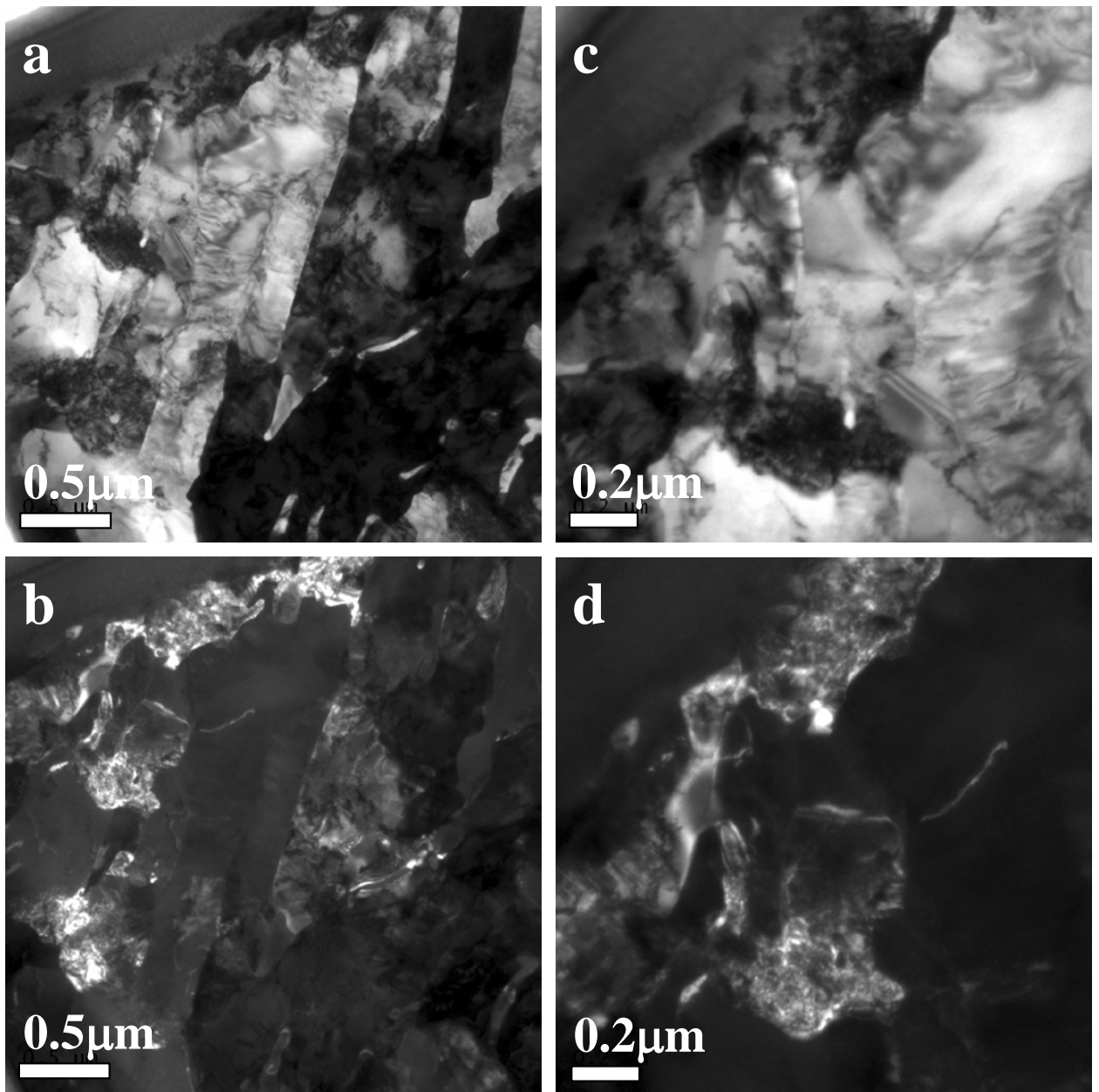


Figure 6-18 TEM micrographs of alloy A141 a) centered on region 2 and b) corresponding dark field image of the  $\sigma$ -phase and c) higher magnification of the  $\sigma$  and  $\gamma$  phases and d) corresponding dark field image of the  $\sigma$ -phase.

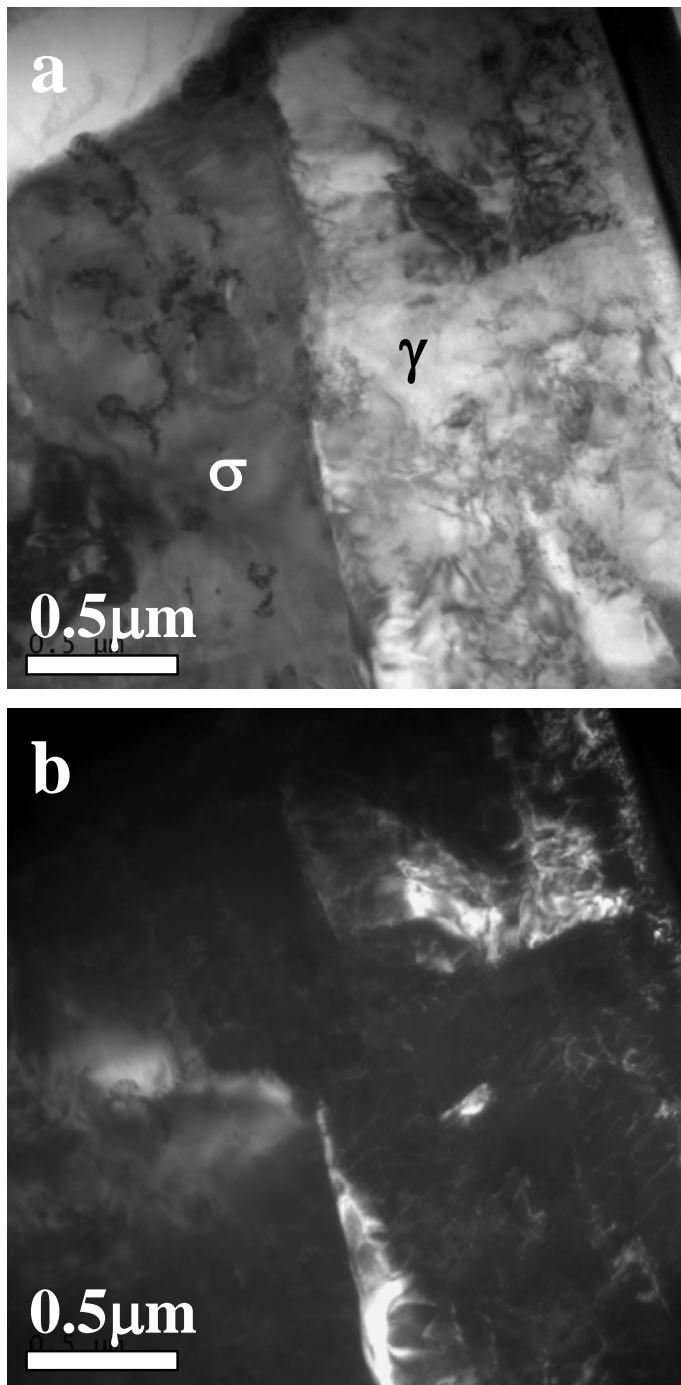


Figure 6-19 TEM micrographs of alloy A141 a) centered on region 2 showing the  $\sigma$  and  $\gamma$  phases and b) corresponding dark field image of the  $\beta$ -phase adjacent to the  $\sigma$  and  $\gamma$  phases.

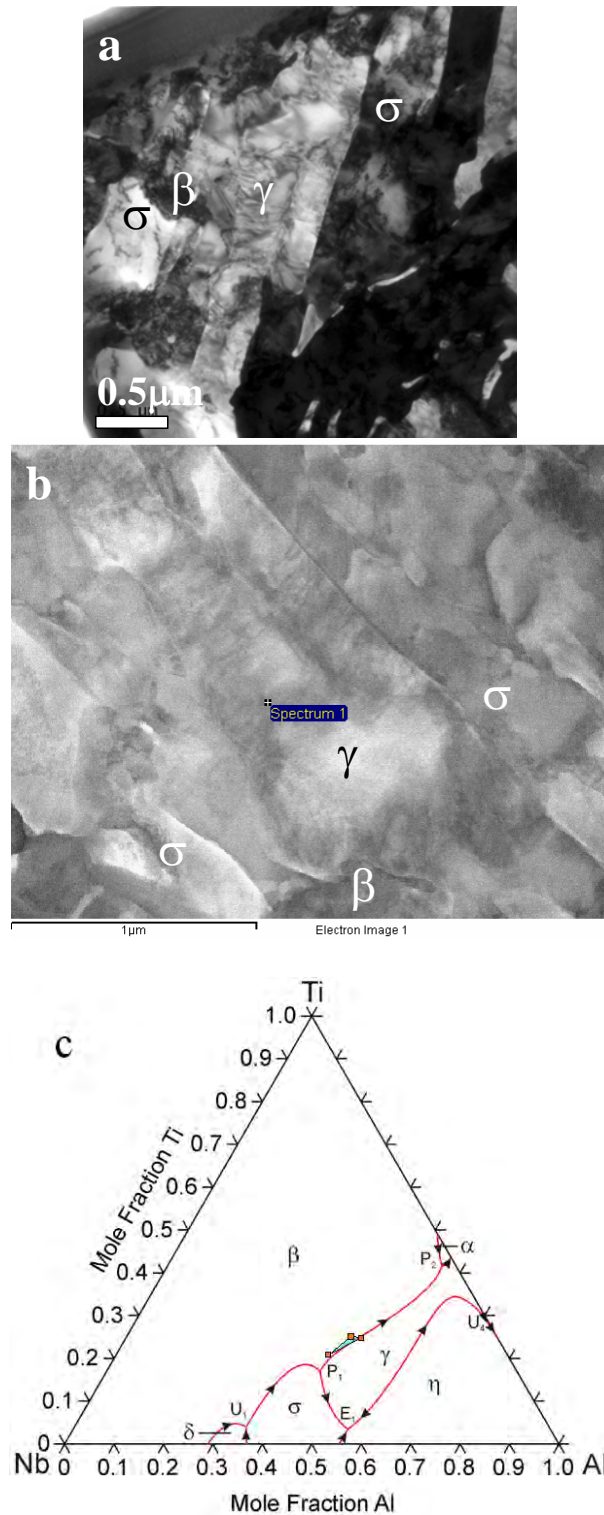


Figure 6-20 TEM micrograph of region 2 showing a) the  $\gamma$ ,  $\sigma$  and  $\beta$  phases b) corresponding STEM image of the same region and c) TEM EDS compositional analysis of the  $\sigma$ ,  $\gamma$  and  $\beta$  phases in region 1 plotted on a calculated liquidus projection.

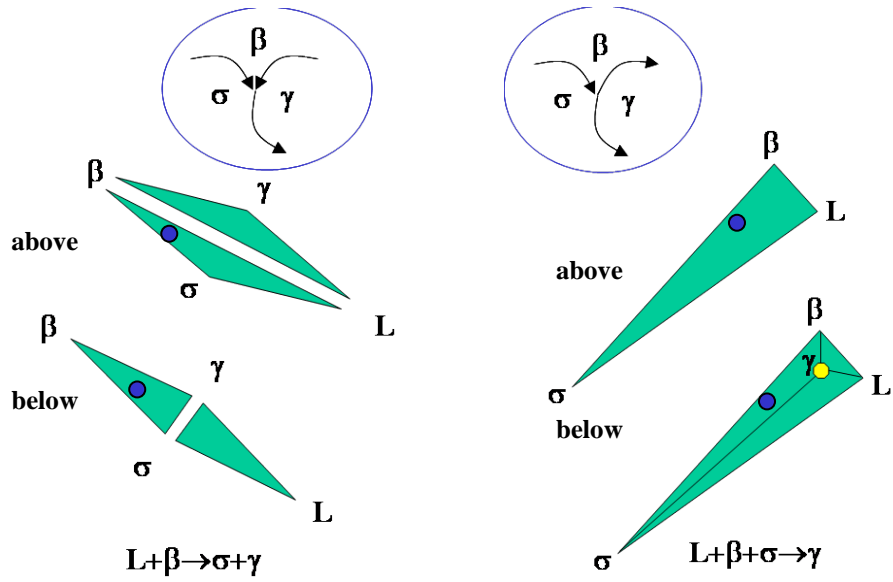


Figure 6-21 Three-phase tie-triangles that react at the invariant temperature shown slightly above and below the reaction shown for the ternary peritectic and transition reactions along with the respective liquidus projections.

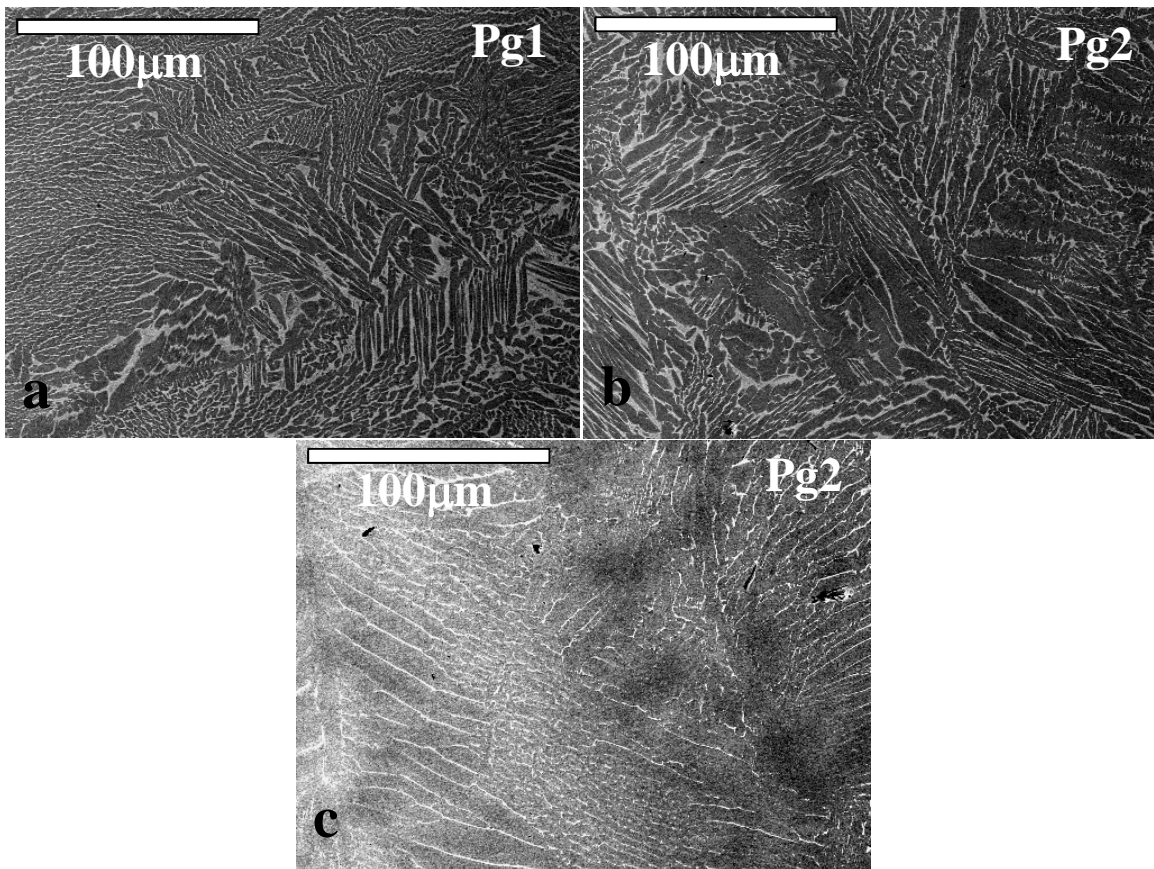


Figure 6-22 SEM micrographs of as-cast alloys a) Pg1 b) Pg2 and c) Pg3.

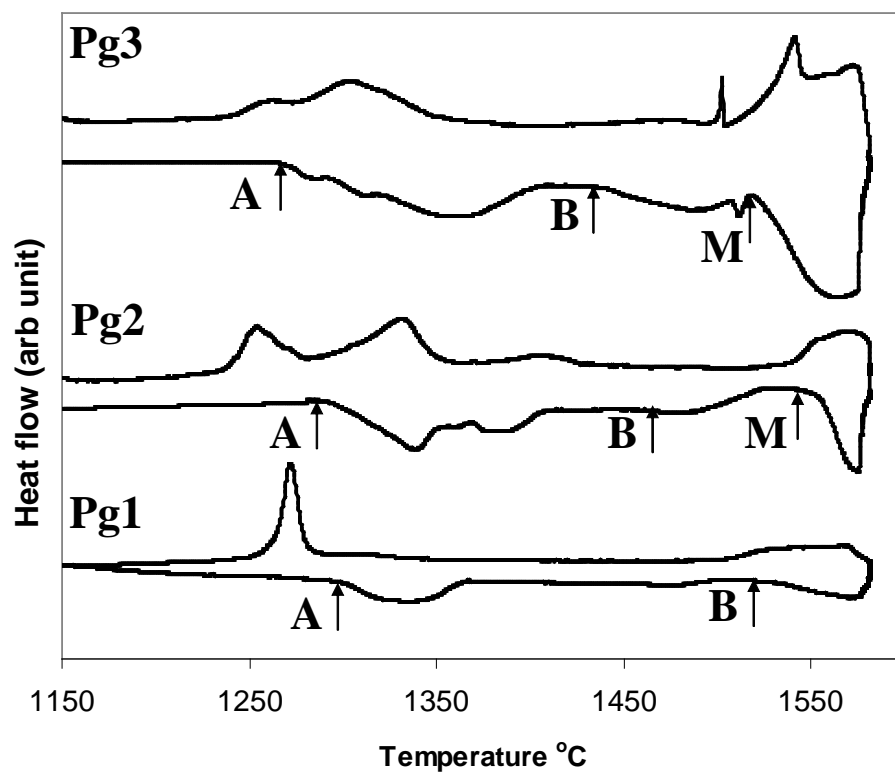


Figure 6-23 DTA curves at 10K/min of thermally cycled alloys Pg1, Pg2 and Pg2 marked with peaks a and b as well as solidus peak M in alloys Pg2 and Pg3.

CHAPTER 7  
HIGH TEMPERATURE EQUILIBRIUM AMONG THE L,  $\gamma$ ,  $\sigma$ ,  $\beta$  PHASES

**7.1 Introduction**

Our work on the L,  $\gamma$ ,  $\sigma$ ,  $\eta$  invariant reaction, the details which were discussed in Chapter 5, revealed a solid-state transformation between the temperatures of 1510C and 1410C. This transformation was linked to a compositional retraction of the  $\gamma$  phase field between 1510C and 1410C as the  $\gamma$ -phase abruptly loses solubility for Nb. The  $\gamma$  corner of the  $\gamma$ ,  $\sigma$ ,  $\eta$  tie-triangle is important to the development of  $\gamma+\sigma$  alloys since it defines the point at which the three-phase field meets the  $\sigma+\gamma$  two-phase field and the  $\gamma$  single phase field. Knowing that the solid-state transformation is linked to the movement of this three-phase equilibrium, an experimental isothermal section at 1510C, which is slightly above the solid-state transformation, was developed.

**7.2 Selection of Alloys**

A series of 9 alloys were designed in conjunction with the L,  $\gamma$ ,  $\sigma$ ,  $\eta$  invariant reaction alloys in order to develop the phase equilibria between the  $\beta$ ,  $\gamma$ ,  $\sigma$  phases. The alloy selection was based on  $\gamma$ ,  $\sigma$ ,  $\eta$  tie-triangle that, on one side, attaches to the  $\gamma+\sigma$  phase field boundaries. This provided guidance to the selection of alloys that exist in the  $\gamma+\sigma$  or  $\gamma+\beta$  two-phase regions at 1510C as well as the somewhat elusive  $\gamma+\sigma+\beta$  three-phase field that connects the latter two.

The bulk alloy compositions of the 9 alloys were measured by EPMA from the as-cast materials using a wide, defocused, 5 $\mu$ m beam. The average of five measurements is given in Table 7-1. These alloys were wrapped in Ta foil and heat-treated at 1510C for 4 hours under an argon atmosphere. The heat-treatment was terminated with a drop quench into a water bath. The samples were then sectioned and prepared via standard metallographic techniques. Details of the

heat-treatment and sample preparation are given in Chapter 3 along with the selection of the 4hr isothermal hold time. Three groups of alloys were formed based on their equilibrium state at 1510C, namely  $\gamma+\sigma$  alloys (A133, A170 and A171),  $\beta+\sigma$  (A120, A134, A139 and A163) alloys and the  $\gamma+\beta+\sigma$  alloy (A132). The thermal, microstructural, and structural behavior of these groups are discussed individually in the following sections.

Table 7-1 The bulk composition of the experimental alloys measured by EPMA

Alloy	Nb at%	Al at%	Ti at%
A133	42.7	42.6	14.7
A170	41.9	41.8	16.3
A171	42.8	44.3	12.8
A132	40.8	40.7	18.5
A138	36.7	29.8	33.5
A120	41.8	36.8	21.3
A134	43.7	35.1	21.2
A139	49.8	30.3	19.8
A163	45.8	32.7	21.5

### 7.3 $\sigma+\gamma$ Equilibrium: Alloys A133, A170, and A171

#### 7.3.1 Evaluation of A133 Alloy

##### 7.3.1.1 Thermal analysis

The transformation temperatures of alloy A133 were examined by DTA of the as-cast thermally cycled material. Due to instrumental limitations it was not possible to melt this alloy fully or obtain any significant information regarding the solidus temperature. In order to determine the equilibrium transformation temperatures the as-cast material was heated to the DTA's maximum temperature of 1600C and held isothermally for 2 hrs before thermal cycling. This was an attempt to remove the microstructural history of the as-cast material, after which three thermal cycles were performed from 1100C to 1600C. The transformation temperatures were recorded from the thermally cycled materials.

Alloy A133's thermally cycled DTA curve is shown in Figure 7-1. Upon heating this curve shows a sharp highly endothermic peak, with a first deviation from the baseline at 1418C that is followed by a shallow, wide peak with a start temperature of 1454C and a return to the baseline at 1565C. On this figure the 1510C heat-treatment temperature is marked with an arrow. This arrow is located within the second wide peak thus associating 1510C with a region of multi-phase stability. Subsequent DTA hold experiments for this alloy are discussed in the experimental section.

### **7.3.1.2 Structural and chemical analyses: as-cast alloys**

Alloy A133's as-cast microstructure varied within the arc melted button. Two types of microstructures were found in the as-cast material, a highly dendritic microstructure near the center to top of the button and a more compositionally homogeneous microstructure near the bottom of the button. The microstructure became more dendritic further from the copper chill. Optical micrographs of chemically etched samples taken from the cross-section of the as-cast materials are shown in Figure 7-2. Figure 7-2a reveal a highly dendritic microstructure, whereas Figure 7-2b shows a more uniform microstructure. There was evidence of a solid-state transformation in both microstructures that were coarser in the interdendritic regions.

SEM-BSE revealed two contrast phases (a low z and high z) in the as-cast microstructure shown Figure 7-3. Again a dendritic structure was evident. The interdendritic regions consisted of a higher volume fraction of the darker contrast phase shown in Figure 7-3a and b. A grain boundary phase was present that was uniformly located along every boundary examined as shown in Figure 7-3 c and d. The grain boundary phase appeared with the same contrast as the bright phase throughout the microstructure. Figure 7-3d reveals that the grain boundary phase provided nucleation sites for the bright contrast phase to grow into the grains. The fact that the light contrast phase forms as a grain boundary phase implies that it nucleated on the prior grain

boundaries of a higher temperature phase. Closer evaluation of the region within the grains indicated that the bright contrast phase's growth consumes the dark contrast phase.

### **7.3.1.3 Structural and chemical analyses: heat-treated alloys at 1510C**

An optical micrograph of etched alloy A133 equilibrated at 1510C is shown in Figure 7-4, which reveals a multi-phase microstructure. X-ray diffraction was performed on a powdered sample prepared from heat-treated alloy A133 shown in Figure 7-4c. The XRD pattern of Alloy A133 was identified to consist of the  $\sigma$  and  $\gamma$  phases, but, as will be demonstrated in Chapter 8, the  $\gamma$ -phase decomposed upon quenching to a  $\gamma$ -phase with slightly different composition and h-phase. Correspondingly, two regions were identified in the optical micrographs shown in Figure 7-4. The  $\sigma$ -phase region appears bright in the optical micrograph, whereas the second region that appears dark provides evidence of a single phase that underwent a solid phase transformation. The morphology of this region was comparable to the microstructure that developed when the  $\gamma$ -phase transforms upon quenching as discussed in Chapter 8 for alloy A2.

Close inspection of the dark contrast phase in Figure 7-4 revealed that at least two different phases formed on a fine scale within the prior phase boundaries. A bright field TEM image of this region is shown in Figure 7-5 with the associated SAD pattern of the  $\gamma$ [111] zone axis, confirming a solid-state transformation of the  $\gamma$ -phase upon quenching. This verified the existence of a prior single  $\gamma$ -phase in equilibrium with the  $\sigma$ -phase. The average compositions of each region were measured by EPMA and are tabulated in Table 7-1. These compositions were used to form a  $\sigma+\gamma$  tie-line.

### **7.3.2 Evaluation of Alloys A170 and A171**

Similar to Alloy A133, structural and chemical analyses were performed on alloys A170 and A171. SEM-BSE micrographs of the alloys equilibrated at 1510C and then quenched are

shown in Figure 7-6, revealing a comparable microstructure to that of alloy A133. In both these alloys a high-z phase that appears bright is in equilibrium with a dark contrast lower-z region that underwent a solid-state transformation upon quenching. The compositions of these regions as evaluated by EPMA are given in Table 7-2 and were used to form a series of  $\sigma+\gamma$  tie-lines.

Table 7-2 The composition of phases equilibrated at 1510C for each alloy.

Alloy	Sigma			Gamma			Beta		
	Nb at%	Al at%	Ti at%	Nb at%	Al at%	Ti at%	Nb at%	Al at%	Ti at%
A133	48.1	40.3	11.5	38.5	45	16.5			
A170	47.9	39.6	12.5	37.3	43.8	18.9			
A171	48.8	41.6	9.7	39.8	46.4	13.8			
A132	47.4	38.4	14.3	37	42.3	20.7	37.6	41.2	21.2
A120	47.5	36	16.4				38.4	38.2	23.4
A134	48.4	34.5	17.1				40.1	36.4	23.6
A139	52.1	31.7	16.2				46.7	28.6	24.7
A163	50	33.4	16.6				42.7	32.5	24.9

## 7.4 $\gamma+\beta+\sigma$ Equilibrium: Alloy 132

### 7.4.1 Thermal Analysis

A DTA curve of thermally cycled alloy A132 is shown in Figure 7-7. Upon heating a single wide endothermic peak with an onset temperature of 1385C persisted up to 1553C. Alloy A132's thermal behavior differed from that of alloy A133 in that there was the absence of a sharp exothermic peak prior to the wide peak hinting at a difference in the nucleation mechanism. The heat-treatment temperature of 1510C falls within the wide endothermic peak suggesting a multiphase equilibrium existed in this state.

### 7.4.2 Microstructural and Chemical Analyses

As shown in Figure 7-8, X-ray diffraction of powdered alloy A132 showed the presence of two phases, namely the  $\sigma$  and  $\gamma$  phases. However, optical and SEM/BSE micrographs revealed that alloy A132 equilibrated at 1510C consists of three phases. Optical microscopy of the heat-

treated materials, that are shown in Figure 7-9, revealed three distinct phases based on their morphology, hence suggesting the possibility of a three-phase equilibrium as marked on the figure. Similar to the previously reported alloys, the  $\sigma$ -phase that appears bright did not show any evidence of a solid-state transformation upon quenching. The region adjacent to this phase, marked as the  $\gamma$ -phase, shows clear evidence of a solid-state transformation upon quenching. Finally there is the bright phase located in the center of the  $\gamma$ -phase region marked as the  $\beta$ -phase, which clearly shows a different morphology than the  $\sigma$ -phase. This phase is believed to be the  $\beta$ -phase, which showed concaved shape boundaries suggesting that it was consumed by the  $\gamma$ -phase. However, the  $\sigma$ -phase boundary has a convex shape, indicating that this phase grew into another phase.

The presence of three phases at 1510C in Alloy A132 was further established by investigating the compositional differences in the three regions detected on the optical micrographs. The three regions of interest are marked as the  $\sigma$ ,  $\gamma$  and  $\beta$  phases. The  $\beta$ -phase region showed a fine transformed microstructure with at least two compositionally different microconstituents. The  $\sigma$  and  $\beta$  phase were found to be compositionally homogenous. The results of the EPMA analysis as listed in Table 7-2 confirmed three significantly different composition phases. The composition of the bright contrast phase in Figure 7-9 is chemically located near the  $\sigma$ -phase boundary extrapolated from the analysis of alloys A133, A170 and A171. Both the  $\gamma$  and  $\beta$  phases are chemically located near the extrapolated  $\gamma$ -phase field boundary and their compositions are close to each other. Measurements taken from many different locations consistently revealed two separate compositions for  $\gamma$  and  $\beta$  phase regions indicating that at 1510C they existed as separate phases in equilibrium.

In order to examine the nature of the  $\gamma$ -phase region a site specific FIB TEM foil was prepared. A bright field TEM micrograph of the region is shown in Figure 7-10 revealing a fine scale two microconstituent microstructure. EDS compositional analysis of the microconstituents revealed the  $\gamma$ -phase had transformed into two separate compositions Nb32.4 Al48.0 Ti19.6 and Nb42.4 Al37.7 Ti19.9 marked on Figure 7-10. The  $\beta$ -phase region was also compositionally located within the just mention bounds yet it did not transform. This phenomenon confirms that the structure of the  $\gamma$ -phase region prior to quenching was different from that of the  $\beta$ -phase region prior to quenching. This combination of microstructural, compositional and structural evidence was considered to be sufficient to accept the three-phase tie-triangle between the  $\sigma$ ,  $\gamma$  and  $\beta$  phases.

## 7.5 $\sigma$ + $\beta$ Alloys

### 7.5.1 Thermal Analysis

The transformation temperatures of alloys A120 A134 A139 and A138 were examined by DTA of the as-cast cycled materials shown in Figure 7-11 a, b, c and d, respectively. The solidus temperature was above 1600C in this series of alloys as melting did not occur. In order to determine the equilibrium transformation temperatures, the as-cast material was heated to the DTA's maximum temperature of 1600C. After a 2hr isothermal hold, thermal cycling was performed in an attempt to remove the microstructural history of the as-cast materials. Finally, three thermal cycles were performed from below the solid-state transformations up to 1600C.

Each alloy exhibited one or more endothermic peaks upon heating of the cycled materials. A higher temperature wide shallow peak was evident in all the alloys. The onset temperature of this peak was 1310C, 1361C, 1362C, and 1416C for alloys A120 A134 A139 and A138 respectively. The heat-treatment temperature of 1510C is marked in each DTA curve. With the

exception of A138, in each alloy, 1510C falls within the higher temperature peak. At 1510C alloy A138 is near the temperature where this peak ends and returns to the baseline.

### 7.5.2 Microstructural and Chemical Analysis

As expected alloy A138 was found to exist as a single phase at high temperatures as shown in Figure 7-12a. The SEM-BSE micrographs divulge some evidence of incomplete solutionizing however, overall there was little to no variation in the back scattered electron yield throughout the sample. The combination of thermal analysis and microstructural evaluations was correlated to a  $\beta$ -phase transus of 1526C.

Optical microscopy of alloy A134 shown in Figure 7-13a revealed a two-phase microstructure. Powder XRD of the heat-treated materials identified the presence of the  $\sigma$  and  $\gamma$  phases (Figure 7-13d). One key difference that exist between the this curve and the XRD of alloy A133 is the disappearance of the  $\gamma(310)$  peak. A similar effect was noticed in alloy A11 when it was quenched from the  $\beta$ -phase field with the  $\gamma$ -phase forming upon quenching of the metastable  $\beta$ -phase [77]. Simulations revealed that the  $\gamma(310)$  peak increases by a factor of 5 when Nb is randomly substituted into the Ti and Al sites in the TiAl structure. The loss of reflected intensity from the  $\gamma(310)$  in alloys that undergo a  $\beta$  to  $\gamma$  transformation upon quenching may be inherited from the disordered distribution of elements in the high-temperature  $\beta$  BCC phase.

SEM-BSE of alloy A134 shown in Figure 7-13b and c revealed a bright and dark contrast region. The bright contrast phase is marked as the  $\sigma$ -phase and the dark contrast phase is marked as the  $\beta$ -phase. The dark phase provided evidence of a solid-state transformation upon quenching that formed a fine two-phase structure. The EPMA compositional evaluation of each phase is listed in Table 7-2.

Parallel compositional analysis was performed on heat-treated alloys A120, A139 and A163 in order to form a series of  $\sigma+\beta$  tie-lines thus defining this two-phase region in the composition ranges of interest. SEM-BSE micrographs of these alloys are shown in Figure 7-14 and Figure 7-15 with the pertinent phases marked with  $\sigma$  or  $\gamma$  phase. The compositions of these phases as evaluated by EPMA are listed in Table 7-2.

It should be noted that alloy A139 (Figure 7-14c and d) showed two different contrast in the  $\beta$ -phase region. Extensive EPMA and EDS showed no compositional difference on either contrast phase within the prior  $\beta$ -phase region. The contrast mechanism thus originated from the formation of a compositionally equal yet less dense phase through a solid-state transformation. In Chapter 4 it was shown that the  $\beta$ -phase transforms to the  $\gamma$ -phase upon quenching. In alloy A139 it is possible that some of the  $\beta$ -phase transformed upon quenching that causes two separate contrast in Figure 7-14c and d.

## 7.6 Summary

A series of 9 alloys were developed in order to investigate the high-temperature equilibrium between the  $\beta$ ,  $\sigma$  and  $\gamma$  phases in the Al-Ti-Nb. The compositional boundaries of the multi-phase equilibrium were determined through a series of tie-lines and a tie-triangle. The compositions of the series of  $\beta+\sigma$  and  $\gamma+\sigma$  tie-lines listed in Table 7-2 along with the  $\beta+\sigma+\gamma$  tie-triangle are plotted on a 1510C isothermal section of our optimized phase diagram (Figure 7-16). Generally there is an excellent agreement with calculations and experimental evaluations. Slight differences were seen in the location and span of the  $\beta+\sigma+\gamma$  tie-triangle. In Chapter 4 it was established that the high-temperature  $\beta$ -phase transforms to the  $\gamma$ -phase upon quenching. This rapid transformation, however, did not allow sufficient time for long range diffusion to take place.

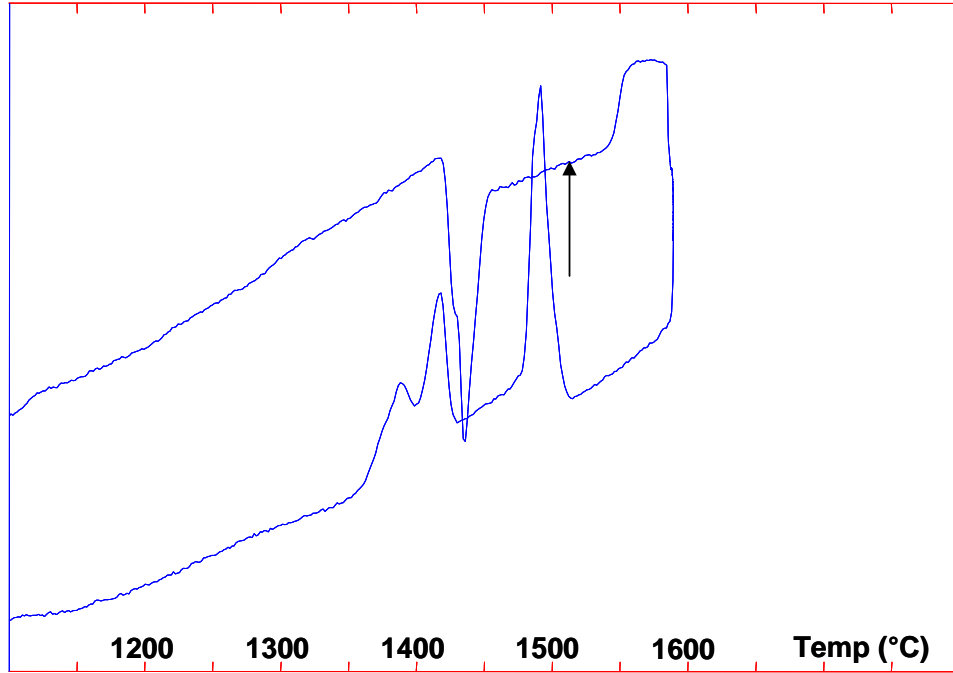


Figure 7-1 DTA of thermally cycled alloy A133 at 10K/min marked with the 1510C heat-treatment temperature.

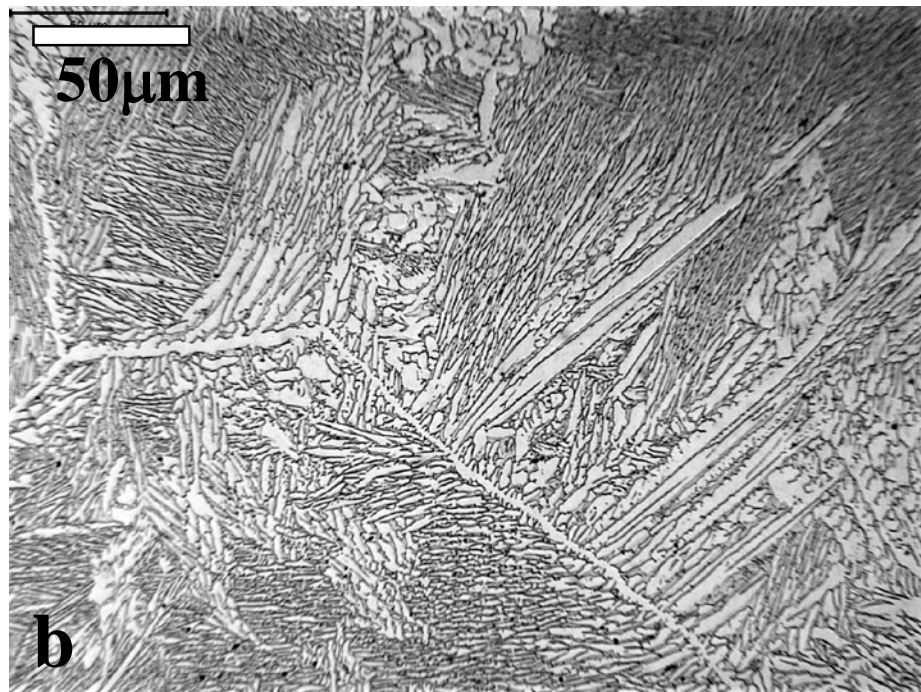
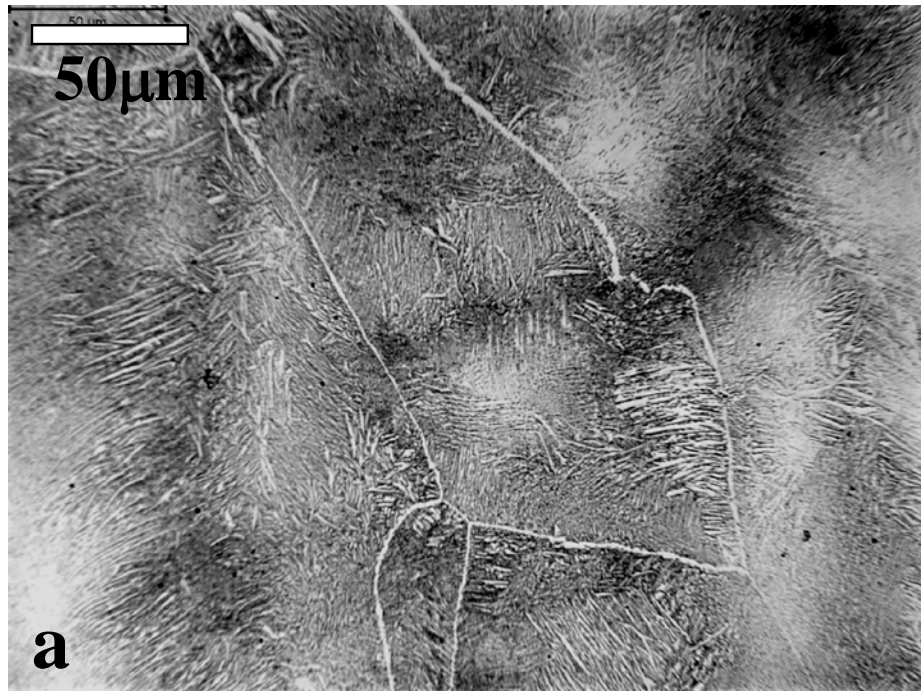


Figure 7-2 Optical micrographs of as-cast alloy A133 showing a) a dendritic structure and grain boundaries and b) a more uniform structure near the copper chill centered on the grain boundaries within the uniform region.

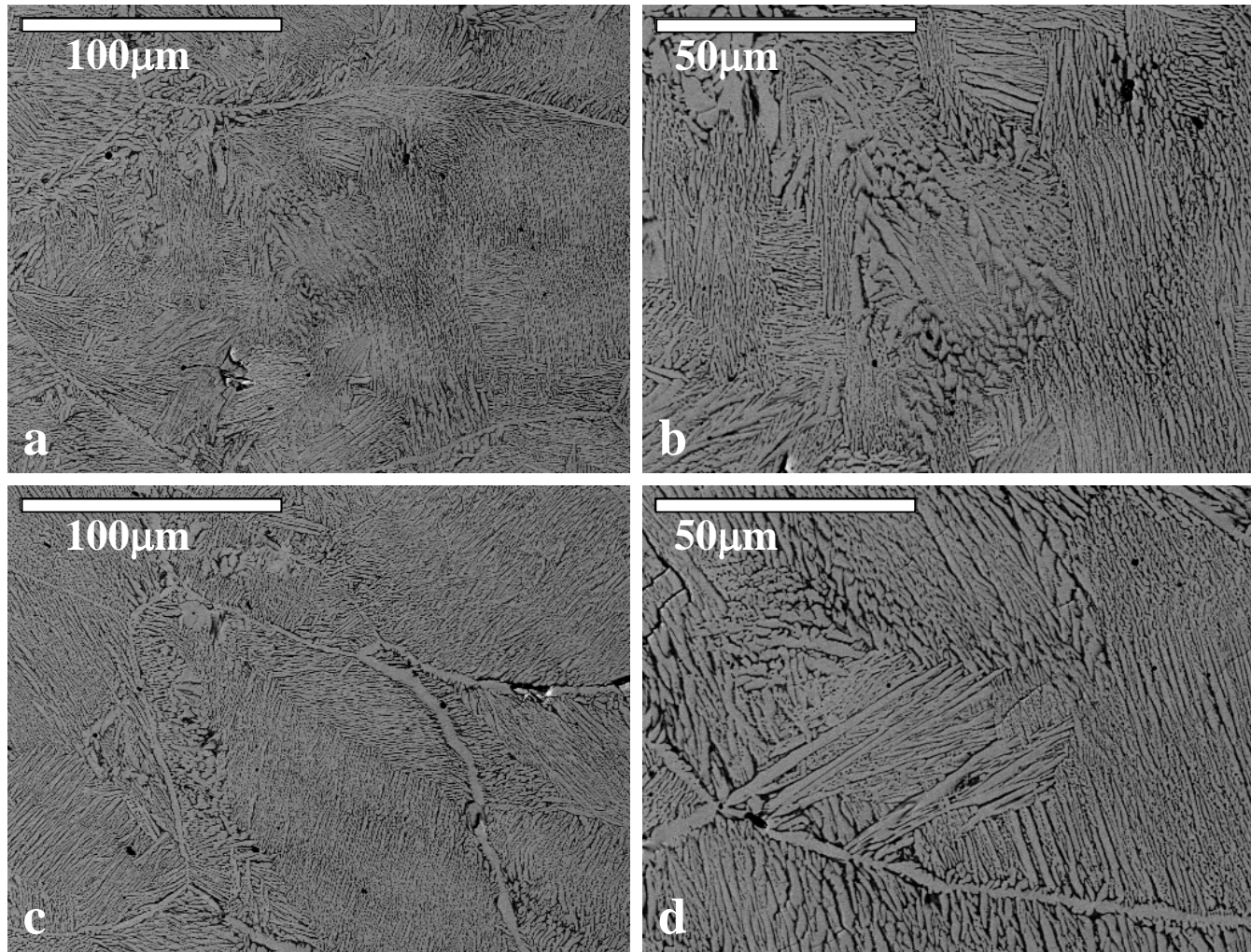


Figure 7-3 SEM micrographs of as-cast alloy A133 showing a) a dendritic structure and b) higher magnification of the dendritic structure while in the micrographs are c) centered around the grain boundary phase and d) higher magnification showing phase that nucleates at the grain boundaries.

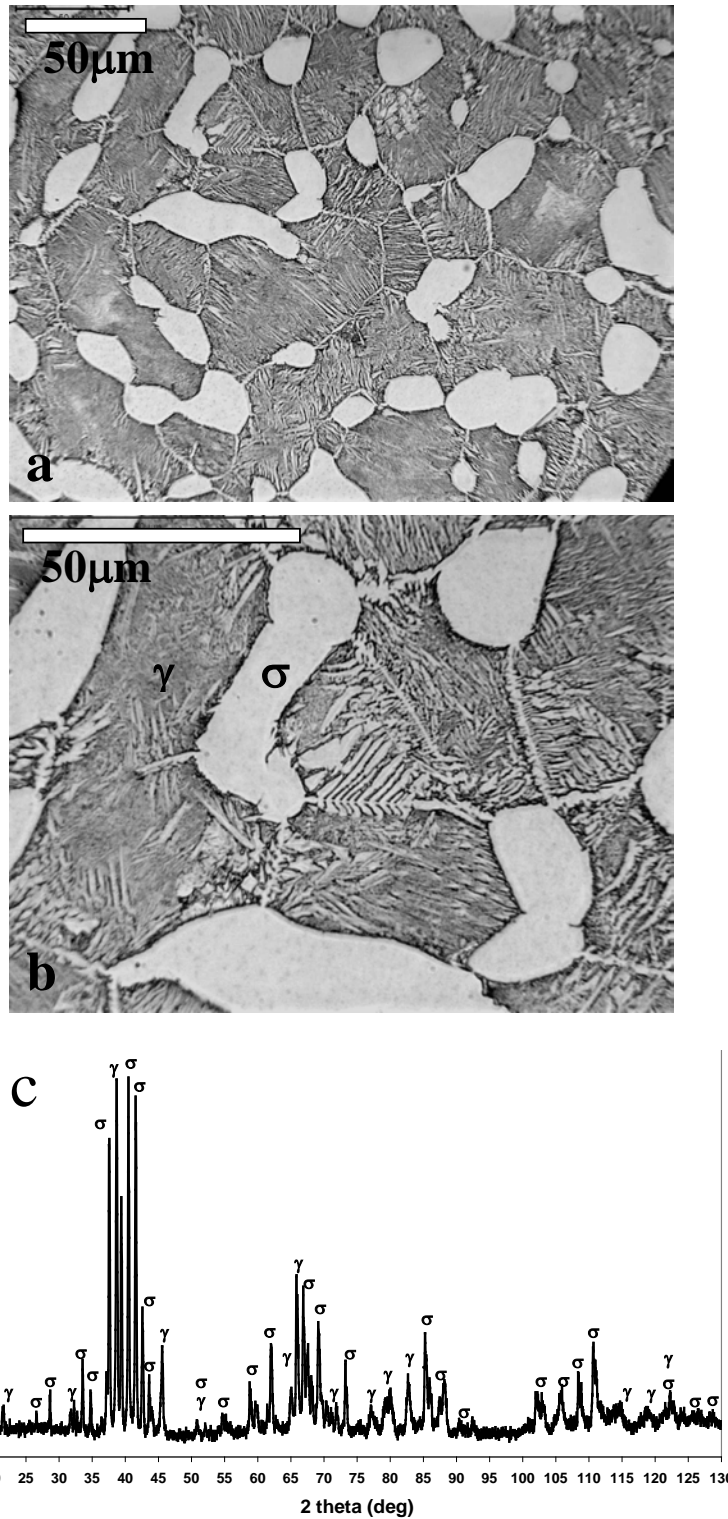


Figure 7-4 Optical micrographs and XRD of alloy A133 heat-treated at 1510C showing a) the overall microstructure, b) higher magnification marked with the  $\sigma$  and  $\gamma$  phases, and c) XRD profile of alloy A133 identifying the  $\sigma$  and  $\gamma$  phases.

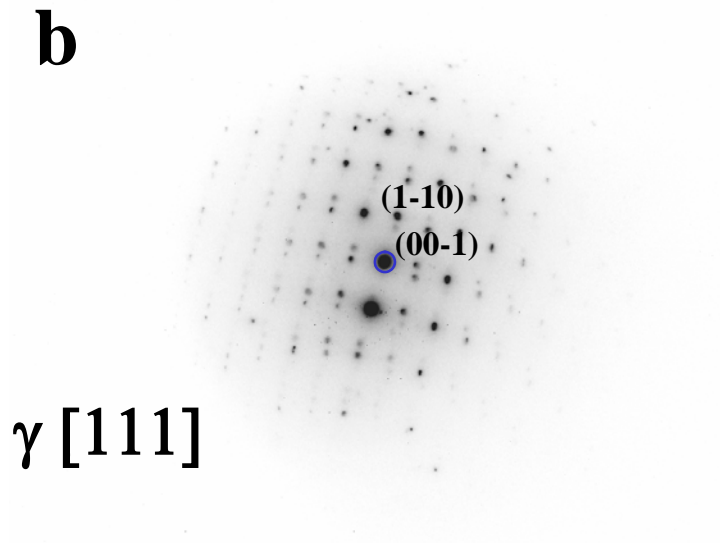
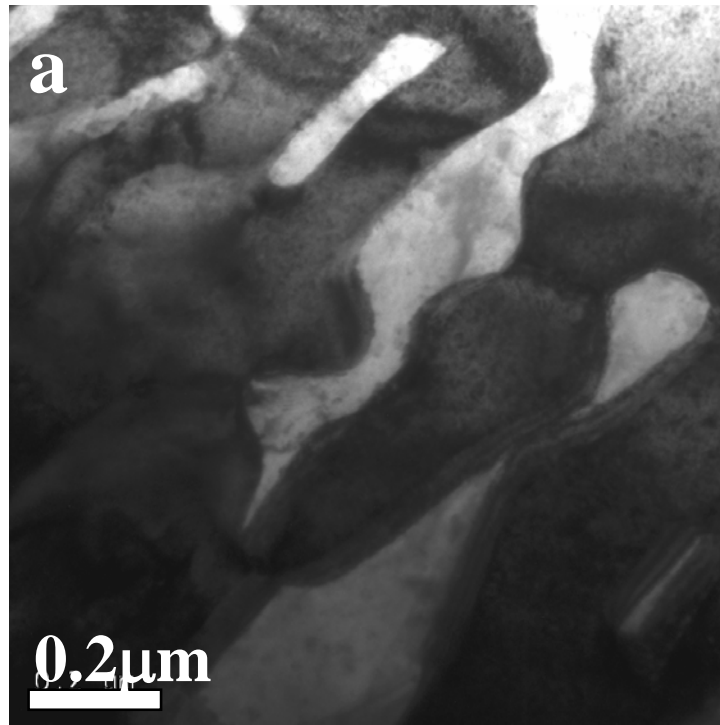


Figure 7-5 a) A bright field TEM micrograph centered on the  $\gamma$ -phase in alloy A133 heat-treated at 1510C and b) the corresponding SAD pattern.

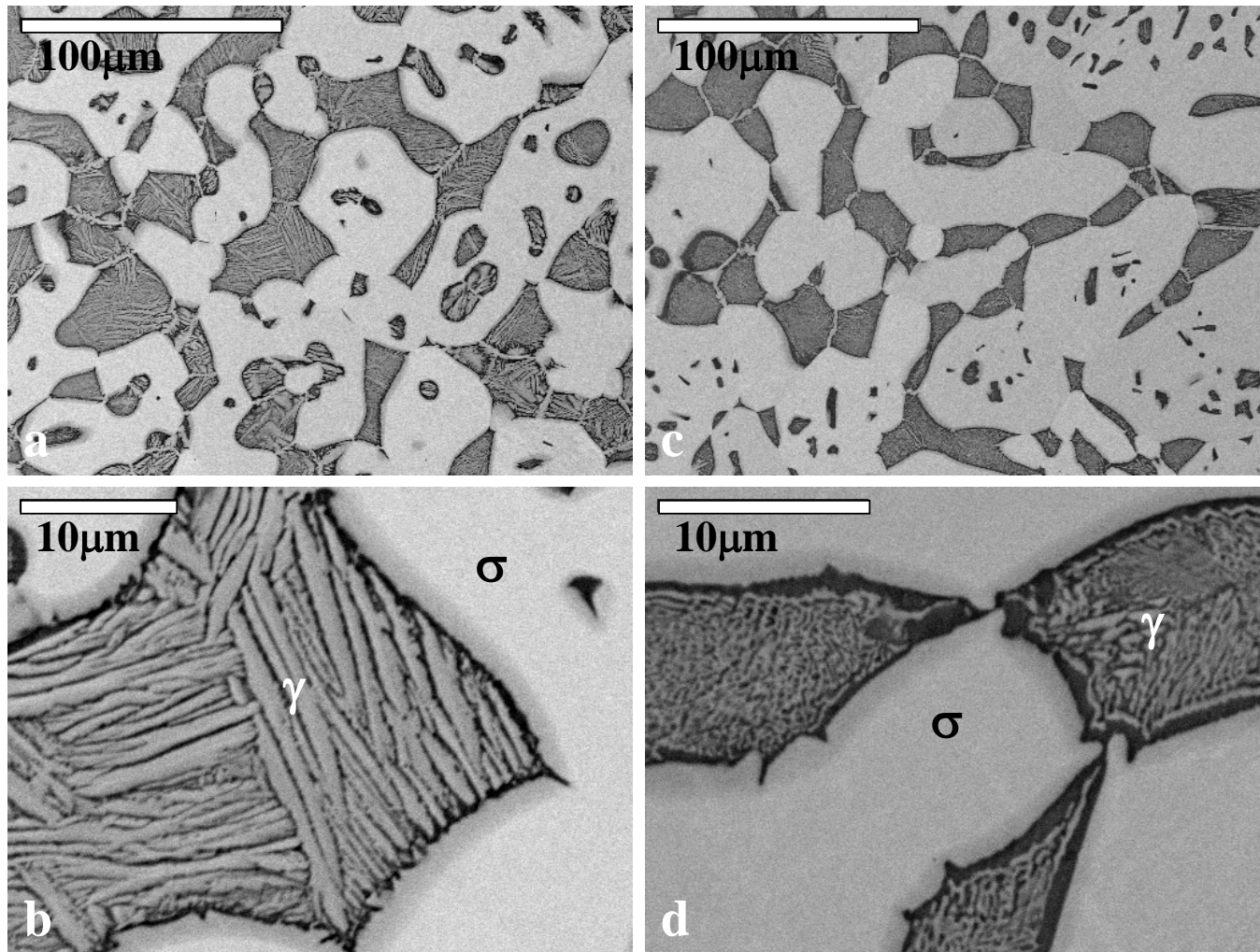


Figure 7-6 SEM micrographs of alloys heat-treated at 1510C showing a) the overall microstructure of alloy A170, b) higher magnification of (a) marked with the  $\sigma$  and  $\gamma$  phases, c) the overall microstructure of alloy A171 and d) higher magnification of (c) marked with the  $\sigma$  and  $\gamma$  phases.

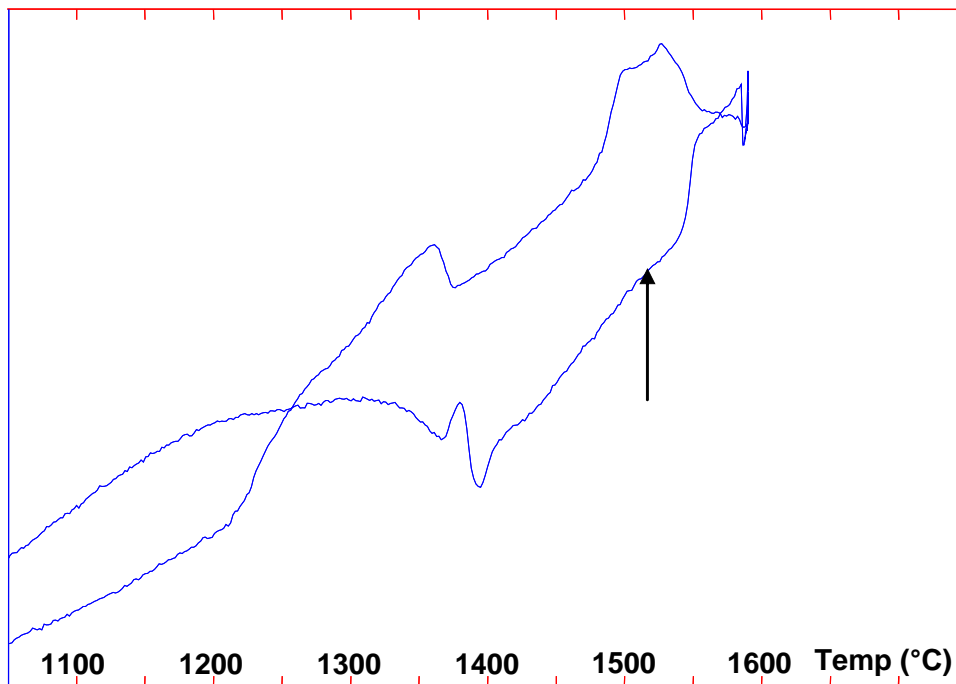


Figure 7-7 DTA of thermally cycled alloy A132 at 10K/min marked with the 1510C heat-treatment temperature.

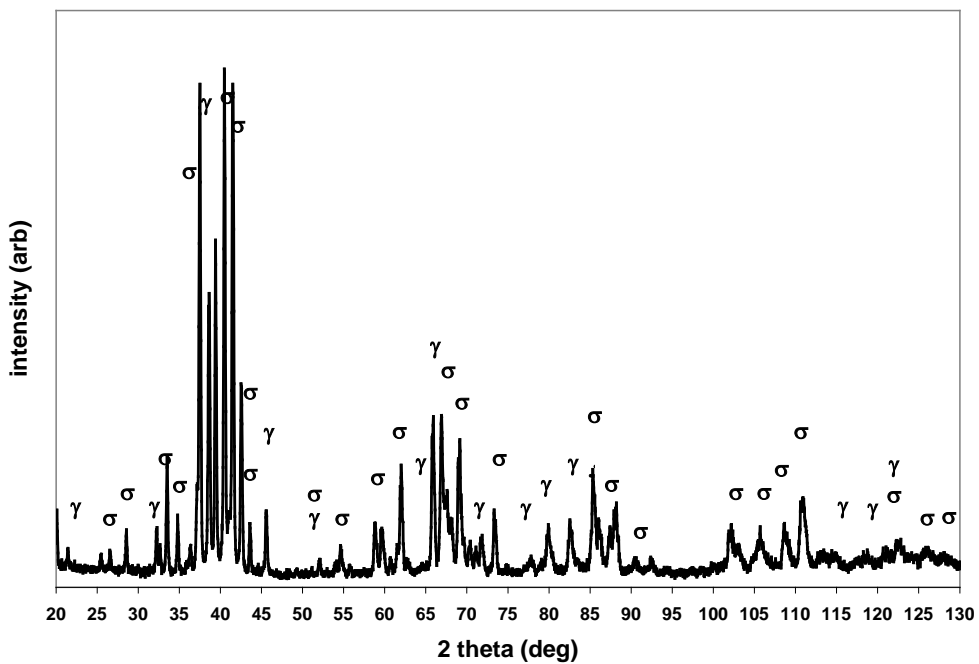


Figure 7-8 XRD profile of alloy A132 heat-treated at 1510C identifying the  $\sigma$  and  $\gamma$  phases.

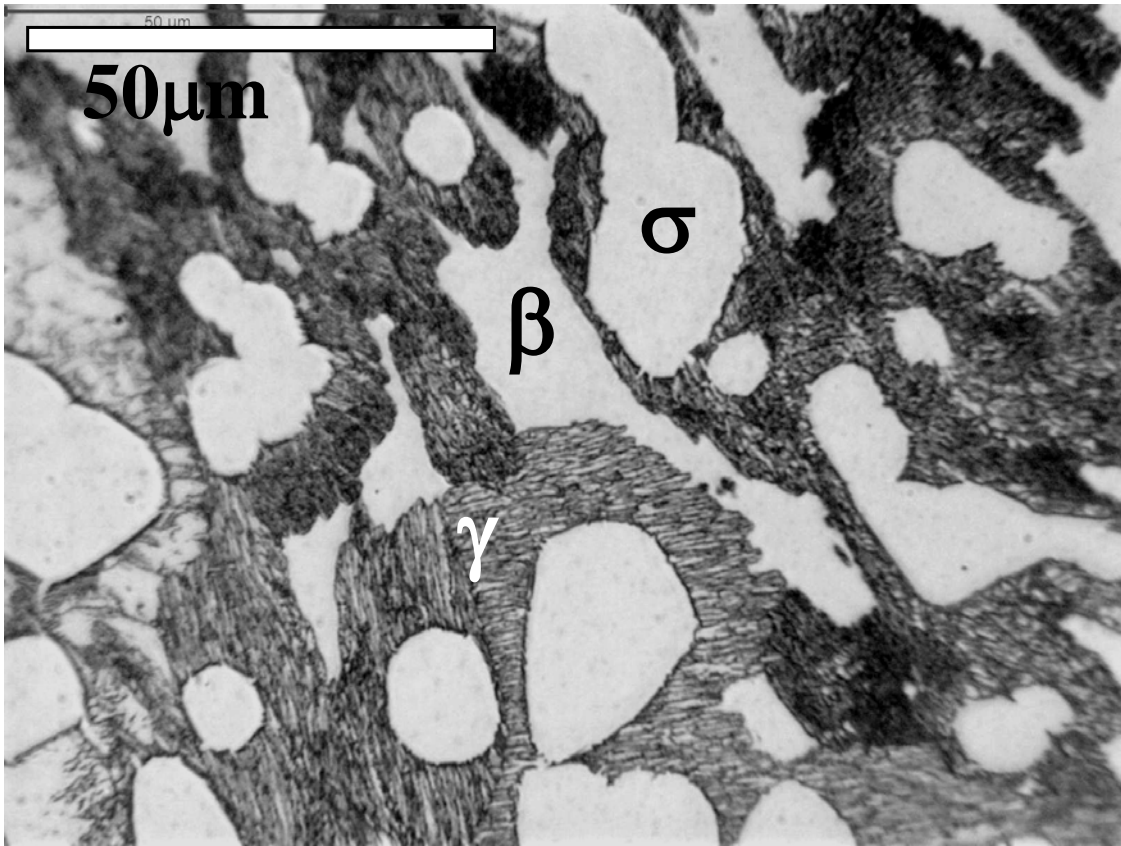


Figure 7-9 Optical micrograph of alloy A132 heat-treated at 1510C showing the overall microstructure in which the  $\gamma$ ,  $\sigma$  and  $\beta$  phases are marked.

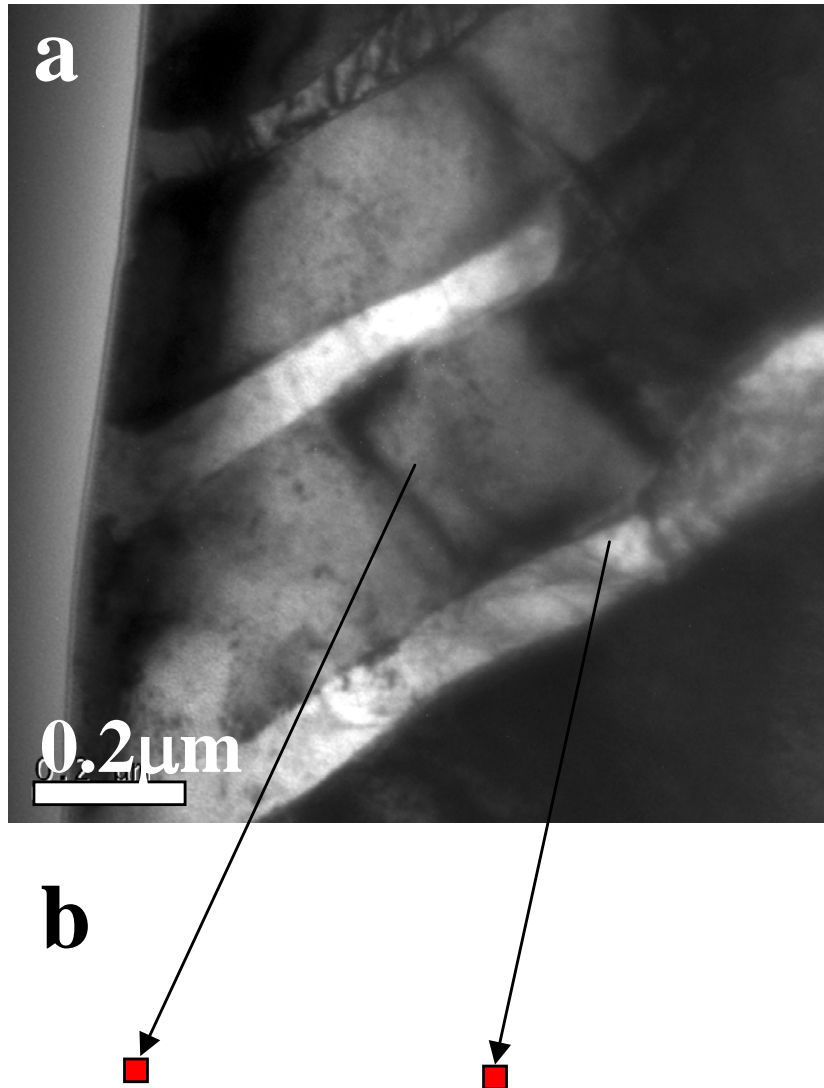


Figure 7-10 BF-TEM micrograph of alloy A132 heat-treated and quenched from 1510C showing a) the transformed  $\gamma$ -phase and b) TEM EDS compositional analysis of the phases that form upon quenching along with the bulk compositions of the  $\beta$ ,  $\sigma$  and  $\gamma$  phases.

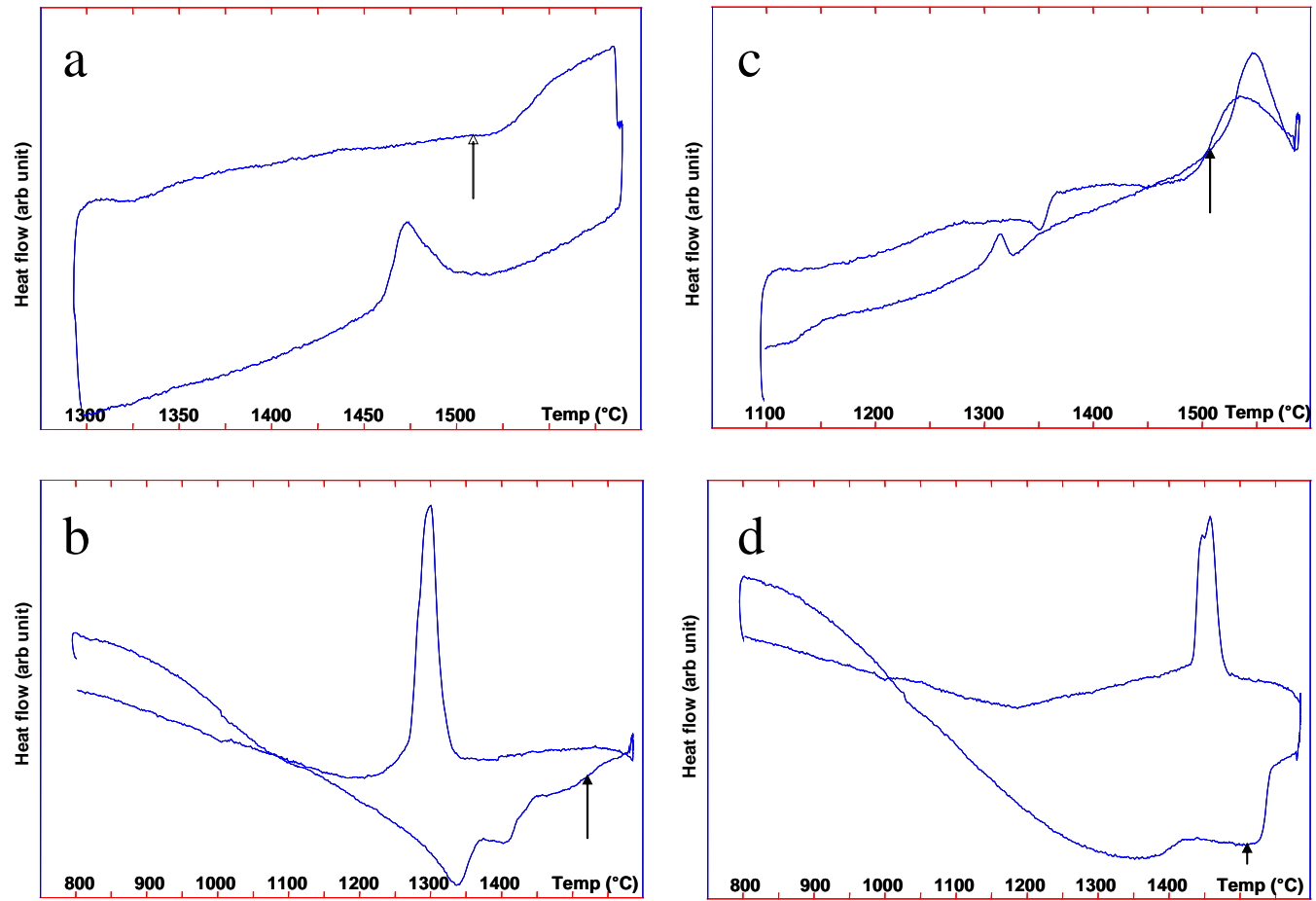


Figure 7-11 DTA at 10K/min of thermally cycled alloy a) A120 b) A134 c) 138 and d) A139. The arrow indicates the 1510C heat-treatment temperature.

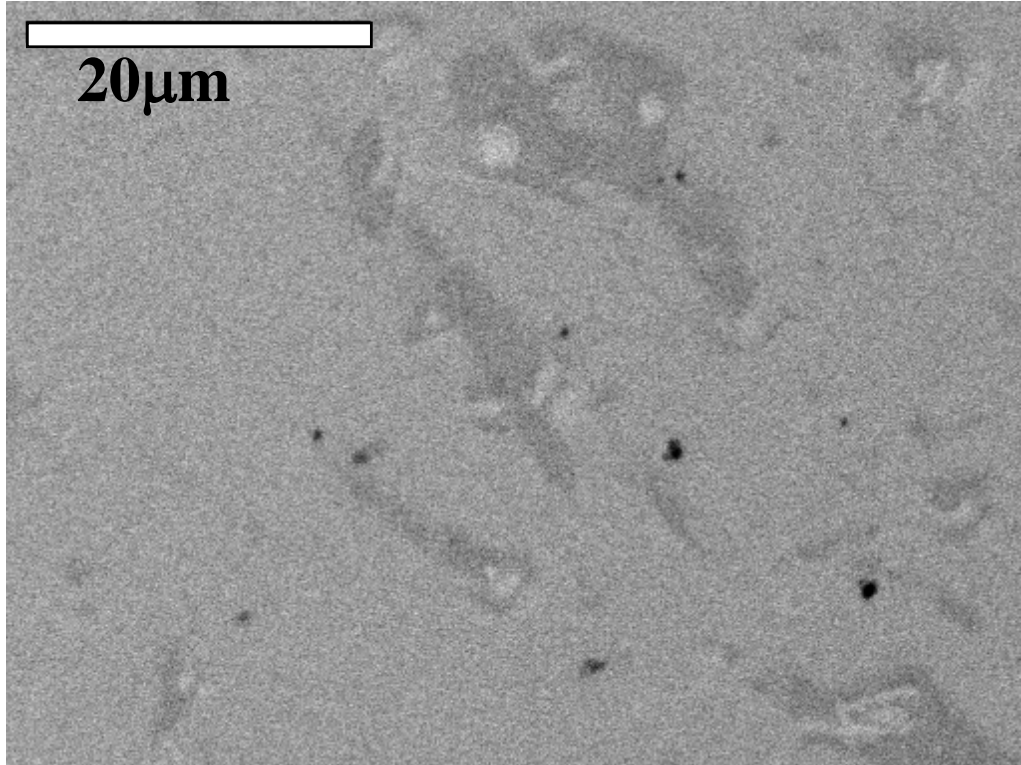


Figure 7-12 SEM micrographs of alloy A138 heat-treated at 1510C.

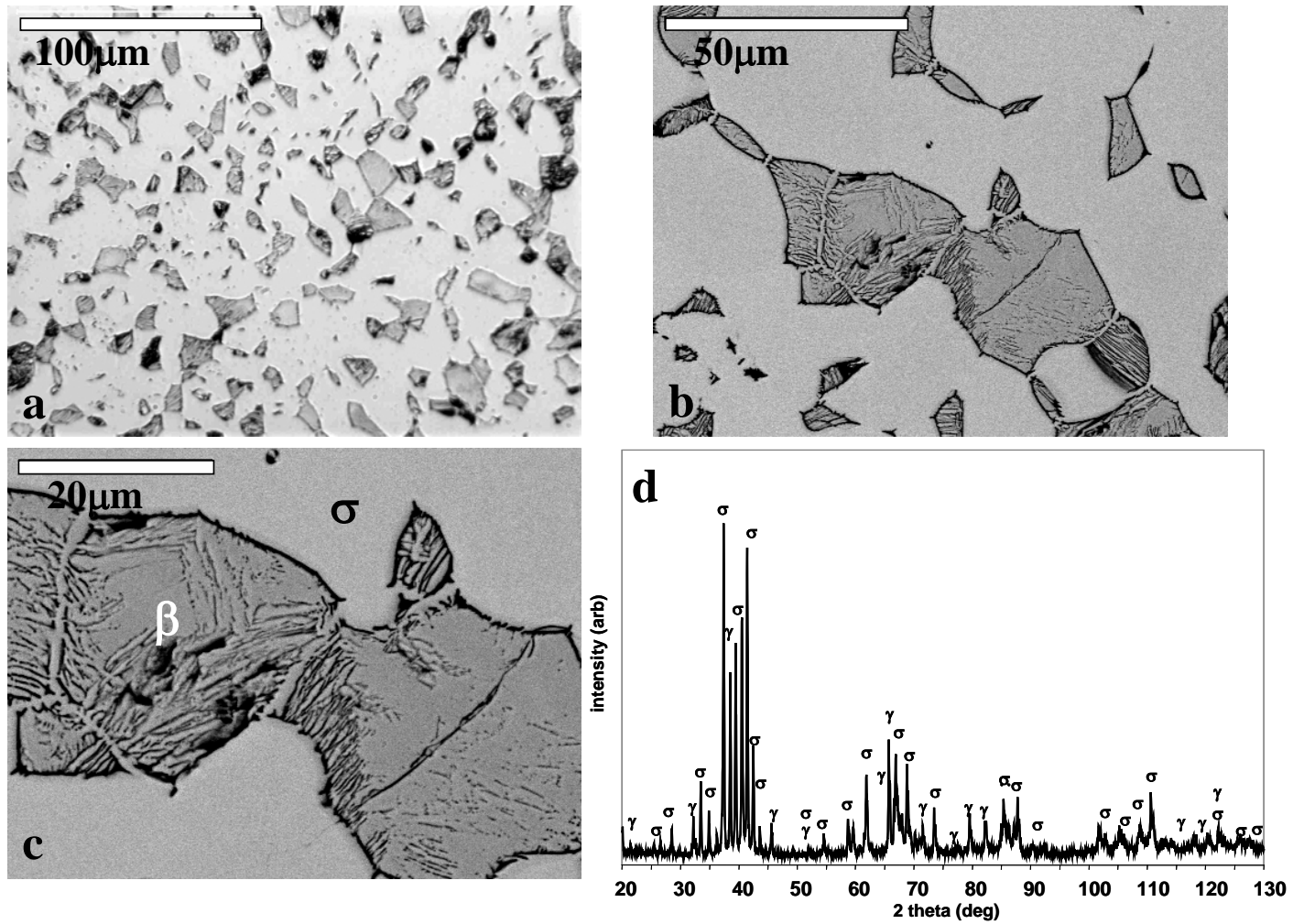


Figure 7-13 Alloy A134 heat-treated at 1510C that shows a) optical micrographs of two phases, b) SEM micrograph of overall two phase region, c) higher magnification SEM with  $\sigma$  and  $\beta$  phases marked, and d) XRD profile identifying the presence of the  $\sigma$  and  $\gamma$  phases.

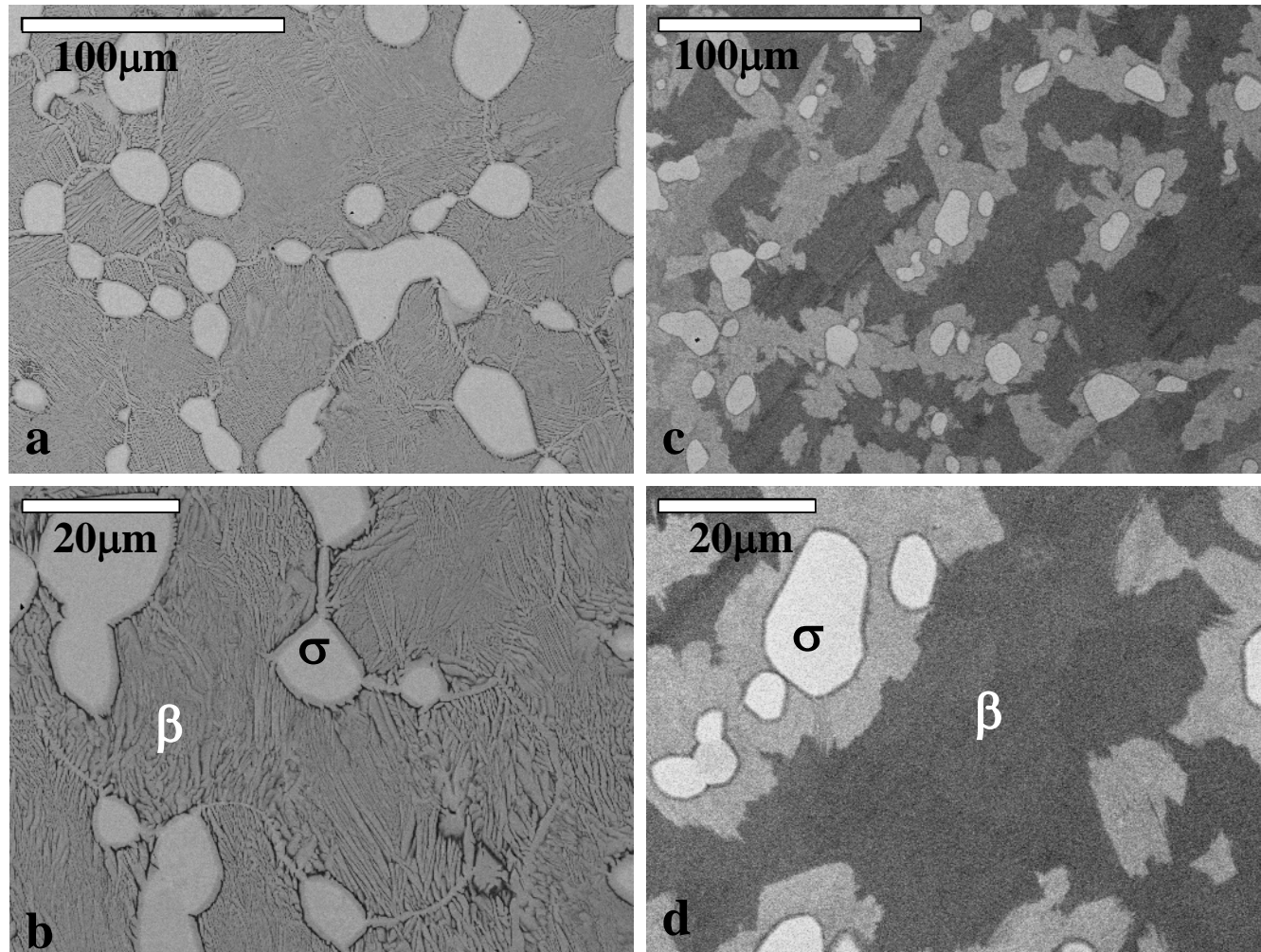


Figure 7-14 SEM micrographs of alloys heat-treated at 1510C showing a) the overall microstructure of alloy A120, b) higher magnification of (a) marked with the  $\sigma$  and  $\gamma$  phases, c) the overall microstructure of alloy A139, and d) higher magnification of (c) marked with the  $\sigma$  and  $\gamma$  phases.

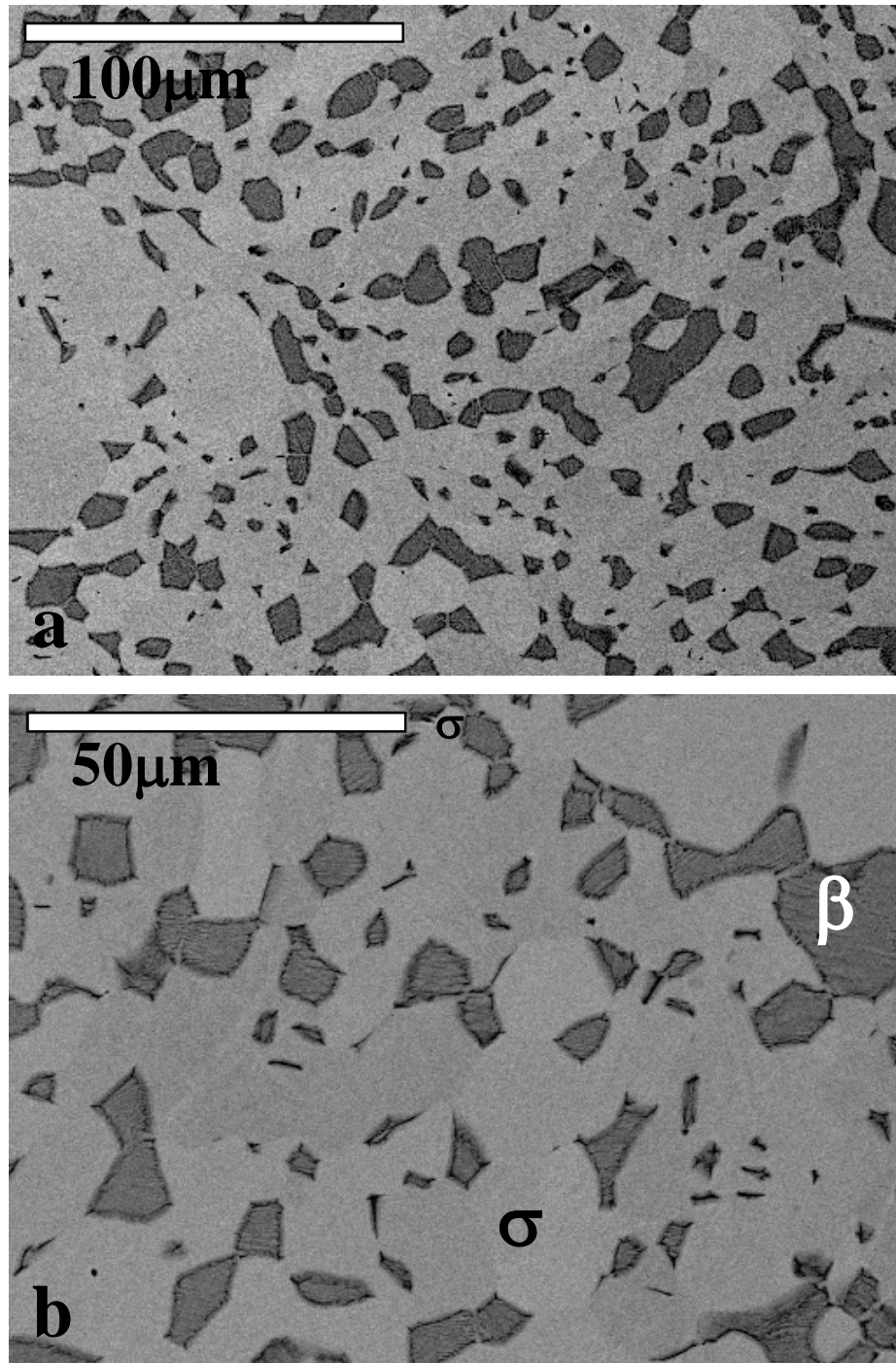


Figure 7-15 SEM micrographs of alloy A163 heat-treated at 1510C showing a) the overall microstructure and b) a higher magnification micrograph marked with the  $\sigma$  and  $\beta$  phases.

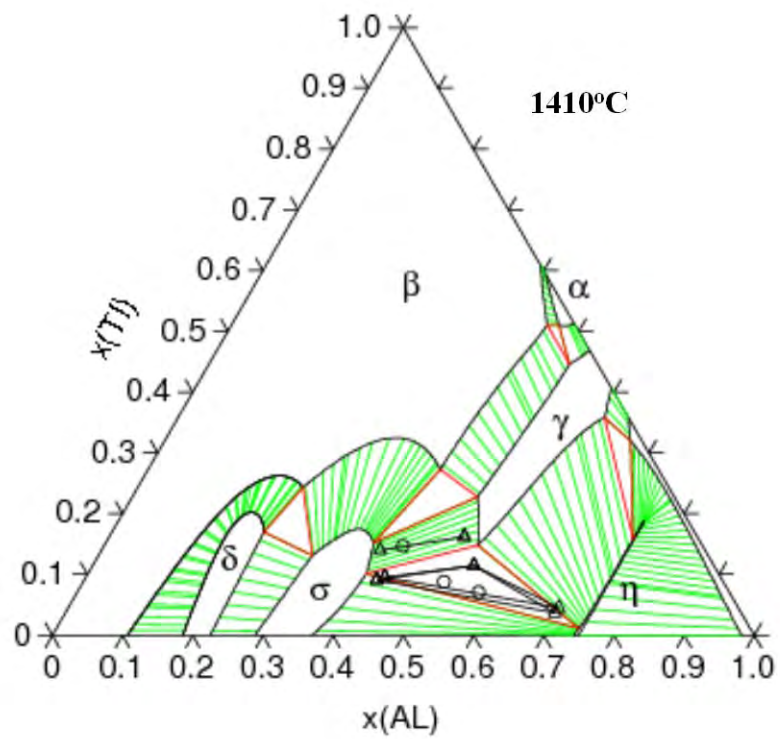
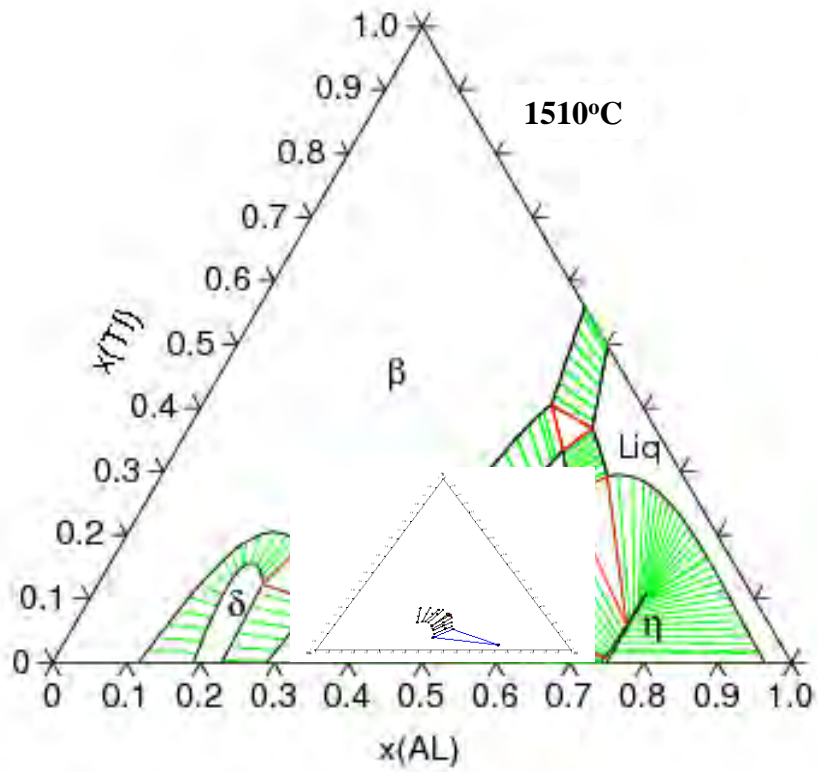


Figure 7-16 Calculated isothermal sections at a) 1510C and b) 1410C marked with the experimental data obtained from the respective heat-treatments.

## CHAPTER 8 TRANSFORMATION OF THE $\gamma$ -PHASE UPON QUENCHING

### 8.1 Introduction

The results presented in Chapter 5 revealed that the  $\gamma$ -phase in equilibrium at 1510C was not stable upon quenching to room temperature. It was shown that the  $\gamma$ -phase has extensive solubility for Nb at temperatures above 1510C that decreases drastically within a 100C window. The details of the retraction of the  $\gamma$ -phase field are shown graphically in Figure 5-11. The phase transformation of the  $\gamma$ -phase upon quenching from 1510C resulted in an ultra-fine multiphase structure that was of interest. This chapter discusses the transformational changes in the  $\gamma$ -phase when the formation of equilibrium phases is kinetically inhibited. Literature reviews did not disclose any reported structural transformations in ternary high Nb containing  $\gamma$ -phase alloys. In the Ti-Al binary system, however, several references reported two metastable structures, that form upon the quenching of the off-stoichiometry TiAl, namely the  $\text{Al}_2\text{Ti}$  (h-phase) and  $\text{Al}_5\text{Ti}_3$  phase [42, 43]. Both of these phases are superstructures that form by the reordering of Al atoms to form layers on particular lattice sites of the TiAl  $L1_0$  structure. Among other possibilities these structures were used as comparative starting point for consideration in the identification of the phases within the transformed  $\gamma$ -phase boundaries found in this study.

### 8.2 Microstructural Evaluation

Alloy A2 in the heat-treated and quenched from 1510C condition was selected for evaluating the  $\gamma$ -phase transformation. This is the same material and heat-treatment used in the development of the L,  $\gamma$ ,  $\sigma$ ,  $\eta$  invariant reaction discussed in Chapter 5. In this alloy quenching from the  $\gamma$ ,  $\sigma$ ,  $\eta$  three-phase region forced the  $\gamma$ -phase to undergo a solid-state transformation. An SEM micrograph centered on the transformed  $\gamma$ -phase is shown in Figure 8-1. The  $\sigma$  and  $\eta$

phases also marked on this micrograph. Close observation of the prior  $\gamma$ -phase boundary revealed a dark contrast phase that seemed to grow into the  $\gamma$ -phase. In addition to the material within the  $\gamma$ -phase, the interfacial region was also investigated.

To further investigate the structure and composition of the microconstituent phases within the transformed region, TEM analysis was employed. A 15 $\mu\text{m}$  wide site specific TEM foil was prepared from alloy A2. The marker on Figure 8-1 shows the location of the TEM sample made using FIB. The sample was selected to consist mostly of the transformed  $\gamma$ -phase region while cutting through the  $\sigma/\gamma$  interface and include a small region of the  $\sigma$ -phase

A typical bright field STEM image is shown in Figure 8-2a. Two contrast phases are revealed within the prior  $\gamma$ -phase boundary, a bright and dark contrast phase that are adjacent to a third contrast phase ( $\sigma$ -phase). Higher magnification bright and dark field STEM images of this region that includes both prior  $\gamma$ -phase and the  $\sigma$ -phase across the  $\sigma/\gamma$  interface are shown in Figure 8-2c and d. High Angle Annular Dark Field imaging was employed to facilitate z-contrast based images by the acquisition of only incoherently scattered electrons. The  $\sigma$ -phase produced a uniform contrast throughout the region indicating little to no compositional variation in this phase. The transformed  $\gamma$ -phase region conversely showed two distinct phase contrasts suggesting a compositional difference between the two phases that formed from the prior  $\gamma$ -phase. This observation is indicative of a diffusional solid-state transformation. These phases are labeled as 1 or 2 on both the bright and dark field images shown in Figure 8-2.

The dark contrast phase in bright field was located at the  $\sigma/\gamma$  interface as well as throughout the transformed  $\gamma$ -phase marked with “1” in Figure 8-2c and d. This phase was observed on every  $\sigma/\gamma$  interface essentially encasing the transformed  $\gamma$ -phase region. Dark field

imaging of this phase revealed that it was the higher z-phase. A bright contrast phase was seen in the interior of the transformed  $\gamma$ -phase region that is marked with a 2. Within the interior the region the two phases existed adjacent to each other to form a “wormy” like morphology.

### 8.3 Compositional Analysis

Dark field STEM imaging provided supporting evidence that the two contrast phases were compositionally distinct. EPMA measurements revealed that the bulk composition of the prior  $\gamma$ -phase on both alloy A1 and A2 was 40.0Nb 47.5Al 12.2Ti at%. The details of the bulk compositional analysis were discussed in Chapter 5. TEM EDS was used to further investigate the compositions of the individual phases. A bright field STEM image of one of the regions examined by TEM EDS is shown in Figure 8-3a.

The EDS analysis revealed that the bulk composition was made up of two statistically distinct compositions. The composition of region “2” was determined to be 31.2Nb 57.2Al 11.6Ti at% while the region “1” contained 45.2Nb 43.9Al 10.9Ti.at%. These compositions are marked on a ternary plot showing the  $\sigma$  and  $\eta$  phases in equilibrium the  $\gamma$ -phase at 1510C and 1410C (Figure 8-3b). This set of tie-triangles was developed in Chapter 5 from both alloys A1 and A2. The bulk composition of the transformed phase is represented by the  $\gamma$  corner of the 1510C tie-triangle. It was determined that the high-temperature  $\gamma$ -phase that existed as a stable phase at 1510C decomposes into two composition phases. The examination revealed that the bright phase (region “2”) rejected sufficient Nb for Al bringing its composition near the  $\gamma$ -phase’s equilibrium composition below the solid-state transformation. The lower z phase in region “2” is compositionally located near the  $\sigma$ -phase corner of the 1410C tie-triangle. In the studies conducted here as well as the work of group members it has been shown that the nucleation of the  $\sigma$ -phase is difficult therefore it is unlikely that it nucleated out of the  $\gamma$ -phase

upon quenching. The dark contrast phase is suspect to be a metastable phase that forms upon quenching.

#### 8.4 Structural Analysis

Structural analysis was performed by recording SAD patterns of phases individually as well as two adjacent phases simultaneously. Two SAD patterns near the zone axis of each phase are shown in Figure 8-4. The analysis of the diffraction patterns revealed that two structurally distinct phases existed in the microstructure. The gamma phase was identified through the analysis of the diffraction patterns. A diffraction pattern near the  $\gamma[110]$  zone axis is shown in Figure 8-4a. The second phase was determined not to be the  $\gamma$ -phase.

Inspection of the diffraction patterns of the second phase near its zone axis revealed that the lattice parameter of this phase is close to triple that of the  $\gamma$ -phase (Figure 8-4b). Among many phases considered there is evidence in the literature of a metastable orthorhombic  $\text{Al}_2\text{Ti}$  phase that forms in the binary  $\text{TiAl}$  system upon quenching the  $\gamma$ -phase [42, 43, 81].

Morphological similarities were found between the h-phase within the  $\text{TiAl}$  matrix and the  $\gamma$ -phase transformation observed in this study. A structural model shown in Figure 8-5a and b was generated using the Crystal Maker software package from the reported structural data for both the  $\text{TiAl}$  [40, 48] and  $\text{Al}_2\text{Ti}$  phases [43]. The details of these structures are discussed in Chapter 2. The  $\text{Al}_2\text{Ti}$  phase is a super lattice that forms by ordering of the Al atoms on the (100) and (002) planes of the  $\text{TiAl}$   $L1_0$  structure thus its lattice parameter is inherent to that of parent  $\gamma$ -phase. Essentially the h-phase contains two lattice parameters that are equal to those of the  $\gamma$ -phase and a third parameter that is three times  $L1_0$ 's length. Investigation of the diffraction patterns shown in Figure 8-4b and Figure 8-6 revealed the second phase within the transformed

$\gamma$ -phase boundary is indeed the h-phase. A diffraction pattern near the h[001] zone axis confirmed the large lattice parameter supporting the orthorhombic super lattice structure.

The acquisition of SAD patterns individually from each phase was possible in the FE-TEM (Figure 8-4), however; the implementation of a very small aperture decreased the transmitted beam intensity excessively. A larger aperture in the conventional TEM was employed for diffraction contrast based imaging. This aperture roughly covered 2 to 3 phase boundaries simultaneously. A diffraction pattern taken near the  $\gamma$ [110] zone axis and slightly off the h[001] zone axis is shown in Figure 8-6a. Several diffracting planes from each phase are marked on this figure. The  $\gamma$ [110] zone axis is nearly parallel to the h[001] zone axis while there is a  $35^\circ$  rotation between  $\gamma$ -phase's (00-1) and the h-phase's (020) planes. The relative orientation of the two crystals are shown in Figure 8-5c and d, where the models are positioned such that they are representative of the measured orientations.

The foil was tilted slightly in order to reach a two beam condition off the  $\gamma$ [110] zone axis. This diffraction pattern was recorded and is shown in Figure 8-6b. The  $\gamma$ (-110) diffracted beam and the h(1-10) diffracted beams shown on this zone axis were used for dark field imaging of each phase. The transmitted beam shown in Figure 8-6b was used for bright field imaging. Low and high magnification bright field images are shown in Figure 8-7a and b. These micrographs show bright and dark contrast phases both that have a similar morphology. The bright contrast phase is continuous while the dark contrast phase in every observed instance is isolated by the bright phase best seen in Figure 8-7a.

Dark field imaging using the  $\gamma$ -phase's (-110) diffracted beam are shown in Figure 8-7c and d. This identifies the location of the  $\gamma$ -phase in the microstructure. Using the h-phase's (-1-10) diffracted beam, dark field images of approximately the same area were taken that are shown

in Figure 8-7 e and f. This analysis was combined with STEM imaging and compositional analysis to correlate phase identification with the measured composition of each phase. The  $\gamma$ -phase shown in Figure 8-7 was determined to be the dark phase in bright field STEM imaging that is marked with a 1 in Figure 8-2. The composition of the  $\gamma$ -phase is identified as 31.2Nb 57.2Al 11.6Ti at%. The darker contrast phase in STEM imaging is identified as the h-phase that has a composition of 45.2Nb 43.9Al 10.9Ti.at%.

### 8.5 Discussion

In alloy Al quenching from 1510C caused a solid-state transformation in the  $\gamma$ -phase, whereas a 1410C heat-treatment and quenching of the same alloy resulted in no detectable structural changes in the gamma phase. DTA results presented in Chapter 5 disclosed significant heat evolution or absorption between these two temperatures indicating a compositional and volume fraction change. TEM/STEM analyses revealed that during the transformation upon quenching from 1510C two phases identified as  $\gamma$  and h phases evolve. The composition the  $\gamma$ -phase attained upon quenching was 31.2Nb 57.2Al 11.6Ti at% and it was close to the equilibrium composition of this phase found in the microstructure equilibrated at 1410C. This is shown in Figure 8-2c where now region 1 has been identified as the  $\gamma$ -phase.

The h-phase, that showed a dark contrast in the STEM image, exhibited a composition of 45.2Nb 43.9Al 10.9Ti.at%. Based on the composition measured, assuming Ti only sits in Ti sites and Al only sits in Al sites in the  $Al_2Ti$ , in the ternary system, approximately 66% of Ti sites are filled with Nb atoms, whereas only 33% of the Al sites are occupied by Nb atoms. This indicates that Nb is preferentially sitting in the Ti lattice positions. Apparently the  $\gamma$ -phase has a high solubility for Nb at elevated temperatures that drastically decreases with temperature. When the formation of  $\sigma$  and  $\eta$  phases are inhibited by water quenching, the metastable  $\gamma$ -phase releases its

Nb by undergoing a spinodal decomposition. The significant change in the solubility of Nb in the  $\gamma$ -phase upon cooling is identified as the component driving this transformation.

The morphology of the  $\gamma$  and h phases suggested a coupled growth mechanism. Microstructural evidence also provided evidence that the  $\gamma$ -phase underwent a spinodal decomposition. The morphology of the h-phase that could be described as appearing wormy when viewed in a 2 dimensional cross-section. The characteristic spacing between the phases of under 200nm scale suggests that nucleation was not the rate limiting mechanism. This spacing is also consistent with a slightly coarsened spinodal decomposition [82, 83]. Observation of the interface between the  $\sigma$ -phase and the transformed  $\gamma$ -phase region revealed that the h-phase covered the boundary. Compositional analysis revealed that the h-phase is a Nb rich phase therefore it is logical that it is found adjacent to the high Nb  $\sigma$ -phase. In contrast near the Al rich  $\eta$ -phase boundaries the h-phase was not observed. This further confirms that this phase forms by diffusion of Al and Nb.

In the observed microstructure the orientation relationship is such that many coincidence sites exist between the two phases yet perfect alignment of the crystals was not found. The coincidence sites are shown in Figure 8-5 c and d and are marked with a series of circles. The h-phase is suggested to form on the coincidence sites with minor lattice shifts and grows by diffusion thus resulting in a three dimensional morphology typical of a spinodal decomposition [83]. The instability of this microstructure under high intensity of the electron beam prevented high resolution TEM, therefore it was not possible to take lattice images of the phase boundaries.

## **8.6 Thermal Stability of the Quenched Materials**

In the process of conducting TEM on the transformed  $\gamma$ -phase it was observed that this microstructure is highly unstable. In the TEM, it is common to select different size incident

beams by varying the strength of the 1<sup>st</sup> condenser lens. This is accomplished through the adjustment of the “spot size”. During the process of performing bright field imaging it is common to switch between spot size 1, 2 and 3. In imaging the transformed  $\gamma$ -phase region the sample was subjected to spot size 1, during which a phase transformation was observed to take place in situ. The spot size was immediately decreased to spot size 2 that stopped the transformation. After that a diffraction pattern was recorded. This procedure was repeated a second time and a third diffraction pattern was recorded.

The diffraction pattern of the untransformed material prior to exposure to the higher intensity electron beam is shown in Figure 8-8a. Both the  $h$  and  $\gamma$  phases were identified in their [001] and [110] zone axes, respectively. After approximately 2 minutes of exposure to spot size 1 a second diffraction pattern was recorded. The  $\gamma$ [021] and  $\eta$ [110] zone axes were found to exist indicating the precipitation of the  $\eta$  phase and the dissolution of the  $h$  phase (Figure 8-8b). A final 2 minute exposure to the high intensity electron beam resulted in coarsening of the  $\eta$ -phase while consuming the majority of the microstructure (Figure 8-8c).

The bulk composition of the high-temperature  $\gamma$ -phase at low temperatures should, under equilibrium conditions, exist as a two-phase region, namely the  $\sigma$ + $\gamma$  two-phase region. It has been shown that the  $\sigma$ -phase has difficulties nucleating, therefore  $\eta$ -phase alone forms. The two phase  $\gamma$ + $h$  microstructure that is unstable at low temperatures transforms under e-beam excitation to the  $\eta$ -phase thus lowering the free energy of the system. A similar transformation of the binary  $Al_2Ti$   $h$ -phase has been reported in the literature [42]. In the binary system, however, long term heat-treatments at 900C are required to precipitate out the  $\eta$ -phase [42]. The highly unstable ternary alloy studied here, in contrast, undergoes a structural change under the generally mild excitation of the electron beam.

## 8.7 Summary

In Chapter 5 it was shown that the  $\gamma$ -phase field retracts significantly by rejecting Nb into the  $\sigma$ -phase. This retraction was most drastic in between the temperatures of 1510C and 1410C. The retraction of the  $\gamma$ -phase was linked to instability during quenching from 1510C, conversely water quenching the sample directly from 1410C resulted in no major structural changes within the  $\gamma$ -phase. The high temperature  $\gamma$ -phase was found to compositionally separate by a spinodal decomposition to a lower Nb content  $\gamma$ -phase phase and a high Nb ternary h-phase based on the  $\text{Al}_2\text{Ti}$  structure. The h-phase is a super lattice that forms by the ordering of atoms on specific planes on the  $\text{L1}_0$  structure. The driving force for the  $\gamma$ -phase to transform was linked to the drastic decrease in the solubility of Nb in this phase at high temperatures. This transformation brought the composition of the  $\gamma$ -phase near its equilibrium value at 1410C. The wormy morphology of the h-phase within the  $\gamma$ -phase confirms that h-phase formed through a spinodal decomposition. The orientation relationship between the phases is such that the h-phase and  $\gamma$ -phase lined up on coincidence sites. High resolution TEM was not possible due to the instability of the transformed  $\gamma$ -phase region. It was also shown that this region when excited by a high density e-beam transforms to more thermodynamically stable phases.

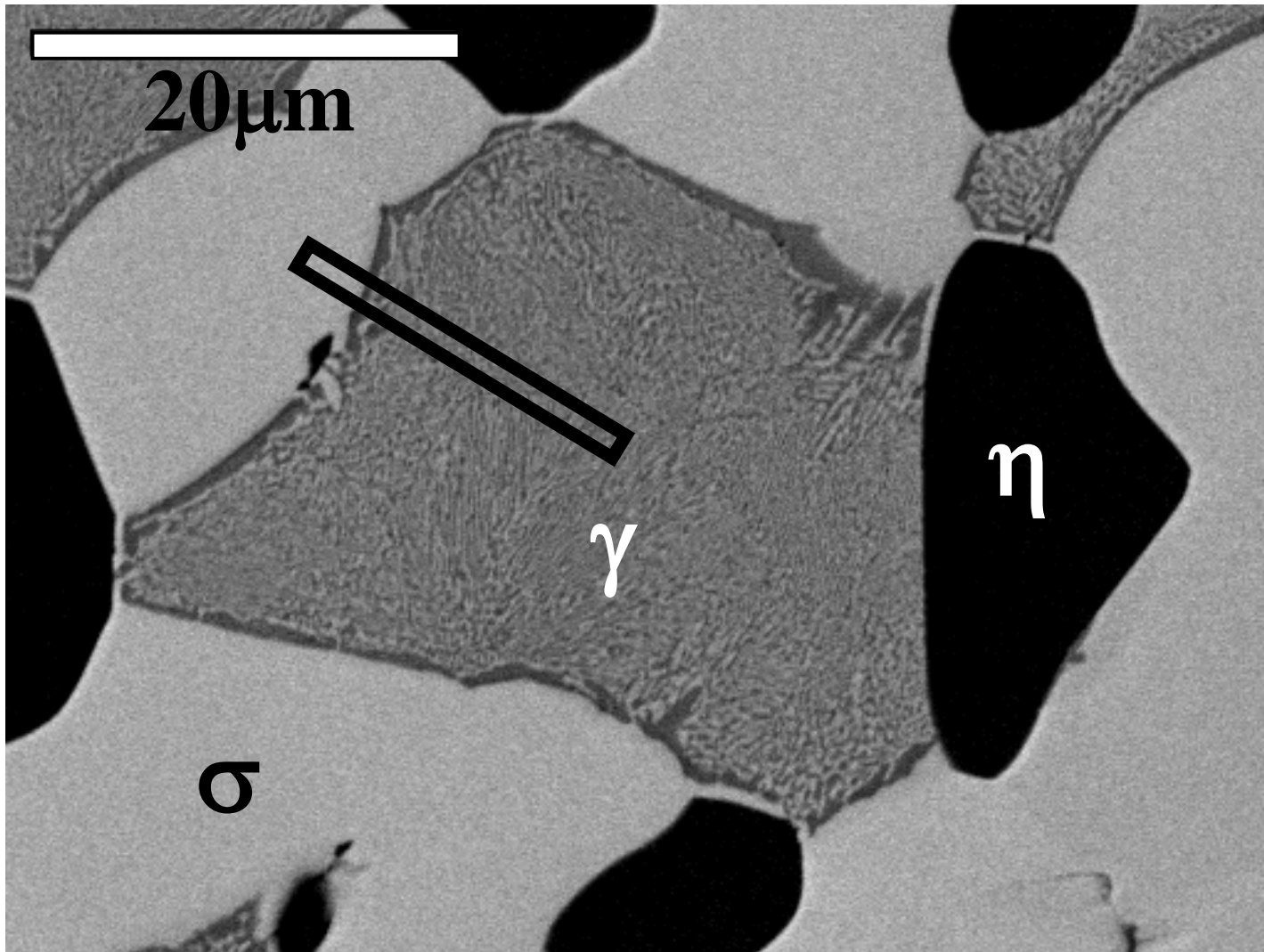


Figure 8-1 SEM micrograph of alloy A1 heat-treated at 1510C and quenched marked with the location of the thin foil machined via FIB.

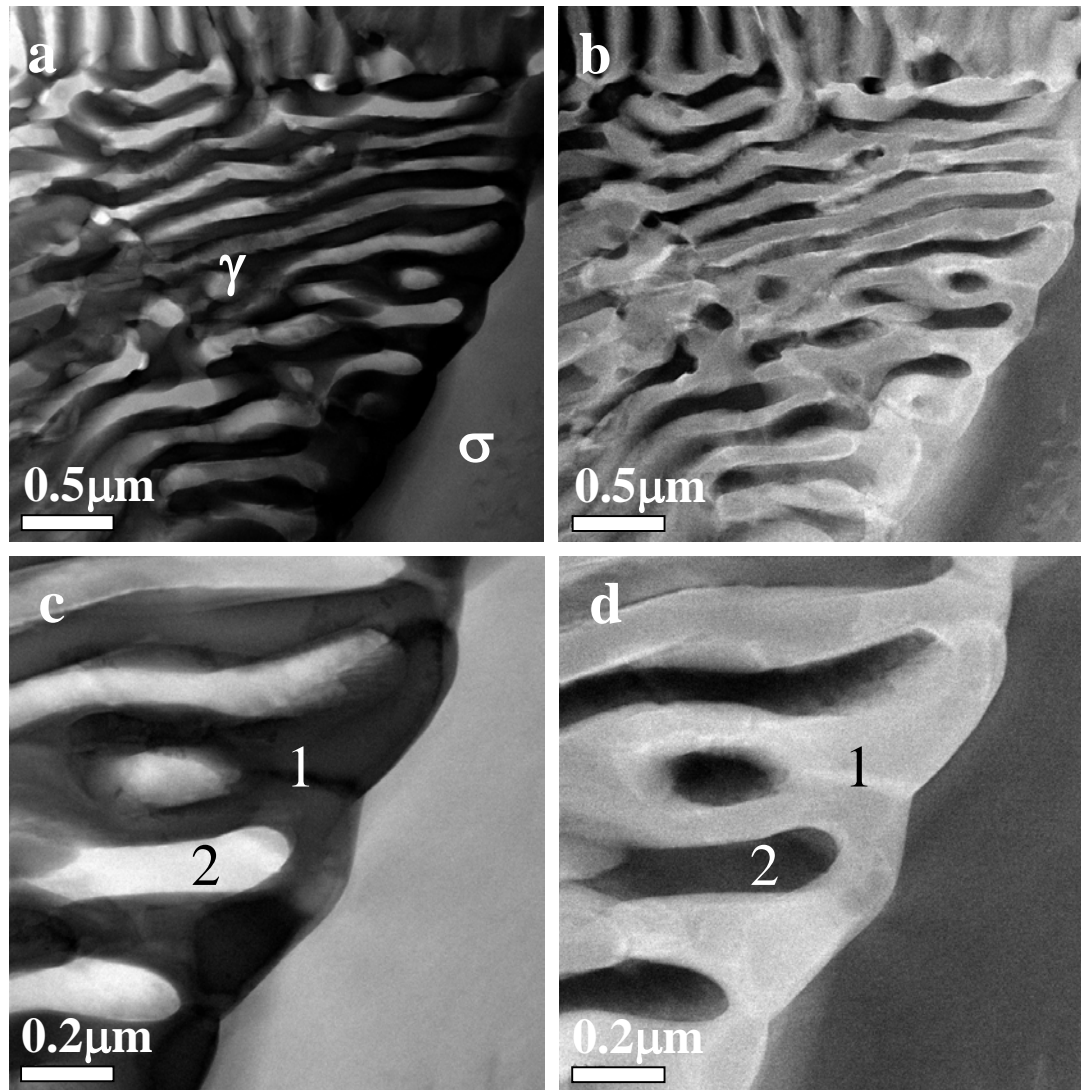


Figure 8-2 STEM micrographs of alloy A1 showing a) bright field image marked with the  $\sigma$  and prior  $\gamma$ -phase, and b) corresponding dark field micrograph, c) higher magnification bright field image with regions 1 and 2 defined, and d) corresponding dark field image.

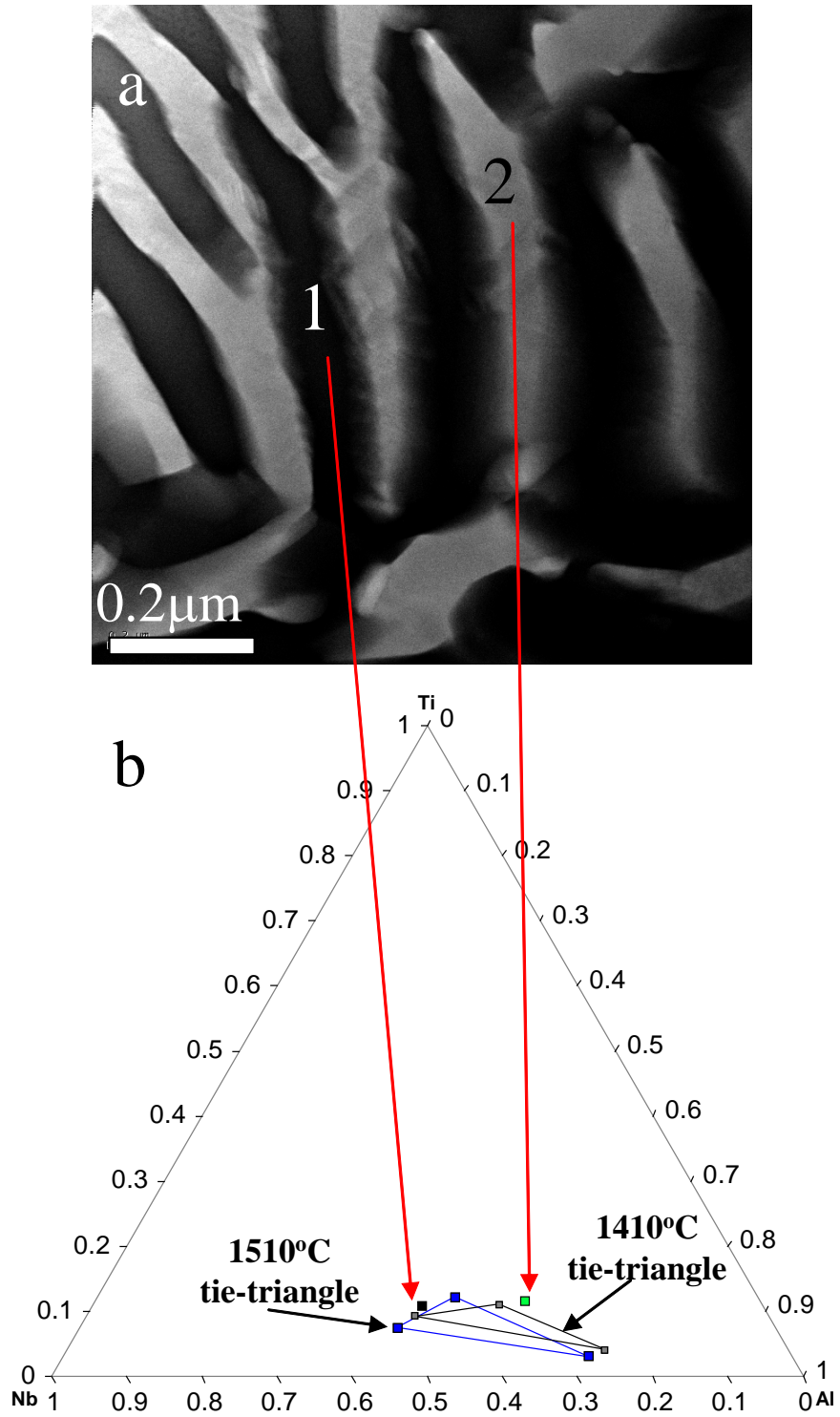


Figure 8-3 TEM micrograph of alloy A1 heat-treated and quenched from 1510C showing a) the transformed  $\gamma$ -phase and b) TEM EDS compositional analysis of the phases that form upon quenching along with the 1510C and 1410C tie-triangles.

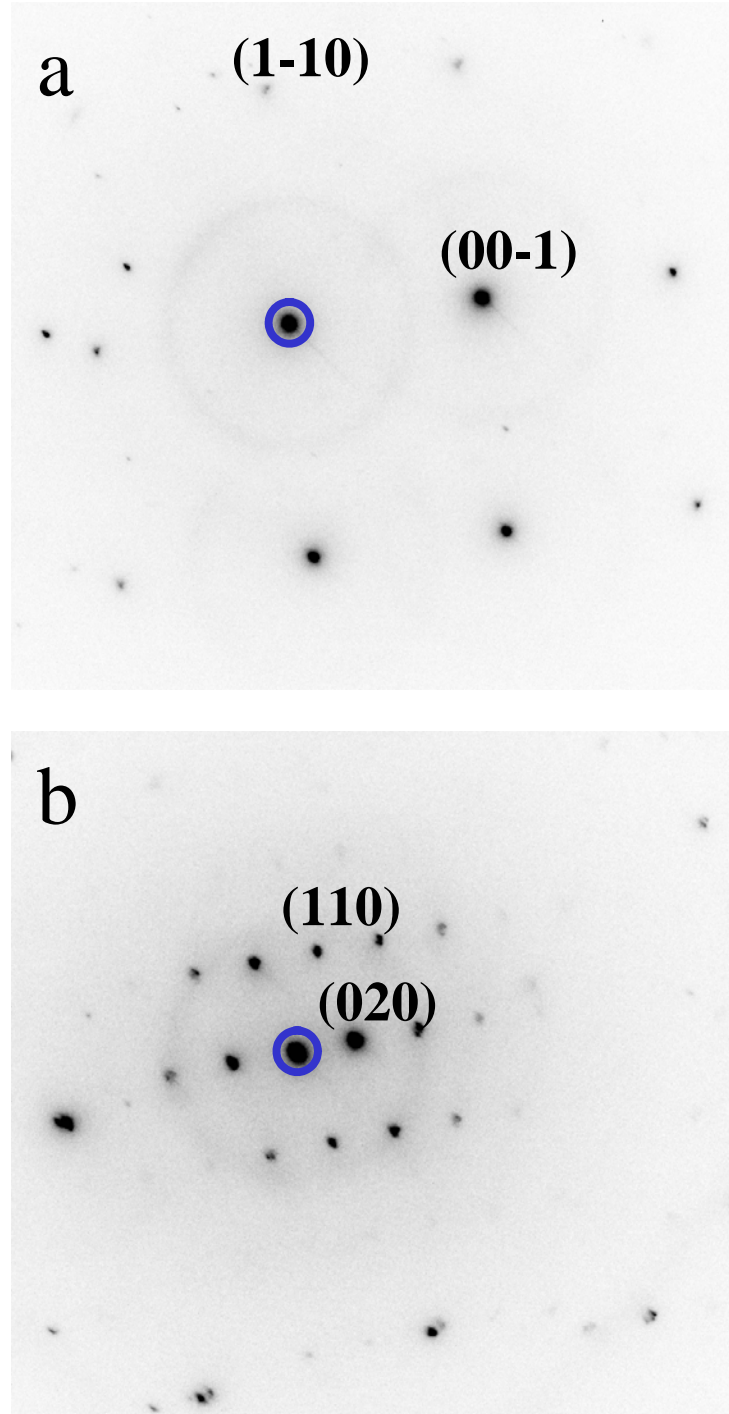


Figure 8-4 SAD patterns of the phases found within the prior  $\gamma$ -phase boundary in that a) shows the  $[110]$  zone axis of the  $\gamma$ -phase and b) shows the  $[001]$  zone axis pertaining of the h-phase.

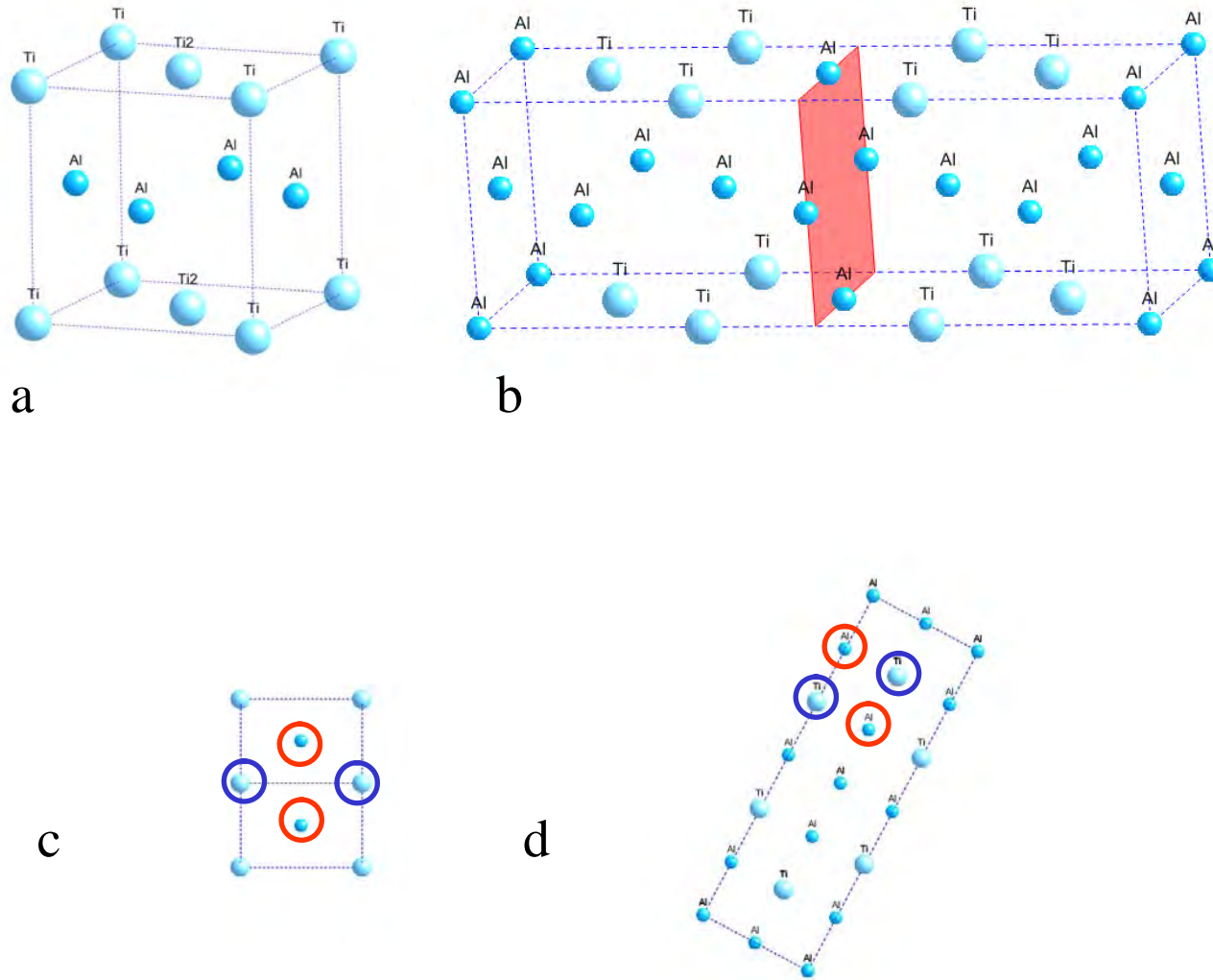


Figure 8-5 Lattice models of a) the  $\gamma$ -phase and b) the h-phase along with the relative orientation each crystal as measured in heat-treated and quenched alloy Al which is also marked with coincidence sites in c) the  $\gamma$ -phase and d) the h-phase

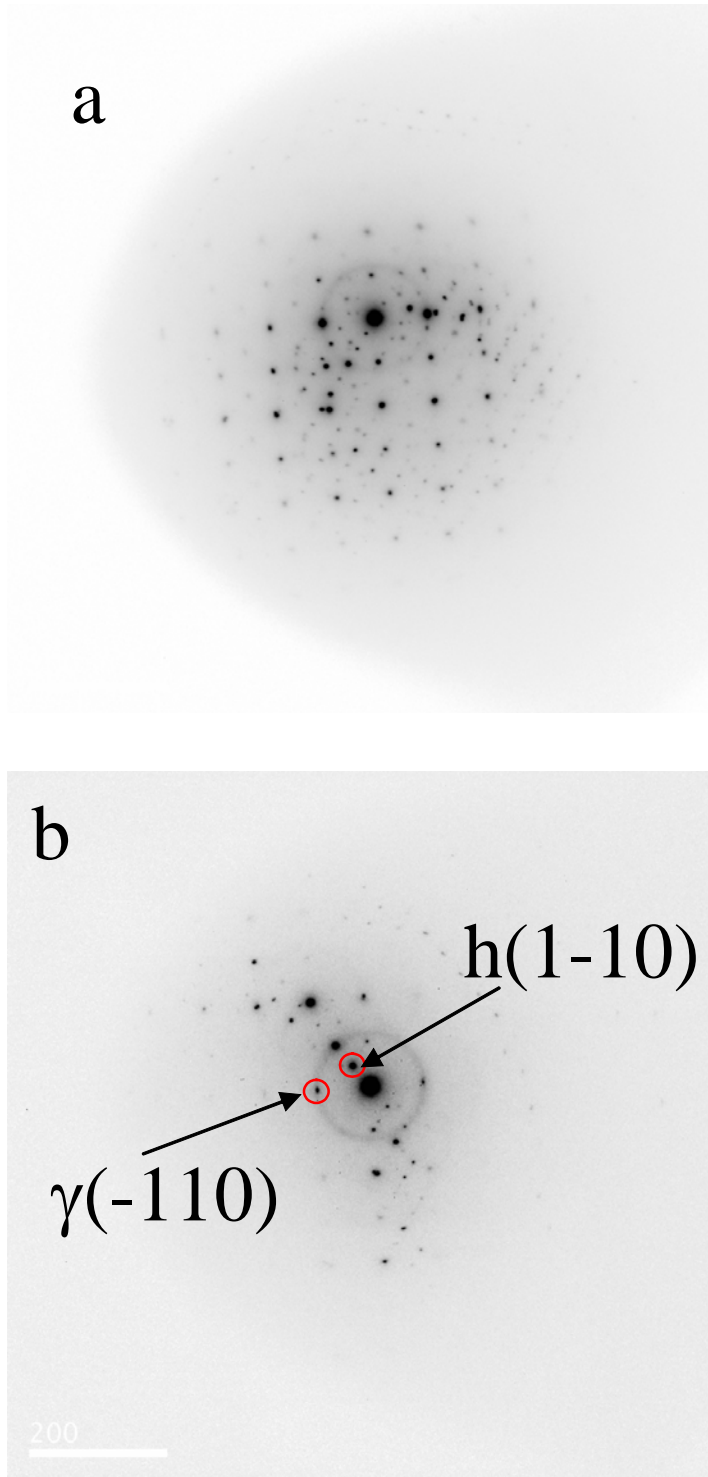


Figure 8-6 SAD patterns of a) the  $\gamma$  and  $h$  phases along with b) a two beam condition off the  $\gamma$ -phase's zone axis.

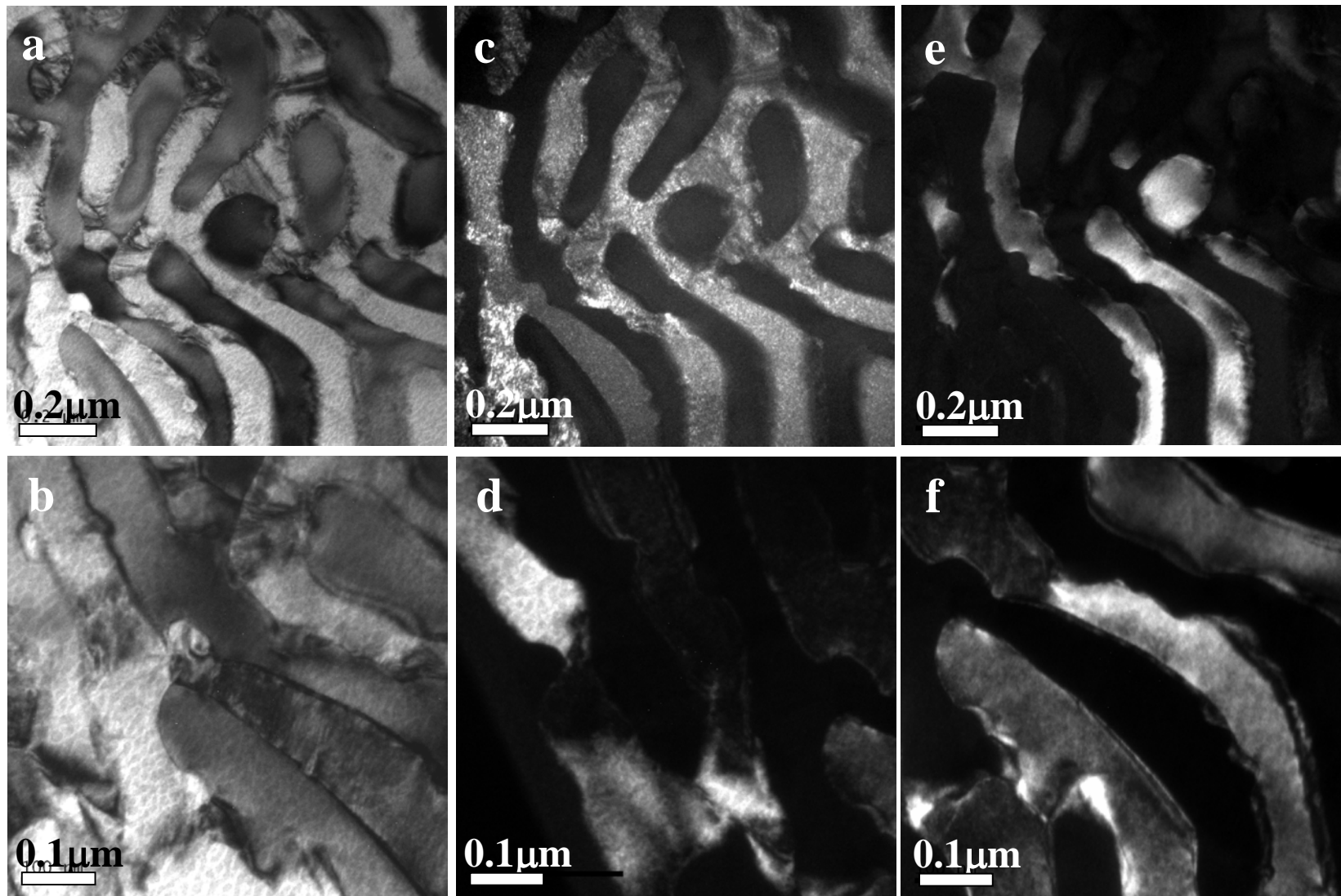


Figure 8-7 TEM micrographs of the transformed  $\gamma$ -phase region in a) and b) which are bright field images of the  $\gamma$  and h phases at two different magnifications. c) and d) show dark field images of the  $\gamma$ -phase corresponding to (a) and (d), while e) and f) are dark field images of the h-phase corresponding to bright field images in (a) and (b).

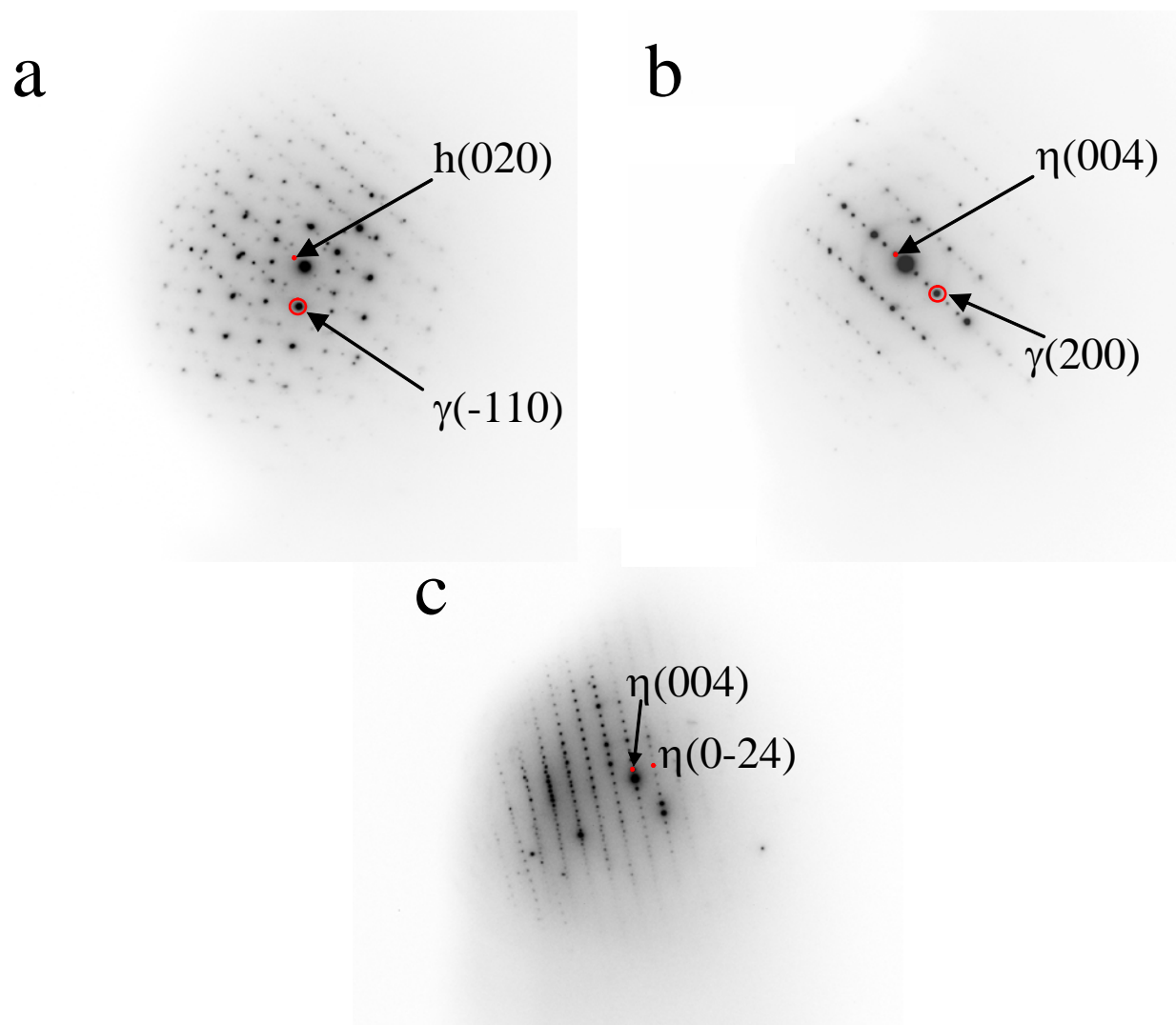


Figure 8-8 TEM SAD diffraction patterns with a)  $\gamma[110]$  and  $h[001]$  zone axes, b) formation of the  $\eta$ -phase after high intensity e-beam exposure, and c) complete transformation of the  $\gamma$  and  $h$  phases to the  $\eta$ -phase after further exposure to the high intensity e-beam.

## CHAPTER 9 CONCLUSIONS AND SUGGESTED FUTURE STUDIES

### 9.1 Summary and Conclusions

High-temperature equilibrium in the Ti-Al-Nb system was studied through the examination of microstructure, transformation temperatures, composition and structure. Several regions of interest within the ternary phase diagram were targeted. These were motivated by the critical role of the phase diagram in the development of high-temperature  $\gamma+\sigma$  alloys. In this study the  $\beta$ -phase field, the invariant reactions involving the L,  $\gamma$ ,  $\sigma$ ,  $\beta$  and L,  $\eta$ ,  $\sigma$ ,  $\beta$  phases, high-temperature equilibrium among L,  $\gamma$ ,  $\sigma$ ,  $\beta$  phases and a metastable transformation occurring upon quenching of the  $\gamma$ -phase from 1510C were examined. These results and their analyses led to an assessment of the primary crystallization fields of the  $\beta$ ,  $\gamma$ ,  $\sigma$  and  $\eta$  phases along with high-temperature equilibrium in the central portion as well as the high Al corner of the ternary Ti-Al-Nb phase diagram.

Based on the results of this study it was concluded that the primary  $\beta$ -phase field extends further into the ternary than was previously predicted. It was demonstrated that the transformation of the  $\beta$ -phase to the  $\gamma$ -phase cannot be suppressed by quenching, that was probably the cause of controversy in the previously reported studies. A reinvestigation of alloy D2 (33Ti-40Al-27Nb, at%) combined with a detailed study of alloy 11 (37Ti-44.5Al-18.5Nb, at%) using DTA, microstructural analysis and high-temperature XRD measurements revealed that the single  $\beta$ -phase exists below the solidus temperature in the latter alloy.

Through the evaluation of thermal and microstructural evidences for two alloys, the invariant reaction involving the L,  $\gamma$ ,  $\sigma$ ,  $\eta$  phases is concluded to be a ternary eutectic reaction. Analysis of the as-cast alloy as well as slowly solidified alloy A2 (8.5Ti-51.5Al-40Nb, at%)

revealed that the  $\sigma$ -phase failed to nucleate directly from the liquid even though heat-treatment experiments at temperatures slightly under the invariant reaction (1510C) confirmed that this phase should be a primary phase. Analysis of this alloy's as-cast microstructure in the absence of heat-treatment experiments and thermal evidence could obscure the evaluation of the ternary eutectic reaction that quite possibly is a source for the discrepancies reported experimentally.

The results of this investigation revealed that within 1510C to 1410C temperature range the solubility of Nb in the  $\gamma$ -phase decreases by over 10 at%. The solid-state transformation, that follows the eutectic invariant reaction, as well as the spinodal decomposition of the  $\gamma$ -phase upon fast cooling are suggested to be associated with this retraction of the Nb content.

A series of 9 alloys were designed in conjunction with the L,  $\gamma$ ,  $\sigma$ ,  $\eta$  invariant reaction alloys in order to develop the phase equilibria between the  $\beta$ ,  $\gamma$ ,  $\sigma$  phases at 1510C. The  $\sigma+\gamma$  and  $\sigma+\beta$  two regions along with the  $\sigma+\gamma+\beta$  three-phase tie-triangle were measured and combined with the alloys used to develop the eutectic reaction. The isothermal section was compared to the optimized phase diagram in that the equilibrium involving the  $\beta$ ,  $\gamma$  and  $\sigma$  phases were found to be in good agreement. The composition difference between the  $\beta$  and  $\gamma$  phases in equilibrium with the  $\sigma$ -phase was found to be smaller than predicted. This difference however, was consistent with the  $\beta$ ,  $\sigma$ ,  $\gamma$  tie-triangle measured near the L,  $\gamma$ ,  $\sigma$ ,  $\beta$  invariant reaction. These alloys and the isothermal section were searched for evidences associated with the L,  $\gamma$ ,  $\sigma$ ,  $\eta$  invariant reaction, however, it was determined that 1510C was too far below the invariant temperature to directly link the isothermal section to the invariant reaction.

The study of seven alloys targeting the somewhat elusive L,  $\gamma$ ,  $\sigma$ ,  $\beta$  invariant reaction revealed the ternary peritectic formation of the  $\gamma$ -phase. The  $\gamma$ -phase was concluded to form through a peritectic reaction involving the L,  $\sigma$ , and  $\beta$  phases. A tie-triangle representative of the

composition of the  $\gamma$ ,  $\sigma$  and  $\beta$  phases just below the invariant plane was measured by TEM/EDS of the interdendritic regions. The peritectic composition was found to be near 27.4Nb-47.9Al-24.7Ti, at%.

The results of this study were employed in a collaborative effort to optimize the high-temperature phase equilibrium in the Ti-Al-Nb alloy system. The optimized phase diagrams were compared to the experimental results though out this study that after several iterations was generally in good agreement. This information combined with the isothermal section at 1510C compiles into a representative assessment of high-temperature equilibrium that fills in some of the gray areas where experimental results were lacking.

## 9.2 Suggested Future Work

Equilibrium in the Ti-Al-Nb alloy system forms an interesting and complex phase diagram. As with every complex phase diagram there is almost endless room for further optimization and experiments. In this study the focus was on examining a very specific region of the ternary phase diagram at generally high temperatures. We have shown two of the invariant reactions involving the liquid as well as developed and isothermal section at 1510C and a tie-triangle at 1410C. In any series of targeted experiments the researchers must choose what areas to focus on being mindful of time and resources. This work focused heavily on accurately determining equilibrium by interpretation of the attainable evidence. Many questions are left unanswered that could prove quite useful to the design of modern high-temperature alloys. The following are a few ideas from a wealth of interesting areas available to further address.

- 1 Determine the effect of Nb on the  $\gamma$ -phase. The  $\gamma$ -phase interestingly formed through a peritectic reaction then extended toward the Nb corner of the ternary phase diagram at 1510C followed by a retraction at lower temperatures. It may prove helpful to investigate the fundamental reasons as to why this phase is stabilized by Nb at high temperatures.

- 2 Perform further thermal analysis on the ternary peritectic reaction. The temperature capabilities of the DTA instrument were not sufficient to reach the peritectic invariant plane. Higher temperature thermal analysis could prove useful to measure the temperature of the invariant plane as well as allow for analysis of the melting curve through the peritectic reaction. To the best of the authors knowledge there is no DTA data showing the melting and solidification of a ternary peritectic reaction.
- 3 Further investigate the nucleation of the  $\sigma$ -phase. The  $\sigma$ -phase did not nucleate in several alloys although there was a driving force for the event. It would be interesting to investigate why the  $\sigma$ -phase does not nucleate and what are the effects of alloying additions on the probability of its nucleation.

## LIST OF REFERENCES

- [1] Reed RC. The Superalloys: Fundamentals and Applications: Cambridge University Press, 2006.
- [2] Harris K. Single-Crystal Superalloy Drives Turbine Advances. *Advanced Materials & Processes* 1995;147:39.
- [3] Subramanian PR, Mendiratta MG, Dimiduk DM. The development of Nb-based advanced intermetallic alloys for structural applications. *Jom-Journal of the Minerals Metals & Materials Society* 1996;48:33.
- [4] Subramanian PR, Mendiratta MG, Dimiduk DM, Stucke MA. Advanced intermetallic alloys - beyond gamma titanium aluminides. *Materials Science and Engineering a-Structural Materials Properties Microstructure and Processing* 1997;240:1.
- [5] Hayes RW, London B. On the Creep Deformation of a Cast near Gamma TiAl Alloy Ti-48Al-1Nb. *Acta Metallurgica Et Materialia* 1992;40:2167.
- [6] Martin PL, Mendiratta MG, Lipsitt HA. Creep Deformation of TiAl and TiAl+W Alloys. *Metallurgical Transactions a-Physical Metallurgy and Materials Science* 1983;14:2170.
- [7] Kandra JT, Lee EW. Temperature and Microstructural Dependence of the Deformation of a High Nb Ti-Al Alloy. *Metallurgical and Materials Transactions a-Physical Metallurgy and Materials Science* 1994;25:1667.
- [8] Xu XJ, Xu LH, Lin JP, Wang YL, Lin Z, Chen GL. Pilot processing and microstructure control of high Nb containing TiAl alloy. *Intermetallics* 2005;13:337.
- [9] Kawabata T, Fukai H, Izumi O. Effect of ternary additions on mechanical properties of TiAl. *Acta Materialia* 1998;46:2185.
- [10] Masahashi N, Mizuhara Y, Matsuo M, Hanamura T, Kimura M, Hashimoto K. High-Temperature Deformation-Behavior of Titanium Aluminide Based Gamma Plus Beta Microduplex Alloy. *Isij International* 1991;31:728.
- [11] deAragao BJG, Ebrahimi F. High temperature deformation of Nb-Ti-Al alloys with sigma+gamma microstructure. *Materials Science and Engineering a-Structural Materials Properties Microstructure and Processing* 1996;208:37.
- [12] Brady MP, Gleeson B, Wright IG. Alloy design strategies for promoting protective oxide scale formation. *Jom-Journal of the Minerals Metals & Materials Society* 2000;52:16.
- [13] Ebrahimi F, Castillogomez JR. The Effect of Plastic-Deformation on Fracture Morphology of the Sigma-Phase in the Nb-Ti-Al System. *Acta Metallurgica Et Materialia* 1992;40:1409.

- [14] Ebrahimi F, Dearagao BJK, Castillogomez JR. Evaluation of Fracture-Toughness of Duplex Microstructures by an Indentation Technique. *Materials Science and Engineering a-Structural Materials Properties Microstructure and Processing* 1994;177:L7.
- [15] Ebrahimi F, Hoelzer DT, Castillogomez JR. Fracture-Toughness of Sigma+X Microstructures in the Nb-Ti-Al System. *Materials Science and Engineering a-Structural Materials Properties Microstructure and Processing* 1993;171:35.
- [16] Raghavan V. Al-Nb-Ti (aluminum-niobium-titanium). *Journal of Phase Equilibria and Diffusion* 2005;26:360.
- [17] H. L. Lucas SGF, B. Sundman. *Computational thermodynamic: The Calphad method*. Cambridge: Cambridge University Press, 2007.
- [18] Servant C, Ansara I. Thermodynamic assessment of the Al-Nb-Ti system. *Berichte Der Bunsen-Gesellschaft-Physical Chemistry Chemical Physics* 1998;102:1189.
- [19] Hoelzer DT. Phase transformations in the central portion of the Nb-Ti-Al ternary system. *Material Science and Engineering*, vol. Doctors. Gainesville: University of Florida, 1996. p.320.
- [20] Duwez P, Taylor JL. Crystal Structure of TiAl. *Journal of Metals* 1952;4:70.
- [21] Zhang LC, Palm M, Stein F, Sauthoff G. Formation of lamellar microstructures in Al-rich TiAl alloys between 900 and 1100 degrees C. *Intermetallics* 2001;9:229.
- [22] Hall EO, Algie SH. Sigma Phase. *Journal of the Institute of Metals* 1966;94:61.
- [23] Potzschke M, Schubert K. Zum Aufbau einiger zu T4-B3 Homologer Und Quasihomologer Systeme .2. Die Systeme Titan-Aluminium, Zirkonium-Aluminium, Hafnium-Aluminium, Molybdan-Aluminium Und Einige Ternare Systeme. *Zeitschrift Fur Metallkunde* 1962;53:548.
- [24] Kohmoto H, Shyue J, Aindow M, Fraser HL. Observation of a Metastable-B2 Phase in Rapidly Solidified Ribbons of Nb-Al Alloys. *Scripta Metallurgica Et Materialia* 1993;29:1271.
- [25] Hellwig A, Palm M, Inden G. Phase equilibria in the Al-Nb-Ti system at high temperatures. *Intermetallics* 1998;6:79.
- [26] Sadi FA, Servant C. On the B2 -> O phase transformation in Ti-Al-Nb alloys. *Mater. Sci. Eng. A-Struct. Mater. Prop. Microstruct. Process.* 2003;346:19.
- [27] Wu B, Shen JY, Chu MY, Shang SL, Zhang Z, Peng DL, Liu SQ. The ordering behaviour of the O phase in Ti<sub>2</sub>AlNb-based alloys. *Intermetallics* 2002;10:979.

- [28] Sadi FA, Servant C, Cizeron G. Phase transformations in Ti-29.7Al-21.8Nb and Ti-23.4Al-31.7Nb (at.%) alloys. *Mater. Sci. Eng. A-Struct. Mater. Prop. Microstruct. Process.* 2001;311:185.
- [29] Mishurda JC, Vasudevan VK. An estimate of the kinetics of the beta(0) to orthorhombic phase transformation in the Nb-Ti-Al system. *Scr. Mater.* 2001;45:677.
- [30] Muraleedharan K, Nandy TK, Banerjee D, Lele S. Phase-Stability and Ordering Behavior of the O-Phase in Ti-Al-Nb Alloys. *Intermetallics* 1995;3:187.
- [31] Bendersky LA, Roytburd A, Boettinger WJ. Phase-Transformations in the (Ti,Al)<sub>3</sub>Nb Section of the Ti-Al-Nb System .1. Microstructural Predictions Based on a Subgroup Relation between Phases. *Acta Metall. Mater.* 1994;42:2323.
- [32] Bendersky LA, Boettinger WJ. Phase-Transformations in the (Ti,Nb)<sub>3</sub>Al Section of the Ti-Al-Nb System .2. Experimental Tem Study of Microstructures. *Acta Metall. Mater.* 1994;42:2337.
- [33] Bendersky LA, Boettinger WJ, Biancaniello FS. Intermetallic Ti-Al-Nb Alloys Based on Strengthening of the Orthorhombic Phase by Omega-Type Phases. *Mater. Sci. Eng. A-Struct. Mater. Prop. Microstruct. Process.* 1992;152:41.
- [34] Bendersky LA, Boettinger WJ, Roytburd A. Coherent Precipitates in the Bcc Orthorhombic 2-Phase Field of the Ti-Al-Nb System. *Acta Metall. Mater.* 1991;39:1959.
- [35] Muraleedharan K, Naidu SVN, Banerjee D. Orthorhombic Distortions of the Alpha-2 Phase in Ti<sub>3</sub>Al-Nb Alloys - Artifacts and Facts. *Scr. Metall. Materialia* 1990;24:27.
- [36] Mozer B, Bendersky LA, Boettinger WJ. Neutron Powder Diffraction Study of the Orthorhombic Ti<sub>2</sub>AlNb Phase. *Scr. Metall. Materialia* 1990;24:2363.
- [37] Kestnerweykamp HT, Ward CH, Broderick TF, Kaufman MJ. Microstructures and Phase-Relationships in the Ti<sub>3</sub>Al + Nb System. *Scripta Metallurgica* 1989;23:1697.
- [38] Banerjee D, Gogia AK, Nandi TK, Joshi VA. A New Ordered Orthorhombic Phase in a Ti<sub>3</sub>Al-Nb Alloy. *Acta Metallurgica* 1988;36:871.
- [39] Banerjee D, Nandy TK, Gogia AK. Site Occupation in the Ordered Beta Phase of Ternary Ti-Al-Nb Alloys. *Scripta Metallurgica* 1987;21:597.
- [40] Konitzer DG, Jones IP, Fraser HL. Site Occupancy in Solid-Solutions of Nb in the Intermetallic Compounds TiAl and Ti<sub>3</sub>Al. *Scripta Metallurgica* 1986;20:265.
- [41] Wilson CG, Spooner FJ. Sphere-Packing Model for Prediction of Lattice-Parameters and Order in Sigma-Phases. *Acta Crystallographica Section A* 1973;A 29:342.

- [42] Hayashi K, Nakano T, Umakoshi Y. Meta-stable region of Al<sub>5</sub>Ti<sub>3</sub> single-phase in time-temperature-transformation (TTT) diagram of Ti-62.5 at.% Al single crystal. *Intermetallics* 2002;10:771.
- [43] Nakano T, Negishi A, Hayashi K, Umakoshi Y. Ordering process of Al<sub>5</sub>Ti<sub>3</sub>, h-Al<sub>2</sub>Ti and r-Al<sub>2</sub>Ti with FCC-based long-period superstructures in rapidly solidified Al-rich TiAl alloys. *Acta Materialia* 1999;47:1091.
- [44] Palm M, Zhang LC, Stein F, Sauthoff G. Phases and phase equilibria in the Al-rich part of the Al-Ti system above 900 degrees C. *Intermetallics* 2002;10:523.
- [45] Chen GL, Wang JG, Ni XD, Lin JP, Wang YL. A new intermetallic compound in TiAl plus Nb composition area of the Ti-Al-Nb ternary system. *Intermetallics* 2005;13:329.
- [46] Chen GL, Wang JG, Wang XT, Ni XD, Hao SM, Ding JJ. Reply to the "Comment on 'Investigation on the 1000, 1150 and 1400 degrees C isothermal section of the Ti-Al-Nb system'" - Part I. Ordering of Nb in gamma-TiAl and gamma(1) phase. *Intermetallics* 1998;6:323.
- [47] Chen GL, Wang XT, Ni KQ, Hao SM, Cao JX, Zhang X. Investigation on the 1000, 1150 and 1400 degrees C isothermal section of the Ti-Al-Nb system. *Intermetallics* 1996;4:13.
- [48] Jackson AG. Identification of the L60 Phase in a Gamma-Ti-Al-Nb Alloy. *Scripta Metallurgica Et Materialia* 1993;28:673.
- [49] Liu HW, Luo CP, Yuan Y, Liu JM, Liu ZG. Interpretation of the morphology and crystallography of precipitate (gamma 1)-Ti<sub>4</sub>Nb<sub>3</sub>Al<sub>9</sub> in L1(0)-TiAl(Nb)-based intermetallics by invariant line theory. *Intermetallics* 2007;15:1497.
- [50] Liu HW, Yuan Y, Liu ZG, Liu JM, Zhao XN, Zhu YY. TEM characterization of the precipitation reaction in Ti-48Al-10Nb alloy. *Mater. Sci. Eng. A-Struct. Mater. Prop. Microstruct. Process.* 2005;412:328.
- [51] Wilson CG, Spooner FJ. Order in NbAl and TaAl Type Sigma-Phases. *Journal of Materials Science* 1977;12:1653.
- [52] Jorda JL, Flukiger R, Muller J. A New Metallurgical Investigation of the Niobium-Aluminum System. *Journal of the Less-Common Metals* 1980;75:227.
- [53] Kaltenbach K, Gama S, Pinatti DG, Schulze K, Henig ET. A Contribution to the Ternary-System Al-Nb-Ti. *Zeitschrift Fur Metallkunde* 1989;80:535.
- [54] Leonard KJ, Mishurda JC, Vasudevan VK. Examination of solidification pathways and the liquidus surface in the Nb-Ti-Al system. *Metallurgical and Materials Transactions B-Process Metallurgy and Materials Processing Science* 2000;31:1305.

- [55] Zdziobek A, Durandcharre M, Driole J, Durand F. Experimental Investigation of High-Temperature Phase-Equilibria in the Nb-Al-Ti System. *Zeitschrift Fur Metallkunde* 1995;86:334.
- [56] Kattner UR, Boettinger WJ. Thermodynamic Calculation of the Ternary Ti-Al-Nb System. *Materials Science and Engineering a-Structural Materials Properties Microstructure and Processing* 1992;152:9.
- [57] J. H. Perepezko YAC, L. E. Seitzman, J. C. Lin, N.R. Bonda, T. J. Jewett, and J. C. Mishurda. High Temperature Phase Stability in the Ti-Al-Nb System. In: S. H. Whang CTL, D. P. Pope, J. O. Stiegler, editor. *High Temperature Aluminides and Alloys*, vol. 19: TMS, Warrendale, PA, 1990.
- [58] Kazantseva NV, Lepikhin SV. Study of the Ti-Al-Nb phase diagram. *Phys. Metals Metallogr.* 2006;102:169.
- [59] Chladil HF, Clemens H, Leitner H, Bartels A, Gerling R, Schimansky FP, Kremmer S. Phase transformations in high niobium and carbon containing gamma-TiAl based alloys. *Intermetallics* 2006;14:1194.
- [60] Kainuma R, Fujita Y, Mitsui H, Ohnuma I, Ishida K. Phase equilibria among alpha (hcp), beta (bcc) and gamma (L1(0)) phases in Ti-Al base ternary alloys. *Intermetallics* 2000;8:855.
- [61] Eckert M, Kath D, Hilpert K. Thermodynamic activities in the alloys of the Ti-Al-Nb system. *Metall. Mater. Trans. A-Phys. Metall. Mater. Sci.* 1999;30:1315.
- [62] Hou DH, Fraser HL. The ordering scheme in N-B aluminides with the B2 crystal structure. *Scr. Mater.* 1997;36:617.
- [63] Menon ESK, Subramanian PR, Dimiduk DM. Phase transformations in Nb-Al-Ti alloys. *Metall. Mater. Trans. A-Phys. Metall. Mater. Sci.* 1996;27:1647.
- [64] Nakamura H, Takeyama M, Yamabe Y, Kikuchi M. Phase-Equilibria in Tial Alloys Containing 10 Percent and 20 at Percent Nb at 1473-K. *Scr. Metall. Materialia* 1993;28:997.
- [65] Suryanarayana C, Lee DS. Phase-Relations in Ti-Al-Nb Alloys at 1200-Percent-C. *Scr. Metall. Materialia* 1992;26:919.
- [66] Menon ESK, Subramanian PR, Dimiduk DM. Phase-Equilibria in Niobium Rich Nb-Al-Ti Alloys. *Scr. Metall. Materialia* 1992;27:265.
- [67] Rhines FN. *Phase Diagrams in Metallurgy*: McGraw-Hill Inc., 1956.
- [68] Gulliver GH. The quantitative effect of rapid cooling upon the constitution of binary alloys. *Journal of the Institute of Metals* 1913;9:120.

- [69] Scheil E. model. *Zeitschrift fur metallkunde* 1942;70.
- [70] Glicksman ME, Hills RN. Non-equilibrium segregation during alloy solidification. *Philos. Mag. A-Phys. Condens. Matter Struct. Defect Mech. Prop.* 2001;81:153.
- [71] Johnson DR, Oliver BF. Ternary Peritectic Solidification in the Ni-Al-Ni<sub>2</sub>Al<sub>3</sub>-NiAl<sub>3</sub> System. *Materials Letters* 1994;20:129.
- [72] Boettinger WJ, Kattner UR, Moon KW, Perepezko JH. DTA and Heat-flux DSC Measurements and Alloy Melting and Freezing NIST 2006;SP 960-15.
- [73] Hö hne G, W. Hemminger, and H.-J. Flammersheim. *Differential scanning calorimetry: an introduction for practitioners.* Berlin: Springer-Verlag. , 1996.
- [74] DeHoff RT. *Thermodynamics in materials science:* Boca Raton: CRC/Taylor & Francis., 2006.
- [75] Leonard KJ, Vasudevan VK. Phase equilibria and solid state transformations in Nb-rich Nb-Ti-Al intermetallic alloys. *Intermetallics* 2000;8:1257.
- [76] Cupid DM, Fabrichnaya O, Rios O, Ebrahimi F, Seifert HJ. Thermodynamic re-assessment of the Ti-Al-Nb system. *International Journal of Materials Research* 2009;100:218.
- [77] Rios O, Goyel S, Kesler MS, Cupid DM, Seifert HJ, Ebrahimi F. An evaluation of high-temperature phase stability in the Ti-Al-Nb system. *Scripta Materialia* 2009;60:156.
- [78] Cupid DM, Rios O. 2008.
- [79] Cupid DM. THERMODYNAMIC ASSESSMENT OF THE TI-AL-NB SYSTEM. University of Florida, 2009.
- [80] Witusiewicz VT, Bondar AA, Hecht U, Velikanova TY. The Al-B-Nb-Ti system. IV. Experimental study and thermodynamic re-evaluation of the binary Al-Nb and ternary Al-Nb-Ti systems. *Journal of Alloys and Compounds* 2009;472:133.
- [81] Stein F, Zhang LC, Sauthoff G, Palm M. TEM and DTA study on the stability of Al<sub>5</sub>Ti<sub>3</sub>- and h-Al<sub>2</sub>Ti-superstructures in aluminium-rich TiAl alloys. *Acta Materialia* 2001;49:2919.
- [82] Cahn JW. On Spinodal Decomposition. *Acta Metallurgica* 1961;9:795.
- [83] Glotzer SC, Dimarzio EA, Muthukumar M. Reaction-Controlled Morphology of Phase-Separating Mixtures. *Physical Review Letters* 1995;74:2034.

## BIOGRAPHICAL SKETCH

Orlando Rios is the son of Jose and Marta Rios. Orlando was raised in Miami, Florida where he had his primary schooling. At the age of eight, he began attending karate classes. This continued until he began college at the age of 19. He received high marks and recognition in several competitions. Orlando is also an established scuba diver and has completed advanced training in scuba diving including night, wreck, blue water, search and recovery and deep diving. Orlando loves outdoors and is an avid fisherman and hunter.

Upon completion of high school, Orlando was educated as automotive technician at Linsy Hopkins in Miami, Fl. After which he worked on rotary engines for two years while attending College where he received an associate in arts in engineering sciences. He then attended the University Of Florida where received a bachelor's degree in materials science and engineering.

Orlando's early graduate student career began with a study of naturally aging aluminum alloys. Afterwards, Orlando completed his master's at the University of Florida during which he was awarded a National Aeronautics and Space Administration funded Graduate Student Researchers Program fellowship. His research focused on instrument development and design, alloy development and advanced thermomechanical testing of high temperature shape memory alloys. Orlando completed his PhD with Dr. Fereshteh Ebrahimi on the study presented here.

Orlando had an undergraduate internship at Christian-Albrechts University of Kiel Germany where he had experience working with III-V semiconductors and porous silicon. He was fortunate to be nominated by his advisor and later selected to be a member of the United States Delegation at the Meeting of the Nobel Laureates in Lindau. Orlando also had teaching experience at the University of Florida during which he taught undergraduate chemistry. Upon completion of his doctoral degree, Orlando will begin conducting research at Oak Ridge National Labs.